UNIVERSITY OF BIRMINGHAM

AN INVESTIGATION OF THE ABILITY OF A NUMERICAL MODEL TO PREDICT THE CROSS SECTIONAL SHAPE OF AN ALLUVIAL CHANNEL

by

JOSE MANUEL RAMIREZ-LEON

A thesis to be submitted to

The University of Birmingham

for the degree of

DOCTOR OF PHILOSOPHY

Supervisors:

Prof. Mark Sterling and Dr. Xiaonan Tang

The University of Birmingham
School of Engineering
Department of Civil Engineering
Edgbaston
Birmingham
B15 2TT
United Kingdom

January 2014

Abstract

The research analyses the behaviour of the flow in an open channel with self-formed banksides, with the purpose of exploring the ability of a numerical model to predict such geometries. The strategy consists in contrast a numerical model with physical model data. With respect to the numerical model, it is divided in two main parts, the first one describing the flow and the second one defining the cross sectional geometry. For the first part, a quasi 2D flow structure was selected to model the flow, *i.e.* the Shiono and Knight Model (SKM) (Shiono and Knight, 1991), due to its simplicity and flexibility. It allows users to incorporate the variation of friction factor, f, secondary flow gradient, Γ, and dimensionless eddy viscosity, λ, across the section. In order to calculate the bankside geometry, the Yu and Knight Model (1998) was chosen, because it relates the equilibrium of particles on the boundary to the shear stress, τ_0, distribution.

With respect to the physical model, the shape of a self-formed bankside has been reproduced and assessed in a tilting flume, in order to identify its flow pattern by measuring velocity and shear stress. Such data was used for calibration and validation of the numerical model. The cross section was inspired in the bankside obtained by Ikeda (1981), fitting it into a flume 46cm wide. The experiment consists of testing the channel by three different slopes, three depths and two surfaces (smooth and rough), mapping velocity and measuring shear stress on the boundary across the section. The novelty of the work is to improve the flow estimation for this type of cross section, incorporating the secondary flow, and subsequently enhancing the approximation to the geometry that will be formed in alluvial channels.

TO MY PARENTS AND TO MY TEACHERS

Acknowledgments

I would like to express my gratitude to the ones that helped me during the elaboration of this thesis. I apologise in advance, if involuntarily I skipped someone.

First and foremost, a special thanks to my supervisor, Prof. Mark Sterling, for his long patience, dedication and trust. Besides the technical problems -that he helped me to solve- his direction shaped my formation and character as a researcher. Also to my co-supervisor, Dr. Xiaonan Tang for his kind support.

I would like also to thank my examiners, Prof. David Hargreaves and Dr. Hassan Hemida for assessing this document. Your comments and suggestions were very informative, they strengthened my thesis. Additionally, to my annual reviewers, Prof. Chris Baker, Dr. Andrew Quinn and Prof. John Bridgeman, your feedback had a tremendous impact in my research.

A special thanks to my family. Words cannot express how grateful I am to them for all of the sacrifices that you have made on my behalf. I would also like to thank all of my friends who supported me in writing, and encourage me to strive towards my goal.

Finally, this document would have been impossible without a scholarship, granted by CONACYT (Mexican Council for Science and Technology), and a PGTA Award. My eternal gratitude to my sponsors,

Table of Contents

List of Figures

List of Tables

Notation and Acronyms

A :	hydraulic area
a:	area of the particle
a_0 :	coefficients proposed by Vigilar and Diplas (1998)
a_1 :	coefficients proposed by Vigilar and Diplas (1998)
a_2 :	coefficients proposed by Vigilar and Diplas (1998)
a_3 :	coefficients proposed by Vigilar and Diplas (1998)
B :	surface half top width
b:	width of the central flatbed
b_c :	width of the contraction
b_f :	width of the flume
b_x :	transversal width of the transition at a distance x
C:	coefficient of secondary flow
C_2:	coefficient depending on μ and β
C_3:	coefficient depending on μ and β
C_4:	coefficient depending on μ and β
C_5:	coefficient depending on μ and β
C_L:	centerline of the channel
C_u:	coefficient of uniformity
$\hat{D}$	a function of the diameter $\hat{D} = 2d\left(\rho * g/\nu^2\right)^{1/3}$
$\overline{d}$	diameter of the Preston tube
d:	diameter of the soil particle
d_{50} :	median diameter size
d_{90}:	representative diameter that is bigger than the 90% of the sample
f:	Darcy-Weisbach friction factor
F_1:	lift force
F_d:	drag force
g:	acceleration due to gravity
h^*:	dimensionless local depth, h/h_c
h:	local depth
h_c:	central depth

h_{cn}:	central normal depth obtained by an iteration process
L_T :	transition length
m:	top width of the channel in threshold (see figure 1); m, the
m_c :	transversal slope, 1:m_c, vertical: horizontal
n:	friction resistance coefficient of the Manning equation
Q :	discharge
Q_{flmtr} :	discharge obtained by flowmeter readings
Q_{Pitot} :	discharge based on the velocity measurements taken by a Pitot-Static tube
p_i	coefficient of secondary flow affecting the corresponding SKM panel i
P:	wetted perimeter of the cross section
P_T:	total pressure
P_S:	static pressure
R^2	coefficient of determination
R:	hydraulic radius
RANS	Reynolds Averaged Navier-Stokes equation
s :	transversal slope;
S:	longitudinal slope
S':	static head read at the manometer
S_{ci}:	scale reading controlling the flume inclination for the corresponding set i
SKM:	Shiono and Knight Method
S_s :	ratio of solid to water density
S_w:	water surface slope of the corresponding flow profile
T :	top width of the channel bankside
T':	total head read at the manometer
t_g:	aperture of the tailgate
t_{gr}:	resultant aperture of the tailgate that produces the uniform flow condition
U:	longitudinal velocity
U_d:	local depth average velocity
U_{dmax}:	maximum depth average velocity, usually located at the centre line of the channel
U_{dtoe}:	depth average velocity at the junction between the flatbed and the bankside
U^*:	shear velocity
V:	average velocity of the channel's cross section, defined as Q/A
V_c:	mean velocity of the flow in an infinitely wide channel
V_d :	transversal depth-average velocity

V_o:	mean velocity at the centre of the channel
V_{Pitot}:	Average velocity of the section obtained by Pitot-Static tube measurements
y^*:	dimensionless horizontal distance from the junction
y:	transversal distance from the centre
z:	vertical distance from the bottom
Z_T:	vertical elevation at x
α':	inclination of the manometer, degrees
β:	ratio of lift to drag force, taken as 0.85
β_s:	dimensionless secondary flow, taken as 0.15
Γ:	lateral gradient of secondary flow , also known as secondary flow
γ:	water specific weight
ΔB:	contraction of the transition
ΔP:	pressure difference between total and static pressures
ΔZ:	step between the flume and the channel
θ:	side slope angle
Θ_c:	critical shields parameter
θ_{lg}:	longitudinal angle slope
λ:	dimensionless eddy viscosity
μ:	static coefficient of Coulomb friction ; tan φ
ν :	kinematic viscosity of water
ρ^*:	dimensionless submerged density of sediments:$(\rho_s-\rho)/\rho$=1.65
ρ:	density of water, 1000 kg/m^3
ρ_s:	density of sediments, 2650 kg/m^3
σ:	nonuniform sand coefficient, d_{90}/d_{50}
τ:	shear stress
τ_0:	local boundary or wall shear stress
τ_{0c}:	wall or boundary shear stress at channel centreline
τ_c:	critical shear stress
τ_{cr}:	critical shear stress of Shields
τ_{max}:	maximum boundary shear stress over the channel's cross section
τ_{toe}:	boundary shear stress at the toe (junction between the flatbed and the bankside)
φ:	angle of repose of the soil material

CHAPTER 1

INTRODUCTION

A common problem in river engineering is to predict the stable cross section that a stream can form, due to be under a dynamic process of erosion-deposition that alters its shape and by this, its conveyance capacity. To overestimate such geometries implies a waste of resources, and to underestimate them to put the surrounding area under flood risk. The stable condition of a section will be reached when the sediments inflow are equal to the sediments outflow.

Figure 1. A reach of the river Thames at Desborough Channel.

In order to predict this kind of section numerous methods exist, which can be separated interactive force and regime theory, this last can be divided in empirical (*e.g.* Kennedy, 1895, Lacey, 1930, Leopold and Maddock, 1953, etc.) and analytical

or rational (*e.g.* Griffiths, 1981, Julien and Wargadalam, 1995, Cao and Knight, 1996a, Yalin and Da Silva, 1999, Huang et al., 2002, Lee and Julien, 2006, etc). Among the methods, some others were found that predict the geometry of stable cross sections, like the regime theory, but defining the bankside shape, and taking into account the resistant shear stress of the bottom material, for example: Glover and Florey (1951), Henderson (1961), Stebbings (1963), Parker (1978a, 1978b, 1979), Diplas and Vigilar (1992), Cao and Knight (1996b, 1997, 1998), Yu and Knight (1998), Dey (2001), Ikeda (1981), Ikeda et al. (1988), Diplas (1990), Babaeyan-Koopaei and Valentine (1998), Vigilar and Diplas (1997, 1998) and Paquier and Knodashenas (2002).With respect to the drawbacks, it was found that: little attention has being paid to the influence of the secondary flow to the banksides, when evidence shows its existence and impact on the boundary (see Ikeda, 1981, Diplas, 1990); the shape of the central channel bed is not defined, and is not flat; most of the approaches are for nonuniform material, except from Ikeda (1988) and Cao and Knight (1998); and neither vegetation nor cohesive material were not considered by any author.

1.1 Aim

Hence, the aim of this research is to investigate the capacity of a simple quasi 2D flow model, *i.e.* the SKM(Shiono and Knight, 1990), in combination with bank side equations, to determine the bed profile of an alluvial channel, incorporating the secondary flow variables. It is expected to obtain flow parameter relations, that will clarify the mechanisms involved in rivers. This will enable engineers to predict stable self-formed sections in a long term, by using powerful and accessible methods. This fits in improving the prediction of natural streams, its hydraulic capacity estimation,

helping to prevent floods, protecting urban infrastructure and human life.

1.2 Objectives

In order to accomplish the aim, the following objectives were followed:

1. **Numerical modelling.** To build a numerical model that predicts the flow behaviour and the prediction of self-formed cross sections, *i.e* .the Yu and Knight (1998).
2. **Physical experiments.** To design, construct and implement a physical model to observe the flow behaviour in a cross section representing a self-formed bankside. It consists of a tilting flume using a parabolic section, inspired in the shape obtained experimentally by Ikeda (1981). The channel was tested by two surfaces, one smooth (PVC) and one rough (glue sand). The variables measured were discharge, water surface slope, and the distributions across the section of velocity and boundary shear stress.
3. **Calibration and comparisons.** To calibrate the numerical models with the physical results, adjusting three key factors: friction, f, secondary flow gradient, Γ, and dimensionless eddy viscosity, λ.
4. **Analysis.** From the calibration procedure, parameters for the hydraulics variables are proposed.
5. **Validation.** The relations proposed were applied to different examples, *i.e.*in order to corroborate them.

1.3 Structure of the document

The document is divided into: introduction, literature review, numerical model, physical model, calibration and validation, and finally conclusions. The literature review is about methods to predict self-formed cross section. The numerical model

explains the relationship between the flow model and the self-formed section. Meanwhile, the physical model refers to the lab experiment and the apparatus. The calibration and validation process shows the relationships obtained and its corresponding procedure. Finally the conclusions summarizes the findings obtained by the research. Furthermore, two appendices are included: appendix A reports the relationships between bankside width and depth by four methods; and appendix B shows the results of the simulations to determine the limits of the numerical model;

CHAPTER 2

LITERATURE REVIEW

Prediction of self-formed cross sections

Alluvial streams are erodible channels, characterized by transported sediments, reaching the dynamic stable condition when the inflow sediments are equal to the outflow sediments of a cross section. In order to predict this kind of channel, two main types of methods have been applied: the tractive force, and the regime theory. The regime theory consists of a set of equations proportioning the stable width, depth and slope of a stream, depending only on the discharge and the channel soil material. The first attempt of this type was given by Kennedy (1895), when he found a relationship between the main velocity and the depth of an irrigational channel without silting or scouring, based on observations on the Bari Doab canal system in India. His work was continued by Lindley, Ingles and Blench, and Lacey, producing the first set of equations (according to Simons and Senturk, 1992). Numerous efforts have been developed since then, and among authors the regime approaches can be divided into: empirical (*e.g.* Lacey, 1930, Leopold and Maddock, 1953) and analytical or rational (*e.g.* Huang et al., 2002, Yalin and Da Silva, 1999, Cao and Knight, 1996a, Griffiths, 1981, Julien and Wargadalam, 1995, Lee and Julien, 2006). The first type is based in geometrical observations, and the second one in physical laws that form part of the phenomenon.

Originally, the hydraulic geometry for alluvial streams was considered rectangular or trapezoidal. Later the importance of the banksides was noticed, as

proposed by Glover and Florey(1951) the first banksides in threshold of motion as parabolas connected by a central flatbed (see figures2 and 3). Later, Henderson (1961) continued the work and incorporated the critical shear stress of Shields to the central flatbed, methodology that was subsequently adopted by the USBR. The parabolic shape is mentioned by Chow (1959) as the a common section formed by rivers, while Mironenko *et al.*(1984) and Babaeyan-Koopaei *et al.*(2000) remarked its stability similar to a trapezoidal channel.

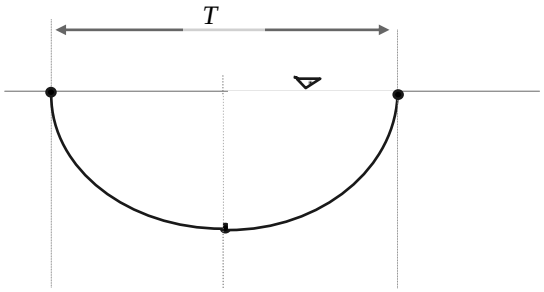

Figure 2. Cross section of a channel in threshold without flatbed.

Stebbings (1963) conducted experiments in a tilting flume (8.23m long, 91.5cm wide, and 25.4cm deep) with a bed full of uniform sand (d_{50}=0.88mm, σ=1.30), obtaining self-formed channels with cross sections at threshold of motion. The shape of such sections was parabolic and an equation describing them was proposed. Further approaches have been developed, being the one of Parker (1978b, and 1979) one of the most significant, due to infer a dynamic equilibrium between banks at threshold and an active bed, being this incompatible for a threshold channel, it was called the stable channel paradox (see figure 3).

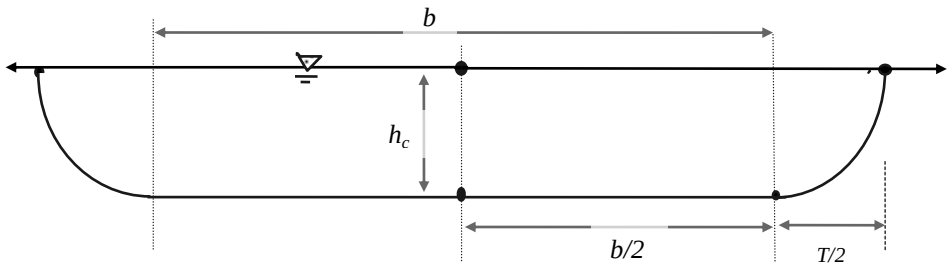

Figure 3. Cross sectional shape of a self-formed channel, constituted by banks in threshold and an active central flatbed.

Following the conceptof a parabolic bank profile, the next researches were: Diplas and Vigilar (1992), Cao and Knight (1996b, 1997, and 1998), and Yu and Knight (1998), and Dey (2001). While others have proposed equations describing the whole cross section, based on laboratory best fitted curves, for example: Ikeda (1981), Diplas (1990), and Babaeyan-Koopaei and Valentine(1998). These approaches provide a different solution to the Parker's (1978b, and 1979) paradox, but still an active bed exists. While Paquier and Khodashenas (2002) combined the shear stress variation with respect to the depth from the Merged Perpendicular Method (Khodashenas and Paquier, 1999) with the sediment conservation mass equation to determine an stable cross section, being the obtained shape similar to the one of Diplas and Vigilar (1992).

The experiments of Ikeda (1981) and Diplas (1990) show parabolic shapes in the sides and ridges in the central bed. It was inferred by Ikeda (1981) the influence of the secondary flow in the formation of such bed forms, but it was not considered in their approaches.At the present, there are tools able to incorporate the secondary flow in a velocity distribution model, like the Shiono and Knight Method (SKM, 1991), subsequently the shear stress and bed load, improving the channel prediction

approximation.

The common suppositions for the different approaches are: noncohesive material, straight channels, no vegetation. While just a few considered nonuniform sand diameter (*e.g.* Ikeda et al., 1988, Cao and Knight, 1998).In order to examine them, they have been divided in: bank profile equations, cross sectional equations and computational approaches.

In relation to the bankside equations the shapes draw parabolas joined by a central flatbed, resisting the critical shear stress, τ_{cr}, at the toe. While the cross sectional equations consist of exponential or hyperbolic functions, supporting τ_{cr} at the centreline. For both cases active beds are yielded. In the first type the shear stress is higher at the centreline than at the toe, and in the second type ridges are reported from experiments at the bottom of the channel. Such condition of stable sides and active bed satisfies the paradox of Parker (1978b, and 1979).

With respect to the methods of estimating the boundary shear stress for self-formed cross sections, four are reported: Lundgren and Jonsson(1964); Diffusion Momentum of Parker(1978a); Shiono and Knight Method (SKM, 1991); Merged Perpendicular Method (Khodashenas and Paquier, 1999). The penultimate was found with more advantages, being flexible enough to incorporate the variation of the friction factor,f, and secondary flow gradient,Γ, across the section, but this last was neglected on the original publication.It should be noted that all the methods were developed for: noncohesive materials, no vegetation, straight channels, no wash load and uniform sand diameter, except for Ikeda et al. (1988) and Cao and Knight (1998).

Ikeda (1981) and Diplas (1990) proportioned the geometry, velocity distribution and bed load measured, besides area, slope and discharge. The bottom of their channels presented ridges, and were analysed through the area method, neglecting the secondary flow. Nowadays, the SKM is available and is able to incorporate turbulence diffusion, as well as secondary flow variation to obtain the boundary shear stress, and subsequently the transversal geometry.

From the analysis of Dey (2001), whom compared six bank equations, is noted that the following approaches are in the same order: Parker (1978b, and 1979), Dey (2001), Diplas and Vigilar (1992), and Yu and Knight (1998). Among them, the last one is distinguished, because it involves the SKM.

In order to examine the different approaches to the optimized channel, they have been divided in: bank profile equations, cross sectional equations and computational approaches. The physical experiments are described in the same section that mentions the corresponding equation, and a global summary is added at the end of the section.

2.1.1 Bank profile equations

2.1.1.1 Shape of Glover and Florey

The first researchers in suggest banks in threshold were Glover and Florey(1951) (see figure 2), while looking for a stable cross section for erodible channels, in order to avoid changes in its geometry due scoring or deposition. They analysed the equilibrium of a particle in the sides, obtaining a cosine curve:

$$h = h_c \cos\left(y \frac{\tan\phi}{h_c} \right) \quad (1)$$

where$h$ is the local depth; h_c, the central depth; y, the transversal distance from the centre; and φ, the angle of repose of the soil material. Determining h_c from:

$$\tau = \rho S h_c \left(\frac{V_o}{V_c} \right)^2 \quad (2)$$

where τ is the shear stress; ρ, the water density; S, longitudinal slope; V_o, the mean velocity at the centre of the channel; and V_c, the mean velocity of the flow in an infinitely wide channel. To obtain V_o/V_c,a diagram was proportioned with S as input datum. The equation is valid for noncohesive soil, under steady and uniform flow.

2.1.1.2 Shape of Henderson

Henderson (1961) took up the work of Glover and Florey(1951) (equation 1) and combined it with the critical shear stress of Shields,τ_{cr}. Then, the central depth,h_c, was obtained from the shear stress equation to wide channels:

$$\frac{\tau_c}{\gamma(S_s - 1)d} = \tau_{cr} = 0.056 \quad (3)$$

$$\tau_c = \rho g h_c S \quad (4)$$

where $S_s$is the ratio of solid to water density; γ, the water specific weight; d, the diameter of the soil particle; τ_c, the critical shear stress; and g, the acceleration due to gravity. Later, the method was adopted by the USBR. A central bed was added, assuming this as flat and with a depth equal to h_c,obtaining a section without bed load (see figure 3).

2.1.1.3 Shape of Stebbings

Stebbings (1963) did experiments in a tilting flume full of sand, looking for a self-formed channel in regime state (no silting or scouring). The test consisted in give a discharge to an incision made in the streamwise direction, with a top width of 7.62 cm (3 in). The discharge, Q, was lightly increasing until the required value was obtained. Different values for Q were tested, obtaining a full range of cross section. The common behaviour among the experiments was a threshold cross section in the inlet (1) (figure 2), braiding before the outlet and, just before braiding,a cross section with parabolic sides joined by a flatbed (2) (figure 3). Between section 1 and 2 a range of cross sections were formed, with the bed load being the transport mechanism. Then, it is assumed that A has no bed load and B has the maximum. The figure 4 describes this.

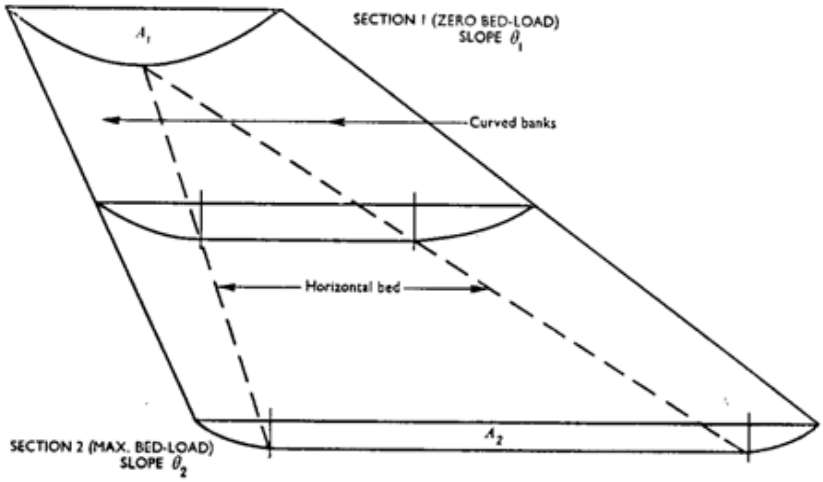

Figure 4. Change in channel cross section (Stebbings, 1963).

Additionally, the equilibrium of a particle in the sides was analysed, adding the variation of shear stress through, obtaining a curve similar to the one of Henderson (1961), but based on the sine curve:

$$h = h_c \sin\left(\frac{y\pi}{T}\right) \quad (5)$$

$$h_c = \frac{m\,g\tan\phi}{a\,\gamma\tan\theta_{lg}} \quad (6)$$

$$T = \frac{\pi\, m\ g}{a\,\gamma\ \sin\theta_{lg}} \quad (7)$$

where$T$ is the top width of the channel in threshold (see figure 2); m, the mass of the soil particle; a, the area of the particle; and θ_{lg}, the longitudinal angle slope. The results were compared to the top width of threshold cross sections without central bed (section 1).

2.1.1.4 Shape of Parker

Parker (1978b, and 1979) noted that natural streams can transport its own bed-load without altering their width, contrasting with the threshold channel concept. Such concept states that every particle in the channel boundary should be at the edge of incipient motion, otherwise bed load will exist, modifying the cross section and subsequently its width. But, by applying the concept of lateral transfer of downstream momentum of Lundgren and Jonsson, Parker demonstrated the existence of stable banks along with an active bed-load. The combination of both ideas (sides at threshold and active bed) is called the stable channel paradox.

The model does not consider the secondary flow into account, assuming it as week to alter the bank shape. Also, a particle equilibrium analysis was done, incorporating submerged static coefficient of Coulomb friction,μ, and the ratio of lift to drag force,β, obtaining a cosine curve (equation 8). The central depth,h_c, was determined by the critical Shield stress, as Henderson (1961).

$$h = \frac{h_c}{1-\mu\beta}\left[\cos\left(\mu\sqrt{\frac{1-\mu\beta}{1+\mu\beta}}\,\frac{y}{h_c}\right)-\mu\beta\right] \quad (8)$$

2.1.1.5 Shape of Diplas and Vigilar

A polynomial approach was given by Diplas and Vigilar (1992), whom depart from the equilibrium of a particle affected by the shear stress distribution, based on the modified area method of Lundgren and Jonsson, as Parker (1978b, and 1979). The shape of the cross section is obtained from a third-order, nonlinear, nonhomogeneous, ordinary differential equation, which is solved numerically, finding:

$$h^* = C_5\, y^{*5} + C_4\, y^{*4} + C_3\, y^{*3} + C_2\, y^{*2} + 1 \quad (9)$$

where h^* is the dimensionless local depth; C_5, C_4, C_3 and C_2, coefficients depending on μ and β; and y^*, the dimensionless transversal distance.

2.1.1.6 Shape of Cao and Knight

Cao and Knight (1996b, 1997, and 1998) departed from the entropy concept of Shannon (1951), applying it to the side slope probability of an alluvial channel. The result was a parabolic equation, depending on the submerged static coefficient of Coulomb friction, μ, and the top width, T:

$$h_c = \frac{\mu T}{4} \quad (10)$$

$$h = \frac{\mu T}{4}\left[1-\left(\frac{2y}{T}\right)^2\right] \quad (11)$$

Also, the same authors proposed the following equation in order to relate the central depth, h_c, with the critical shields parameter, Θ_c, the streamwise slope, S, and the dimensionless secondary flow, β_s (taken as 0.15):

$$h_c = \frac{\rho * d\,\Theta_c}{S\left(1-\beta_s\right)} \tag{12}$$

where ρ* is the dimensionless submerged density of sediments $[(\rho_s - \rho)/\rho]$. Then, if the diameter, d, and the streamwise slope, S, are known, the system can be solved. The velocity and shear stress distributions are obtained by the Shiono and Knight Method (SKM, 1991), which has the advantage to take the secondary flow, Γ, and the eddy viscosity, λ, into account. Assuming the banks in threshold, a flatbed was incorporated, as previous authors, with the same depth as h_c, being consistent with the Parker's paradox and improving it by the use of Γ and λ.

Cao and Knight (1998) mention an averaged difference of 18.6% between the shear stress at the centreline and at the junction of a channel. This implies a bed load, but not necessary means that the calculated bed load, Q_{sc}, will be equal than the observed one, Q_{so}, just the stability of the sides. By corroborating both data, a better approximation for the shape of the central bed will be obtained.

2.1.1.7 Shape of Yu and Knight

Yu and Knight (1998) proposed a shape function for self-formed banks for straight channels in threshold and with uniform bed material, based on the static equilibrium of particles on the channel boundary. The novelty in this work is the incorporation of the shear stress distribution to determine the side slope variation. The equation found and the free body diagram is shown below.

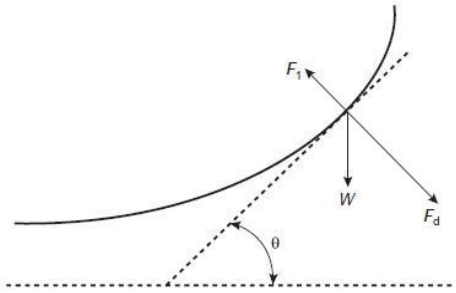

Figure 5. Forces acting on a particle on channel boundary (Yu and Knight, 1998).

$$\cos\theta = \frac{\mu^3\beta(\tau_0/\tau_{0c}) + \sqrt{(1+\mu^2)(1+\mu\beta)^2 + \mu^2(\tau_0/\tau_{0c})^2(1-\mu^2\beta^2+\mu^2)}}{(1+\mu\beta)(1+\mu^2)} \quad (13)$$

Where $\theta$is the side slope angle; τ_0, the local boundary shear stress; τ_{0c}, the boundary shear stress at channel centreline; F_1, the lift force; F_d, the drag force; β, the ratio F_1/F_d, taken as 0.85. The shear stress distribution is obtained through the SKM, capable of incorporate the secondary flow, Γ, and the dimensionless eddy viscosity, λ. But in the original publication the authors took $\Gamma=0$.The input data for the model are the diameter, d, the longitudinal slope, S, and the central depth, h_c. This last is determined by a critical shear stress condition, the authors suggest the one of van Rijn, because it proportions different values to the dimensionless critical shear stress according to d. So far no published document has used this method to predict an optimum cross section for a given discharge, but it is inferred that a flatbed can be add between the sides in threshold. In this thesis is presented an example using this shape.

2.1.1.8 Shape of Dey

Dey (2001) presented an approach based on the equilibrium of a particle on the side slope expressed by Ikeda (1982), in combination with the modified area

method of Lundgren and Jonsson. The equilibrium of the particle takes into account its submerged weight, the lift force and drag force, through the relative shear stress of a particle in threshold, $\tilde{\tau} = \tau_0 / \tau_{0c}$. The integration of this elements results in a differential equation drawing a parabola:

$$\sqrt{\beta^2 \mu^2 - 1}\,\frac{d\hat{z}}{d\hat{y}} = \mu \sqrt{\left[\left(1 - \hat{z} + C\,m\,\hat{y}^{m-1}\right)\left(1 - \beta\mu\right) + \beta\mu\right]^2 - 1} \tag{14}$$

where $\hat{z}$ is the dimensionless vertical distance, $\hat{z} = z/h_c$; $\hat{y}$, the dimensionless transverse distance, $\hat{y} = y/h_c$; C and m, coefficients given by Stebbings (1963). In order to determine h_c, the author proportioned four relationships for the threshold shear stress, τ_{0c}, when $\theta = 0$, similar to the work of van Rijn:

$$\begin{aligned}
&\hat{\tau} = 0.142\hat{D}^{-0.35} && \text{for} \quad \hat{D} \le 1 \\
&\hat{\tau} = 0.148\hat{D}^{-0.60} && \text{for} \quad 1 < \hat{D} \le 15 \\
&\hat{\tau} = 0.013\hat{D}^{0.32} && \text{for} \quad 15 < \hat{D} \le 50 \\
&\hat{\tau} = 0.045 && \text{for} \quad \hat{D} > 50
\end{aligned} \tag{15}$$

$$\hat{\tau} = \frac{\tau_{0c}}{\gamma\,\rho^{*}\,d} \tag{16}$$

$$\hat{D} = 2d\left(\frac{\rho^{*}\,g}{\nu^2}\right)^{1/3} \tag{17}$$

$$h_c = \frac{\tau_{0c}}{\rho g S} \tag{18}$$

where $\hat{\tau}$ is the dimensionless shear stress in threshold when $\theta=0$; $\hat{D}$, a function of the diameter, d; and ν, the kinematic viscosity of water. A cross section in threshold without flatbed was compared with the experimental data of Stebbing (1963), finding its calculations in agreement with the observations.

2.1.2 Cross sectional equations

2.1.2.1 Work of Ikeda

Ikeda (1981) carried out experiments looking for the self-formed shape of a channel. The experiments were done in two different tilted flumes full of sand, with an initial trapezoidal cross section, working at bankfull, deforming the cross section by the flow. The water, as well as the sediment flow were recirculated. A stable cross section in threshold was obtained after approximately 10 hours. The sand diameter used was d_{50}=1.3 mm, where $\sigma = d_{90}/d_{50} = 1.38$. The shape of the cross section fits an exponential function, being the first attempt to predict it with a single expression:

$$\frac{h}{h_c} = 1 - e^{\frac{-\xi}{\Delta}} \tag{19}$$

Where h is the local depth; h_c, the depth at centreline; ξ, the lateral distance from the margin; and Δ, the dimensionless area between the curve and the bottom of the channel. The author does not provide any clue for determining Δ, but remarks that the exponential function describes the shape of the channel better than a cosine curve. Also, the relationship is valid even for the widening process regardless the initial shape, discharge and sand diameter.

During the experiments, parallel ridges were formed along the bed of the channel, attributing them to the secondary flow. This differs with other theories were the secondary flow was not considered a factor to shape margins and was neglected to affect the bottom of the self-formed channel. Additionally, this activity in the bed agrees with the stable channel paradox of Parker (1978b, and 1979), because it describes well the banks with a central bed-load.

Ikeda *et al.*(1988) repeated the experiment, but this time with nonuniform soil

material, employing the same d_{50}=1.3 mm and different σ, 1.72, 1.89 and 2.44. This coefficient was incorporated to the analysis, which departed from the bank equation of Parker (1978b) and the lateral diffusion momentum of Lundgren and Jonsson. Four equations describing the optimum channel geometry were obtained:

$$h_c = \frac{0.0615\ \rho * \sigma d_{50}}{S\ \left(\log 19\sigma\right)^2} \tag{20}$$

$$B = b + T \tag{21}$$

$$b = \frac{Q}{h_c\sqrt{g h_c S}\ 2.5\ln\left(11\frac{h_c}{k}\right)} \tag{22}$$

$$T = h_c\left[2.571 + \frac{2.066}{\ln\left(11\frac{h_c}{k}\right)}\right] \tag{23}$$

where ρ* is the dimensionless submerged density of sediments; S, longitudinal slope; B, surface top width; b, width of the central flatbed; T, top width corresponding to the side banks; Q, discharge; and $k = 1.50\,d_{90} = 1.5\sigma\,d_{50}$.

The shape of the channel agrees with the paradox of Parker (1978b). With respect to the heterogeneous soil material, it is demonstrated that increasing gradation increases the critical shear stress, obtaining a bigger depth and decreasing the width. The model was compared to laboratory and field data, finding agreement.

2.1.2.2 Equation of Diplas

Following the same strategy as Ikeda (1981), Diplas (1990) carried out experiments in a tilted flume full of sand, recirculating water and sediments. The flume used was 14.6 m long and 0.53 m wide, measuring the discharge, sediment load and velocity profiles. He also departed from a trapezoidal channel and after

approximately 17hoursit reached a stable condition. The expression obtained describing the cross section, was exponential as well, depending on the central depth, h_c, and surface top width, B. The top width can be obtained from the cross section area expression, A, and h_c from a critical threshold shear stress condition (*e.g.* equation 3and 4). Then, the section is proposed, the discharge is calculated, Q, modifying B until satisfy Q. The equations involved are shown below.

$$\frac{h}{h_c} = 1 - e^{\frac{-y_T}{h_c}} \tag{24}$$

$$y_T = \frac{B}{2} - y \tag{25}$$

$$A = \left(B - 2h_c\right) h_c \tag{26}$$

The stable cross section reached from experiments also presents ridges along the stream, that are suggested to be because of the secondary flow as Ikeda (1981) pointed out.

2.1.2.3 Equation of Babaeyan-Koopaei and Valentine

Babaeyan-Koopaei and Valentine(1998) conducted physical experiments, like the type of Ikeda (1981, and 1988) and Diplas (1990). The flume used was 22 m long and 2.5 m wide, using uniform sand (d_{50}=1 mm). The initial cross section was trapezoidal as well. From the laboratory data, two best fitted curves were obtained, both of them hyperbolic, one for the bank profile and the other for the whole cross section:

$$\frac{h}{h_c} = 1 - 3.5\left[\tanh\left(\frac{-y}{4h_c}\right)\right]^4 \tag{27}$$

$$\frac{h}{h_c} = \tanh\left(\frac{B/2 - y}{1.36\,h_c}\right) \tag{28}$$

where h is the local depth; h_c, the central depth; y, the lateral distance from the centre; and B, the surface top width. It is implied that h_c can be obtained from a critical shear stress condition (equations 3and 4). Both equations were compared to laboratory data and other approaches, achieving better results than the previous ones.

2.1.3 Computational approaches

2.1.3.1 Vigilar and Diplas

Vigilar and Diplas (1997, and 1998) proposed a solution for the momentum-diffusion equation given by Parker (1978b), finding an expression for the dimensionless stress depth, δ^*. The shape of δ^* along a cross section identifies the zones where the bed is active, happening this only in the central part of the channel, keeping the banks at threshold, satisfying the stable channel paradox of Parker. The differential equation obtained from δ^* defines the geometry of the channel, in order to solve it, boundary conditions were given according the type of channel, sediment load and slope, subsequently a numerical solution was applied.

The disadvantage of this model is its complexity, and in order to simplify it a graphical approach was proposed, depending on the static coefficient of Coulomb, μ, the ratio of lift to drag force,β, sand diameter, d, streamwise slope, S, and discharge, Q; obtaining the lengths of the flatbed, b, and banks, T, depth, h, and shape of the bank by the following equation:

$$h^* = a_3 y^{*3} + a_2 y^{*2} + a_1 y^* + a_0 \tag{29}$$

where h^* is the dimensionless depth, h / h_c ; y^*, the dimensionless horizontal distance from the junction, y / h_c ; and a_3, a_2, a_1 and a_0, coefficients proportioned by the author.

The results were compared to experimental and field data, showing agreement. The model neglects the secondary flow, based on authors whom shown that its velocity is less than 1.5% of the maximum downstream velocity, simplifying the process. With respect to the new bank shape, it's less steeper than a typical cosine curve (e.g. Parker, 1978b), finding this last as unstable.

2.1.3.2 Paquier and Khodashenas

Paquier and Knodashenas (2002) proposed a method to estimate the deformation of a cross section channel, based on the variation of the boundary shear stress, τ_0, and bed load, Q_s, through the equation of sediment mass conservation. τ_0 was obtained from the Merged Perpendicular Method (Khodashenas and Paquier, 1999) and Q_s from the Meller-Peter and Muller equation.

$$\frac{\partial S_{1D}}{\partial t} + \frac{\partial Q_s}{\partial x}\frac{1}{1-p} = 0 \qquad (30)$$

The conservation of sediment mass equation of Exner is expressed above, where ΔS_{1D} is the deformation of the section in one direction; x, the distance along channel axis; t, time; and p, porosity. The expression finds ΔS_{1D}, then is transformed in 2D based on the critical shear stress distribution on the sides of Ikeda. The model assigns erosion to the node if its shear stress is bigger than the critical, and deposition when the opposite.

The presented examples were compound channels, resulting in parabolic

shapes similar to other authors (e.g. Henderson, 1961, Parker, 1978b, Cao and Knight, 1996b), and in perfect agreement with Diplas and Vigilar (1992), see figure 6. The deposition process in the section is criticisable, especially in the banks, because the particle gets attached to the sides instead of follow the gravity. The shapes of Diplas (1992) and Ikeda (1981) are validated with self-formed channels obtained from a widening process. It is inferred that the deposition process is governed by gravity.

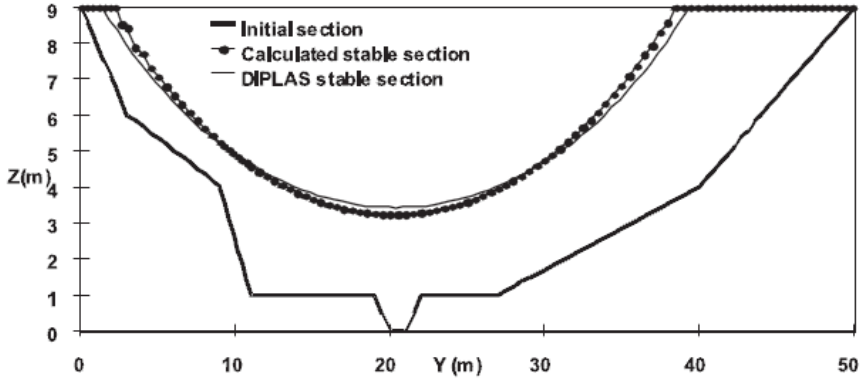

Figure 6. Comparison between the section obtained of "Paquier and Knodashenas(2002)" and "Diplas and Vigilar (1992)".

CHAPTER 3

THE NUMERICAL MODEL

The numerical model consists of the Yu and Knight Method to determine self-formed cross sections. The methodology implies the SKM to link the shear stress variation across the section, and reach the equilibrium of the particle. Both parts are described following.

3.1 The SKM

The SKM (Shiono and Knight, 1991) offers an ingenious solution to the Reynolds Averaged Navier-Stokes (RANS) equations, obtaining the streamwise depth-average velocity, U_d, distribution across the section, and subsequently the boundary shear stress,τ_0, expressed as:

$$\rho g h S - \rho \frac{f}{8} U_d^2 \left(1+\frac{1}{s^2}\right)^{1/2} + \frac{\partial}{\partial y}\left[\rho \lambda h^2 \left(\frac{f}{8}\right)^{1/2} U_d \frac{\partial U_d}{\partial y}\right] = \frac{\partial}{\partial y}\left[h\left(\rho UV\right)_d\right] \quad (31)$$

Where ρ is the water density; g, the acceleration due to gravity; h, the local depth; S, the longitudinal slope; f, the Darcy-Weisbach friction factor; s, the transversal slope; y, the transversal distance from centreline; λ, the dimensionless eddy viscosity; and $\frac{\partial}{\partial y}\left[h\left(\rho UV\right)_d\right]$, the lateral gradient of secondary flow, Γ.

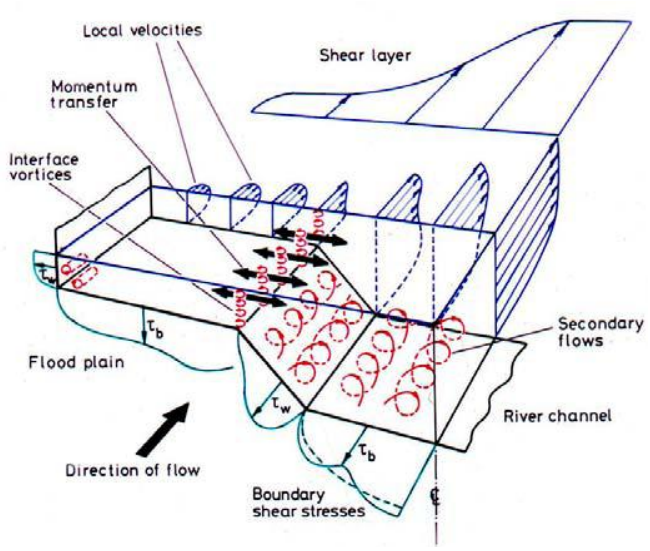

Figure 7. Hydraulic parameters associated with flow in a two-stage channel (Shiono and Knight, 1991).

It is possible to solve equation (1) using numerical or analytical techniques. The numerical solution can be solved, for example, by the finite volume method. While for the analytical two equations were proposed by the same authors, one for constant depth (equation32) and other for side slope depth (equation33):

$$U_d = \left[A_1 e^{\gamma_k y} + A_2 e^{-\gamma_k y} + k \right]^{1/2} \tag{32}$$

$$U_d = \sqrt{A_3 h^{\alpha} + A_4 h^{-(\alpha+1)} + \omega h + \eta} \tag{33}$$

where A_1, A_2, A_3 and A_4 are coefficients which are determined by employing boundary conditions; γ_k, k, α, ω, and η are functions of h, f, S, s, Γ and λ. The solution can be obtained from a linear system.

$$\gamma_\kappa = \frac{1}{h}\sqrt{\frac{2}{\lambda}}\left(\frac{f}{8}\right)^{1/4}$$

$$k = \frac{8gSH}{f}\left(1-\beta_\kappa\right)$$

$$\alpha = \frac{-1}{2} + \frac{1}{2}\sqrt{1 + \sqrt{8f}\left(\frac{s\sqrt{1+s^2}}{\lambda}\right)}$$

$$\omega = \frac{gS}{\left(\frac{f}{8}\right)\frac{\sqrt{1+s^2}}{s} - \frac{\lambda}{s^2}\sqrt{\frac{f}{8}}}$$

$$\eta = \frac{-\Gamma}{\rho\left(\frac{f}{8}\right)\sqrt{1+\frac{1}{s^2}}}$$

$$\beta_k = \frac{\Gamma}{\rho g h S}$$

3.2 The Yu and Knight Model

Yu and Knight (1998) proposed a shape function for self-formed straight channels in threshold and with uniform bed material, based on the static equilibrium of particles lying at threshold on the channel boundary (figure 8 and equation 34).

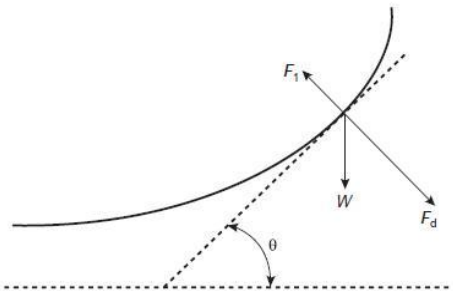

Figure 8. Forces acting on a particle on channel boundary (Yu and Knight, 1998).

$$\sqrt{F_d^2 + W^2 \sin^2\theta} = \mu\left(W\cos\theta - F_1\right) \tag{34}$$

where F_d is the drag force; W, the submerged weight; θ, the angle of the side slope; μ, the Coulomb static friction of the sediment particle; and F_1, the lift force. The equation 34 can be rewritten as:

$$\cos\theta = \frac{\mu^3\beta\left(\tau_0/\tau_{0c}\right)+\sqrt{\left(1+\mu^2\right)\left(1+\mu\beta\right)^2+\mu^2\left(\tau_0/\tau_{0c}\right)^2\left(1-\mu^2\beta^2+\mu^2\right)}}{\left(1+\mu\beta\right)\left(1+\mu^2\right)} \quad (35)$$

where $\beta = F_1/F_d$,taken as 0.85; τ_0, the local boundary shear stress; and τ_{0c}, the boundary shear stress at channel centreline, defined as:

With respect to τ_0 and τ_{0c}, these variables can be obtained by the Shiono and Knight Method (SKM) (Shiono and Knight, 1990, 1991). Then, combining these results with the threshold condition of Ackers and White (1975):

$$\tau_{0c} = \tau_{cr}\left(\gamma_s - \gamma\right)d \quad (36)$$

and the resistance law of White *et al*. (1980) is possible to obtain a cross section in threshold of motion. The SKM applied by Yu and Knight did not consider secondary flow ($\Gamma=0$) and took the eddy viscosity as λ=0.16.

3.3 Methodology

The model requires as input data the mean material diameter, d, the longitudinal slope, S_o, and the Coulomb skin friction of submerged sediments, μ. Then, a central depth is proposed, h_c, follow by a top width, T. These two dimensions define the shape of the cross section, departing from a triangular bankside, dividing it into elements. Later the SKM is applied in order to obtain the depth velocity variation, U_d, and with it the shear stress variation, τ_o, through the cross section. Once τ_o is known, it is possible to determine a new cross section based on the equation 35. The new section is compared with the previous one and if the difference in depth, at a

given point, is more than the tolerance, then the section is recalculated, keeping the same h_c and adopting the T of the new cross section. The process is repeated until the tolerance is reached. The next step is compare the shear stress in the centre, τ_{0c}, with the shear stress in threshold, τ_{*cr}, (equation 36), if this condition is not accomplish a new h_c is proposed and the process restarts, until get $\tau_{0c} = \tau_{*cr}$. Then, the output data are the top width, T, the variation of depth, h, and subsequently the calculated discharge, Q_c. Once the threshold condition is satisfied, the design discharge, Q_d, is compared to the calculated one, Q_c, and if $Q_c < Q_d$, the central flatbed, b, is increased and the iteration process of h_c is repeated until $Q_c \approx Q_d$, obtaining an stable cross section on threshold.

The output data delivers the cross section geometry, *i.e.* the top width, T, the variation of depth, h, followed by the discharge, Q. It should be noted that Yu and Knight (1998) did not explore the behaviour of their model with respect to the variation of flatbed. The figure 9 shows the flowchart of the computational procedure.

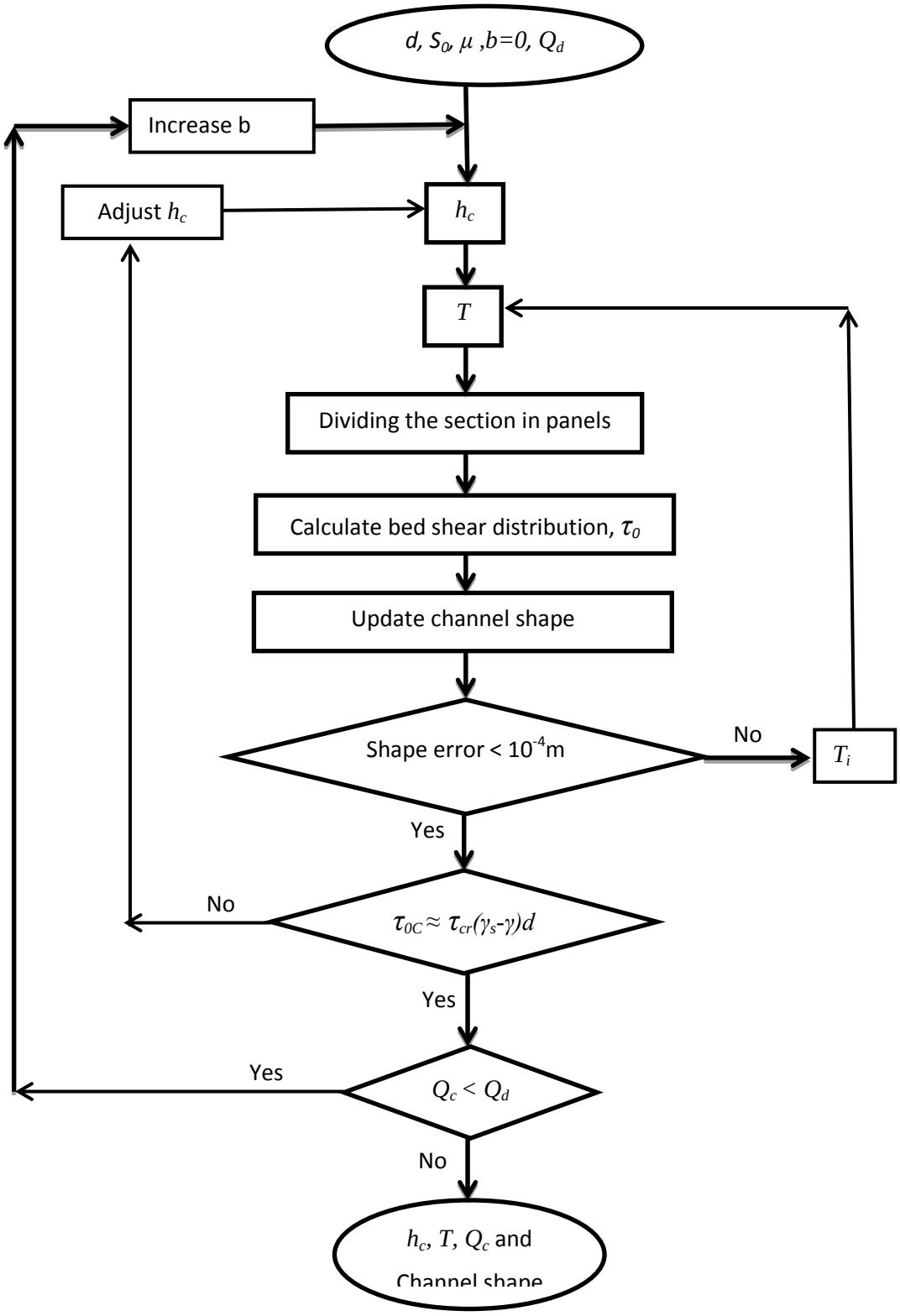

Figure9. Modified methodology flowchart of Yu and Knight (1998).

3.4 The numerical model behaviour

It was noted that the bed shape of Yu and Knight (1998) is steeper when a flatbed exists, than without it. This was explained due to the maximum velocity moved from the junction point to the centre, displacing in the same direction the location of maximum shear stress. A comparison was carried out between those banks, where S=0.002146 d=1.3mm and μ=0.60, the central flatbed was considered infinitely wide. See figures 10, 11 and 12.

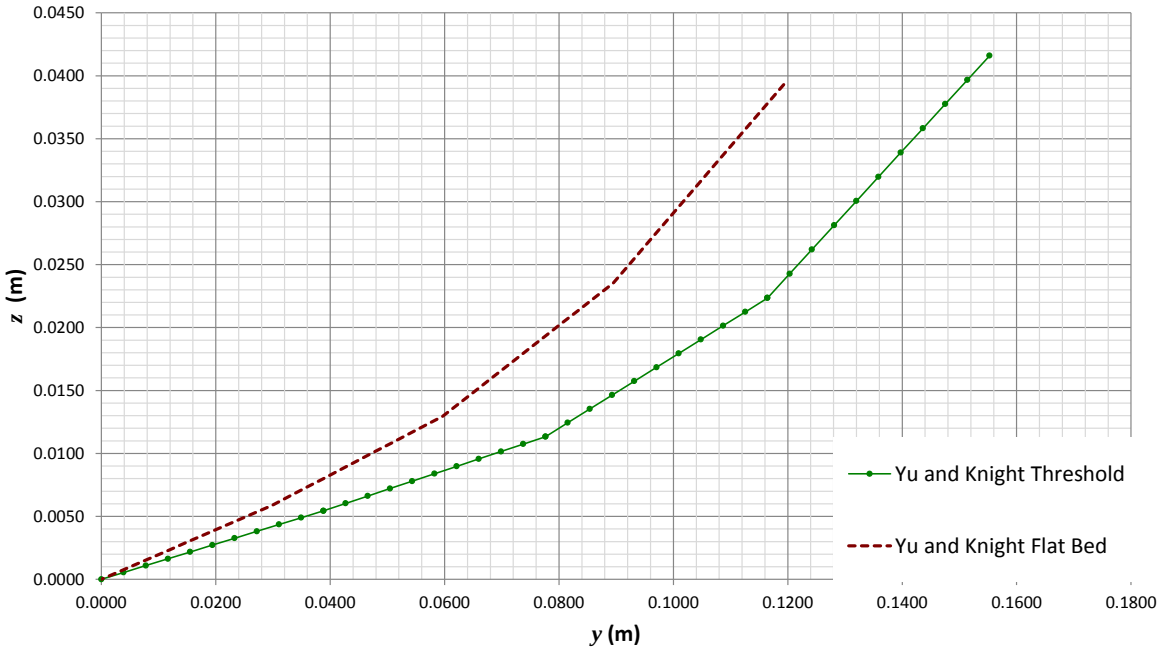

Figure 10. Comparison between two banks obtained for a self-formed cross section with flatbed and a bank without flatbed (threshold condition), both calculated by the Yu and Knight (1998) method. S=0.002146 d=1.3mm μ=0.60.

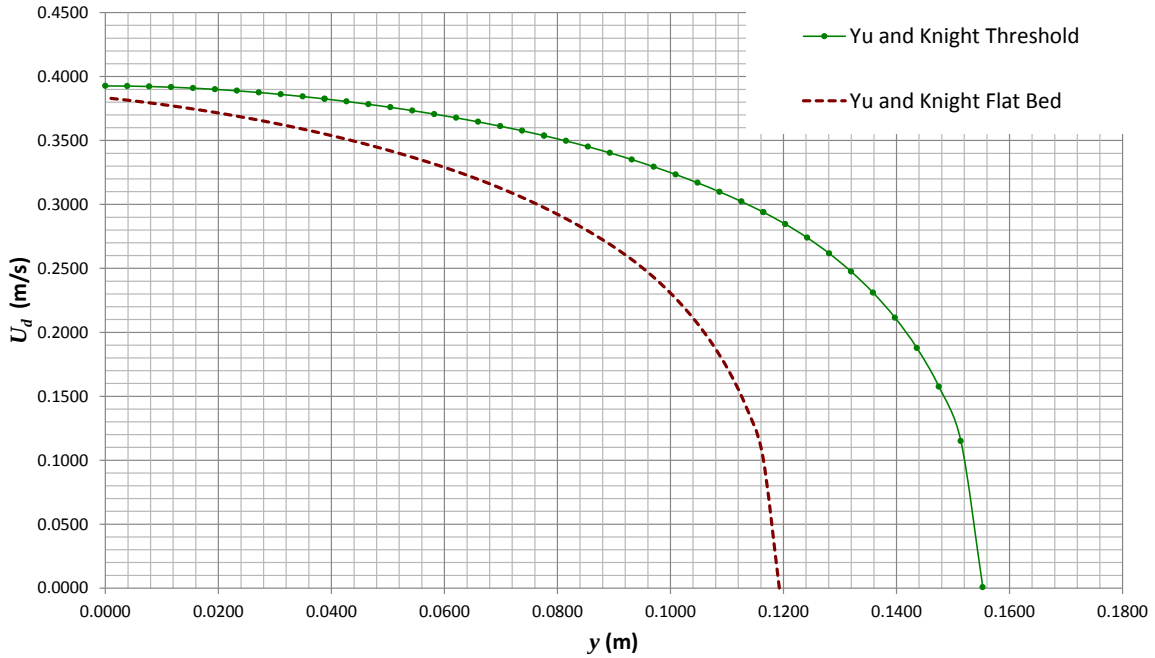

Figure 11. Comparison between the velocity profiles obtained for two banks obtained for a self-formed cross section with flatbed and bank without flatbed, both calculated by the Yu and Knight (1998) method. S=0.002146 d=1.3mm μ=0.60. The centreline is located at y=0, and the margin at the extreme, *i.e.* y=0.12m and y=0.156m.

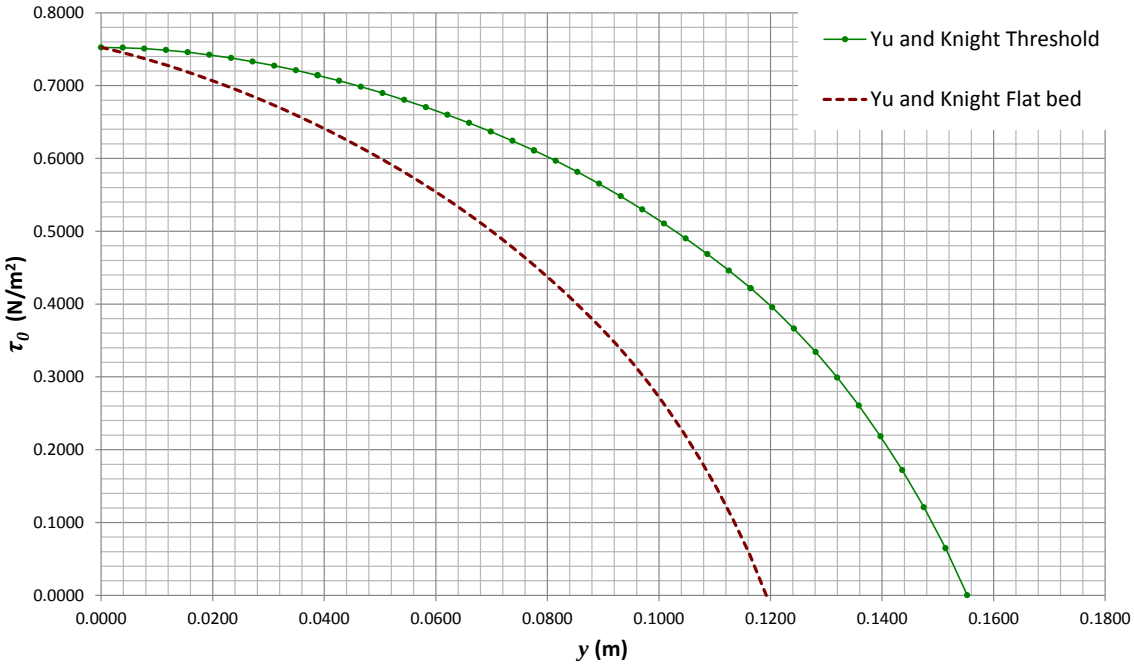

Figure 12. Comparison between the shear stress profiles obtained for two banks obtained for a self-formed cross section with flatbed and a bank without flatbed, both calculated by the Yu and Knight (1998) method. S=0.002146 d=1.3mm μ=0.60. The centreline is located at y=0, and the margin at the extreme, *i.e.* y=0.12m and y=0.156m.

Therefore, in order to critically investigate the behaviour of the Yu and Knight model (1998) in combination with the SKM (Shiono and Knight, 1991), the six variables that govern the model were evaluated: λ, dimensionless eddy viscosity; φ, angle of repose of the soil material; S, longitudinal slope; Γ, secondary flow gradient; and $b/2h_c$, ratio between half central flatbed and central depth. Firstly, different values of λ, φ and S where organized in six cases (table 1). The two values of λ correspond to 0.16, that is the value recommended by Yu and Knight (1998), and 0.07 a value obtained from experimental measurements of the viscosity distribution (*e.g.* Knight et al., 2010, p. 120-121). The soil material considered was d=1.3 mm. With respect to the values of φ taken, these were 32.97º and 36.36º, being the first one the measured angle of soil repose of the experiments of Ikeda (1981), and the second one resulted from a equation proposed by Yu and Knight (1998), which is based on d. About the slopes, 1/479 was considered due to is the one used in the run 16 of Ikeda (1981), as is the best known experimental cross section for self-formed channels. The other two were just smaller values (1/530 and 1/650).

Table 1. The six cases evaluated, with their corresponding variables: λ, dimensionless eddy viscosity; φ, angle of repose of the soil material; S, longitudinal slope

Case	λ	φ	S	
I	0.16	32.97º	1/479	
II	0.07	32.97º	1/479	
III	0.07	36.36º	1/479	
IV	0.16	32.97º	1/530	1/650
V	0.07	32.97º	1/530	1/650
VI	0.07	36.36º	1/530	1/650

Then, each case was tried by five Γ values on the bankside, following the sign distribution shown on figure13: $\Gamma/\rho g h_c S$=0, neglecting the secondary flow; $\Gamma/\rho g h_c S$=0.05, a value used for inbank flow (Knight et al., 2010, p.123); $\Gamma/\rho g h_c S$=0.15, a value used for overbank flow (Knight et al., 2010, p.123); $\Gamma/\rho g h_c S$=0.10, and $\Gamma/\rho g h_c S$=0.025. Later, every combination was tested by different central flatbed values (see table 2):$b/2h_c$=0, considering a cross section in threshold, without flatbed; $b/2h_c$=2, a minimum observed value that has reached a stable T/h_c; and$b/2h_c$=0.25 and 0.50, intermediate values between 0 and 2. The obtained output data for each condition were: central depth, h_c, bankside shape and width, T, hydraulic area, A, depth average velocity, U_d, and boundary shear stress,τ_0, profiles, friction factor, f, and discharge, Q. In total 120 simulations were carried out, their results were plotted in order to appreciate the distinct relationships between variables.

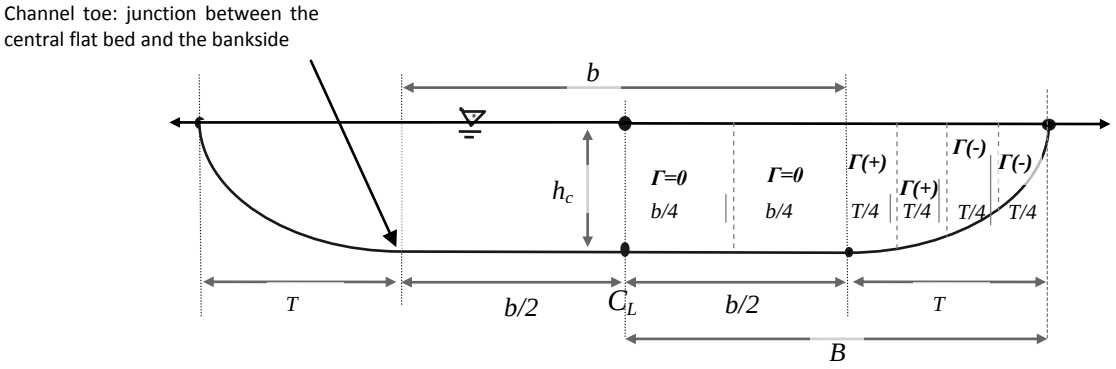

Figure 13. Cross sectional shape of a self-formed channel, constituted by banks in threshold and an active central flatbed. Half of the cross section is divided in six SKM panels.

Table 2. Summary of the combinations evaluated, obtaining their geometry, velocity and shear stress profiles.

Cases:	I		II		III		IV		V		VI	
	S	$b/2$ h_c	S	$b/2$ h_c	S	$b/2$ h_c	S	$b/2$ h_c	S	$b/2$ h_c	S	$b/2$ h_c
$\Gamma/\rho g h_c S$= 0	1/479	0.00	1/479	0.00	1/479	0.00	1/530	0.00	1/530	0.00	1/530	0.00
		0.25		0.25		0.25		0.25		0.25		0.25
		0.50		0.50		0.50		0.50		0.50		0.50
		2.00		2.00		2.00		2.00		2.00		2.00
$\Gamma/\rho g h_c S$= 0.025	1/479	0.00	1/479	0.00	1/479	0.00	1/650	0.00	1/650	0.00	1/650	0.00
		0.25		0.25		0.25		0.25		0.25		0.25
		0.50		0.50		0.50		0.50		0.50		0.50
		2.00		2.00		2.00		2.00		2.00		2.00
$\Gamma/\rho g h_c S$= 0.05	1/479	0.00	1/479	0.00	1/479	0.00	1/650	0.00	1/650	0.00	1/650	0.00
		0.25		0.25		0.25		0.25		0.25		0.25
		0.50		0.50		0.50		0.50		0.50		0.50
		2.00		2.00		2.00		2.00		2.00		2.00
$\Gamma/\rho g h_c S$= 0.10	1/479	0.00	1/479	0.00	1/479	0.00	1/650	0.00	1/650	0.00	1/650	0.00
		0.25		0.25		0.25		0.25		0.25		0.25
		0.50		0.50		0.50		0.50		0.50		0.50
		2.00		2.00		2.00		2.00		2.00		2.00
$\Gamma/\rho g h_c S$= 0.15	1/479	0.00	1/479	0.00	1/479	0.00	1/650	0.00	1/650	0.00	1/650	0.00
		0.25		0.25		0.25		0.25		0.25		0.25
		0.50		0.50		0.50		0.50		0.50		0.50
		2.00		2.00		2.00		2.00		2.00		2.00

The SKM was solved by the analytical solution (equations 32 and 33) using six panels: two equidistant for the flatbed and four equidistant for the bankside. The central panels were considered as Γ=0, in order to not affect the bankside flow behaviour. While Γ on the side used constant values $\Gamma\neq0$, varying just the sign as: positive, positive, negative and negative, from the toe to the edge (see figure13). Such sign distribution was chosen, considering only one secondary flow cell, rotating clockwise on the on the right half cross sectional bankside, as Knight et al. (2007) mentioned. It was assumed uniform soil material across the section.

3.4.1 Results

The simulation exercise can be summarize in the application of the Yu and Knight model (1998), altering five input variables ($b/2h_c$, Γ, λ, φ, and S), and observing the reaction of the cross section geometry (T, h_c and A) and its flow characteristics (U_d, τ_0, f and Q). Firstly, the changes of the dimensionless bankside, T/h_c, with respect to the variation of the dimensionless half central bed, $b/2h_c$, was plotted for the six cases mentioned on table 1, varying Γ ($\Gamma/\rho g h_c S$ =0, 0.025, 0.05, 0.10 and 0.15) for each case (figure 14). Secondly, in order to observe the effects of the remaining variables (Γ, λ, φ, and S), the output data (T, h_c, A, U_d, τ_0, f and Q) were plotted against $b/2h_c$ (figures20 to 24).

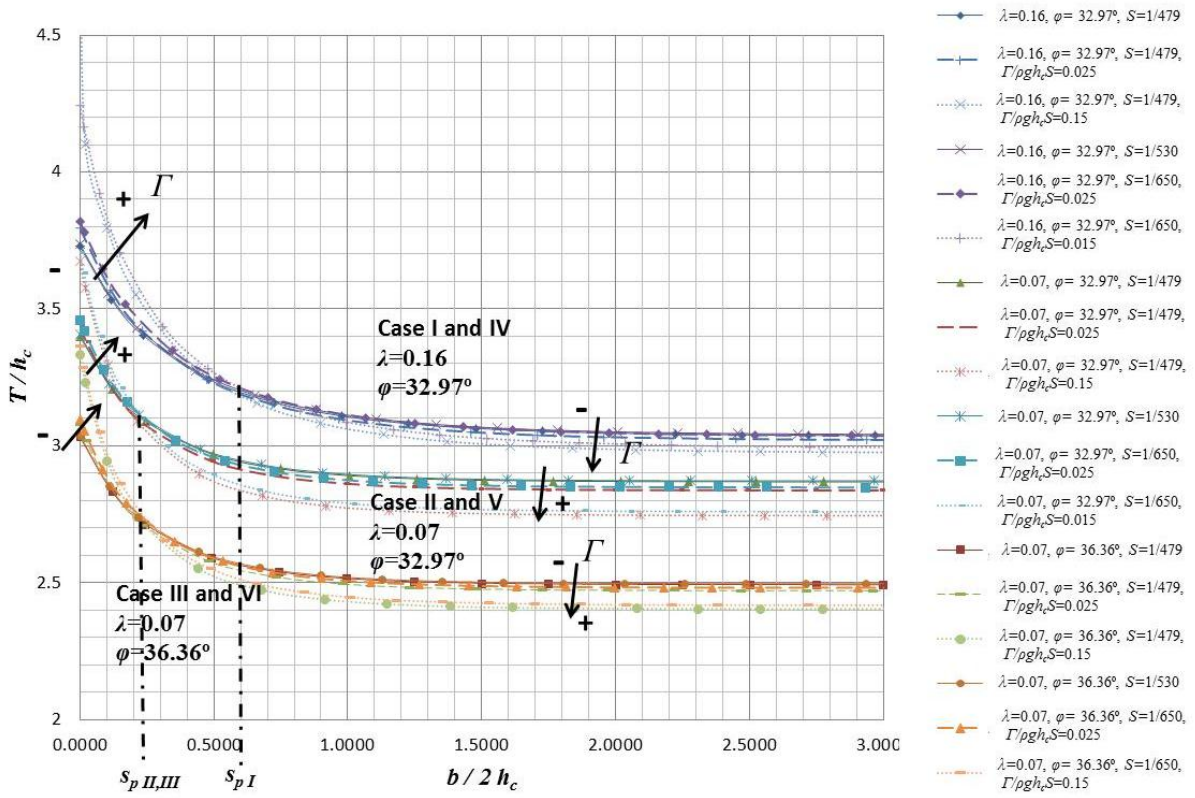

Figure 14. Variation of the dimensionless bank side width, T/h_c, with respect to the dimensionless half central width, $b/2h_c$, for differences values of λ, φ, S and Γ. The arrows are representing how the curve T/h_c vs $b/2h_c$ is rotating clockwise around a convergence point, s_p, while Γ is growing.

3.4.2 Analysis

3.4.2.1 Variation of T/h_c with respect to $b/2h_c$, Γ, λ, and φ

The comparison of T/h_c versus $b/2h_c$ shows that an increase in $b/2h_c$ produces an exponential decrease in T/h_c, until it reaches a stable limit, s_l, (where s_l is a value of $b/2h_c$, such that T/h_c is constant) ($b/2h_c > s_l$) (figure 14). This can be explained due to the threshold condition, which is set at the bankside toe of the cross section. Such a condition implies that the critical shear stress of the soil is achieved at that point. Then, while $b/2h_c$ is growing the maximum shear stress moves from the toe to the centre line of the channel, consequently it changes the shape of the shear stress profile. This is because the SKM boundary condition at the centre line is $\partial U_d / \partial y = 0$, implying $\partial \tau_0 / \partial y = 0$, implying a maximum value, which generates a smoother $\partial \tau_0 / \partial y$ next to the centre and steeper $\partial \tau_0 / \partial y$ next to the margin. The consequence of this is a narrower bankside, which can be observed on figure B- 3 (Appendix B), where four shear stress profiles are shown for the same hydraulic conditions, just altering the central flatbed, the corresponding cross sections and velocity profiles are presented on figures B- 1and B- 2 (Appendix B).

With respect to the influence of λ on T/h_c, figure 14 shows that an increase in λ, increases the dimensionless bank side width, T/h_c. The explanation for this response is that a greater value of λ yields a lower shear stress on the boundary, τ_0 (figures B- 3 and B- 6, Appendix B),requiring a higher central depth, h_c, to satisfy the threshold condition. Subsequently the bankside, which is restricted by the soil repose angle, φ, at the margin, grows until it reaches the allowed h_c (see figures B- 1and B- 4). Since φ<45º, the increase in the horizontal component, T, is greater than the increase in the

vertical one, h_c, justifying the increase on T/h_c.

Examining the effect of φ on the bankside, when it increases a decrease in T/h_c occurs. This happens due to the bankside equation of Yu and Knight (1998) (equation 35) trends to φ at the edge. Then, a bigger φ allows a steeper slope on the bankside, yielding a narrower T for the same h_c. The figures B- 4 and B- 7on Appendix B illustrate such phenomenon.

The effect of Γ on T/h_c vs. $b/2h_c$ is more complex, because Γ is directly proportional to T/h_c when $b/2h_c<s_p$ (s_p:spin point), and inversely proportional to $b/2h_c>s_p$, as is shown on figure 14. Then, the curves T/h_c vs. $b/2h_c$ seems to be rotating clockwise around a convergence point, while Γ grows. Such point has been denominated s_p (spin point), and is an element of $b/2h_c$. It is known that when Γ increases, τ_0 decreases. Later, the model requires a bigger h_c to satisfy the threshold condition at the bankside toe. This is proven by the comparison of two cross sections, with their corresponding velocity and shear stress profiles, using different Γ values (figures B- 1, B- 2 and B- 3, vs. B- 10, B- 11 and B- 12). On the other hand, an increment on h_c yields an augment on T, as was seen above when φ is fixed. Then, it is possible to say $\Gamma \propto hc$ and $\Gamma \propto T$. However, the impact of Γ on T is higher when $b/2h_c<s_l$ (s_l: stable limit), than when $b/2h_c>s_l$ (figure 15), and even bigger than the impact of Γ on h_c when $b/2h_c<s_l$ (figure 16). Then, the combination of these factors (T and h_c) with $b/2h_c$ and Γ yields a series of curves where $\Gamma \propto T/hc$ when $b/2h_c<s_p$ and $\Gamma \propto (T/hc)^{-1}$ for $b/2h_c>s_p$ (see figure 17).

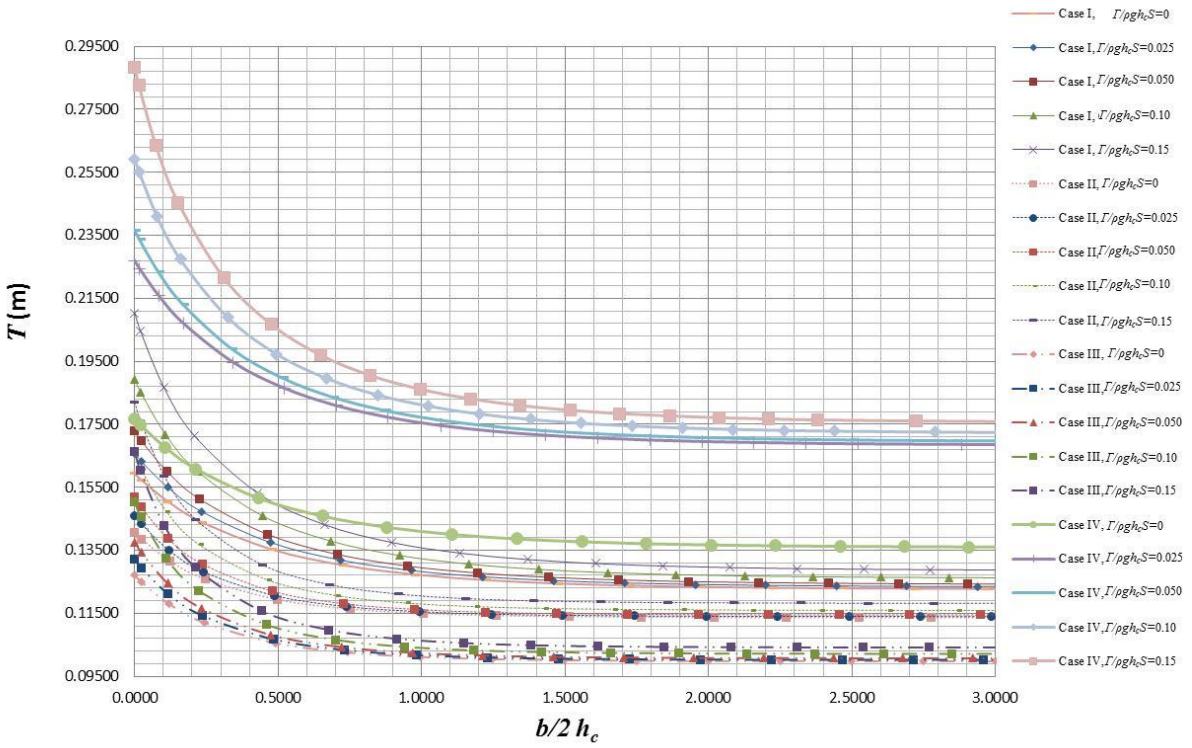

Figure 15. Variation of the bankside width, T, with respect to the dimensionless half central flatbed, $b/2hc$, along with two hydraulic cases

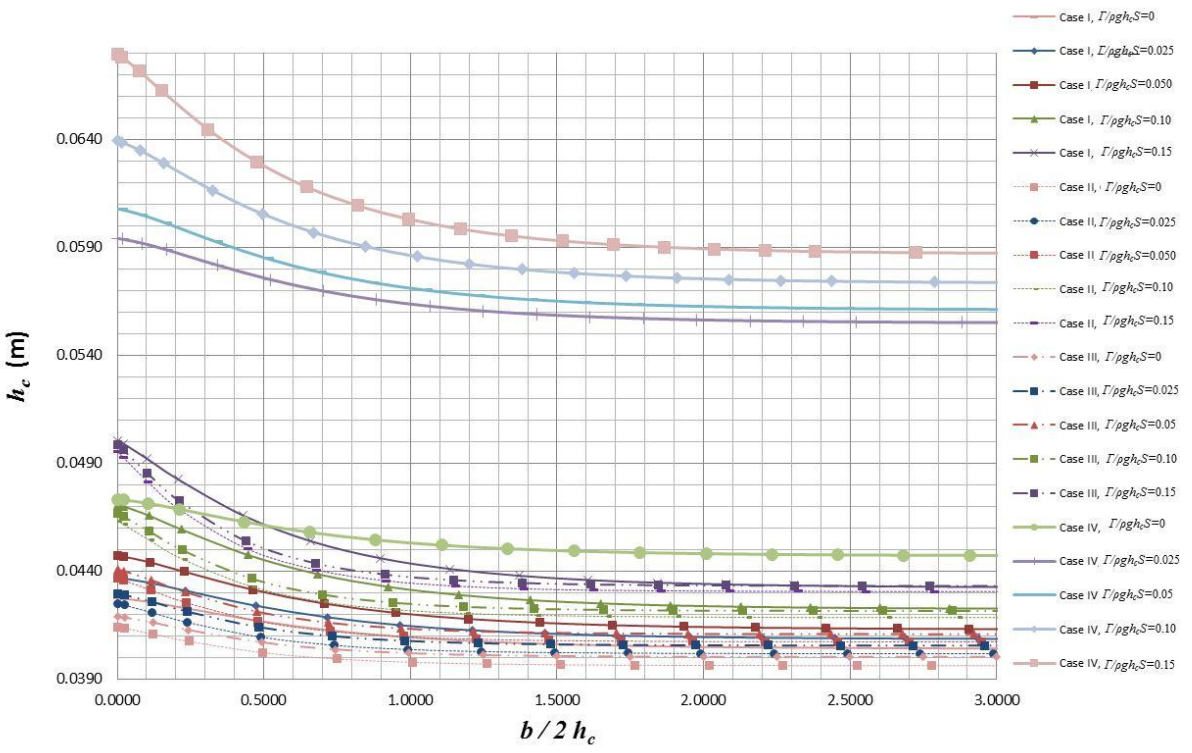

Figure 16. Variation of the central depth, h_c, with respect to the dimensionless half central flatbed, $b/2h_c$, along with two hydraulic cases

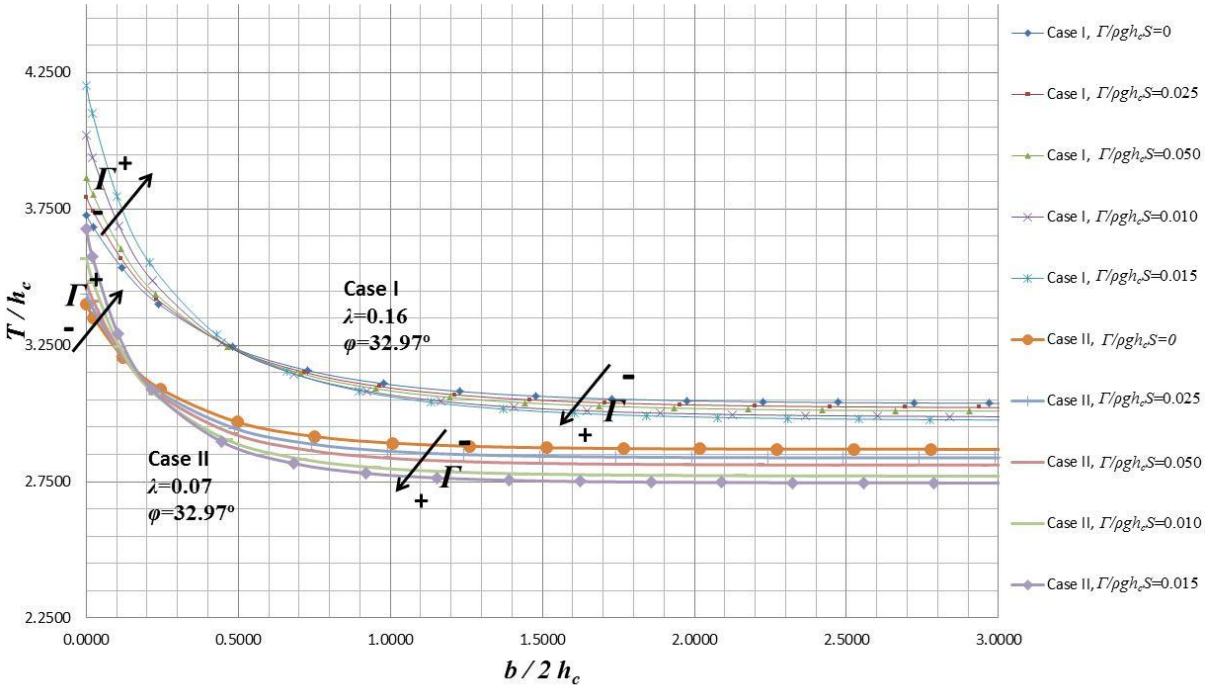

Figure 17.Variation of the dimensionless bankside, T/h_c, with respect to the dimensionless half central flatbed, $b/2h_c$, along with two hydraulic cases. Cases I and II

3.4.2.2 Effect of the input variables on the model

In order to observe the model response to the input variables (Γ, λ, S and φ), the output data (f, A, Q, V, $U_{d\max}$, $U_{d\text{toe}}$, $\tau_{\max}$, τ_{toe}, T, h_c, and T/h_c) were analysed. The methodology was to plot the output results of four cases (see table 2, columns I, II, III and IV), being 20 data per case per variable, and compare them against their corresponding $b/2h_c$ values (see figures 20, 18, 21, 25, 22, 23 and 24). The result was the identification of proportionalities for Γ, λ, S and φ (tables 3, 4, 5 and 6).

With respect to the impact of Γ to the model, when λ, S and φ are fixed, the result is that Γ is directly proportional to the hydraulic area, A, and to the discharge, Q. The reason behind is that when Γ increases, U_d decreases, then h_c needs to grow

in order to satisfy the threshold condition at the toe. Subsequently, if h_c grows, T increases as well, maintaining the cosine bankside shape. Then A is increased, and because A grows more than the velocity decrement, Q grows with Γ. For the average velocity, V, this trends to decrease when Γ increases, but when $b/2h_c$ is close to zero the trend is inverted (see table 3).

Table 3. Effect of varying Γ and holding λ, S and φ on the Yu and Knight model. The symbol (+) represents increase; (-) decrease; and (=) no change.

Variable	Fixed variables	+/-	f	A	Q	V	$U_{d\max}$	$U_{d\text{toe}}$	$\tau_{\max}$	τ_{toe}	T	h_c	T/h_c
Γ	λ, S, φ	+	+	+	+	+/-	-	-	+	=	+	+	+/-
		-	-	-	-	+/-	+	+	-	=	-	-	+/-

The effect of λ on the model, when the rest of the input variables are fixed, is similar to the impact of Γ, because both factors are inversely proportional to U_d. This means that when λ increases, U_d decreases. Then, h_c will increase, as was explained above. About the velocity, it was observed that $U_{d\text{toe}}$ and $U_{d\max}$ are inversely proportional to λ, while the average velocity, V, is directly proportional when $b/2h_c$ trends to zero (table 4).

Table 4. Effect of varying λ and holding Γ, S and φ on the Yu and Knight model. The symbol (+) represents increase; (-) decrease; and (=) no change.

Variable	Fixed variables	+/-	f	A	Q	V	$U_{d\max}$	$U_{d\text{ toe}}$	$\tau_{\max}$	τ_{toe}	T	h_c	T/h_c
λ	Γ, S, φ	+	+	+	+	+/-	-	-	-	=	+	+	+
		-	-	-	-	+/-	+	+	+	=	-	-	-

About the impact of φ on the model, it consists in the reduction of the hydraulic area, A, when φ grows. This is because the cosine bank shape trends to be φ at the margin (equation 35), then when it increases, T decreases. Furthermore, $U_{d\text{toe}}$

reduces when φ increases, allowing a higher depth, h_c, to satisfy the threshold condition, but since T decreases, A decreases as well, regardless of the increment on h_c. With respect to the impact of φ on the average velocity, V, these both are directly proportional, but the discharge, Q, is reduced because A decreased significantly. The ratio T/h_c is inversely proportional to φ. Finally, it was not possible to identify a pattern for f and $U_{d\max}$ when φ varies (table 5).

Table 5. Effect of varying φ and holding Γ, S and λ on the Yu and Knight model. The symbol (+) represents increase; (-) decrease; and (=) no change.

Variable	Fixed variables	+/-	f	A	Q	V	$U_{d\max}$	$U_{d\ toe}$	$\tau_{\max}$	τ_{toe}	T	h_c	T/h_c
φ	Γ, S, λ	+	+/-	-	-	+	+/-	-	+	=	-	+	-
		-	+/-	+	+	-	+/-	+	-	=	+	-	+

With respect to the effect of longitudinal slope, S, on the model, it is possible to say that it is inversely proportional to T and h_c, and subsequently to the cross sectional area, A. But, these two variables (T and h_c) change at the same rate, remaining unaltered the ratio T/h_c. This can be explained due to the bankside equation used does not incorporate S to define the transversal geometry (see equation35).Then, T/h_c prevails constant when Γ, φ and λ are fixed. Since the shape of the cross section does not change with the slope, and seeing that the threshold condition is fixed at the bankside toe, it is logical to expect no differences between shear stress profiles that vary only on slopes, producing equal $\tau_{\max}$, as can be observed on figure 24.

In relation to the impact of S on V, it sounds illogical the reduction of V when S is increased, but this can only be explained by the action of f, being inversely proportional to V and directly proportional to S (table 6). This situation is also

expressed by the equation of Manning:

$$V = \frac{1}{n} R^{2/3} S^{1/2} \tag{37}$$

where n is the Manning's friction factor, that can be related to f as $f = 8 g n^2 h^{-1/3}$ (e.g.Knight et al., 2010). Hence, it is acceptable that S is inversely proportional to V, making emphasis on the sensibility of f to the model. It should be noted that f and n are altered by h, especially f when h is shallow, as have being shown by other authors, *e.g.* Sterling (1998, p. 6.9).

Table 6. Effect of varying *S* and holding *Γ*, *φ* and *λ* on the Yu and Knight model. The symbol (+) represents increase; (-) decrease; and (=) no change.

Variable	Fixed variables	+/-	f	R	A	Q	V	$U_{d\max}$	$U_{d\ toe}$	$\tau_{\max}$	τ_{toe}	T	h_c	T/h_c
S	Γ, φ, λ	+	+	-	-	-	-	-	-	=	=	-	-	=
		-	-	+	+	+	+	+	+	=	=	+	+	=

3.4.3 Figures

3.4.3.1 Variation of A with respect to $b/2h_c$

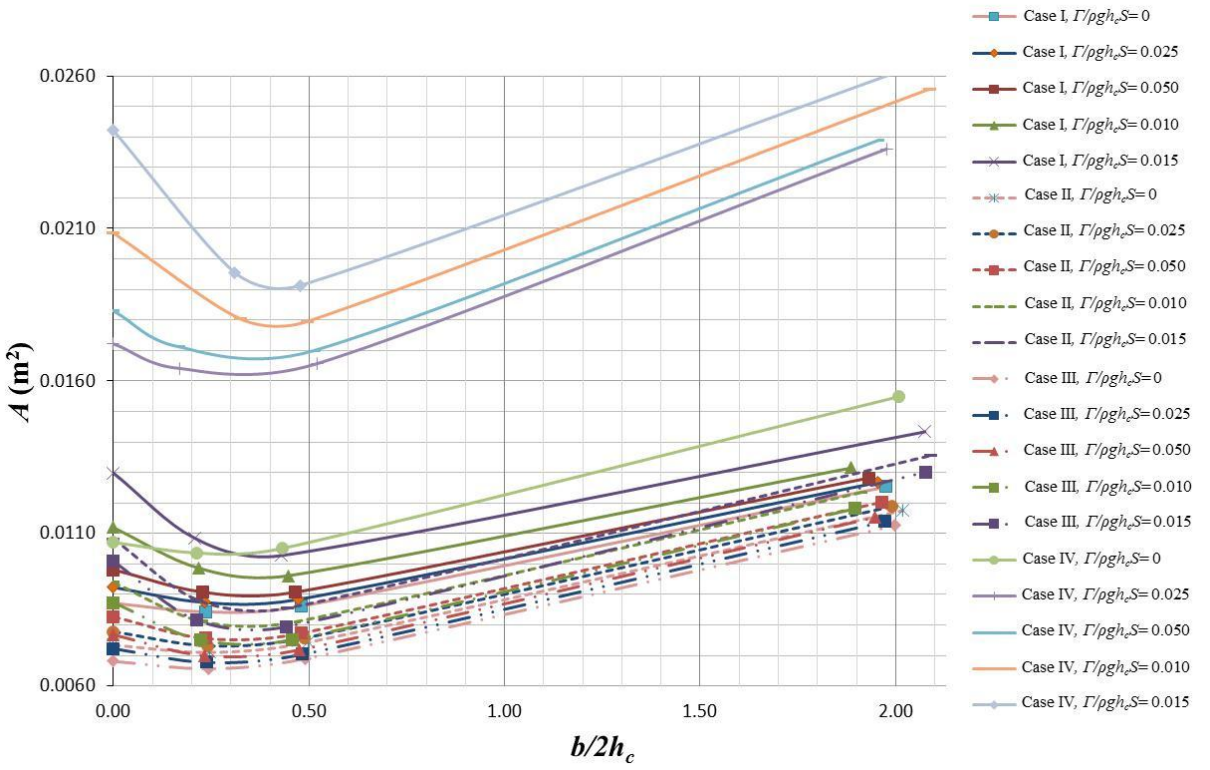

Figure 18. Variation of the hydraulic area, A, with respect to the dimensionless half central flatbed, $b/2h_c$, along with two hydraulic cases. The input variables are Γ, S, λ and φ, corresponding to the cases shown on tables 1 and 2, also mentioned on the legend, and $b/2h_c$. The output variable is A.

Figure 18 shows the variation of the hydraulic area of the channel, A, with respect to the dimensionless half central flatbed, $b/2h_c$, for the cases I-IV, the rest of the cases presentment the same pattern. It is observed that while $b/2h_c$ is growing, A tends to decrease, until it reaches a minimum and then increases. This can be explain due to A is directly proportional to the bankside width, T, and to the central depth, h_c, being both variables affected by $b/2h_c$ as was seen on section 3.4.2.1 (figures 15 and 16). Then, while $b/2h_c$ is growing A decreases due to a reduction on T and h_c. The increment on $b/2h_c$ is not able to compensate the loss area until it has

passed the minimum value of the curve. Such minimum value of A does not coincide with the stable limit, s_l, of the curve T/h_c vs. $b/2h_c$ of the corresponding cases (figure 17). On the other hand, it is observed on figure 18 that A is directly proportional to Γ and λ; and that A is inversely proportional to φ and S.

3.4.3.2 Variation of R with respect to $b/2h_c$

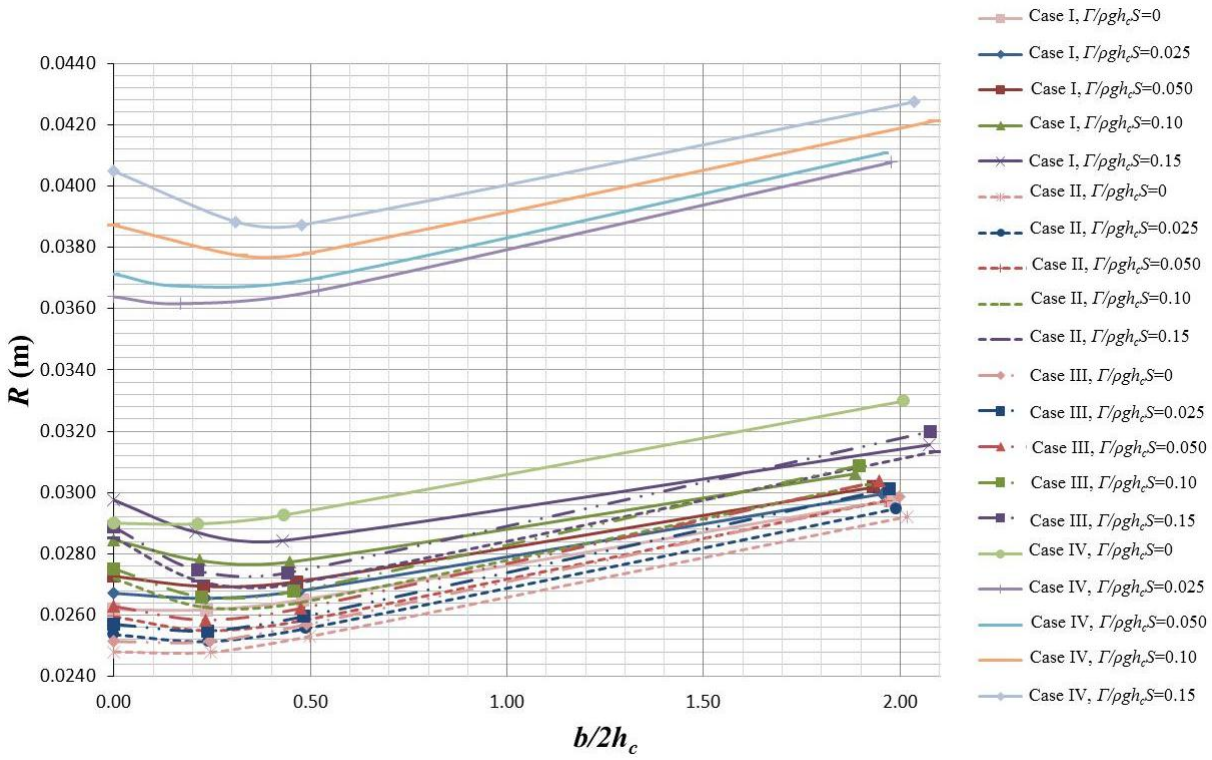

Figure 19.Variation of the hydraulic radius, R, with respect to the dimensionless half central flatbed, $b/2/h_c$, along with four hydraulic cases. The input variables are Γ, S, λ and φ, corresponding to the cases shown on tables 1 and 2, also mentioned on the legend, and $b/2h_c$. The output variable is R.

With respect to the variation of the hydraulic radius, R, against the dimensionless half central flatbed, $b/2h_c$, the figure 19 is showing a pattern similar to the one of A vs. $b/2h_c$ (figure 18). That is reducing R while $b/2h_c$ is growing, until it reaches a minimum, and then it increases proportionally to $b/2h_c$. Such similarity

between figures 19 and 18 is due to R is directly proportional to A. From comparing curves with different values of Γ, λ, φ and S, it was found that R is directly proportional to Γ and λ; and inversely proportional to φ and S.

3.4.3.3 Variation of f with respect to $b/2h_c$

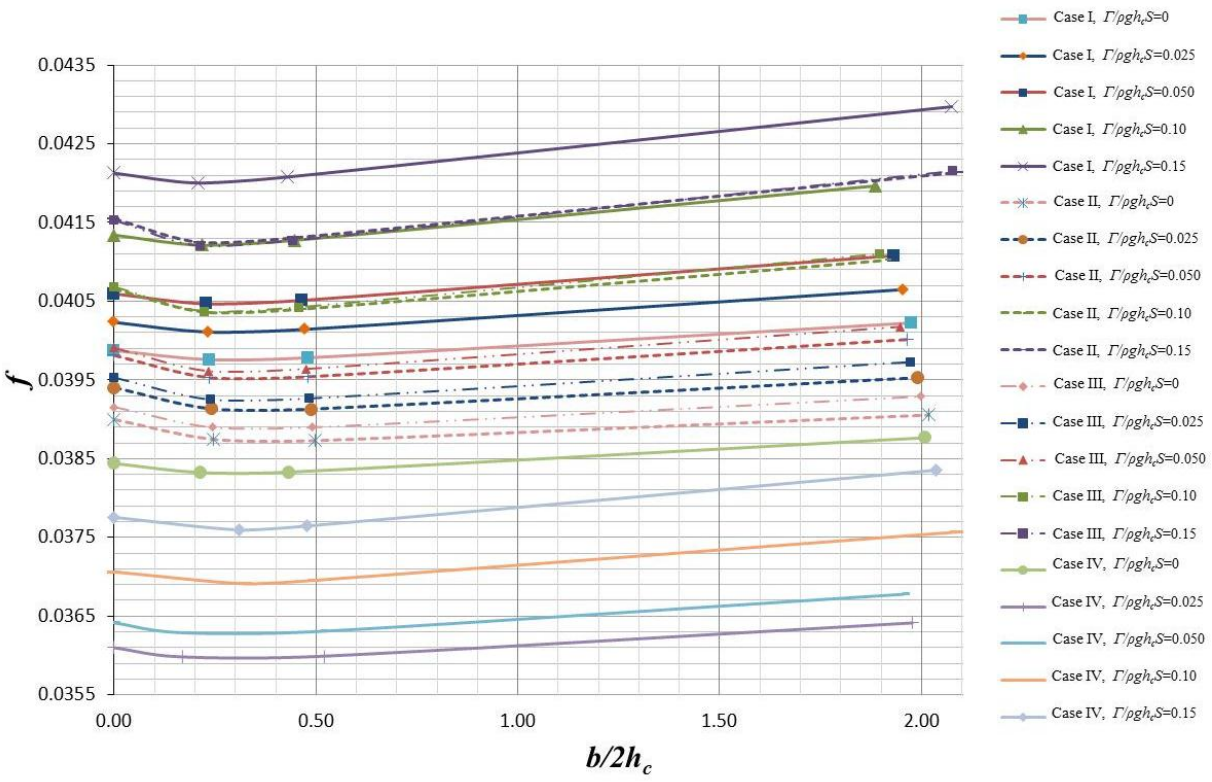

Figure 20. Variation of the friction factor, *f*, with respect to the dimensionless half central flatbed, $b/2h_c$, along with two hydraulic cases. The input variables are Γ, S, λ and φ, corresponding to the cases shown on tables 1 and 2, also mentioned on the legend, and $b/2h_c$. The output variable is *f*.

About the variation of the friction factor, f, with respect to $b/2h_c$, it is observed on figure 20 that its behaviour is similar to the one of A and R on figures 18 and 19. That is reducing the value of f while $b/2h_c$ is growing, until it reaches a minimum, and then it increases. From observing the different curves, corresponding to distinct values of λ, Γ, φ and S, it was found that f is directly affected by Γ and λ, and inversely

proportional to S, without being able to identify a relationship between f and φ. By comparing figures 18 and 20, it is clear that f is directly related to A. It should be noted that the variation of each curve f vs. $b/2h_c$ was less than 3%.

3.4.3.4 Variation of Q with respect to $b/2h_c$

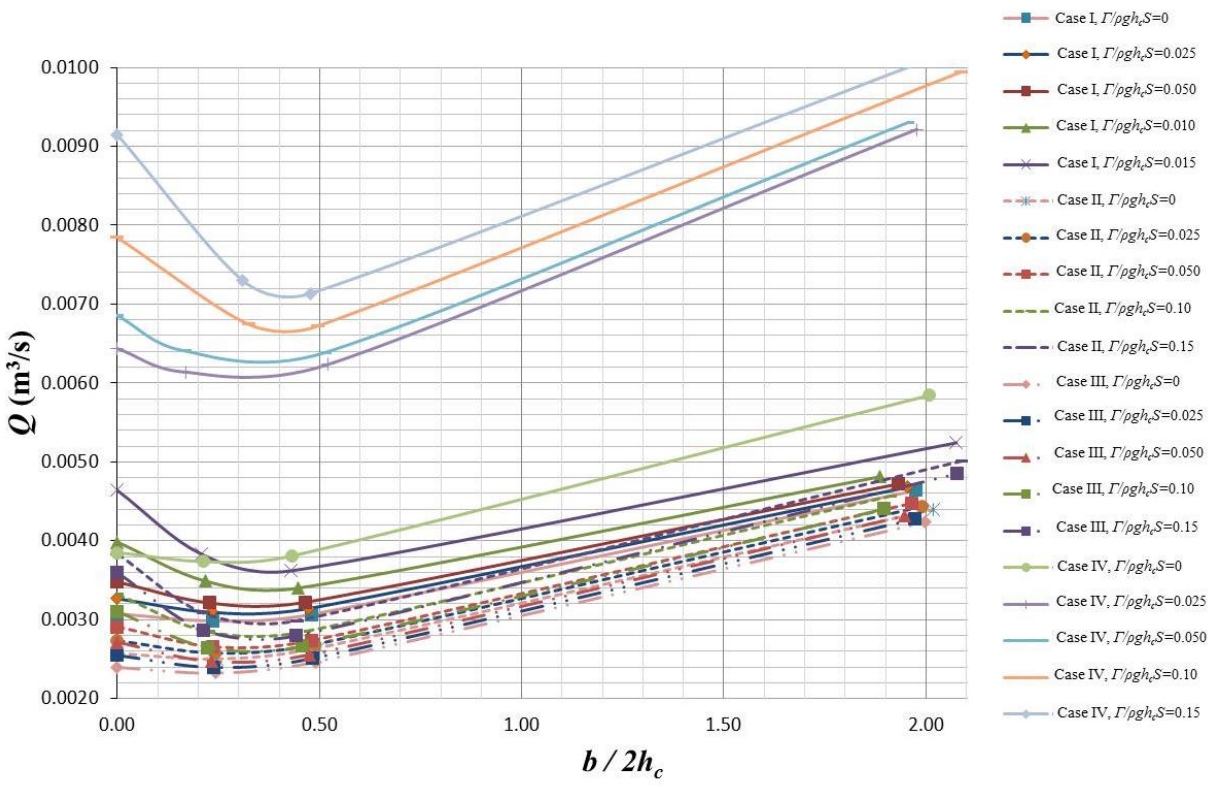

Figure 21. Variation of the discharge, Q, with respect to the dimensionless half central flatbed, $b/2h_c$, along with two hydraulic cases. The input variables are Γ, S, λ and φ, corresponding to the cases shown on tables 1 and 2, also mentioned on the legend, and $b/2h_c$. The output variable is Q.

With respect to the variation of the discharge, Q, along $b/2h_c$, the figure 10 is showing different curves for distinct cases (table 1). It is observed that while $b/2h_c$ increases, Q decreases until it reaches a minimum and then increases. This is similar to the behaviour of A and R (figures 18 and 19), as was expected, due to Q is directly proportional to A and R. About its interaction with λ, Γ, φ, and S, it is shown that Q is directly proportional to Γ and λ, and inversely proportional to φ and S.

3.4.3.5 Variation of U_d with respect to $b/2h_c$

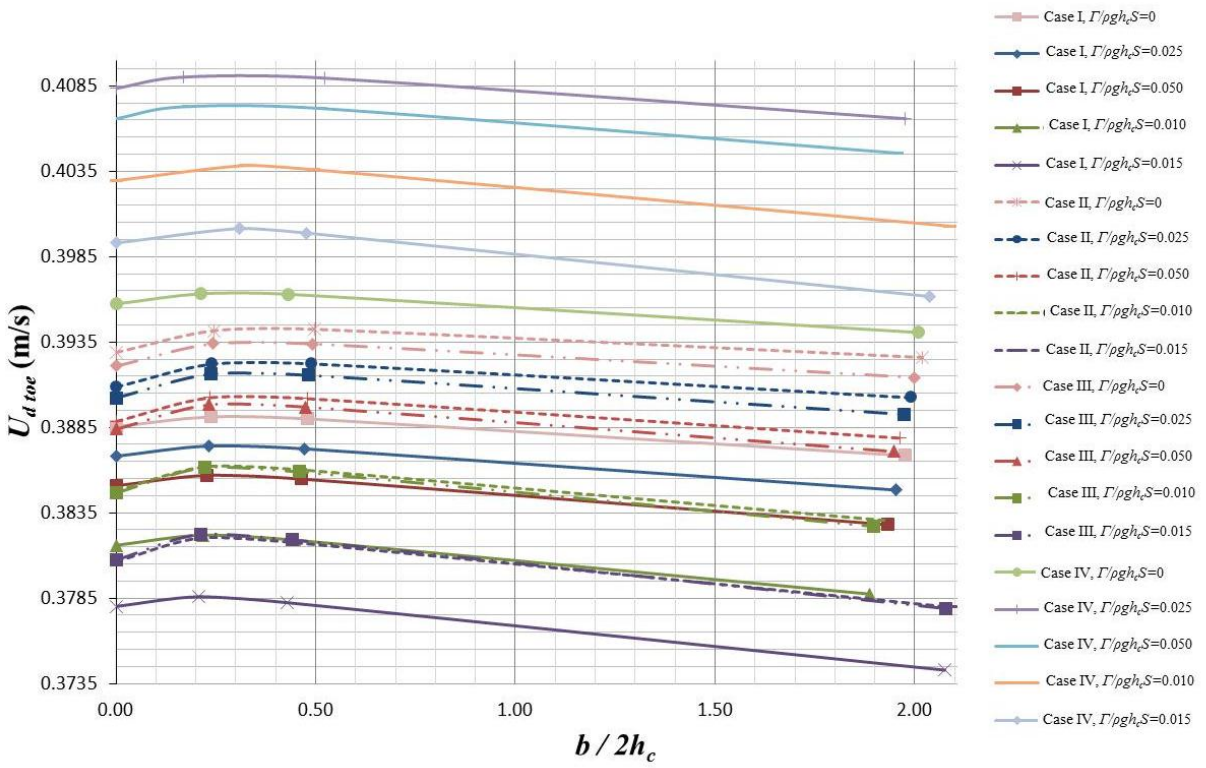

Figure 22. Variation of the $U_{d\,toe}$ with respect to the dimensionless half central flatbed, $b/2h_c$, along with two hydraulic cases. The input variables are Γ, S, λ and φ, corresponding to the cases shown on tables 1 and 2, also mentioned on the legend, and $b/2h_c$. The output variable is U_{dtoe}.

Figure 22 is showing the variation of the depth average velocity at the bankside toe, $U_{d\,\mathrm{toe}}$, with respect to $b/2h_c$ for different hydraulic cases (see table 1). The pattern of each curve consists in to grow while $b/2h_c$ is increasing, until it reaches a maximum point and then decreases. The physical meaning of this behaviour is that when $b/2h_c=0$, $U_{d\,\mathrm{toe}}$ constitutes the maximum depth average velocity of the cross section, $U_{d\,\max}$, such that $U_{d\,\max}$ satisfies the threshold condition at that point, being the SKM boundary condition there $\left(\partial U_d/\partial y=0\right)$. Then, while $b/2h_c$ is growing, $\partial U_d/\partial y=0$ moves with it, yielding a higher $U_{d\,\max}$ located at the channel centre line, as can be observed on figure 23.

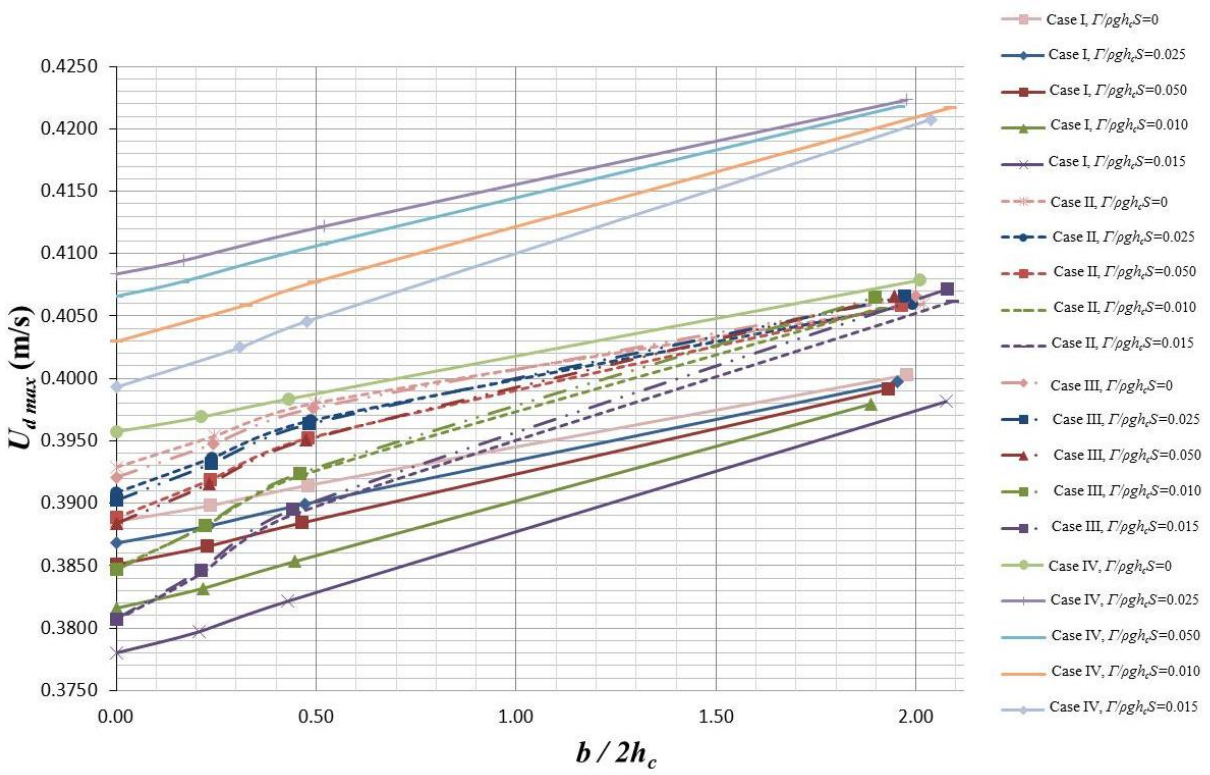

Figure 23. Variation of the U_{dmax} with respect to the dimensionless half central flatbed, $b/2h_c$, along with two hydraulic cases. The input variables are Γ, S, λ and φ, corresponding to the cases shown on tables 1 and 2, also mentioned on the legend, and $b/2h_c$. The output variable is U_{dmax}.

About $U_{d\,\mathrm{toe}}$, it should be less than $U_{d\mathrm{max}}$, obtaining its maximum value when A reaches its minimum (figure 18), what produces an accelerated flow. Subsequently, while $b/2h_c$ and A increase, $\partial U_d / \partial y$ at the bankside toe trends to be smoother, implying minor values for $U_{d\mathrm{toe}}$.

By comparing the curves of distinct hydraulic cases for figures 22 and 23, it is observed that $U_{d\mathrm{toe}}$ is inversely proportional to λ, Γ, φ and S; and $U_{d\mathrm{max}}$ is inversely proportional to λ, Γ and S, with respect to φ, it is not possible to establish a relationship.

3.4.3.6 Variation of τ_{max} with respect to $b/2h_c$

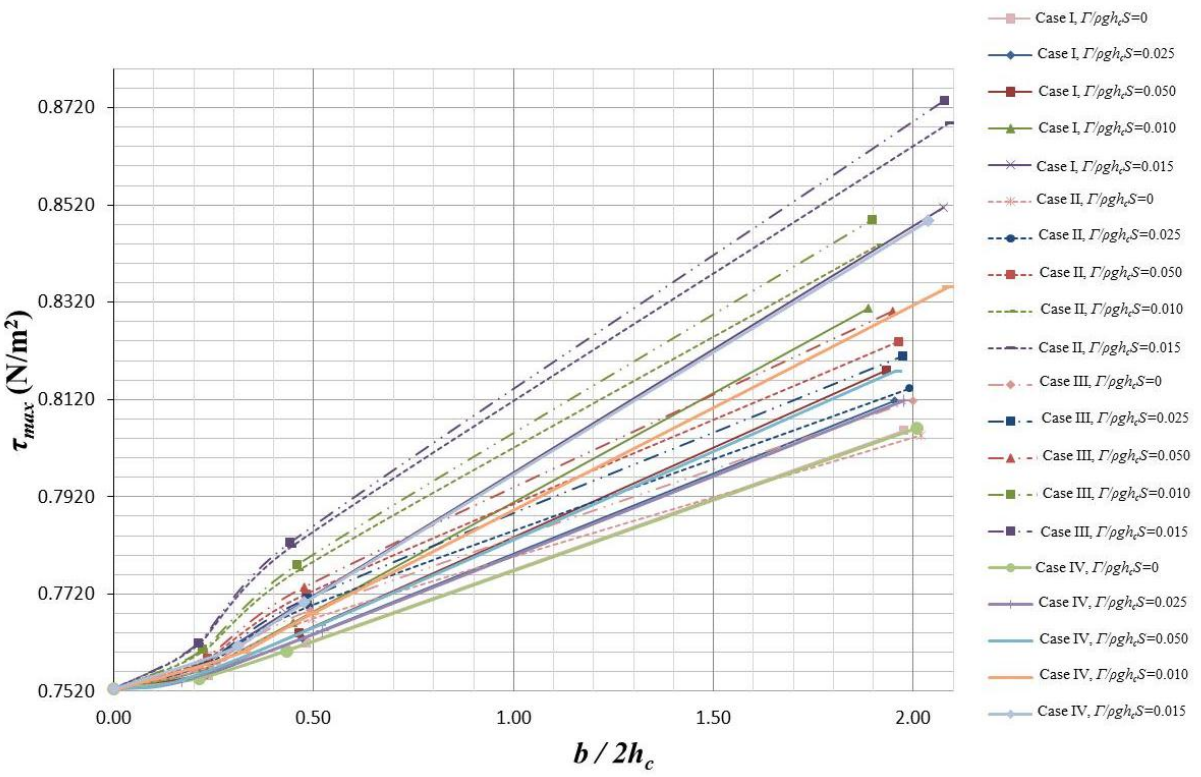

Figure 24. Variation of the τ_{max} with respect to the dimensionless half central flatbed, $b/2h_c$, along with two hydraulic cases. The input variables are Γ, S, λ and φ, corresponding to the cases shown on tables 1 and 2, also mentioned on the legend, and $b/2h_c$. The output variable is τ_{max}.

The figure 24 is showing the variation of the maximum boundary shear stress, $\tau_{\max}$, with respect to $b/2h_c$. Each curve is ascending with an step located on the minimum area zone (figure 18) and the maximum $U_{d\ \mathrm{toe}}$ zone (figure 22). As was explained above, the boundary condition of the SKM flow model is located at the centre line $\left(\partial U_d / \partial y = 0\right)$, where $\tau_0 = \rho f U_d^{\ 2} / 8$, and subsequently $\partial \tau_0 / \partial y = 0$ at the centre line. Then, as happened with $U_{d\max}$, $\tau_{\max}$ keeps increasing while $b/2h_c$ does. The threshold condition is set at the bankside toe, then τ_0 should be constant at that point, being unnecessary to graph it. With respect to the influence of λ, Γ, φ and S to $\tau_{\max}$, from observing figure 24, it is possible to say that $\tau_{\max}$ is directly proportional to Γ and

φ, inversely proportional to λ, and impact less to S. This last is not a surprise, due to S does not intervene on the Yu and Knight (1998) bank equation (equation35).

3.4.3.7 Variation of V with respect to $b/2h_c$

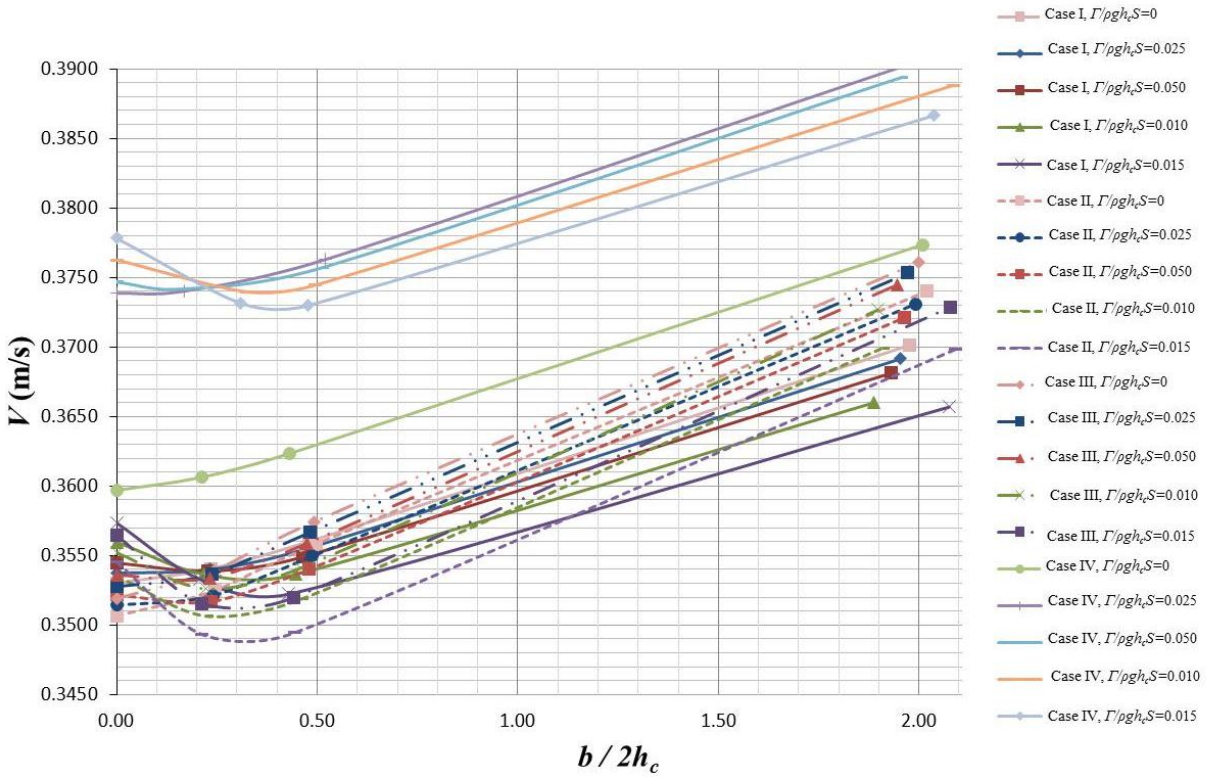

Figure 25. Variation of the average velocity of the cross section, *V*, with respect to the dimensionless half central flatbed, $b/2h_c$, along with hydraulic cases. The input variables are *Γ*, *S*, λ and φ, corresponding to the cases shown on tables 1 and 2, also mentioned on the legend, and $b/2h_c$. The output variable is *V*.

Finally, the variation of the average velocity of the cross section, V, with respect to $b/2h_c$ is shown in figure 25. The curves present in general an ascending behaviour after passed the minimum area point (figure 18). However, the curves are descending before the minimum area point when $\Gamma>0$. The physical meaning is that when $b/2h_c$ is growing, A decreases, and V increases. But, when $\Gamma>0$, A is reduced at

a bigger rate (figure 18), descending V before reach the minimum area point. There is not a constant pattern between Γ and λ to V. With respect to φ, it is possible to say that φ is directly proportional to V, this is due to higher φ support greater τ_0 and consequently greater V.

About S, it is inversely proportional to V, because S is directly proportional to f (figure 20). Physically means that the slope is restricted by the threshold condition, that depends on the critical shear stress, τ_c, and this on the soil diameter, d, of the channel. Then, a channel with a steep S will have a smaller h_c that satisfies the threshold condition, than another one with a smooth S, and subsequently a smaller A, R and V. To guarantee this, the model increases f.

3.5 Main findings

The model of Yu and Knight (1998) predicts the self-formed cross section of an alluvial stream, based on the characteristics of the soil and flow. Because it depends on the flow, it can adjust the bank side according to the length of the flatbed, being the transversal slope steeper when a flatbed exists.

One disadvantage of the methodology applied is that it yields four points on the bankside. This draws a poor shape with an initial slope at the toe greater than the experiments of Ikeda (1981), but coinciding with the width. In the publication Yu and Knight (1998) employed a numerical solution for the SKM, obtaining a better approximation, close to Ikeda (1981) data.

On the other hand, it was noticed from figure 6 of Yu and Knight (1998) and figure 13 of Ikeda (1981), that Yu and Knight did not consider the flatbed of 17.8 cm for their example. However, their results are close to the ones of Ikeda (1981). From

the simulations, it was found that when such bed is taken into account the bank side becomes steeper, separating from Ikeda. This can be adjusted by adding the secondary flow, Γ, to the model of Yu and Knight(1998). Although standard values for this variable have not been calibrated for parabolic sections.

Based on the previous analysis of the Yu and Knight model (1998), the mechanism that relates the variation of T/h_c to $b/2h_c$ was identified. The impact of Γ, λ, φ and S was observed, and the physical meaning identified, founding proportionality relationships with respect to these variables and the output data.

If λ, φ and S are constants, then:

$$\Gamma \propto f,\ A,\ Q,\ \frac{1}{U_d},\ \tau_{max},\ T,\ h_c \tag{38}$$

If Γ, φ and S are constants, then:

$$\lambda \propto f,\ A,\ Q,\ \frac{1}{U_d},\ \frac{1}{\tau_{max}},\ T,\ h_c,\ \frac{T}{h_c} \tag{39}$$

If Γ, λ and S are constants, then:

$$\varphi \propto \frac{1}{A}, \frac{1}{Q}, V,\ \tau_{max},\ \frac{1}{T},\ h_c,\ \left(\frac{T}{h_c}\right)^{-1} \tag{40}$$

If Γ, λ and φ are constants, then:

$$S \propto f,\ \frac{1}{A}, \frac{1}{Q},\ \frac{1}{V}, \frac{1}{U_d},\ \frac{1}{T},\ \frac{1}{h_c} \tag{41}$$

and T/h_c remains constant.

From the cases analysed, it was shown that the curves T/h_c vs $b/2h_c$ reach a

stable limit when $b/2h_c$>2 approximately. Then, it is possible to say that for wide channels ($B/h>15$; B, top width of the channel) the value of T/h_c always will correspond to the one at s_l.

It should be noted the importance of Γ and λ, due to they can modify the predicted cross sectional geometry of the channel. This impacts the estimated hydraulic capacity of the channel, underestimate it implies risk for the surrounding area.

CHAPTER 4

PHYSICAL MODEL

In order to determine the behaviour of the flow in a self-formed cross section, it was required to observe it by mapping its velocity distribution and measuring the boundary shear stress across the section, with the purpose of calibrating a quasi 2D flow model (SKM). Albeit velocity data are available (*i.e* Ikeda, 1981, and Diplas, 1990), they correspond to a half section experiments, having a vertical wall in one side and a self-formed bankside on the other, altering its flow pattern. Then, a channel was constructed with a symmetrical shape inspired in the one of Ikeda (1981) on both margins (figure 26). The channel was tested by two surfaces one smooth (PVC) and one rough (glue sand, d_{50}=1.41mm), being the objective of the first one to have a regular surface with a measurable friction factor (figure 27). While the second one was to validate the results found in the first one, and analyse the flow in a section with rough surface, as happens in self-formed channels.

Figure 26 . Upstream view of the flume during experiments on glue sand surface. Approximated depth: h_c=3.5cm.

Figure 27. Downstream view of the channel without water. Above on smooth surface (PVC). Below on rough surface (glue sand).

4.1 The apparatus

The flume employed is located in the hydraulics laboratory of The University of Birmingham. It tilts and has 11.5 m long, 46 cm width and 43 cm depth (figure 26). The inflow is provided by a pump connected to a 6 in. pipe diameter, who delivers the discharge vertically to the flume by an arrange of pipes (figure 28), being the gap between the pipe and the bed of the flume just 4 cm, producing high turbulence, making difficult the obtention of the fully developed flow condition. Hence, a honeycomb panel was added right after, helping to align the flow (figures 29).

The flume allows setting a specific slope with a precision of 1/10,000 by adjusting the scale that elevates the flume, locating the jack point at half length of the channel. The device has a self-contained water tank with a capacity of 10 m^3. With respect to the discharge capacity of the pump, the minimum is 1L/s and the maximum 40 L/s, controlled by a valve on the arrange of pipes, measured by a digital electromagnetic flowmeter (ABB Kent-Taylor MagMaster, figure 30), located after the valve. With respect to this last, it required to be under a calibration program, which was properly accomplished before starting the experiments.

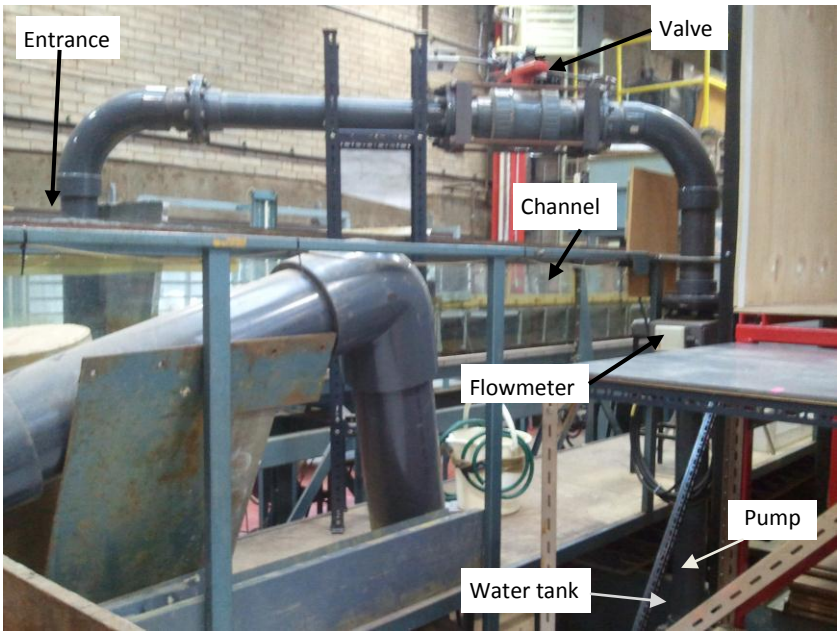

Figure 28. Arrange of pipes conducting water from the tank to the entrance.

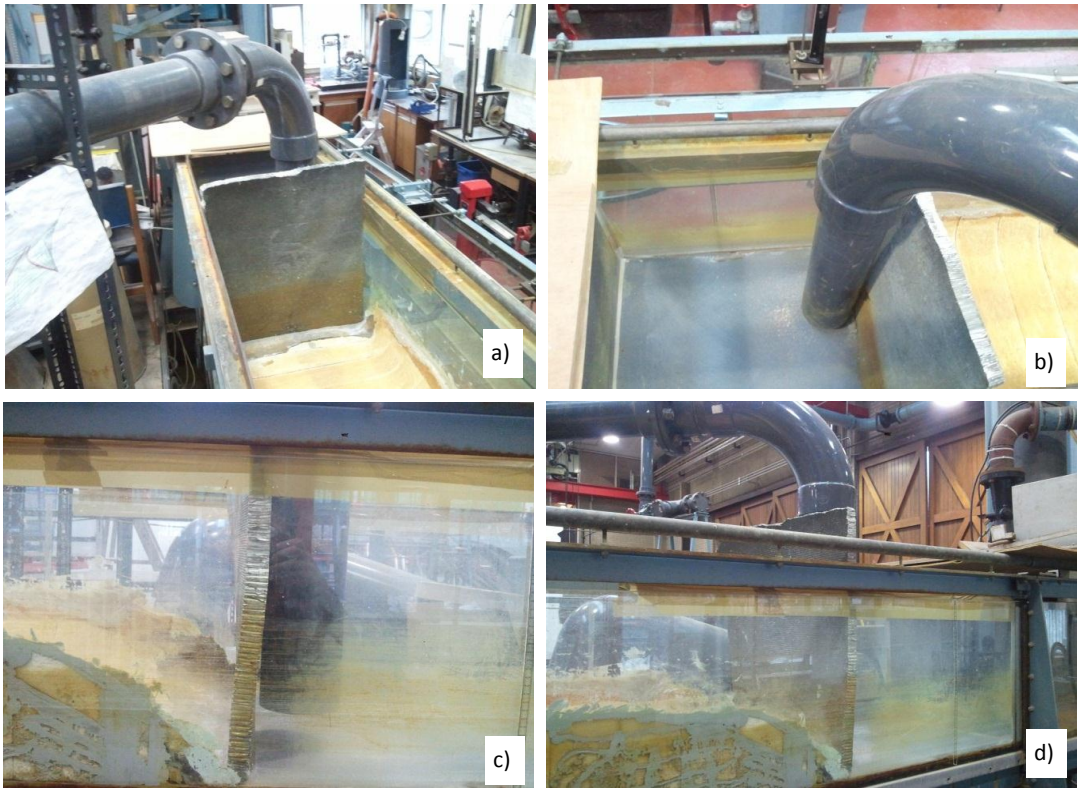

Figure 29. View of the delivery pipe at the entrance of the flume. Four perspective are provided: (a) view from downstream; (b) aerial view; (c) profile view, pipe delivering and transition; and (d) downstream profile view.

Figure 30. Electromagnetic flowmeter used during the experiments: ABB Kent-Taylor MagMaster.

4.2 The cross section

The selected cross section is based on the run 16 of Ikeda (1981), which consists of a self-formed bankside with h_c=4.05cm, d_{50}=1.3mm and S=1/479, but scaled 1.27 times to fit the flume obtaining: h_c=5.14cm, b=19cm, and d_{50}=1.65mm. Later the margin slopes were prolonged 3cm, increasing h_c to 7.17 cm and b to 22cm, leaving 2cm of central flatbed, *i.e.* a section 46cm wide (figure 31). The purpose of the flatbed is to make the shape tangent to the bottom, and the one of the extensions is to allow the corners to be measured since are difficult to reach. Among the advantages of the selected cross section are its symmetry and increment in size with respect to the original, allowing more data to be collected. Since the depth is just 7.17 cm, it is not enough to use an Acoustic Doppler Velocimeter (ADV). Therefore, a Pitot-static tube was recommended instead to measure the longitudinal velocity, U,

and the boundary shear stress,τ_0, by the Preston tube technique. With respect to the Preston tube technique, it was applied only to the smooth surface experiments (*i.e.* PVC surface), due to it presents problems finding precisely the position of the zero velocity datum and the subsequent methodology calibration. Hence, τ_0 was obtained indirectly, by the relationship:

$$\tau_0 = \frac{\rho f U_d^2}{8} \tag{42}$$

where f is Darcy´s friction factor; ρ, the water density; and U_d, the longitudinal depth average velocity. f can be found from the stage discharge curve of the channel, by calculating the average Manning´s n the for a corresponding S. While U_d is determined by finding the average of U along a particular depth.

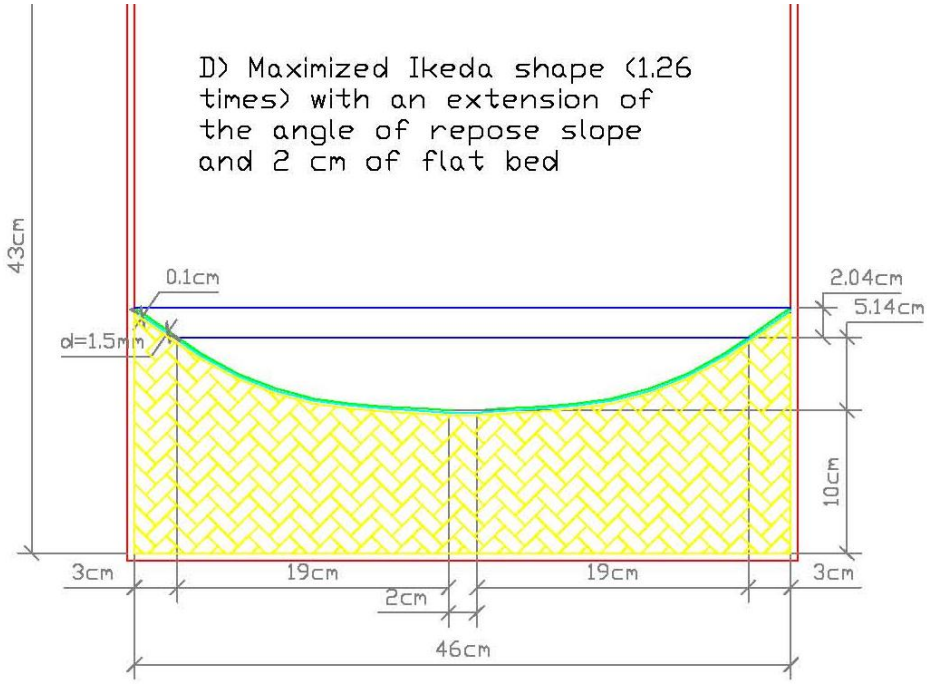

Figure 31. Design of the cross section and support to be placed in the flume. Where B=46cm, b=2cm, T=22cm, and h_c=7.18cm, being B, top width; b, central flatbed; T, bankside width; and h_c, central depth.

4.3 Matrix of experiments

The Yu and Knight (1998) method is restricted by the threshold condition at the bankside toe (section 3.2), it requires that the shear stress at that point, τ_{toe}, should be equal to the resistant shear stress of the soil material, τ_{cr}, *i.e.* $\tau_{toe} = \tau_{cr}\left(\gamma_s - \gamma\right)d$. Then, in order to observe the flow under such condition, it was required a slope that fulfils the requirement. For that purpose, an iteration process was done by using the numerical model (figure 9), changing the slope, S, until reaches $\tau_{toe} = \tau_{cr}$. The variables considered were: d=1.65mm, h_c=5.14cm, n=0.014, Γ=0 and λ=0.07. Due to Γ was unknown at this point, it was not taken into account in order to avoid interference, and λ was considered as previous authors have reported λ=0.07, *e.g.* Abril and Knight (2004). The result was S=1/500 that is bordering the critical flow (Fr=1). Hence, looking for a diameter able to be obtained by sieving, d=1.41mm was proposed (sieve N.14), determining S=1/575 that is farther from the critical slope. However, it was not possible to get commercial sand with such a diameter, but silica sand with similar characteristic was ordered: d_{50}=1.46mm and C_u=1.46. Furthermore, it is desired to observe the behaviour of the flow when S<1/575 and S>1/575. Hence, one slope less than 1/575 and another greater were required. The proposed slope values were: $S2$=$S5$=1/575, $S1$=$S6$=1/675 and $S3$=$S4$=1/200. With respect to $S1$, it was planned for run experiments under subcritical flow and $S3$ for supercritical flow, in order to observe and analyse the flow under such circumstances.

Although the slopes and depths were planned, it was difficult to reach the proposed values, due to the nature of the experiments. Hence, approximated

conditions were obtained, depths: $H1$≈3.50cm, $H2$≈5.0cm and $H3$≈7.17cm; and slopes: $S1$=1/673, $S2$=1/580, $S3$=4/793, $S4$=3/607, $S5$=1/574 and $S6$=1/675, noticing that $S1$≈$S6$≈1/675, $S2$≈$S5$≈1/575 and $S3$≈$S4$≈1/200 (table 7).

Table 7. Code of the experiments with actual slopes tested, and proposed depths.

	Smooth surface (PVC)		
	***S1*=1/673**	***S2*=1/580**	***S3*=4/793**
***H1*≈3.5cm**	H1S1	H1S2	H1S3
***H2*≈5.0 cm**	H2S1	H2S2	H2S3
***H3*≈7.17 cm**	H3S1	H3S2	H3S3

	Rough surface (glue sand)		
	***S4*=3/607**	***S5*=1/574**	***S6*=1/675**
***H1*≈3.5 cm**	H1S4	H1S5	H1S6
***H2*≈ 5.0 cm**	H2S4	H2S5	H2S6
***H3*≈7.17 cm**	H3S4	H3S5	H3S6

4.4 Construction of the channel

4.4.1 Smooth surface

In order to build the channel with the selected transversal geometry (section 4.2), it was recommended to cut supports with such a shape (see figure 31). The material used was PVC, layers of 1cm thickness. Later the supports were placed into the flume, pasting them by using a commercial sealant (Sikaflex 512), being separated by 20cm, covering 10m length (figure 32). With respect to the surface, it was PVC as well, but in layers of 49 cm width, 2 m long and 2 mm thickness, sticking them to the supports by applying sealant between them and pressing the layers until they were able to hold the proposed shape (figures 34 and 35). This was done by using a timber board of 46 cm width and 2 m long with transversal templates made from the waste of the supports, the distance between them was 20 cm. In order to avoid leakage between the layers boundaries, they were covered by brown commercial tape, nullifying the water losses (figure 36). It should be noted that a PVC

layer of 1mm thickness was tried on the channel, but it presented high sinuosity between the supports (peak to peak amplitudes of 2 mm) (figure 33), opting for the 2mm PVC layer.

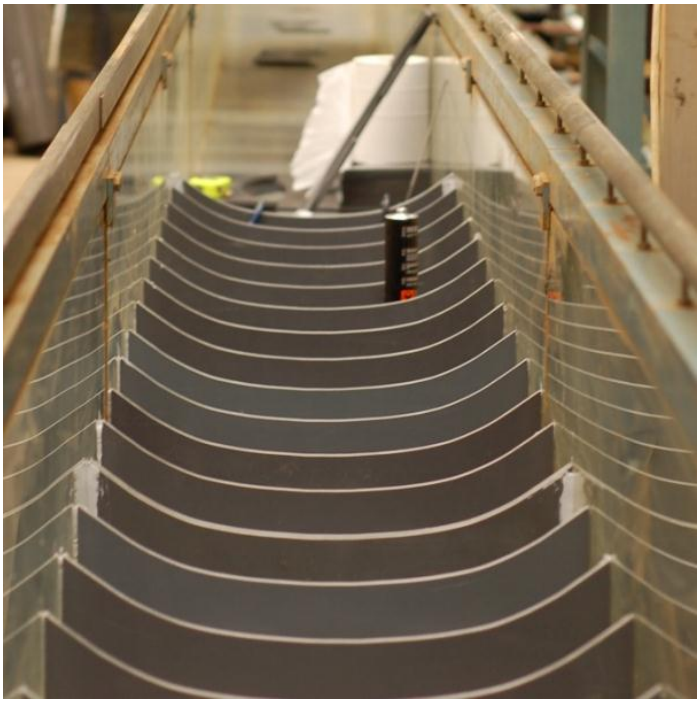

Figure 32. Assembling of transversal supports along the flume.

Figure 33. A PVC layer of 1mm was placed over the supports, showing a high undulation between them.

Figure 34. The 1 mm PVC layer was replaced by a 2mm layer, reducing the undulation.

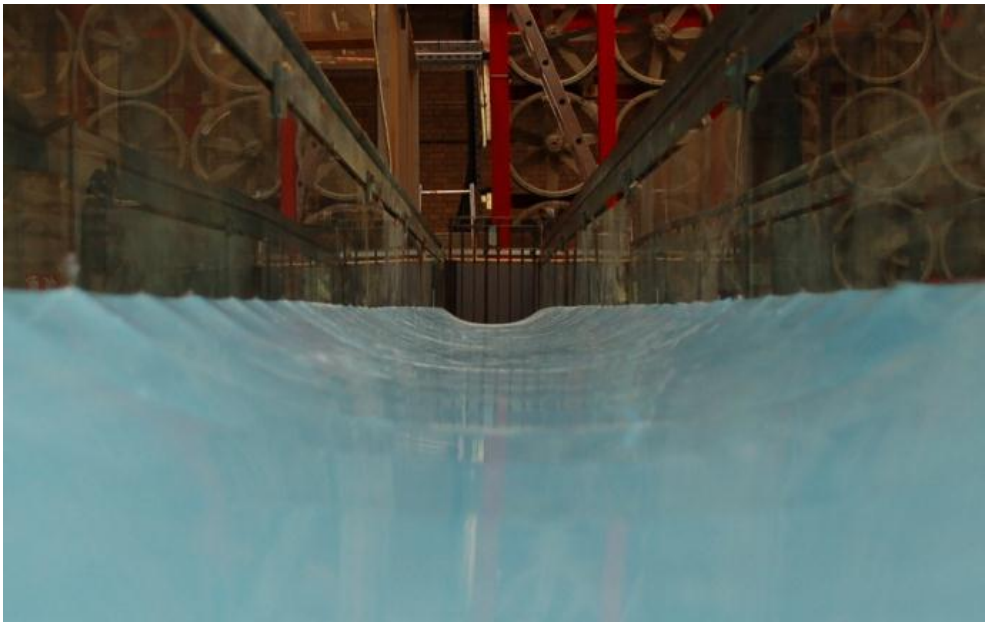

Figure 35. 2mm PVC surface installed.

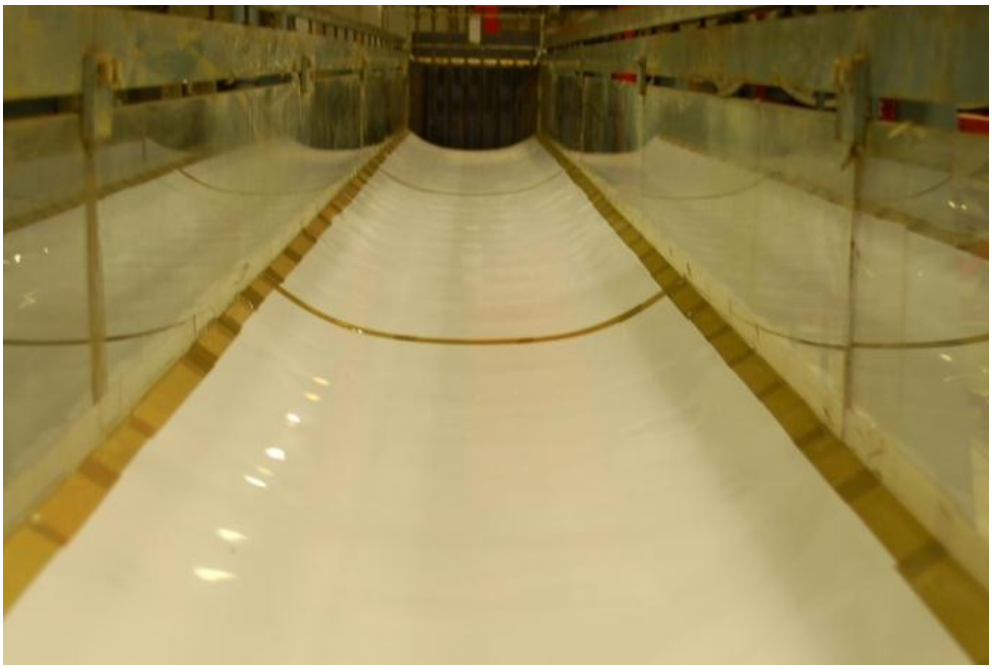

Figure 36. In order to avoid leakage, brown tape was placed between the boundaries.

4.4.2 Rough surface

Once the channel was constructed, and after the set of experiments in smooth surface had finished, a rough surface was installed. The technique consisted of apply a glue layer over the channel surface and then filled with sand, waiting 8 hours to remove the non-stuck sand. With respect to the type of sand used, it had ad_{50}=1.46mmand a coefficient of uniformity C_u=1.46. Since the amount of sand was limited, and it was not possible to fill the whole channel at the same time, the glue was applied by segments (figures 37 to 39).

Figure 37. Glue sand (d_{50}=1.46mm) was applied by segments.

Figure 38. First, glue was applied over a PVC layer, later the section was filled with sand. At the following morning, the excess of sand was removed.

Figure 39.The full length of the channel with glue sand surface.

4.4.3 The transition

As mentioned above the flow was delivered by an arrange of pipes to the flume (figure 29), since the section of the flume was rectangular and the cross section of the channel cosinusoidal with a vertical step of 10 cm, it was required a transition. Among the literature, parameters were found for length, as well as horizontal and vertical contractions, expressed in the following equations given by Akan (2006):

$$L_T = 2.35\Delta B + 1.65 m_c\, h_c \tag{43}$$

$$b_x = b_c + \left(b_f - b_c\right)\frac{x}{L_T}\left[1-\left(1-\left(\frac{x}{L_T}\right)\right)^e\right] \tag{44}$$

$$\left(\frac{x}{L_T}\right)^2 + \left(\frac{z_T}{\Delta z}\right)^2 = 1 \tag{45}$$

where L_T is the transition length; ΔB, the contraction of the transition; m_c, transversal slope (1:m_c, vertical: horizontal); h_c, depth at centre line; b_x, transversal width of the transition at a distance x; b_c, width of the contraction; b_f, width of the flume; z_T, vertical elevation at x; Δz, length of the step between the flume and the channel (figure 40). The value of each variable is shown below:

ΔB=44cm

m_c=1.5

h_c=7.17 cm

Δz=10 cm

b_f=46 cm

$2\,\text{cm} \le b_c \le 46\,\text{cm}$

$0 \le x \le L_T$

obtaining L_T=121.15cm and rounding it to 130cm. Due to b_c varies from 2cm to 46cm, multiple curves were obtained for b_x (figure 41). Finally, the variation of Z_T with respect to x can be observed on figure 42.

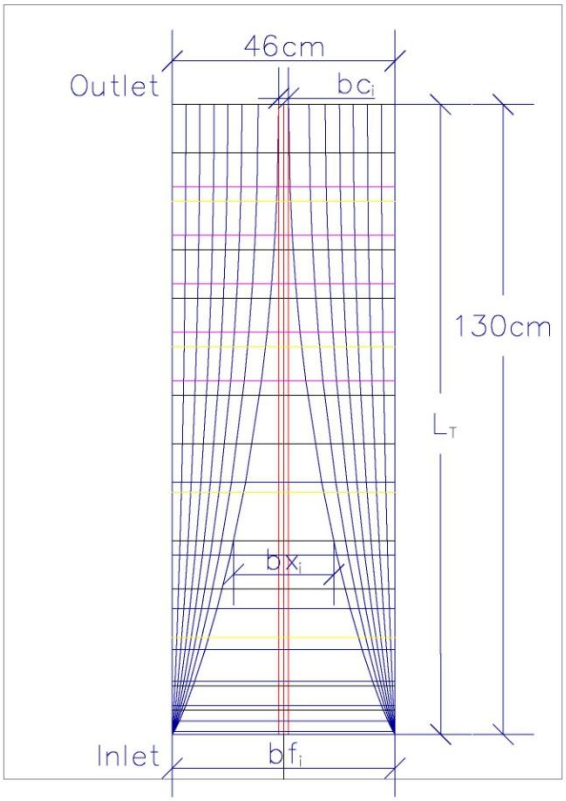

Figure 40. Plan view of the transition describing the variables of the horizontal contraction equation (44). Each curve represents a different horizontal contraction, that is combined with the elevation determined by equation 45 and figure 42.

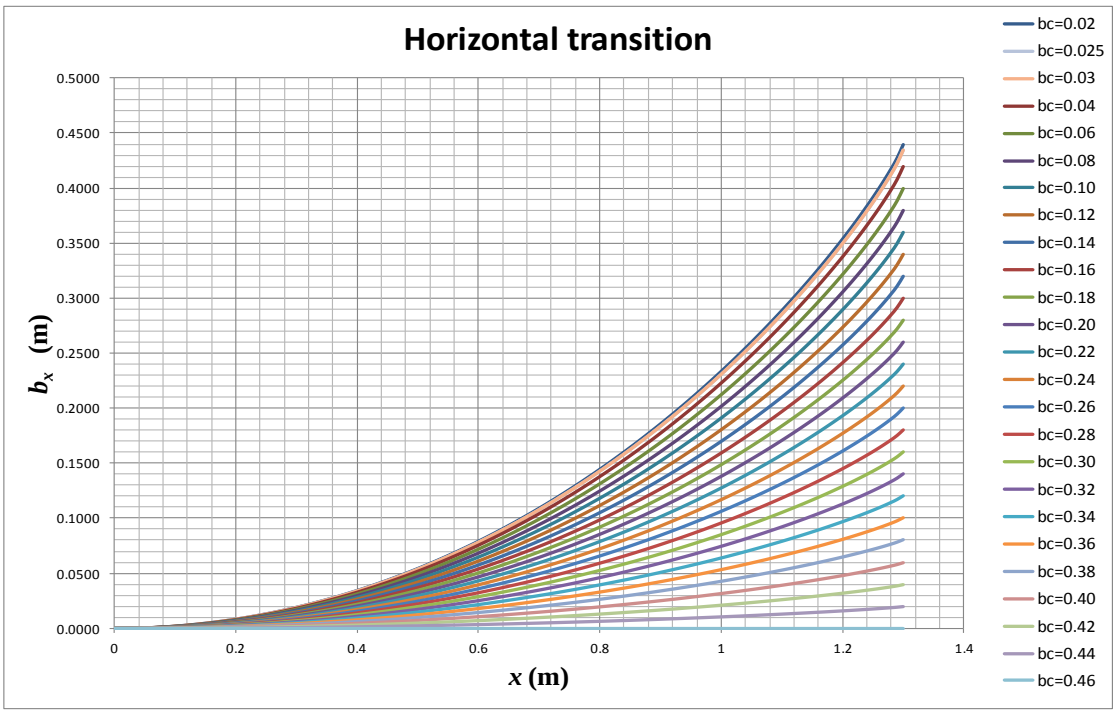

Figure 41. b_x curves for each b_c, departing from the contraction at the origin (cosinusoidal channel) to the rectangular channel on the right hand side end.

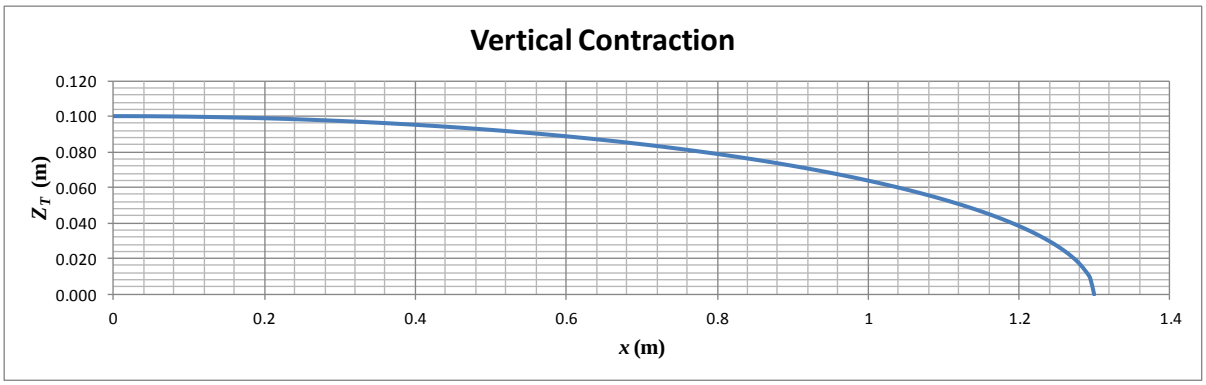

Figure 42. The graph is showing the variation of Z_T with respect to x, based on equation 45.

Once b_c and Z_T were determined, their respective curves were pasted on the AutoCAD drawing, taking the vertical elevation from Z_T for each b_c (figures 43 and 44). The material chosen for the transition was polystyrene, in layers of 10cm. With respect to the construction procedure, first 13 rectangular segments of 46x17cm were trimmed; secondly 13 transversal cross sections of the transition were printed from the drawing at each 10cm. Later the prints were pasted on the polystyrene panels, and by using an electrical saw they obtained the corresponding shape of the transition at a distance X form the cosinusoidal channel. Subsequently the panels were put in order (figure 45), and sanded down until obtain a smooth surface (figure 46.a). Finally, the segments were installed into the flume entrance, pasting them with Sikaflex 512, covering the boundaries with brown tape. Additionally the surface was painted in order to protect the polystyrene (figure 46.b).

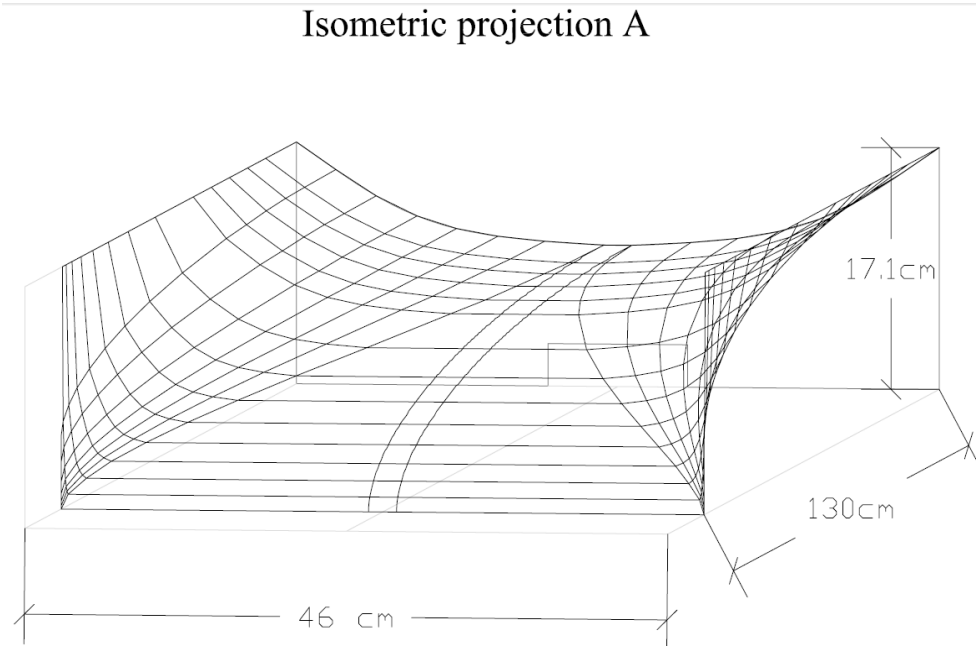

Figure 43. Isometric projection of the transition from the inlet.

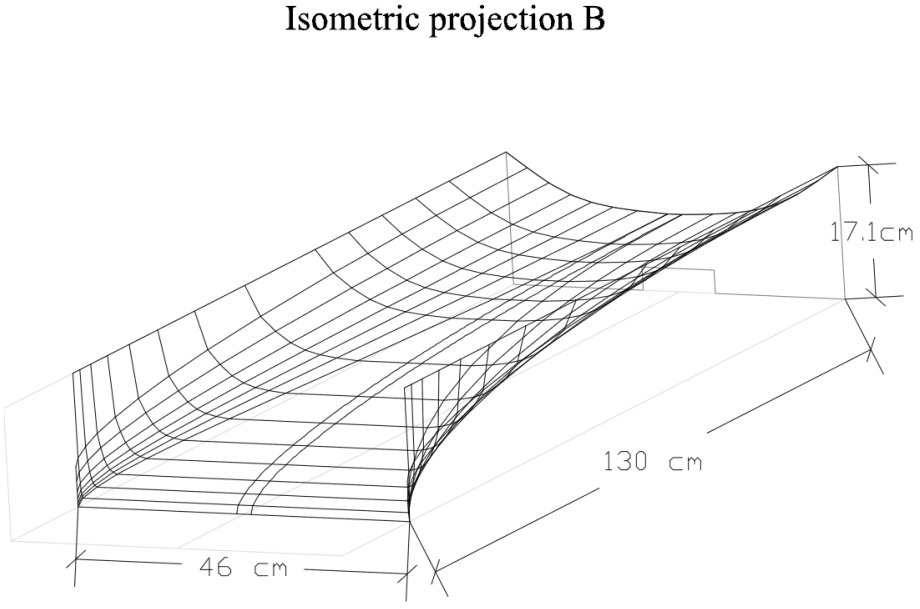

Figure 44. Isometric projection of the transition.

Figure 45**. The material used in the transition was polystyrene. Several transversal panels were cut, and later sanded down.**

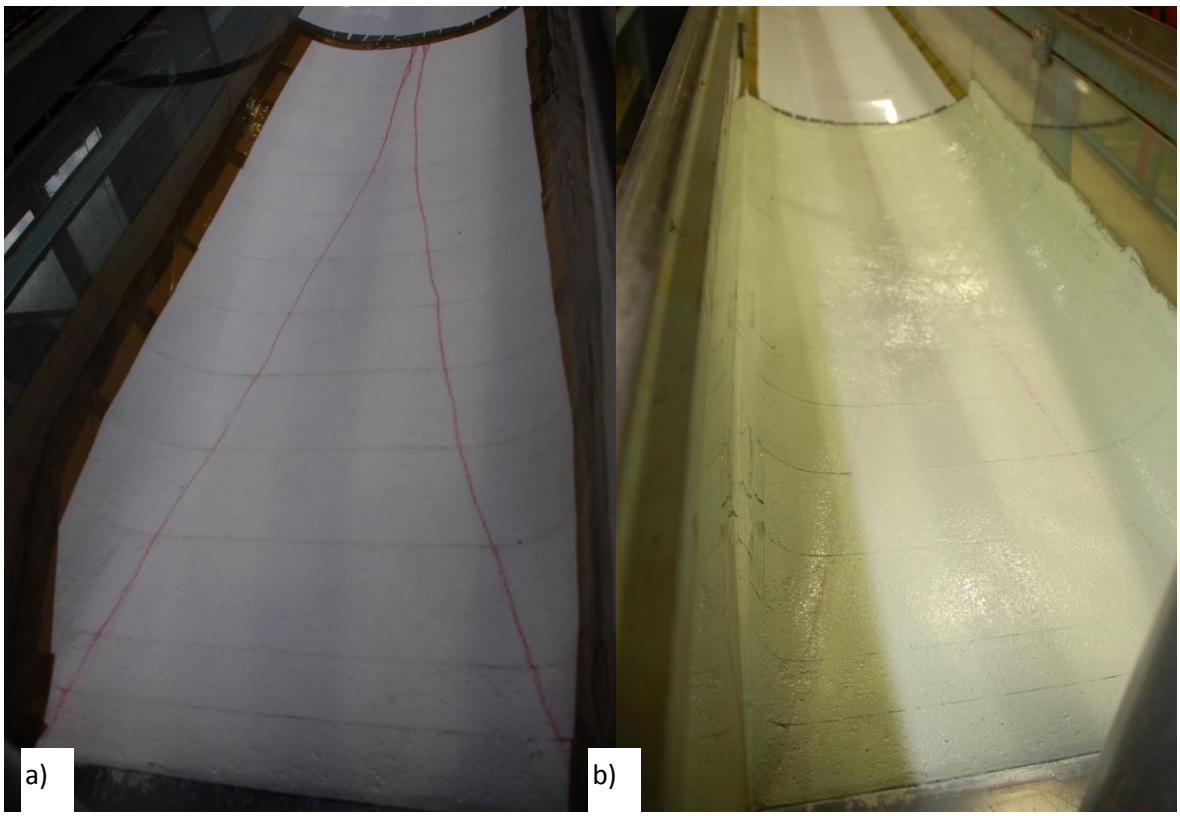

Figure 46**. a) The transition already sanded down and covered with brown tape on the boundaries. b) In order to protect the material, paint was applied to the transition.**

4.5 Methodology and procedures

Before start taking velocity and/or shear stress measurements, it was required to set uniform flow with the corresponding designed slope and depth. Then, the following steps were followed: establishing of the channel bed slope, setting up of the normal depth, mapping the streamwise velocity of the cross section, and measuring the boundary shear stress across the section. Each of the mentioned steps was followed by a series of actions, describing them next.

a) Establishing the channel bed slope

In order to determine the bed slope, S, of the channel, it was required to set a horizontal line along the channel, and to measure the level difference along the channel. Then, the procedure was to fill the channel with water, sealing the outlet, producing a steady water level, and measuring the depths at every 40cm, h_i. It was noticed that a small undulation exists on the channel (figure 35), locating the crests at the PVC supports and the troughs at the mid-distance between them. Hence, in order to incorporate such a difference into the slope, an additional depth was taken 10cm after each reading.

The advantage of h_i with respect to measuring only the extremes lies on collecting more data to include the small imperfections of the channel on the resulting S. Later h_i was plotted against the longitudinal distance, x, proposing a best-fit linear equation, where $S$is the slope of the equation (figure 47). It should be noticed that a similar plot was obtained for each set of experiments, but for practical purposes only one example is shown here.

Due to the flume has a jack point in the centre, and the inclination is controlled by a scale on the upstream extreme, a different slope, S_i, was obtained for each scale reading, S_{ci}. Hence, after moving the flume three times it was possible to set a linear equation relating S_{ci} and S_i. This expression helps to reach the proposed slope faster and with a better approximation (figure 48). The procedure was repeated for both channel surfaces (smooth and rough), because after the application of glue sand small irregularities were added.

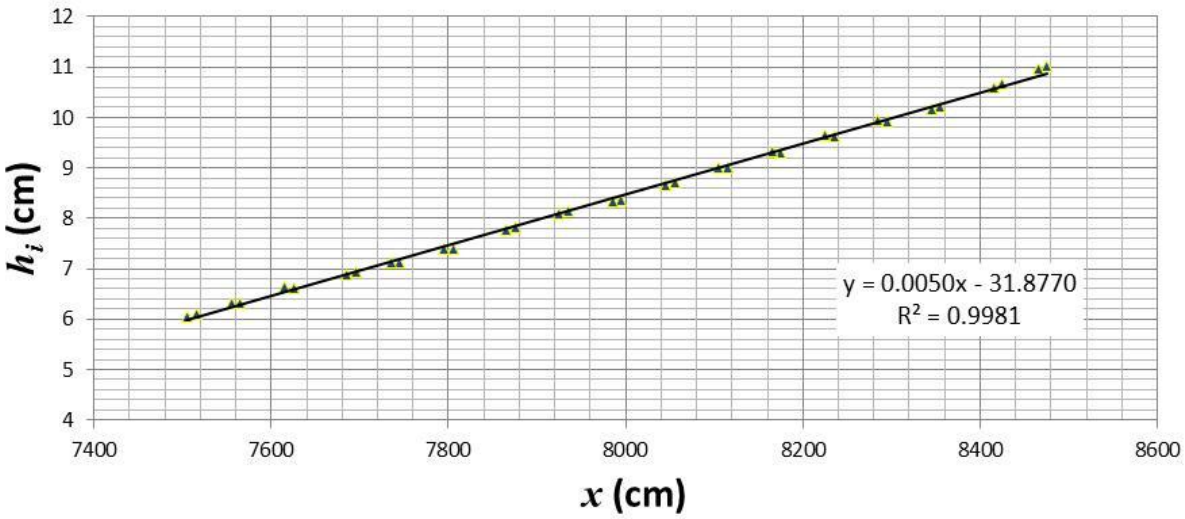

Figure 47.Variation of depth along the channel for a particular slope with constant water level. Technique applied to determine the channel slope.

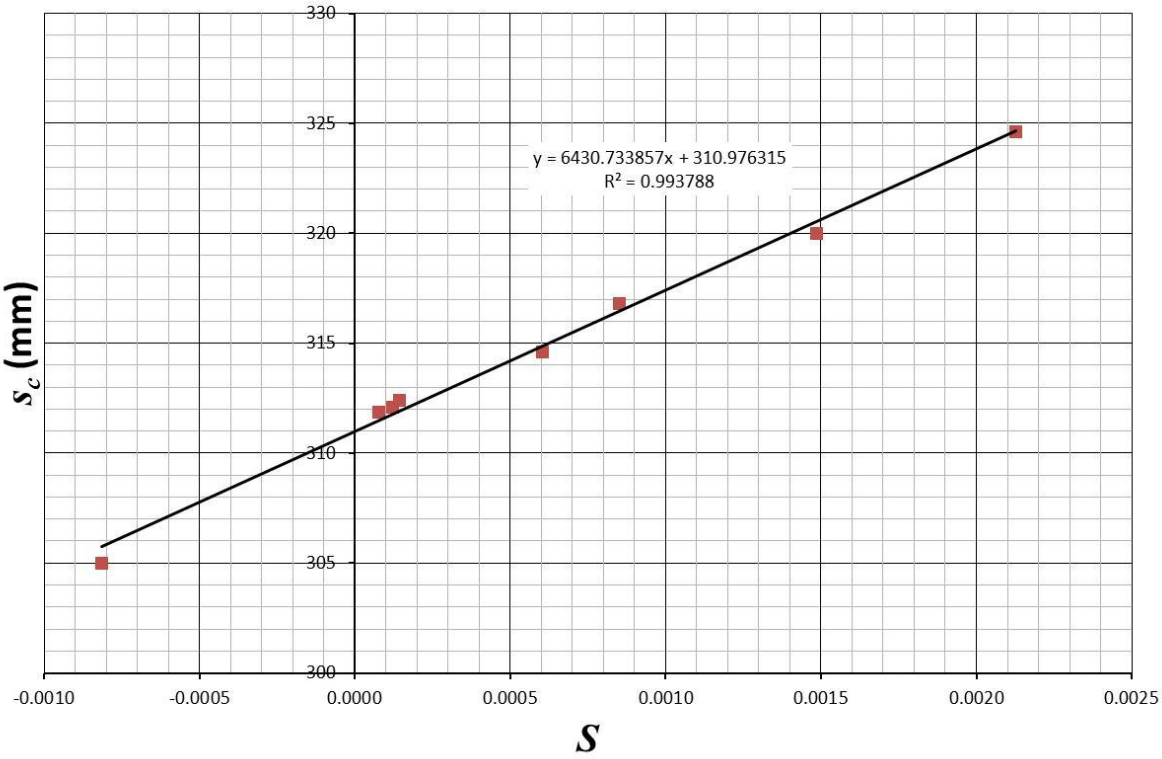

Figure 48.Variation of the governing scale with respect to the channel bed slope. The graph corresponds to the channel using a PVC surface.

b) Stage-discharge curves

Before setting the normal flow for a specific depth, h_c, and once the desired bed slope, S, was established, it was required to know the corresponding discharge, Q, that would produce such h_c. In order to fulfil such purpose, six stage discharge curves were determined, one for each S. The procedure consisted of varying the discharge eight times, from the channel bankfull condition (h_c≈7.17cm) to the minimum discharge (1.5 L/s approximately), and relating Q with the corresponding normal depth, h_c.

Furthermore, with the data obtained for h_c, Q and S, it was possible to calculate the Manning's n for each discharge. Subsequently, an average for n per slope, n_{avg}, was determined. These results would help the simulation process later on.

c) Setting up normal flow

The normal flow condition is reached when the water surface slope along the flow profile, S_w, is equal to the bed slope of the channel, S. Subsequently, the local depth, h, is constant upstream and downstream.

In order to set normal flow for a particular central depth, h_c, in subcritical condition, where Q and S are given, a protocol varying the tailgate aperture, t_g, (figure 49) was necessary, due to it affects h_c and S_w. It consisted of changing S_w by adjusting t_g, obtaining at least three flow profiles of two types, *i.e.* M2 (drawdown, S_w<0) and M1 (backwater, S_w>0), having at least one of a different kind. Such a procedure has been mentioned before by Sterling (1998) and Yuen(1989).

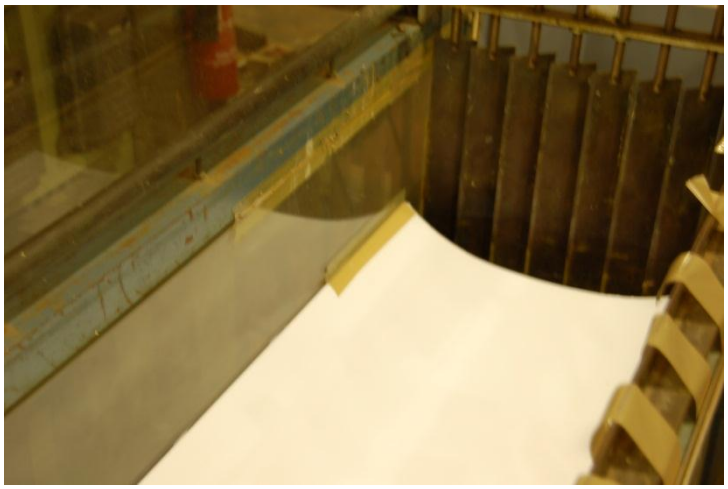

Figure 49. Tailgate of the flume. The aperture mechanism consists of a series of blades that rotate on their own axis.

With respect to S_w, it is defined as $S_w = S + dh_c/dx$, where dh_c/dx is the variation of h_c along the flow profile. Later a linear equation relating h_c is proposed per profile, *i.e.* $h_c = S_w x + \bar{b}$, determining h_c for an arbitrary x at least 1m upstream of the tailgate, and being $\bar{b}$ a reference depth over the flow profile. At the end of the procedure,

there should be at least three set of data, as table 8 is showing the variables.

Since S_w and h_c are affected by t_g, and based on the data obtained, it is possible to express them like, $S_w = f(t_g)$ and $h_c = g(t_g)$, by obtaining best fit equation for both functions. Once both expressions are known, and in order to obtain the normal flow condition, an iterative process is required to find the corresponding t_g that yields S_w=S by adjusting $S_w = f(t_g)$. After finding the resulting tailgate aperture, t_g $_r$, h_c can be determined from $h_c = g(t_g)$, determining the normal depth, h_{cn}.

Table 8. It is showing the three sets of variables required to determine the tailgate aperture that produces normal depth.

Profile	t_g	S_w	$h_c\|_x$
$M2$	t_{g1}	S_{w1}	h_{c1}
$M1$	t_{g2}	S_{w2}	h_{c2}
$M1$	t_{g3}	S_{w3}	h_{c3}

On the other hand, the steep slopes are producing flow profiles S2 type. They consist of an asymptote that is restricted downstream by the normal depth, $h_{c\ n}$. Hence, for supercritical conditions, the uniform flow is reached meters before the tailgate, avoiding the previous iterative process.

It should be noted that in order to verify the uniform flow condition, the depth as well as the velocity were measured upstream and downstream of the chosen section.

d) Velocity measurements

Once the normal depth was established for a particular S and Q, the next step

was to map the velocity across the channel section. It was done by a Pitot-static tube for only half section, in order to save time, taking measurements at each centimetre on the vertical direction, and at each 2cm on the horizontal direction, as figure 50 illustrates. Eventually, additional points were added when possible, allocating them close to the water surface or next to the boundary. Thus, the number of readings taken varied depending on the cross sectional area.

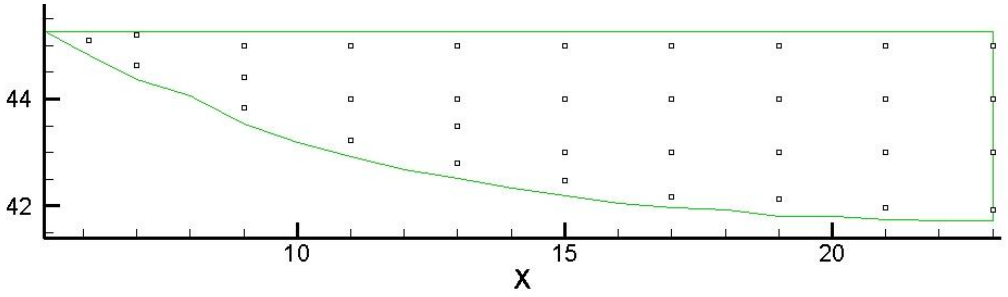

Figure 50. The distribution of velocity measurements taken by a Pitot-Static tube for half cross section. The vertical difference between them is approximately 1cm, while the horizontal one is 2cm. It should be noted that the mesh was set as constant for most of the cases, varying next to the boundary.

With respect to the Pitot-Static tube, it is a device used to measure the fluid flow velocity in the longitudinal component by determining the differential pressure between the static and total pressures. It consists of an L tube composed by two pipes(figure 51): the entrance, located at the tip of the tube with a rounded shape, receiving the total flow pressure; and static taps, located perpendicular to the tube at the lower segment, they record the static pressure only. Each pipe is connected to a manometer and by determining their pressure difference, it is possible to find the longitudinal velocity, U. Since some bed slopes proposed were mild, expecting velocities under 0.50m/s, it was required to incline the manometer, increasing the difference between manometer readings, and subsequently reducing the error related to the device. The angle varied between 8º and 12º, depending on the

maximum pressure of each experiment.

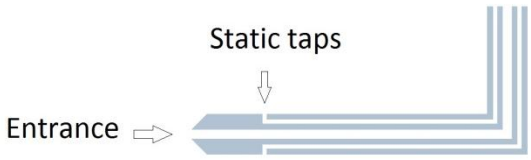

Figure 51. Scheme of a typical Pitot-Static tube. Both parts of the tube can be appreciated: entrance and static taps.

The pressure difference can be determined by applying the Bernoulli principle, at the two mentioned holes:

$$\frac{U_1^2}{2g} + z_1 + \frac{P_T}{\rho g} = \frac{U_2^2}{2g} + z_2 + \frac{P_S}{\rho g} \tag{46}$$

where the left hand side is evaluated at the static taps; and the right hand side at the entrance. U_1 and U_2 are the velocity components; P_T, the total pressure; P_S, the static pressure; Z_1 and Z_2, the elevation points; ρ, the water density; and g, the acceleration due to gravity. It is assumed that U_2=0 and Z_1=Z_2, obtaining:

$$\frac{U_1^2}{2g} + \frac{P_S}{\rho g} = \frac{P_T}{\rho g} \tag{47}$$

being U1, the longitudinal velocity:

$$U_1 = \sqrt{2\left(\frac{P_T - P_S}{\rho}\right)} \tag{48}$$

Due to the manometer had an inclination, it was required to consider this into the analisis. Hence, the total pressure head, T', and static pressure head, S', read at the manometer were affected by $\sin(\alpha')$ in order to find P_T and P_S:

$$P_T = T' \rho g \sin(\alpha') \tag{49}$$

$$P_S = S' \rho g \sin(\alpha') \quad (50)$$

During the experiments, two distinct Pitot-Static tubes were used, with two different main diameters: 3.51mm and 4.0mm. This due to under low pressures, and subsequently low velocities, the smaller diameter presented high resistance to the water flow at the manometer, delaying the water level stabilization (up to 15min). On the other hand, during the opposite condition (high pressure), the Pitot tube with bigger diameter reduced the water flow resistance in the device, reaching an stable water level faster (less than 5min). However, the sensibility of the 4.0mm tube could be appreciated on the fluctuation of the water level, complicating its reading. Hence, for low pressures the 4.0mm diameter was preferred, and the 3.51mm for high pressures, optimising the time between measurements.

e) Boundary shear stress measurements

After measuring the velocity distribution across the channel for a given h_c, S and Q, the boundary shear stress, τ_0, was measured for the smooth surface set of experiments. It was evaluated by a Preston tube for the whole cross section taking readings at each 2cm on the horizontal direction, at the same points that the velocity measurements (figure 50). As the Preston technique requires, the tube was placed next to the boundary, and aligned in the streamwise direction (figure 52). The number of measurements varied depending on the water depth.

With respect to the Preston tube used, two different diameters were tried 3.0mm and 4.8mm. In this occasion, time was not a limitation as happened with the Pitot-Static tube and the velocity measurements, due to the readings converged relative fast, after just 5 minutes. But, the 3.0mm tube produced readings with less

level fluctuations, being preferable for most of the runs. The tube measured the total pressure, P_T, and in order to assess the static pressure, P_s, a static tube of the same diameter was employed.

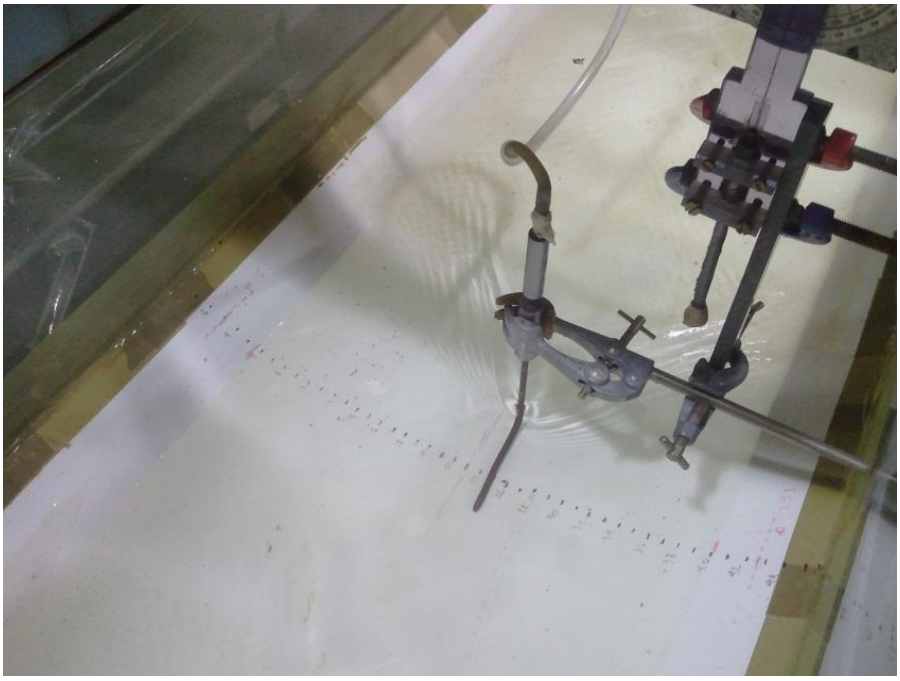

Figure 52. Preston tube in working condition

The Preston tube technique is based on the law of the wall common to boundary layers and in fully developed flow, which predicts the longitudinal velocity, U, at a certain point form the boundary, y :

$$\frac{U}{U^*} = f\left(\frac{yU^*}{\nu}\right) \tag{51}$$

$$U^* = \sqrt{\frac{\tau_0}{\rho}} \tag{52}$$

where U^* is the shear velocity; ν, the water kinematic viscosity; τ_0, boundary shear stress; and ρ, the water density. Since U can be related to the pressured difference,

$\Delta P=P_T-P_S$, as was shown on equation 48, and due to the law of the wall involves U and τ_0, Preston (1954) suggested the following correlation between ΔP and τ_0:

$$y^* = f(x^*) \tag{53}$$

$$y^* = \log_{10}\left(\frac{\tau_0 \bar{d}^2}{4\rho\nu^2}\right) \tag{54}$$

$$x^* = \log_{10}\left(\frac{[P_T - P_s]\bar{d}^2}{4\rho\nu^2}\right) \tag{55}$$

being $\bar{d}$ the diameter of the tube. He carried out experiments using four Pitot tubes with a flat entrance (the so-called Preston tube), obtaining a logarithmic equation:

$$y^* = -2.628 + \frac{7}{8}x^* \tag{56}$$

Years later, Patel (1965) reviewed his research, identifying an error in the calibration of the equation 56. In order to correct the work of Preston, Patel proposed an experimental program, employing 14 different tubes. The result was a segmentation of the relationship between τ_0 and ΔP according to the type of flow. For turbulent and transition flow:

$$\begin{aligned} &\text{if} \quad 1.5 < y^* < 5.3 \quad \text{then}: \\ &\qquad y^* = 0.8287 - 0.1381x^* + 0.1437\left(x^*\right)^2 - 0.0060\left(x^*\right)^3 \end{aligned} \tag{57}$$

and for viscous:

$$\begin{aligned} &\text{or if} \quad y^* < 1.5 \quad \text{then}: \\ &\qquad y^* = 0.37 + 0.50x^* \end{aligned} \tag{58}$$

Hence, the boundary shear stress can be determined by substituting and clearing τ_0:

$$\tau_0 = 4\left(10^{y^*}\right)\frac{\rho\nu^2}{d^2} \tag{59}$$

It should be mentioned that the Preston tube technique presents problems when it is applied to a rough surface. This mainly because the difficulty to estimate the equivalent roughness to be used in the law of the wall. There have been attempts to correct the technique, one of the most significant is the work of Jin (1995), whom proposed an ingenious solution by combining the readings of two tubes. However, such a technique has not been validated yet, mainly due to the lack of data. Hence, for the glue sand surface experiments, τ_0 was determined indirectly by the depth average velocity, U_d, by $\tau_0 = \rho f U_d^2/8$, being highly inaccurate, as the uncertainty analysis shows.

CHAPTER 5

PHYSICAL DATA RESULTS AND ANALYSIS

The current chapter presents the physical data results and analysis of the experiments carried out. A description and analysis of them is presented. The experiments are divided into two stages, according to the boundary channel surface used. The first one corresponds to a smooth surface (PVC), while the second one employs a rough surface (glue sandd_{50}=1.46mm). Three bed slopes were proposed per surface, trying three different depths for each slope. The tables 9 and 10 are showing the matrixes of experiments done. As mentioned on section 4.3, the slopes were distributed as: $S1 \approx S6 \approx$1/675, $S2 \approx S5 \approx$1/575 and $S3 \approx S4 \approx$1/200; but due to technical difficulties approximated values were obtained. All the slopes produced subcritical flow except from S3. With respect of the assessed depths, the original idea was to try $h_c \approx$7.1 cm (bankfull), $h_c \approx$5.1cm (end of the cosine section) and $h_c \approx$3.5cm (1.5 cm below the cosine section), but due to the nature of the experiment, approximated values were reached.

Table 9. The matrix of experiments for smooth surface

	Smooth surface (PVC)		
	S1=0.001485	**S2=0.001725**	**S3=0.005044**
H1 (cm)	3.340	3.520	3.395
H2 (cm)	4.970	5.265	5.065
H3 (cm)	7.020	7.080	6.950

Table 10.The matrix of experiments for rough surface.

	Rough surface (Glue sand d_{50}=1.46mm)		
	S4=0.004943	**S5=0.001742**	**S6=0.001482**
H1 (cm)	3.27	3.49	3.50
H2 (cm)	5.05	5.02	5.02
H3 (cm)	7.02	7.12	7.09

In order to collect data, the procedure described in section 4.5 was followed: establishing of the channel bed slope, determination of the stage-discharge curve, setting up of the normal depth, mapping the streamwise velocity of the cross section, and measuring the boundary shear stress across the section.

5.1 Stage-discharge curves and friction analysis

A stage-discharge curve was obtained per slope, carrying out a friction analysis for each one. It consisted of obtaining the average of Manning's n, n_{Average}. The procedure was to obtain the normal depth for each discharge, departing from a minimum discharge until reach the bankfull condition. Once the central depth, h_c, and the discharge, Q, were known, and being the geometrical variables (area, A; wetted perimeter, P; hydraulic radius, R) obtained by AutoCAD, based on elevation measurements across the channel, it was possible to determine n and f per discharge by:

$$Q = \frac{1}{n} A R^{2/3} S^{1/2} \tag{60}$$

$$n = \frac{1}{V} R^{2/3} S^{1/2} \tag{61}$$

$$f = \frac{1}{R^{1/3}} 8g\,n^2 \qquad (62)$$

Subsequently an average was obtained for the n values per slope, n_{Average}. See tables 11, 12 and 13 for smooth surface runs and tables 14, 15 and 16 for rough surface. It should be noted that for PVC $n_{Average} \neq 0.010$, as is commonly assumed. In fact, it was affected by the slope, obtaining n_{Average1}=0.00969, n_{Average2}=0.00968, and n_{Average3}=0.00844. Since $S1$=0.001485, $S2$=0.001725 and $S3$=0.005044, a first observation is that n_{Average} reduces slightly while S increases. However such hypothesis was not confirmed by the glue sand surface results, which present stable values for n_{Average} around 0.014 (n_{Average4}=0.01489, n_{Average5}=0.01474 and n_{Average6}=0.01443).

Table 11. The experimental data that were used to plot the stage discharge curve for S=0.001485. Q and h_c were measured in the lab, while A and P were obtained by AutoCAD. V was found by $V=Q/A$, $n = R^{2/3}S^{1/2}V^{-1}$, and $f = 8gn^2R^{-1/3}$.

	$S1$= 0.001485						
Q (L/s)	**h_c(cm)**	**A(cm^2)**	**R (cm)**	**P(cm)**	**V (m/s)**	**n**	**f**
1.41	**2.514**	56.551	1.785	31.685	0.2486	0.0106	0.0337
2.95	**3.484**	88.656	2.453	36.136	0.3322	0.0098	0.0259
5.21	**4.610**	130.194	3.220	40.431	0.3998	0.0098	0.0235
6.46	**5.015**	146.084	3.491	41.847	0.4421	0.0093	0.0208
7.92	**5.623**	170.835	3.881	44.024	0.4638	0.0095	0.0210
9.03	**6.081**	190.204	4.168	45.639	0.4747	0.0098	0.0216
10.62	**6.446**	206.070	4.394	46.899	0.5155	0.0093	0.0193
11.97	**6.923**	227.371	4.681	48.576	0.5263	0.0095	0.0197
					n_{Average1}= 0.00969		
					σ_1= 0.00041		

Table 12. The experimental data that were used to plot the stage discharge curve for S=0.001725. Q and h_c were measured in the lab, while A and P were obtained by AutoCAD. V was obtained by $V=Q/A$, $n = R^{2/3}S^{1/2}V^{-1}$, and $f = 8gn^2R^{-1/3}$.

S2=	0.001725						
Q (L/s)	h_c (cm)	A(cm^2)	R (cm)	P(cm)	V(m/s)	n	f
1.24	**2.244**	48.66	1.60	30.34	0.2548	0.0104	0.0334
2.01	**2.763**	64.74	1.96	32.97	0.3105	0.0097	0.0276
3.49	**3.721**	97.41	2.62	37.14	0.3587	0.0102	0.0276
4.96	**4.333**	119.98	3.04	39.47	0.4134	0.0098	0.0241
7.25	**5.170**	152.69	3.60	42.42	0.4750	0.0095	0.0216
9.47	**5.775**	177.62	3.98	44.60	0.5330	0.0091	0.0190
11.91	**6.566**	211.81	4.47	47.34	0.5625	0.0093	0.0191
14.17	**7.202**	240.57	4.87	49.41	0.5890	0.0094	0.0190
					n_{Average2}=	**0.00968**	
					σ_2=	0.00044	

Table 13. The experimental data that were used to plot the stage discharge curve for S=0.005044. Q and h_c were measured in the lab, while A and P were obtained by AutoCAD. V was obtained by $V=Q/A$, $n = R^{2/3}S^{1/2}V^{-1}$, and $f = 8gn^2R^{-1/3}$.

S3=	0.005044						
Q (L/s)	h_c (cm)	A (cm^2)	R (cm)	P (cm)	V (m/s)	n	f
1.92	**2.000**	40.48	1.39	29.11	0.4753	0.0086	0.0244
4.06	**2.810**	65.28	1.97	33.18	0.6220	0.0083	0.0201
6.32	**3.395**	84.94	2.38	35.74	0.7442	0.0079	0.0170
8.53	**4.040**	108.02	2.83	38.22	0.7893	0.0083	0.0180
10.84	**4.590**	128.73	3.20	40.26	0.8423	0.0085	0.0178
13.21	**5.065**	147.39	3.51	42.01	0.8964	0.0085	0.0173
16.92	**5.810**	177.98	3.99	44.61	0.9504	0.0087	0.0175
20.96	**6.400**	203.32	4.36	46.62	1.0307	0.0085	0.0163
25.01	**6.980**	229.21	4.70	48.77	1.0912	0.0085	0.0156
					n_{Average3}=	**0.00844**	
					σ_3=	0.00024	

Table 14. The experimental data that were used to plot the stage discharge curve for $S4$=0.004943. Q and h_c were measured in the lab, while A and P were obtained by AutoCAD. V was calculated by $V=Q/A$, $n = R^{2/3}S^{1/2}V^{-1}$, and $f = 8gn^2R^{-1/3}$.

S4=	0.004943						
Q (L/s)	h_c (cm)	A (cm^2)	R (cm)	P (cm)	V (m/s)	n	f
1.09	**2.111**	42.54	1.46	29.18	0.2569	0.0163	0.0857
2.98	**3.299**	79.75	2.27	35.11	0.3732	0.0151	0.0633
5.09	**4.152**	110.26	2.85	38.63	0.4615	0.0142	0.0520
7.14	**5.013**	143.77	3.44	41.77	0.4969	0.0150	0.0541
8.99	**5.488**	163.33	3.77	43.37	0.5503	0.0144	0.0483
10.99	**6.072**	188.29	4.16	45.22	0.5839	0.0145	0.0474
13.06	**6.670**	214.95	4.57	47.02	0.6074	0.0148	0.0481
15.02	**7.154**	237.21	4.90	48.40	0.6334	0.0149	0.0474
					n_{Average4}=	**0.01489**	
					σ_4=	0.00066	

Table 15. The experimental data that were used to plot the stage discharge curve for *S4*=0.001742. *Q* and h_c were measured in the lab, while *A* and *P* were obtained by AutoCAD. *V* was calculated by *V=Q/A*, $n = R^{2/3}S^{1/2}V^{-1}$, and $f = 8gn^2R^{-1/3}$.

S5=	**0.001742**						
***Q* (*L/s*)**	**h_c (cm)**	***A* (cm^2)**	***R* (cm)**	***P* (cm)**	***V* (m/s)**	***n***	***f***
1.09	**2.666**	59.10	1.84	32.14	0.1841	0.0158	0.0741
2.16	**3.644**	91.75	2.51	36.59	0.2356	0.0152	0.0617
3.26	**4.310**	116.23	2.96	39.23	0.2808	0.0142	0.0514
4.25	**4.898**	139.16	3.36	41.37	0.3055	0.0142	0.0493
5.38	**5.523**	164.79	3.79	43.48	0.3267	0.0144	0.0485
6.54	**6.123**	190.52	4.20	45.38	0.3435	0.0147	0.0487
7.59	**6.569**	210.37	4.50	46.72	0.3610	0.0146	0.0472
8.68	**7.028**	231.37	4.82	48.05	0.3751	0.0147	0.0468
					n_{Average5}=	**0.01474**	
					σ_5=	0.00052	

Table 16. The experimental data that were used to plot the stage discharge curve for *S4*=0.001482. *Q* and h_c were measured in the lab, while *A* and *P* were obtained by AutoCAD. *V* was calculated by *V=Q/A*, $n = R^{2/3}S^{1/2}V^{-1}$, and $f = 8gn^2R^{-1/3}$.

S6=	**0.001482**						
***Q* (L/s)**	**h_c (cm)**	***A* (cm^2)**	***R* (cm)**	***P* (cm)**	***V* (m/s)**	***n***	***f***
1.20	**2.796**	63.18	1.93	32.78	0.1894	0.0146	0.0625
2.16	**3.728**	94.73	2.56	36.94	0.2276	0.0147	0.0576
3.04	**4.335**	117.17	2.98	39.32	0.2591	0.0143	0.0516
4.22	**5.085**	146.68	3.49	42.01	0.2876	0.0143	0.0491
5.10	**5.529**	165.03	3.79	43.50	0.3090	0.0141	0.0462
6.18	**6.106**	189.82	4.19	45.33	0.3257	0.0143	0.0459
7.31	**6.623**	212.83	4.54	46.88	0.3434	0.0143	0.0448
8.21	**6.956**	228.02	4.77	47.84	0.3602	0.0140	0.0427
					n_{Average6}=	**0.01432**	
					σ_6=	0.00023	

5.1.1 Uncertainty analysis of $n_{Average}$

In order to determine the accuracy of $n_{Average}$ an uncertainty analysis was carried out, assuming the following systematic uncertainties:

$\Delta Q_{sys}/Q$: Systematic discharge uncertainty of the electromagnetic flowmeter, error proportioned by the manufacturer, 0.50%

Δh_c: Systematic depth uncertainty, varying from 0.05cm to 0.15cm due to it was affected by water surface undulation, increasing with h_c

$\Delta S/S$: Slope uncertainty, obtained from the slope setting, $\Delta S1/S1$=0.949%, $\Delta S2/S2$=0.906%, $\Delta S3/S3$=0.095%, $\Delta S4/S4$=0.14%, $\Delta S5/S5$=1.10%, and $\Delta S6/S6$=1.48%.

By applying error propagation to equation 61, the expression:

$$\frac{\Delta n}{n} = \sqrt{\left(\frac{2}{3}\frac{\Delta R}{R}\right)^2 + \left(\frac{1}{2}\frac{\Delta S}{S}\right)^2 + \left(\frac{\Delta V}{V}\right)^2} \quad (63)$$

was found. The relative hydraulic radius uncertainty, $\Delta R/R$, was determined by deriving a function that relates h_c and R:

$$R = 0.6581\ h_c + 0.1613 \quad (64)$$

defining $\Delta R = \Delta h_c\ f'(h_c)$, hence:

$$\Delta R = 0.6581\ \Delta h_c \quad (65)$$

With respect to the relative velocity uncertainty, $\Delta V/V$, it was obtained by combining the discharge and area uncertainties:

$$\frac{\Delta V}{V} = \sqrt{\left(\frac{\Delta Q}{Q}\right)^2 + \left(\frac{\Delta A}{A}\right)^2} \tag{66}$$

The relative area uncertainty, $\Delta A/A$, was found from an expression that combines area and depth:

$$A = 1.5729\ h_c^2 + 23.9340\ h_c - 13.2161 \tag{67}$$

obtaining $\Delta A = \Delta h_c\ g'(h_c)$, therefore:

$$\Delta A = \Delta h_c\ (23.934 + 3.1459\ h_c) \tag{68}$$

Once the uncertainty Δn was known for each h_c and Q, it was propagated to n_{Average}, as:

$$\Delta n_{average} = \frac{1}{\tilde{N}} \sum_{k=1}^{\tilde{N}} (\Delta n_i) \tag{69}$$

The calculations are shown on tables 17, 18, 19, 20, 21 and 22, finding $\Delta n_{\text{Average1}} / n_{\text{Average1}} = 3.40\%$, $\Delta n_{\text{Average1}} / n_{\text{Average1}} = 3.16\%$, $\Delta n_{\text{Average1}} / n_{\text{Average1}} = 3.21\%$, $\Delta n_{\text{Average4}} / n_{\text{Average4}} = 3.36\%$, $\Delta n_{\text{Average5}} / n_{\text{Average5}} = 3.32\%$, and $\Delta n_{\text{Average6}} / n_{\text{Average6}} = 3.20\%$.

Table 17. The calculations to determine the $\Delta n_{\text{Average1}}$ for $S1$= 0.001485 and $\Delta S1/S1$=0.949%.

Q (L/s)	h_c(cm)	N	$\Delta R/R$	$\Delta A/A$	$\Delta Q/Q$	$\Delta V/V$	$\Delta n/n$	Δn
1.406	2.514	0.0106	1.84%	2.82%	2.19%	3.57%	3.80%	0.00040
2.945	3.484	0.0098	1.93%	2.83%	1.13%	3.05%	3.34%	0.00033
5.205	4.610	0.0098	1.99%	2.88%	0.64%	2.95%	3.27%	0.00032
6.458	5.015	0.0093	2.01%	2.90%	0.66%	2.98%	3.30%	0.00031
7.923	5.623	0.0095	2.04%	2.94%	0.60%	3.00%	3.33%	0.00032
9.030	6.081	0.0098	2.07%	2.96%	0.58%	3.02%	3.35%	0.00033
10.623	6.446	0.0093	2.08%	2.99%	0.66%	3.06%	3.39%	0.00032
11.967	6.923	0.0095	2.11%	3.02%	0.54%	3.06%	3.40%	0.00032
							$\Delta n_{\text{Average 1}}$=	0.00033
							$\Delta n_{\text{Average 1}} / n_{\text{Average 1}}$=	3.40%

Table 18. The calculations to determine the $\Delta n_{Average2}$ for $S2$= 0.001485 and $\Delta S2/ S2$=0.906%

Q (L/s)	h_c(cm)	n	$\Delta R / R$	$\Delta A / A$	$\Delta Q / Q$	$\Delta V / V$	$\Delta n / n$	Δn
1.240	2.244	0.0104	2.05%	3.18%	2.75%	4.21%	4.45%	0.00046
2.010	2.763	0.0097	1.92%	2.88%	1.47%	3.23%	3.51%	0.00034
3.494	3.721	0.0102	1.77%	2.58%	0.79%	2.70%	2.98%	0.00030
4.959	4.333	0.0098	1.71%	2.47%	0.72%	2.58%	2.85%	0.00028
7.252	5.170	0.0095	1.66%	2.39%	0.67%	2.48%	2.75%	0.00026
9.467	5.775	0.0091	1.64%	2.35%	0.57%	2.42%	2.69%	0.00024
11.914	6.566	0.0093	1.62%	2.32%	0.59%	2.39%	2.66%	0.00025
14.170	7.202	0.0094	2.03%	2.90%	0.61%	2.97%	3.29%	0.00031
							$\Delta n_{Average\ 2}$=	0.00031
							$\Delta n_{Average\ 2}/ n_{Average\ 2}$=	3.16%

Table 19. The calculations to determine the $\Delta n_{Average3}$ for $S3$= 0.005044 and $\Delta S3/ S3$=0.90%

Q (L/s)	h_c(cm)	n	$\Delta R / R$	$\Delta A / A$	$\Delta Q / Q$	$\Delta V / V$	$\Delta n / n$	Δn
1.924	2.000	0.0086	2.37%	3.73%	1.70%	4.10%	4.39%	0.00038
4.061	2.810	0.0083	2.06%	3.09%	0.92%	3.23%	3.51%	0.00029
6.322	3.395	0.0079	1.94%	2.85%	0.66%	2.93%	3.20%	0.00025
8.526	4.040	0.0083	1.84%	2.69%	0.62%	2.76%	3.02%	0.00025
10.843	4.590	0.0085	1.79%	2.60%	0.63%	2.67%	2.93%	0.00025
13.211	5.065	0.0085	1.76%	2.54%	0.71%	2.64%	2.89%	0.00025
16.916	5.810	0.0087	1.73%	2.48%	0.61%	2.55%	2.80%	0.00024
20.956	6.400	0.0085	1.71%	2.45%	0.58%	2.52%	2.76%	0.00024
							$\Delta n_{Average\ 3}$=	0.00027
							$\Delta n_{Average\ 3}/ n_{Average\ 3}$=	3.21%

Table 20. The calculations to determine the $\Delta n_{Average4}$ for $S4$=0.00494349and$\Delta S4/\ S4$=0.143%

Q (L/s)	h_c(cm)	n	$\Delta R/R$	$\Delta A/A$	$\Delta Q/Q$	$\Delta V/V$	$\Delta n/n$	Δn
1.093	2.111	0.0163	2.26%	3.59%	4.43%	5.71%	5.90%	0.00096
2.977	3.299	0.0151	1.93%	2.87%	1.35%	3.17%	3.42%	0.00052
5.088	4.152	0.0142	1.81%	2.63%	0.71%	2.73%	2.98%	0.00042
7.144	5.013	0.0150	1.73%	2.50%	0.64%	2.58%	2.83%	0.00042
8.988	5.488	0.0144	1.70%	2.45%	0.65%	2.54%	2.78%	0.00040
10.994	6.072	0.0145	1.67%	2.41%	0.64%	2.49%	2.73%	0.00039
13.057	6.670	0.0148	1.64%	2.38%	0.61%	2.45%	2.69%	0.00040
15.024	7.154	0.0149	2.01%	2.94%	0.59%	3.00%	3.28%	0.00049
							$\Delta n_{Average\ 4}$=	0.00050
							$\Delta n_{Average\ 4}/\ n_{\ Average\ 4}$=	3.36%

Table 21. The calculations to determine the $\Delta n_{Average5}$ for $S5$= 0.001742 and $\Delta S5/\ S5$= 1.100%

Q (L/s)	h_c(cm)	n	$\Delta R/R$	$\Delta A/A$	$\Delta Q/Q$	$\Delta V/V$	$\Delta n/n$	Δn
1.088	2.666	0.0158	1.79%	2.73%	5.28%	5.95%	6.09%	0.00096
2.162	3.644	0.0152	1.68%	2.47%	1.78%	3.04%	3.29%	0.00050
3.263	4.310	0.0142	1.63%	2.37%	1.05%	2.59%	2.86%	0.00041
4.251	4.898	0.0142	1.60%	2.31%	1.00%	2.52%	2.79%	0.00040
5.384	5.523	0.0144	1.57%	2.27%	0.76%	2.39%	2.67%	0.00039
6.544	6.123	0.0147	1.55%	2.25%	0.68%	2.35%	2.63%	0.00039
7.595	6.569	0.0146	1.54%	2.24%	0.68%	2.34%	2.61%	0.00038
8.678	7.028	0.0147	2.05%	2.99%	0.69%	3.06%	3.40%	0.00050
							$\Delta n_{Average\ 5}$=	0.00049
							$\Delta n_{Average\ 5}/\ n_{\ Average\ 5}$=	3.32%

Table 22. The calculations to determine the $\Delta n_{Average3}$ for $S6$=0.001482 and $\Delta S6/S6$=1.478%

Q (L/s)	h_c(cm)	n	$\Delta R/R$	$\Delta A/A$	$\Delta Q/Q$	$\Delta V/V$	$\Delta n/n$	Δn
1.197	2.796	0.0146	1.71%	2.59%	4.34%	5.05%	5.23%	0.00076
2.156	3.728	0.0147	1.63%	2.39%	1.68%	2.92%	3.20%	0.00047
3.036	4.335	0.0143	1.59%	2.31%	1.07%	2.55%	2.86%	0.00041
4.219	5.085	0.0143	1.56%	2.26%	0.90%	2.43%	2.74%	0.00039
5.099	5.529	0.0141	1.55%	2.24%	0.74%	2.36%	2.68%	0.00038
6.182	6.106	0.0143	1.53%	2.22%	0.76%	2.34%	2.66%	0.00038
7.309	6.623	0.0143	1.52%	2.21%	0.97%	2.41%	2.72%	0.00039
8.214	6.956	0.0140	2.07%	3.01%	0.77%	3.11%	3.48%	0.00049
							$\Delta n_{Average\ 6}$=	0.00046
							$\Delta n_{Average\ 6}/n_{Average\ 6}$=	3.20%

5.1.2 Variation of n and f respect h_c

The next step was to observe the variation of n with respect to h_c, by plotting figure 53. It was noted that n tends to be stable, enclosed in a certain range with the following standard deviations: σ_1=0.00041, σ_2=0.00044,σ_3=0.00024, σ_4=0.00066, σ_5=0.00052, and σ_6=0.00023. This observation is confirmed by the experimental uncertainties of $n_{Average}$ ($\Delta n_{Average1}$=0.00033, $\Delta n_{Average2}$=0.00031, $\Delta n_{Average3}$=0.00027, $\Delta n_{Average4}$=0.00050, $\Delta n_{Average5}$=0.00049, and $\Delta n_{Average6}$=0.00046), being relative close to their corresponding σ_i and in agreement with Manning's equation.

Figure 54 shows the variation of f due to h_c. It is observed that f is inversely proportional to h_c, as expected if equations 60 and 62 are combined. It should be noted that not all the points are following such a tendency, some of them were affected by the experimental error, but the majority of data fulfil the pattern.

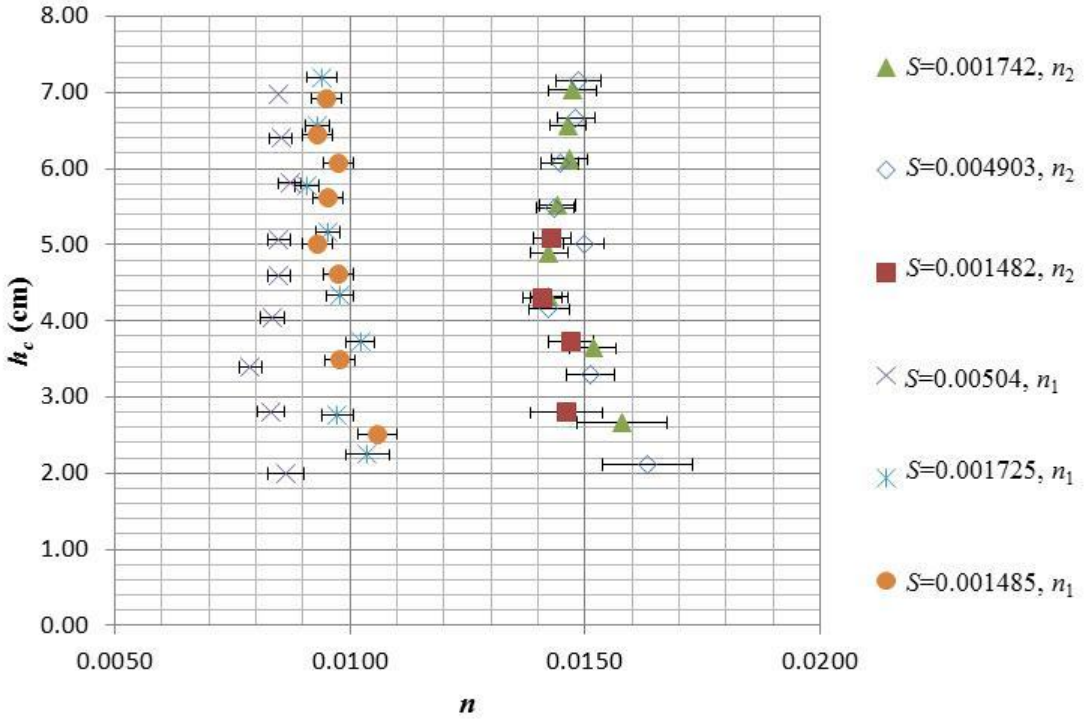

Figure 53. The variation of Manning's n with respect to h_c, for PVC and glue sand surfaces. Both variables were obtained based on experiments, where $n_2$is the rough surface and n_1 the smooth one. The error bars can be observed.

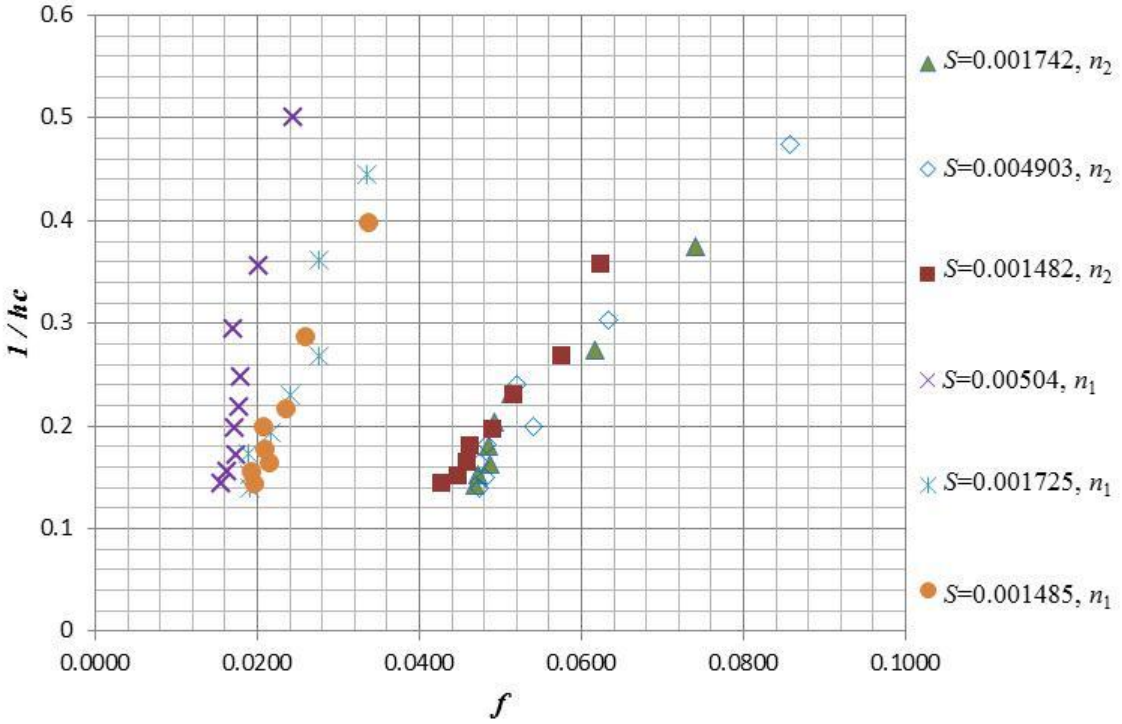

Figure 54. The variation of Darcy's f with respect to $1/h_c$, for PVC and glue sand surfaces. Both variables were obtained based on experiments, where $n_2$is the rough surface and n_1 the smooth one.

5.1.3 Stage discharge curves

Based on experimental results (tables 11 to 16), the stage-discharge curves were plotted, corresponding to both surfaces (smooth and rough) (see figures 55 and 56). For each case, a best-fit power curve was adjusted, obtaining coefficients of determination, R^2, over 0.99. Additionally, an extra curve per slope was sketch along the experimental series, but made from simulations, using Manning's equation (equation 60), and the average resistance friction factor, n_{Average}, found on section 5.1, improving their approach to the lab data. However, a difference exists between the experimental data and the calculated values, especially on *S3*. Such difference can be attributed to the turbulence generated, which seems to have greater impact when the slope is steeper. Trend lines were plotted for the simulated series as well, finding a good approximation for each one (R^2>0.99).

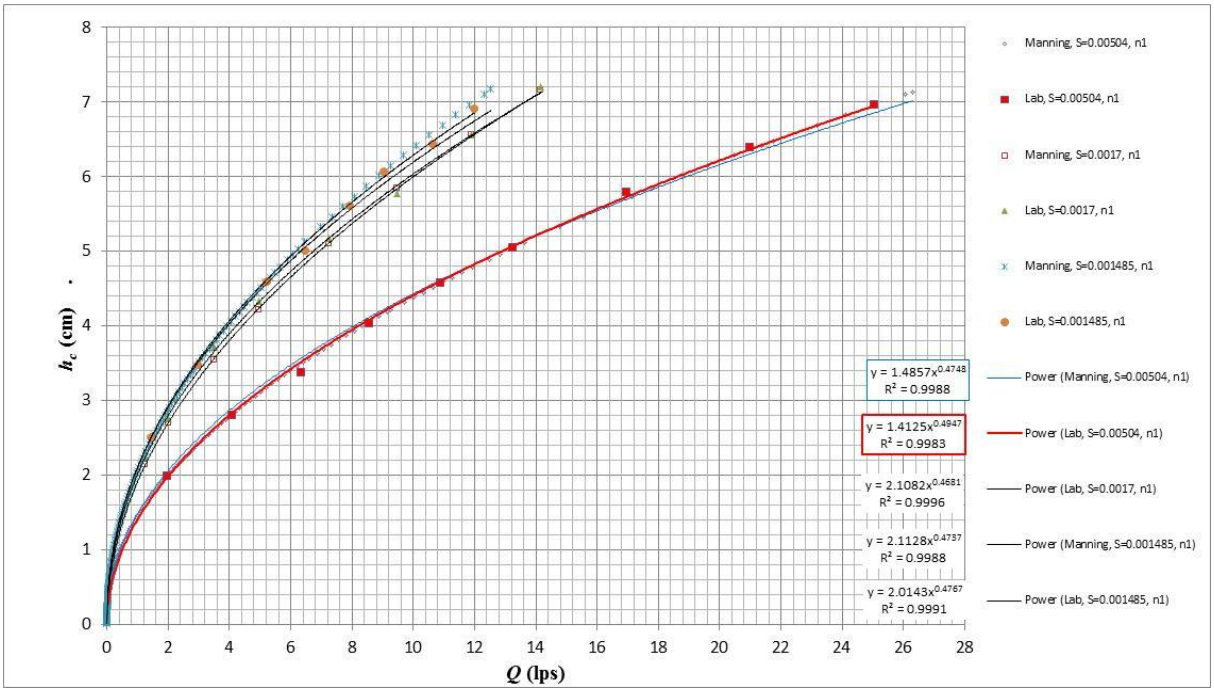

Figure 55. Stage discharge data for PVC surface, based on experiments. Additionally a Manning simulation is shown. Subsequently a trend line for each series was determined, as well as their equations.

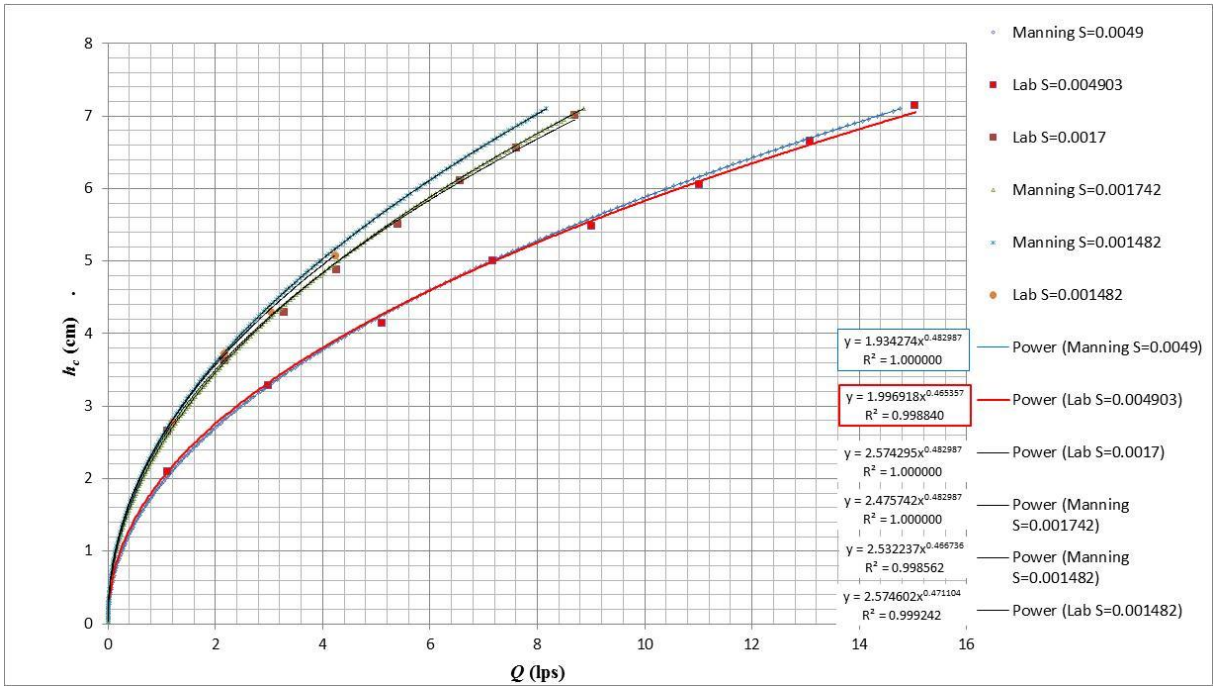

Figure 56. Stage discharge set of data for glue sand surface d_{50}=1.46mm, based on experiments. Additionally a Manning simulation is shown. Subsequently a trend line for each series was determined, as well as their equations.

5.2 Velocity results

The tables 23 and 24 show summaries of the experiments related to the velocity measurements for smooth and rough surfaces respectively. On it, the hydraulics variables can be appreciated (bed slope, S; central depth, h_c; transversal area, A; wetted perimeter, P; hydraulic radius, R), as well as experimental data (average velocity by Pitot tube, V_{Pitot}; discharge based on V_{Pitot}, Q_{Pitot}; discharge from flowmeter, Q_{flwmtr}). V_{Pitot} was calculated by multiplying the depth average velocity, $U_{d\,j}$, of each vertical profile, j, times the area of the corresponding segment, $A_{s\,j}$, accumulating their products, and dividing it by A (figure 57):

$$V_{\text{Pitot}} = \frac{1}{A}\sum_{j=1}^{N} U_{d\,j} A_{s\,j} \tag{70}$$

$U_{d\,j}$ was determined by integrating each vertical velocity profile, and dividing the

integral by its local depth, h_j (figure 58):

$$U_{dj} = \frac{1}{h_j}\int_0^{h_j} U_i \, dz \tag{71}$$

Q_{Pitot} is defined as the average velocity measured by a Pitot-Static tube times the transversal area of the channel:

$$Q_{\text{Pitot}} = V_{\text{Pitot}} A \tag{72}$$

About Q_{flmtr}, it was obtaining from an electromagnetic flowmeter, by reading up to 120 measurements during 5min, and later determining an average. Complementary information is included on the table, like the Pitot-Static tube diameter used and the number of mapped points.

With respect to the experimental error, E_Q, it was defined as:

$$E_Q\% = \left|\frac{Q_{\text{flowmeter}} - Q_{\text{Pitot}}}{Q_{\text{flowmeter}}}\right| 100 \tag{73}$$

In general E_Q is acceptable, varying from 0.82% to 9.56% in PVC, and 0.65% to 7.33% in glue sand, since the experimental uncertainty, $\Delta Q_{\text{Pitot}}/\Delta Q_{\text{Pitot}}$, is between 3.89% to 7.99% for PVC, and between 2.90% and 7.34% for glue sand. The corresponding uncertainty analysis was shown on section 5.2.1.

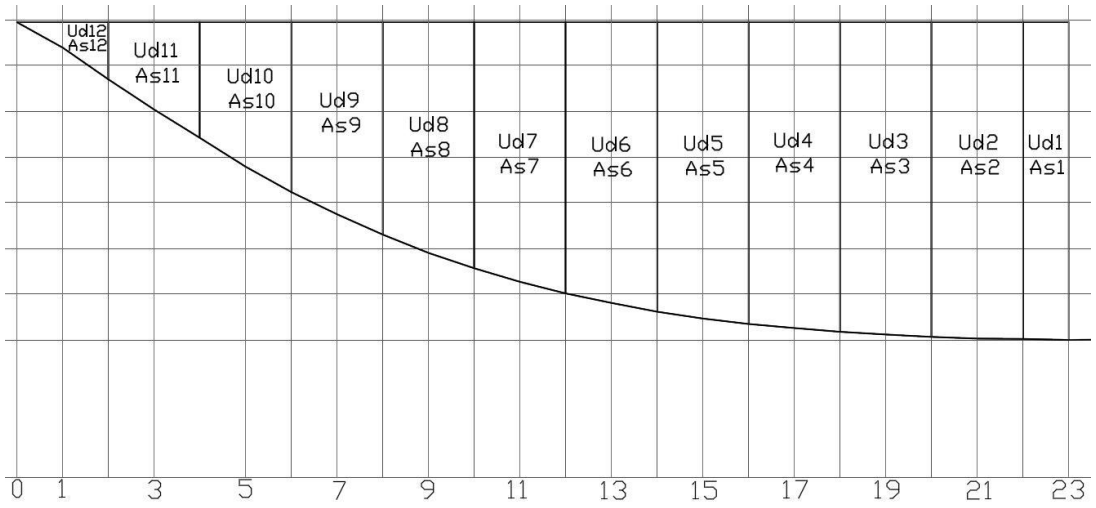

Figure 57.Distribution of segment areas, A_{sj}, that are multiplied by their corresponding depth average velocity, U_{dj}. A_{sj} were determined by AutoCAD. This software was preferable due to it takes into acc

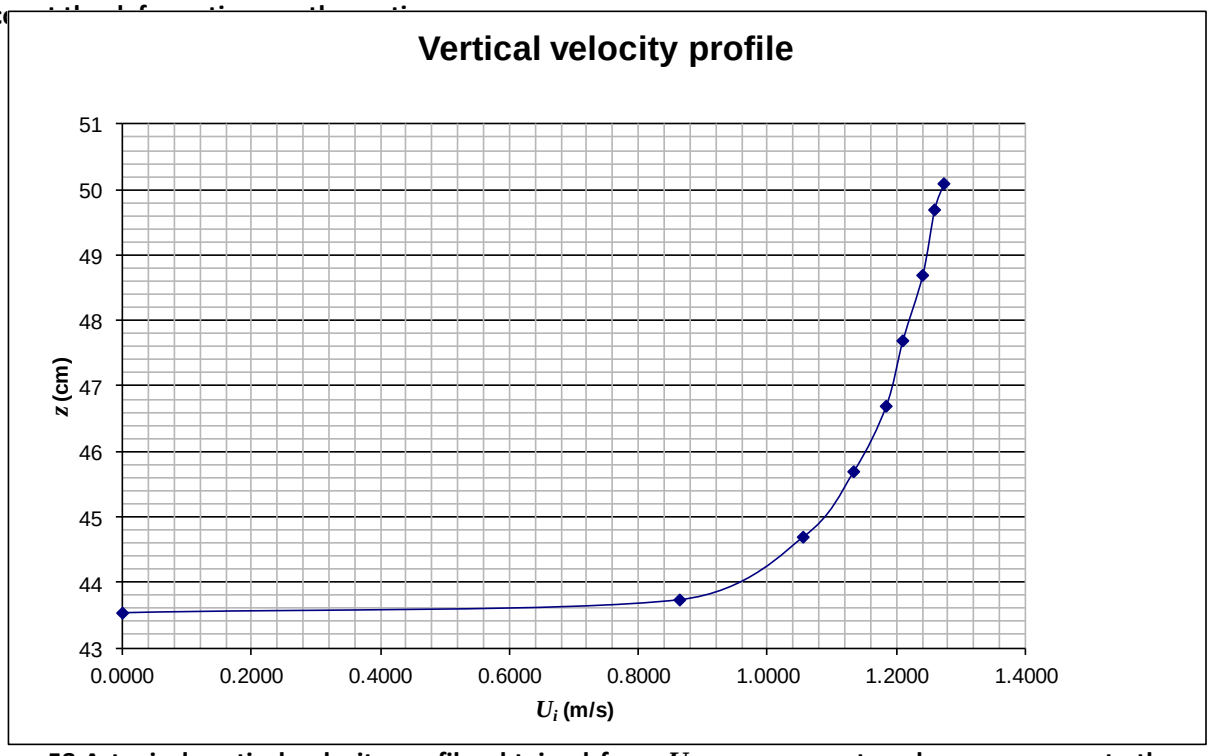

Figure 58.A typical vertical velocity profile obtained from U_i measurements, where z represents the vertical direction. The profile corresponds to a random point across the section.

Table 23. Summary of the experiments carried out in PVC surface. The geometrical, velocity and discharge can be appreciated, as well as their uncertainties.

Smooth surface (PVC)

	S1			*S2*			*S3*		
	H1	*H2*	*H3*	*H1*	*H2*	*H3*	*H1*	*H2*	*H3*
S	0.001485	0.001485	0.001485	0.001725	0.001725	0.001725	0.005044	0.005044	0.005044
h_c (cm)	3.34	4.97	7.02	3.53	5.27	7.08	3.40	5.07	6.95
A (cm^2)	84.00	144.69	228.77	87.82	154.51	234.99	85.41	147.39	227.85
P (cm)	35.59	41.72	48.69	36.04	42.59	49.17	35.76	42.01	48.66
R (cm)	2.36	3.47	4.70	2.44	3.63	4.78	2.39	3.51	4.68
Pitot tube diameter (mm)	4.00	3.51	4.00	4.00	4.00	4.00	4.00	4.00	4.00
No.of U_i readings	32	38	67	33	55	74	34	53	76
V_{Pitot} (m/s)	0.3917	0.4428	0.5377	0.3886	0.4959	0.6223	0.7206	0.9104	1.0722
Q_{Pitot} (L/s)	3.29	6.41	12.30	3.51	7.76	14.62	6.15	13.42	24.43
$\Delta Q_{\text{Pitot}}/Q_{\text{Pitot}}$	**7.99%**	**5.53%**	**4.44%**	**7.91%**	**5.00%**	**3.91%**	**7.76%**	**5.28%**	**3.89%**
Q_{flmtr} (L/s)	3.00	6.04	12.60	3.49	7.26	14.17	6.32	13.21	25.01
$\Delta Q_{\text{flmtr}}/Q_{\text{flmtr}}$	**1.45%**	**0.68%**	**0.63%**	**0.80%**	**0.63%**	**0.63%**	**0.66%**	**0.71%**	**0.59%**
E_Q%	**9.56%**	**6.08%**	**2.37%**	**0.82%**	**6.90%**	**3.22%**	**2.65%**	**1.56%**	**2.32%**

Table 24. Summary of the experiments carried out in rough surface (d_{50}=1.46mm). The geometrical, velocity and discharge can be appreciated, as well as their uncertainties.

Glue sand surface (d_{50}=1.46mm)

	S4			*S5*			*S6*		
	H1	*H2*	*H3*	*H1*	*H2*	*H3*	*H1*	*H2*	*H3*
S	0.004943	0.004943	0.004943	0.001742	0.001742	0.001742	0.001482	0.001482	0.001482
h_c (cm)	3.27	5.05	7.02	3.49	5.02	7.12	3.50	5.02	7.09
A (cm^2)	79.32	144.49	228.27	86.32	142.51	232.57	86.67	143.30	231.43
P (cm)	34.83	41.86	48.47	35.82	41.52	48.79	35.86	41.76	48.70
R (cm)	2.28	3.45	4.71	2.41	3.43	4.77	2.42	3.43	4.75
Pitot tube diameter (mm)	4.00	4.00	4.00	4.00	4.00	4.00	4.00	4.00	4.00
No.of U_i readings	38	58	83	37	55	78	36	47	70
V_{Pitot} (m/s)	0.4423	0.5031	0.6609	0.2158	0.3008	0.3642	0.2057	0.2831	0.3368
Q_{Pitot} (L/s)	3.51	7.27	15.09	1.86	4.29	8.47	1.78	4.06	7.79
$\Delta Q_{\text{Pitot}}/Q_{\text{Pitot}}$	**4.60%**	**3.53%**	**2.90%**	**7.33%**	**4.59%**	**3.63%**	**7.34%**	**5.04%**	**4.25%**
Q_{flmtr} (L/s)	3.31	7.17	14.99	1.95	4.52	8.83	1.92	4.20	8.41
$\Delta Q_{\text{flmtr}}/Q_{\text{flmtr}}$	**1.02%**	**0.36%**	**0.26%**	**1.87%**	**0.58%**	**0.46%**	**1.92%**	**0.83%**	**0.62%**
E_Q%	**5.98%**	**1.43%**	**0.65%**	**4.62%**	**5.16%**	**4.08%**	**7.33%**	**3.39%**	**7.27%**

5.2.1 Uncertainty analysis of Q_{Pitot} and Q_{flmtr}

An uncertainty analysis was done with the purpose of determining the accuracy of Q_{Pitot}. The following systematic uncertainties were assumed, conserving ΔQ_{sys} and ΔS from section5.1.1.

Δh_c: Systematic depth uncertainty, influenced by water surface undulation, 0.15cm

ΔS_m: Systematic static head uncertainty of the inclined manometer, 0.10cm

ΔT_m: Systematic total head uncertainty of the inclined manometer, 0.10cm

$\Delta \alpha'$: Systematic angular uncertainty of the inclined manometer used. 0.10º

$\Delta U_{sys}/U_i$: Systematic velocity uncertainty of the Pitot-Static tube used, 1.0%

The followed procedure was to determine the uncertainty of each U_i, *i.e.* ΔU_i, later it was propagated to U_{dj} and subsequently transmitted to Q_{Pitot}. ΔU_i was obtained by spreading the error of U_i from equation 48 (section 4.5.d):

$$\frac{\Delta U_i}{U_i} = \sqrt{\left(\frac{\Delta d}{d}\right)^2 + \left(\frac{\Delta \sin(\alpha')}{\sin(\alpha')}\right)^2} \tag{74}$$

depending on the angular uncertainty, $\Delta \alpha'$:

$$\frac{\Delta \sin(\alpha')}{\sin(\alpha')} = \frac{\Delta \alpha' \cos(\alpha')}{\sin(\alpha')} \tag{75}$$

and on the head difference uncertainty, Δd:

$$d = T_m - S_m \tag{76}$$

$$\frac{\Delta d}{d} = \frac{\sqrt{\Delta S_m{}^2 + \Delta T_m{}^2}}{T_m - S_m} \tag{77}$$

This last relies on the static and total head uncertainties. The ΔU_{sys} was added to ΔU_i, obtaining the total velocity uncertainty of a measurement, ΔU_T:

$$\Delta U_{Ti} = \sqrt{\left(\Delta U_i\right)^2 + \left(\Delta U_{sys}\right)^2} \tag{78}$$

Once ΔU_T was known, it was propagated to the average velocity uncertainty of each vertical profile, ΔU_{dj}:

$$\Delta U_{dj} = \frac{1}{h_j}\sum_{i=1}^{N} \Delta U_T \tag{79}$$

and later to the corresponding discharge segment, ΔQ_j, by affecting ΔU_{dj} with the segment area uncertainty, ΔA_{sj}:

$$\frac{\Delta Q_j}{Q_j} = \sqrt{\left(\frac{\Delta U_{dj}}{U_{dj}}\right)^2 + \left(\frac{\Delta A_{sj}}{A_{sj}}\right)^2} \tag{80}$$

$$\frac{\Delta A_{sj}}{A_{sj}} = \frac{\delta b_j \ \Delta h_j}{A_{sj}} = \frac{\Delta h_j}{h_j} \tag{81}$$

Finally ΔQ_j was accumulated, finding the discharge uncertainty, ΔQ_{Pitot}, for the whole cross section measured by a Pitot-Static tube:

$$\frac{\Delta Q_{Pitot}}{Q_{Pitot}} = \frac{1}{Q_{Pitot}}\sum_{j=1}^{M} \Delta Q_j \tag{82}$$

The corresponding $\Delta Q_{\text{Pitot}} / Q_{\text{Pitot}}$ of each run is shown on tables 23 and 24.

5.2.2 Isovelocity contours

The velocity was mapped by using a Pitot-Static tube, and following the pattern shown on figure 50. Once U_i was determined, the isovelocity contours were obtained by using the software package Tecplot 10, plotting half cross sections (see figures 60 to 77).

With respect to the behaviour of the flow, it can be observed from the graphs that the $H1$ experiments (h_c≈3.5cm) present isovelocity contours nearly parallel to the boundary (figures 60 to 65). This makes difficult the identification of the secondary flow activity. But, when the depth increases, *i.e.* h_c≈5.1cm on the $H2$ runs (figures 66 to 71), the flow pattern starts changing. In most of the sets kinks were found in the contours, except on the run $H2S3$ (figures 68), indicating the presence of secondary flow. Following the experiments of some authors, *e.g.* Tominaga *et al.* (1989), Wang and Cheng (2005) and Nezu *et al.* (1999), each twist in the isovels can be associate with a divide between secondary flow cells (figure 59). At this point, it is inferred that a higher depth corresponds to an increment in the secondary flow activity, being confirmed by the $H3$ experiments (h_c≈7.1cm). In this set, divides were clearly identified (figures 72 to 77).

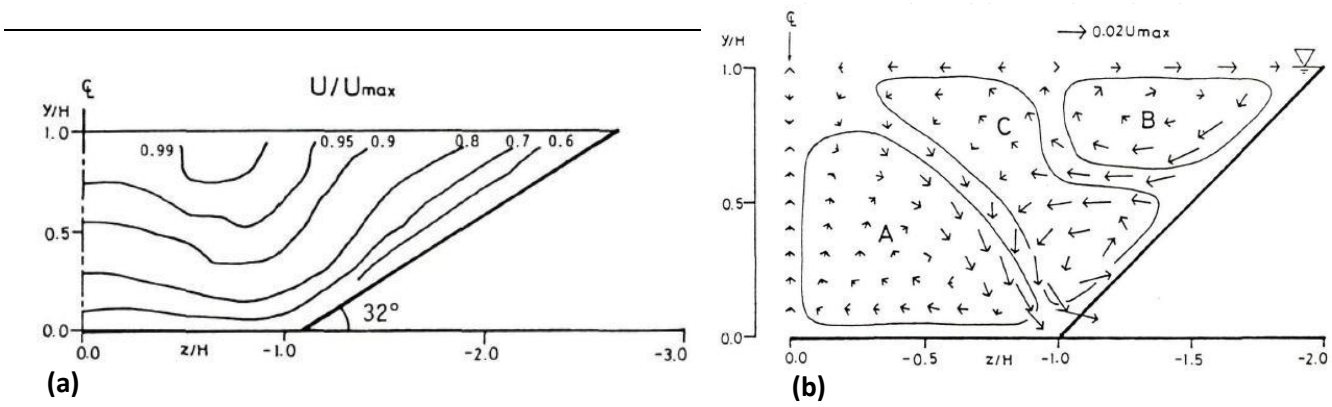

Figure 59. (a) Isovelocity contours obtained for a trapezoidal cross section. (b) Transversal velocity vectors, illustrating three secondary flow cells (Tominaga et al., 1989).

On the other hand, the smooth and rough surface contours with approximated depths and slopes were compared. As expected, the experiments on PVC surface shown higher velocities. Additionally, it was noted that the isovelocity contours presented different flow patterns, noticing this on the divides location and form. This in agreement with Wang and Cheng (2005), where it can be appreciated that the isovels are affected by the surface boundary. That is, for $H3$ experiments on smooth surface (figures 72 to 74) two divides were found, while for rough surface (figures 75 to 77), three were spotted. Similar phenomenon can be appreciated on the $H2$ sets (figures 66 to 71), however there is no difference between the number of divides, identifying one for $H2S3$ and $H2S6$ (figures 68 and 71), and two for the rest. But, the location and inclination of the divides, as well as the contour pattern, are different for each surface condition. About the $H1$ experiments (figures 60 to 65), one divide was found, except for H1S5, who has two (figure 64). With respect to the low number of divides in the $H1$ runs, This can be attributed to the low velocity produced by such a depth (h_c≈3.5cm), and to the number of readings taken 32 to 38 (tables 23 and 24), probably a finer mesh would have improve the resolution of the secondary flow.

The difference in the isovelocity contours patterns can be explained due to the change of boundary condition, which affects the velocity distribution across the section. By matching both types of surface experiments, it is noticed that the inclination of the divide in the rough surface sets implies smaller velocity gradients next to the margin (left hand side). This is verifiable by measuring the distance between isovels, being higher the gradient when the isovels are close to the margin. At this point it is possible to say that a rough surface presents a higher secondary flow activity, this based on the number of kinks and divides determined. In order to observe better the variation of the velocity across 6the section, it is necessary to analyse the respectively depth average velocity, U_d, profiles.

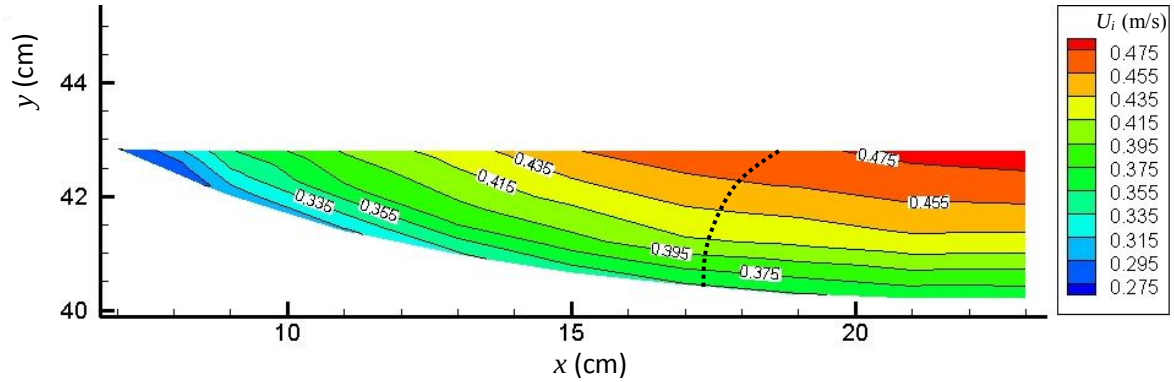

Figure 60.Isovelocity contours for half cross section channel, corresponding to the experiment H1S1, with h_c=3.34cm, S=0.001485 on PVC bed surface. The dashes represent the divides between secondary flow cells.

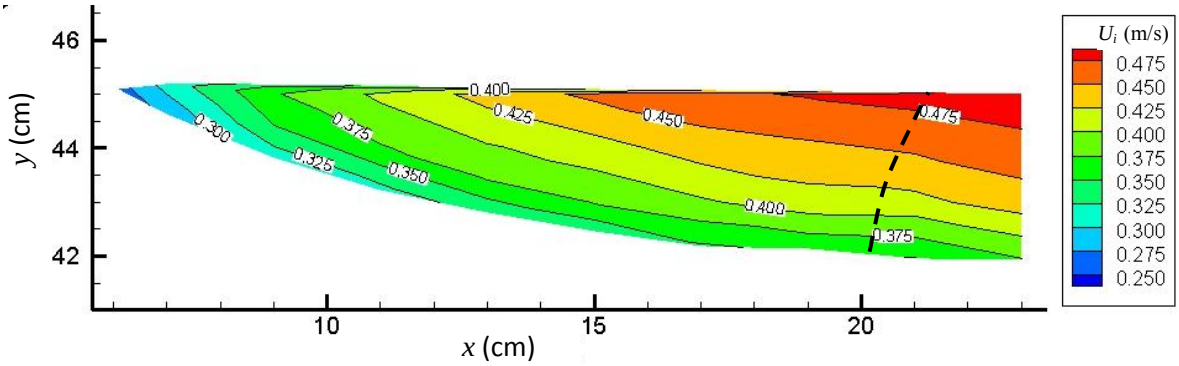

Figure 61. Isovelocity contours for half cross section channel, corresponding to the experiment H1S2, with h_c=3.52cm, S=0.001725 on PVC bed surface. The dashes represent the divides between secondary flow cells.

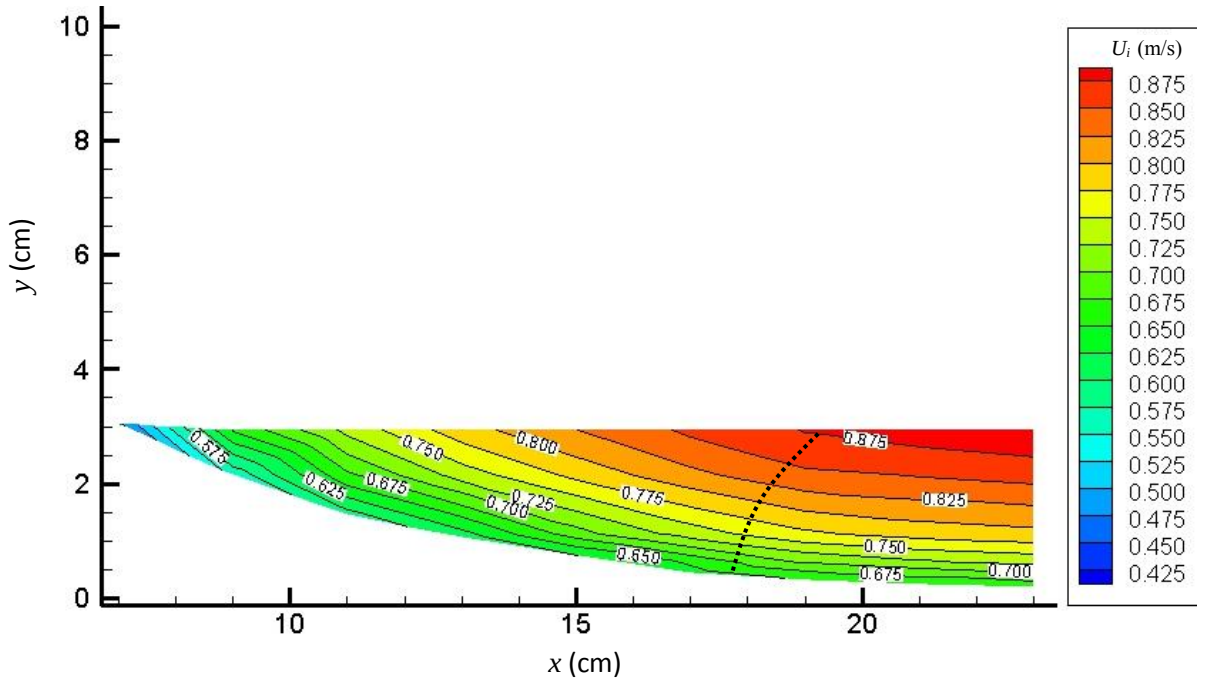

Figure 62. Isovelocity contours for half cross section channel, corresponding to the experiment H1S3, with h_c=3.395cm, S=0.005044 on PVC bed surface. The dashes represent the divides between secondary flow cells.

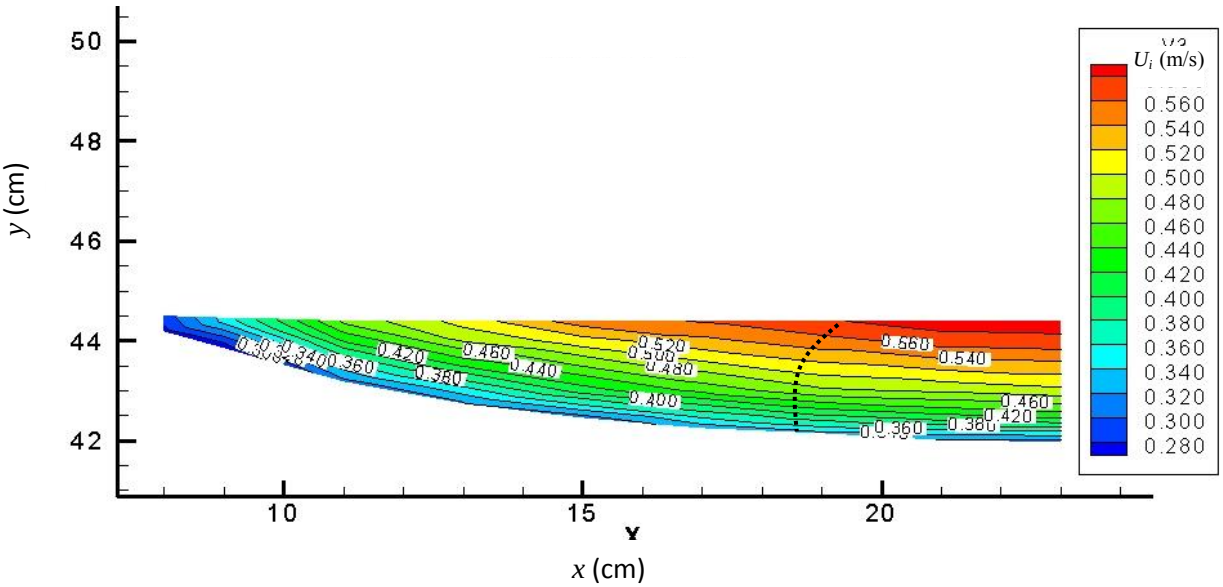

Figure 63. Isovelocity contours for half cross section channel, corresponding to the experiment H1S4, with h_c=3.27cm, S=0.004943 on glue sand bed surface (d_{50}=1.46mm). The dashes represent the divides between secondary flow cells.

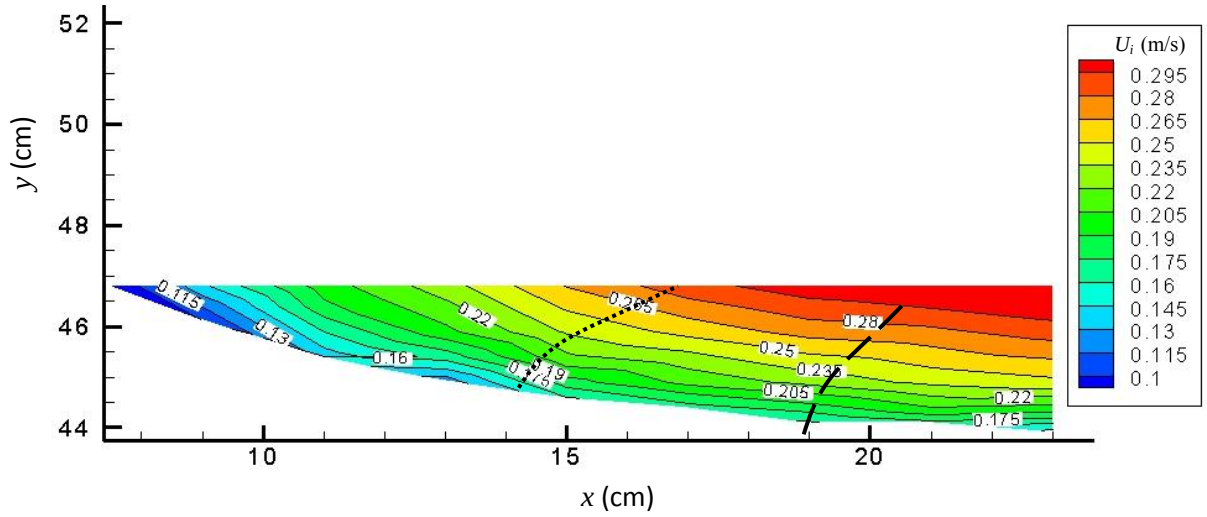

Figure 64. Isovelocity contours for half cross section channel, corresponding to the experiment H1S5, with h_c=3.49cm, S=0.001742 on glue sand bed surface (d_{50}=1.46mm). The dashes represent the divides between secondary flow cells.

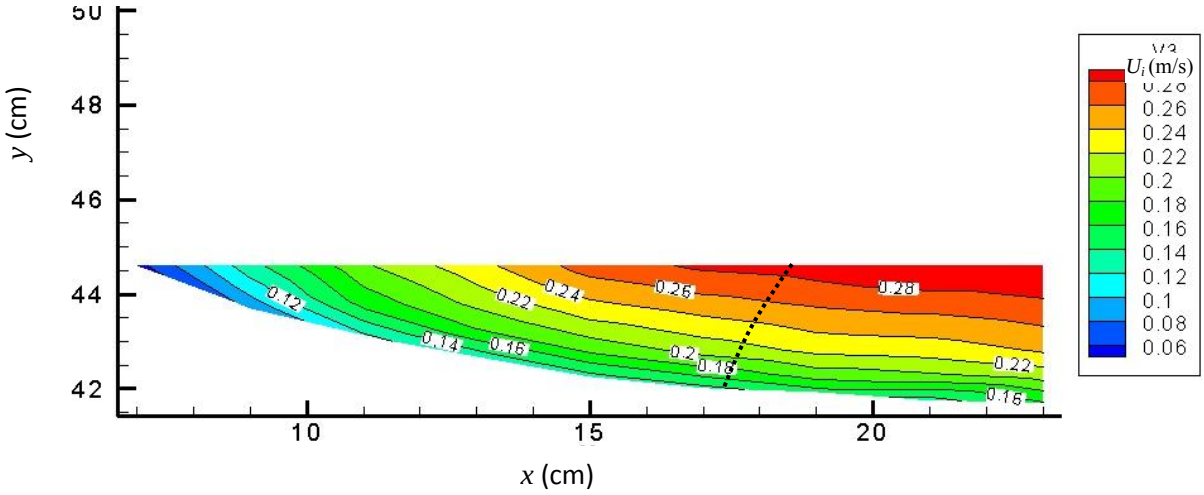

Figure 65. Isovelocity contours for half cross section channel, corresponding to the experiment H1S6, with h_c=3.50cm, S=0.001482 on glue sand bed surface (d_{50}=1.46mm). The dashes represent the divides between secondary flow cells.

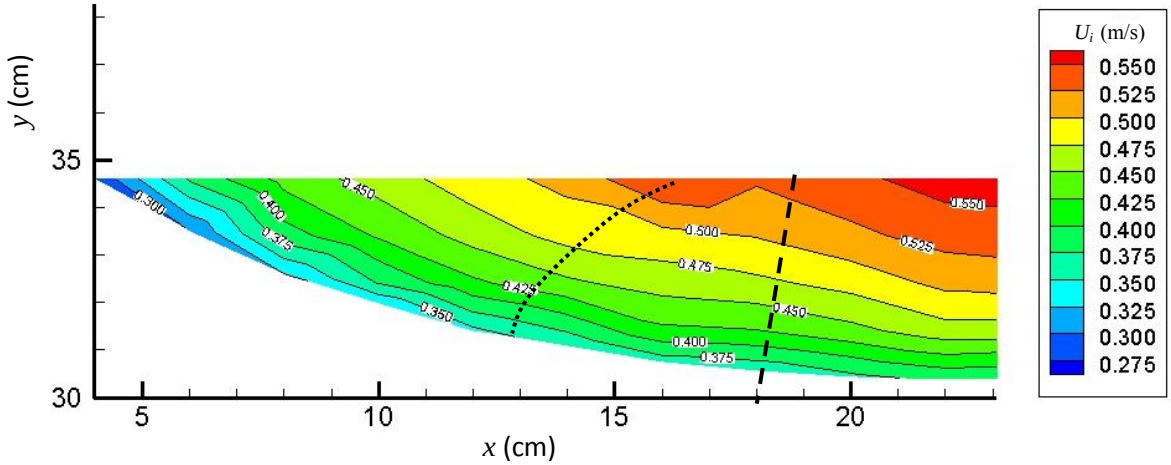

Figure 66. Isovelocity contours for half cross section channel, corresponding to the experiment H2S1, with h_c=4.97cm, S=0.001485 on PVC bed surface. The dashes represent the divides between secondary flow cells.

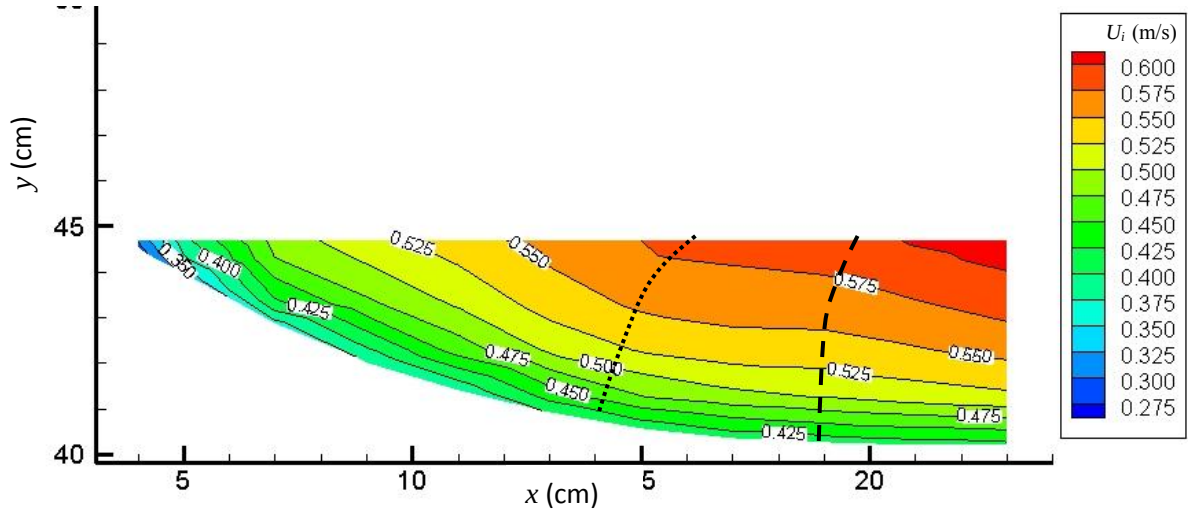

Figure 67. Isovelocity contours for half cross section channel, corresponding to the experiment H2S2, with h_c=5.265cm, S=0.001725 on PVC bed surface. The dashes represent the divides between secondary flow cells.

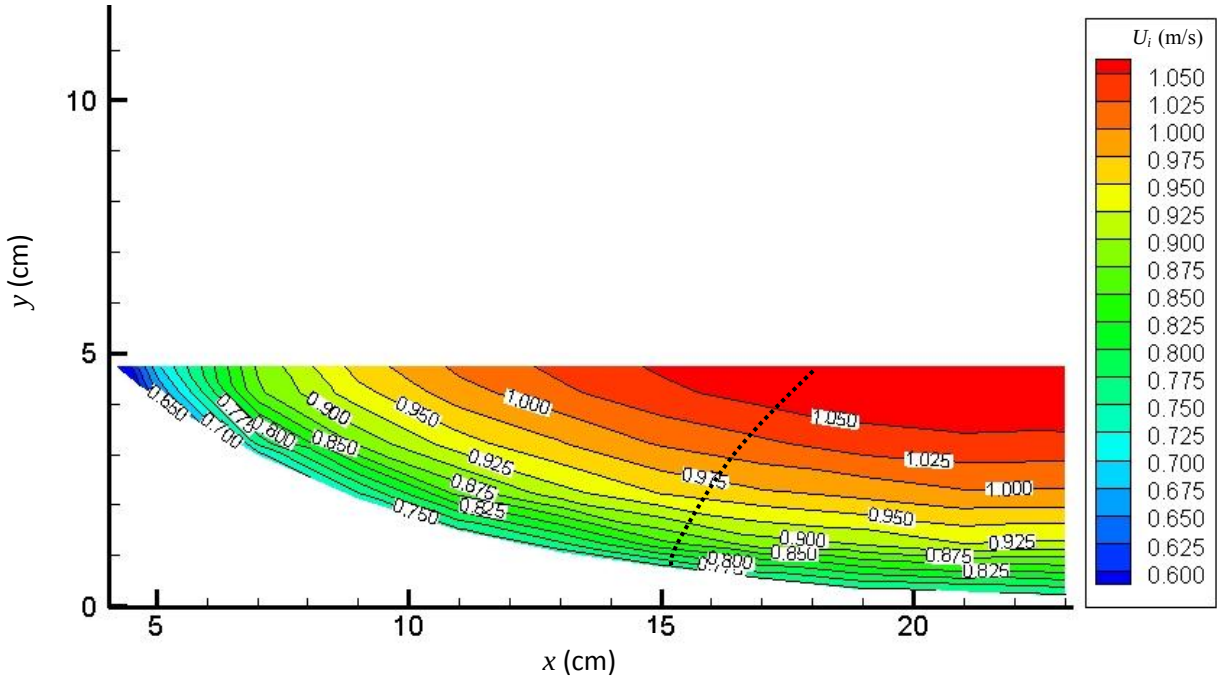

Figure 68. Isovelocity contours for half cross section channel, corresponding to the experiment H2S3, with h_c=5.065cm, S=0.005044 on PVC bed surface. The dashes represent the divides between secondary flow cells.

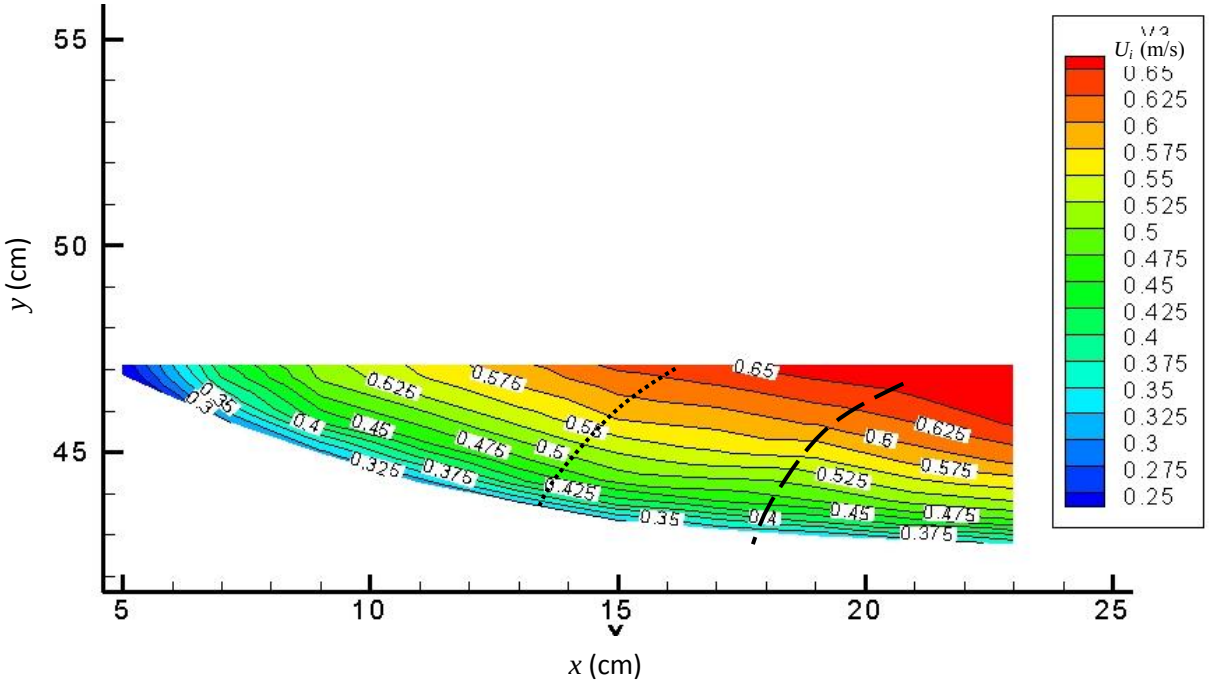

Figure 69. Isovelocity contours for half cross section channel, corresponding to the experiment H2S4, with h_c=5.05cm, S=0.004943 on glue sand bed surface (d_{50}=1.46mm). The dashes represent the divides between secondary flow cells.

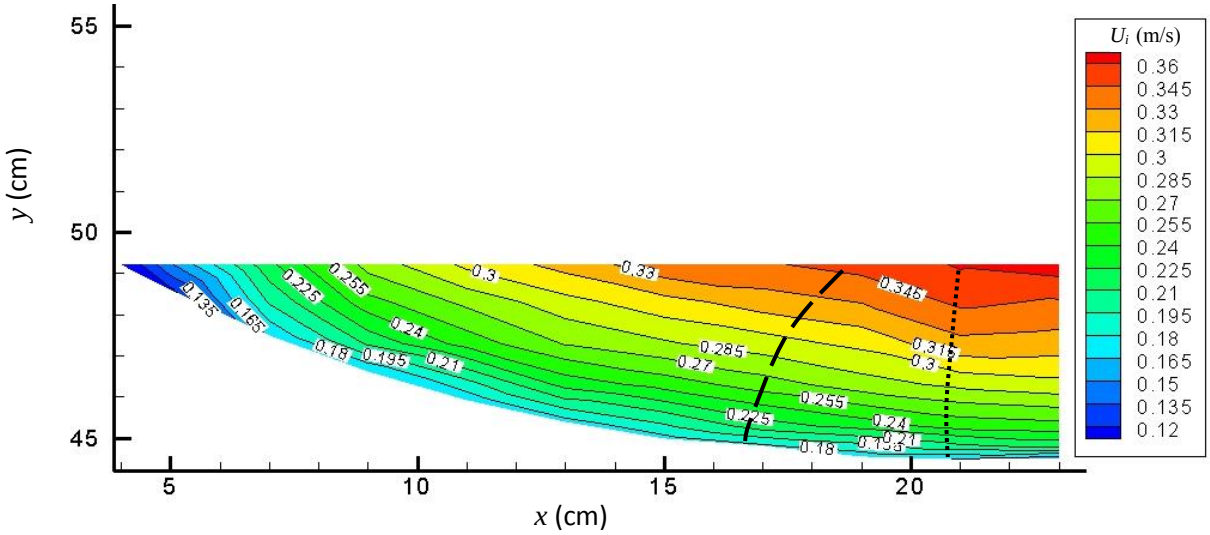

Figure 70. Isovelocity contours for half cross section channel, corresponding to the experiment H2S5, with h_c=5.02cm, S=0.001742 on glue sand bed surface (d_{50}=1.46mm). The dashes represent the divides between secondary flow cells.

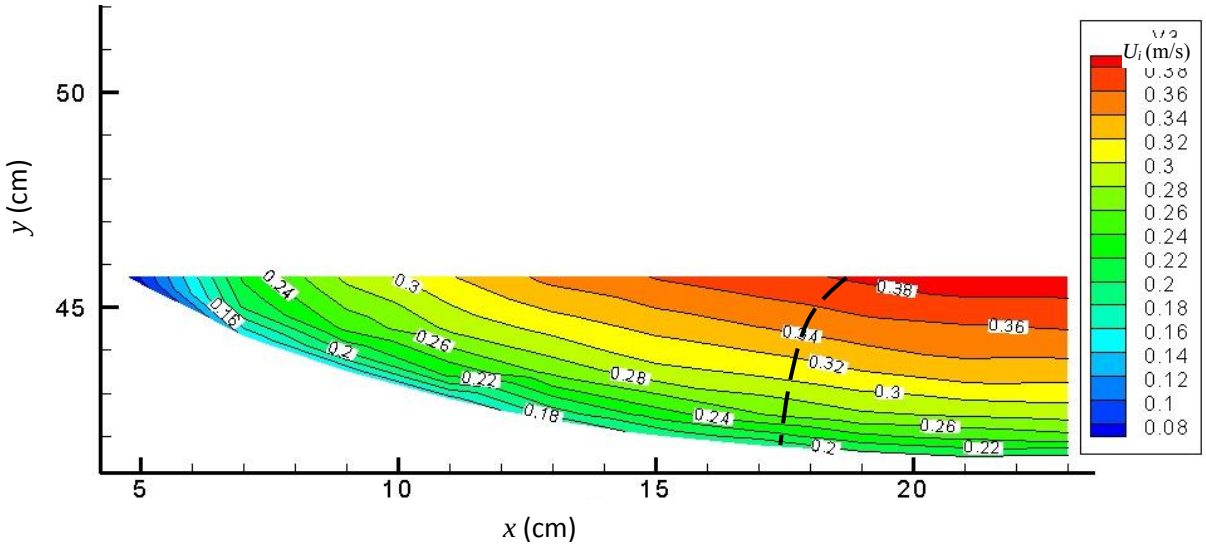

Figure 71. Isovelocity contours for half cross section channel, corresponding to the experiment H2S6, with h_c=5.02cm, S=0.001482 on glue sand bed surface (d_{50}=1.46mm). The dashes represent the divides between secondary flow cells.

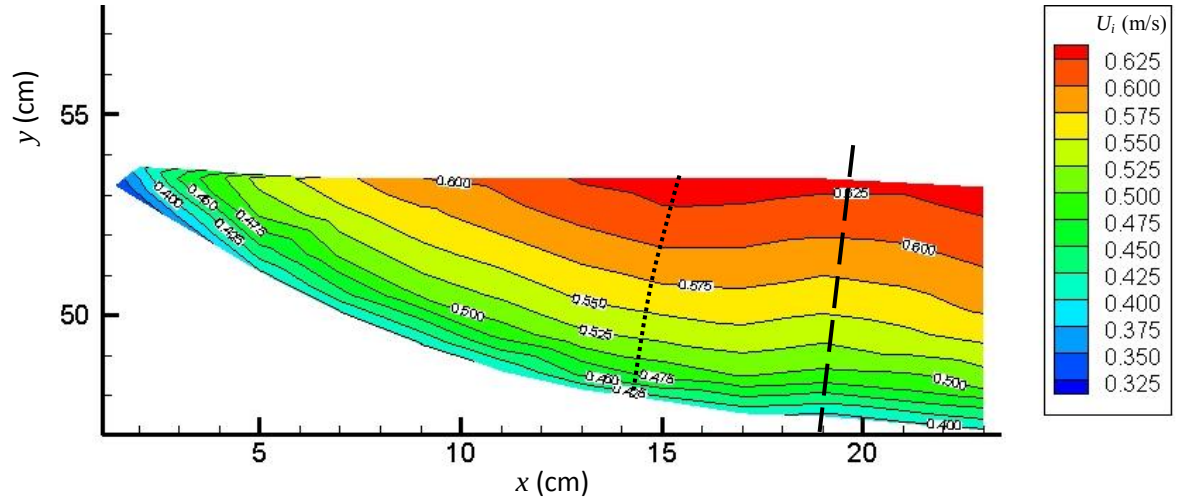

Figure 72. Isovelocity contours for half cross section channel, corresponding to the experiment H3S1, with h_c=7.02cm, S=0.001485 on PVC bed surface. The dashes represent the divides between secondary flow cells.

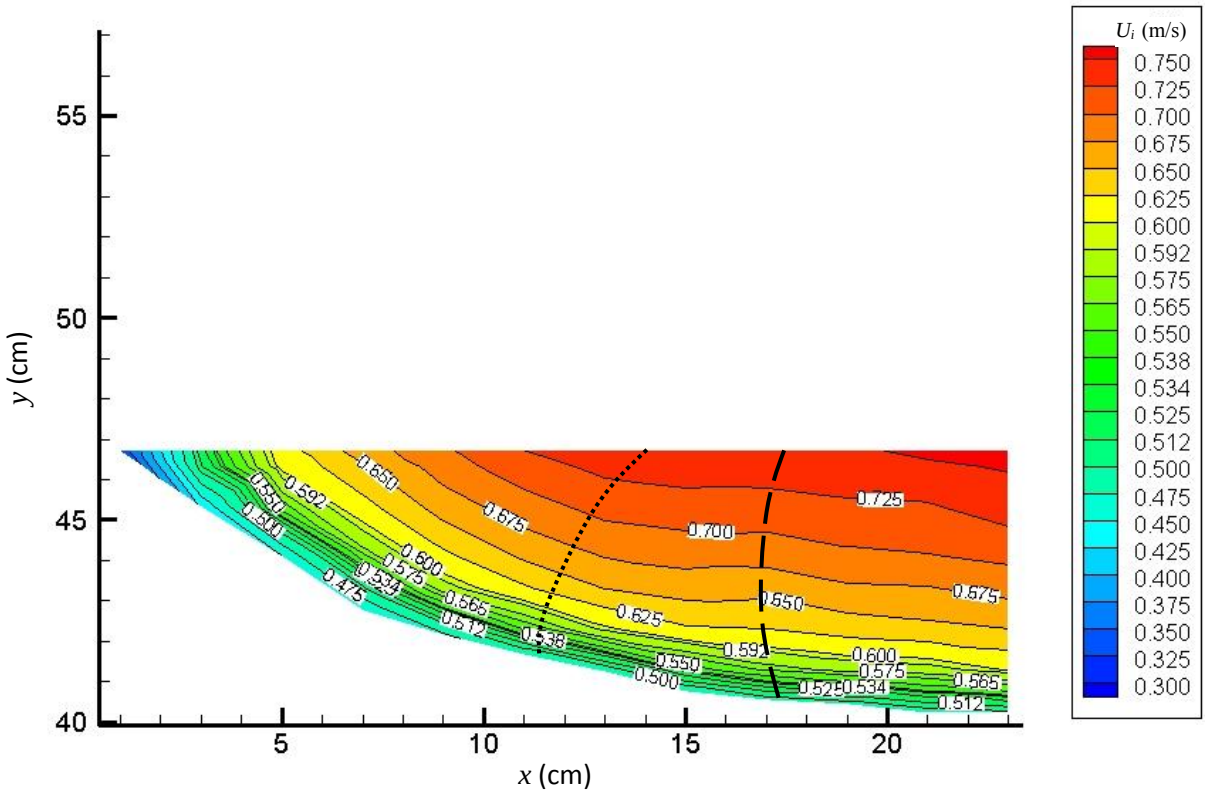

Figure 73. Isovelocity contours for half cross section channel, corresponding to the experiment H3S2, with h_c=7.08cm, S=0.001725 on PVC bed surface. The dashes represent the divides between secondary flow cells.

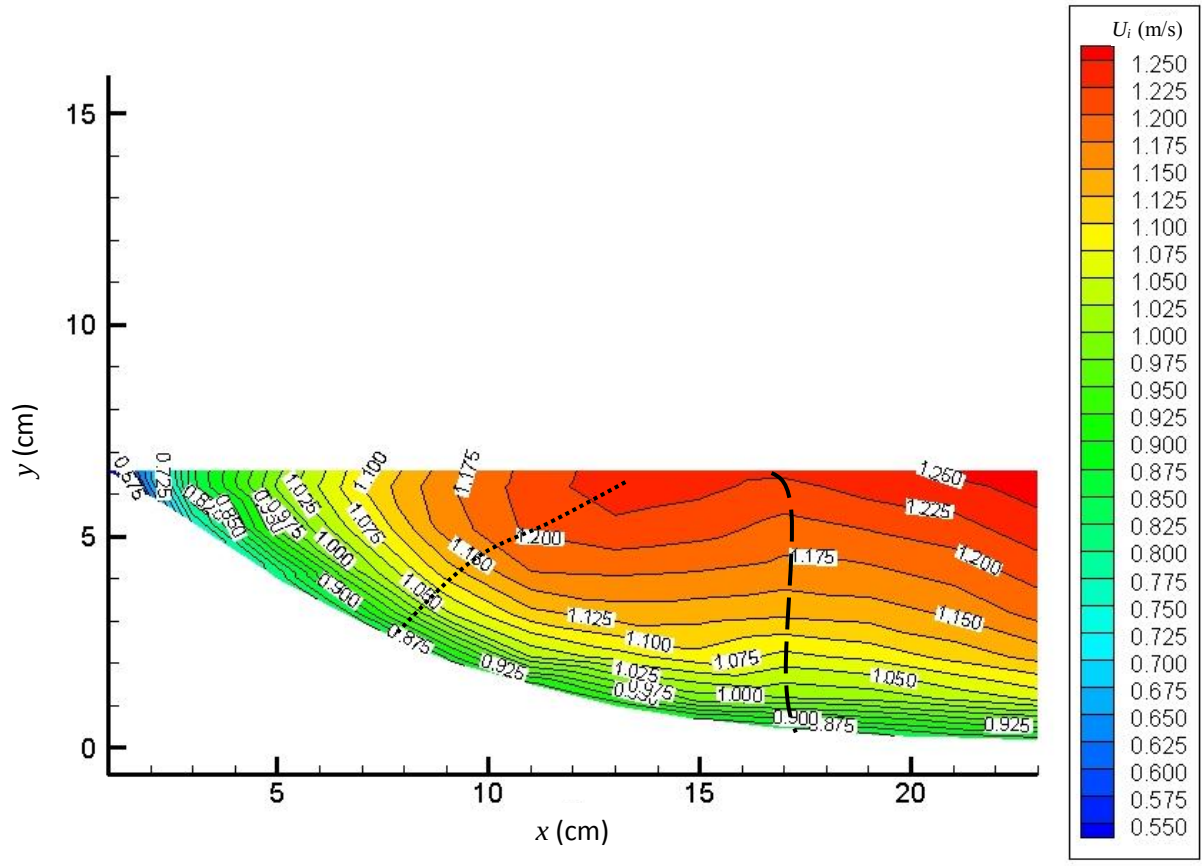

Figure 74. Isovelocity contours for half cross section channel, corresponding to the experiment H3S3, with h_c=6.95cm, S=0.005044 on PVC bed surface. The dashes represent the divides between secondary flow cells.

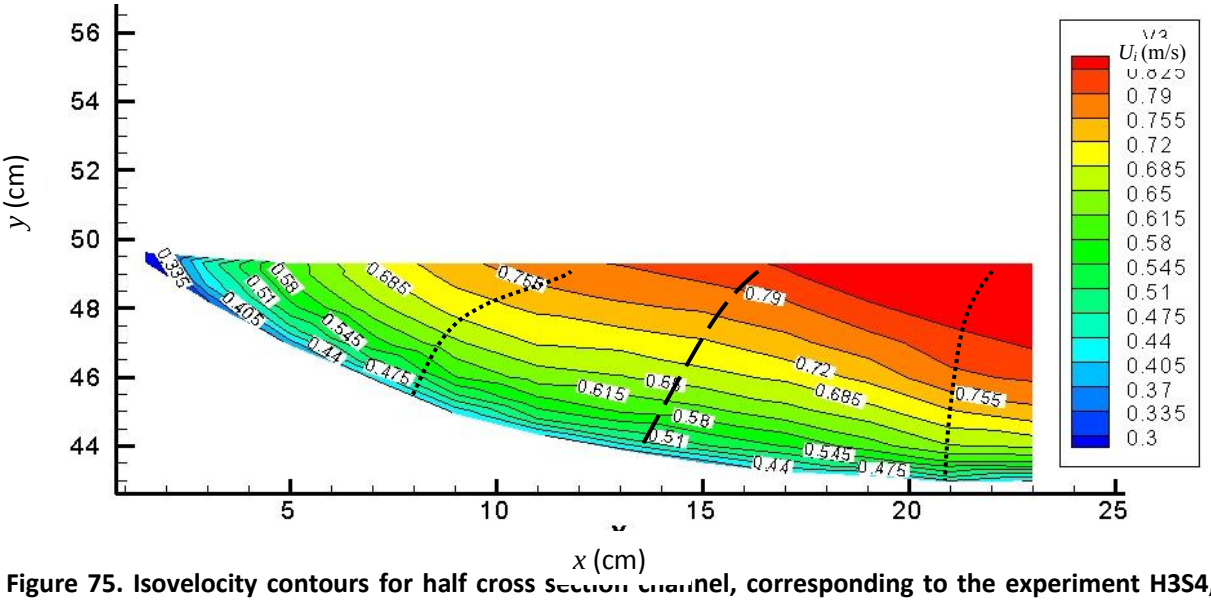

Figure 75. Isovelocity contours for half cross section channel, corresponding to the experiment H3S4, with h_c=7.02cm, S=0.004943 on glue sand bed surface (d_{50}=1.46mm). The dashes represent the divides between secondary flow cells.

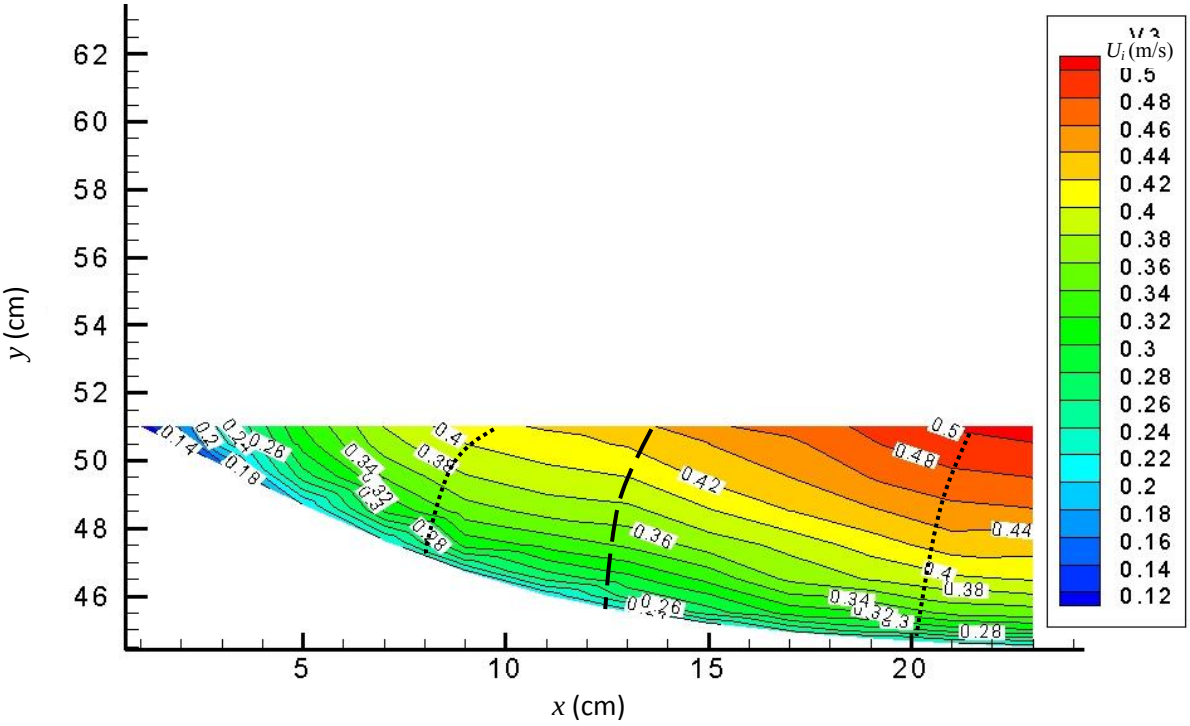

Figure 76. Isovelocity contours for half cross section channel, corresponding to the experiment H3S5, with h_c=7.12cm, S=0.001742 on glue sand bed surface (d_{50}=1.46mm). The dashes represent the divides between secondary flow cells.

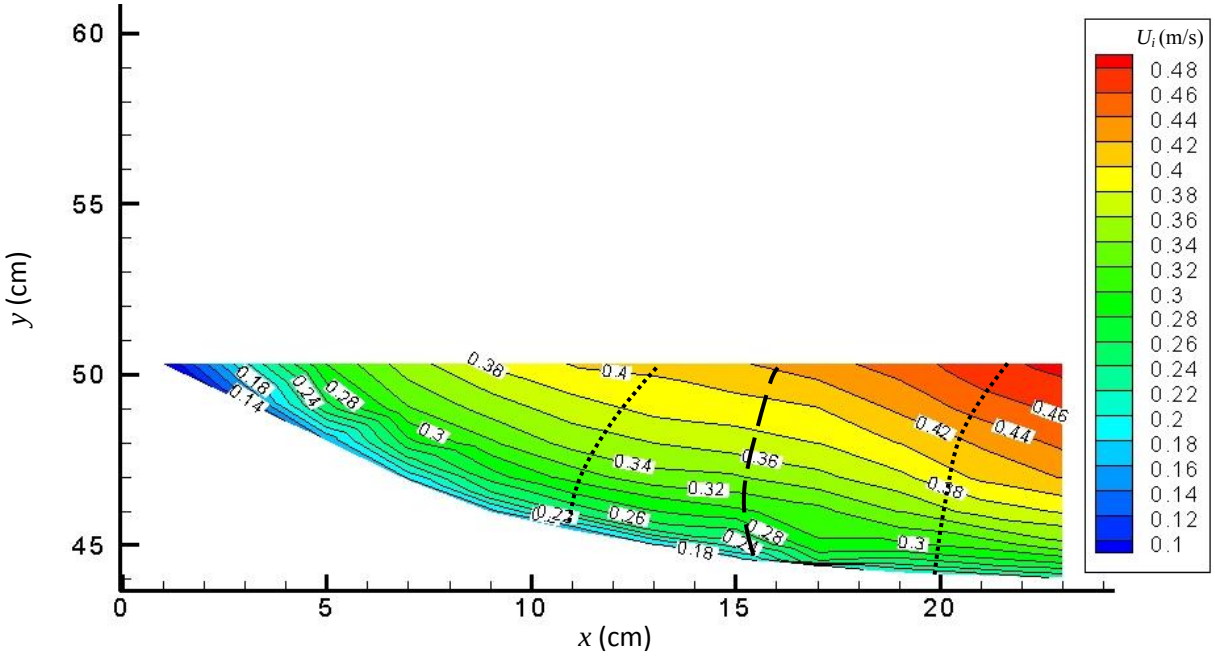

Figure 77. Isovelocity contours for half cross section channel, corresponding to the experiment H3S6, with h_c=7.09cm, S=0.001482 on glue sand bed surface (d_{50}=1.46mm). The dashes represent the divides between secondary flow cells.

5.2.3 Depth average velocity profiles

The depth average velocity, U_d, was obtained by following the equation 71 (section 5.2), determining a value for each point across the channel, and subsequently plotting the transversal velocity profiles for each run. In order to analyse them, the vertical and horizontal axes were presented dimensionless: *i.e.* U_d with respect to V_{Pitot} (average velocity of the channel obtained by Pitot tube measurements), including their corresponding uncertainties; and the horizontal variable, y, respect to half width, $W/2$. Additionally, the runs with similar depths were grouped by boundary surface, producing two graphs: one for smooth and one for rough surface. Finally, an extra chart was obtained, contrasting both types of experiments. In total nine graphs were plotted, three per depth (figures 78 to 86).

By observing $H1$ results (figures 78, 79 and 80), it is noted that the PVC runs are following the same pattern, and their data are within the uncertainty bars (figure 78). Such curves are decreasing smoothly, identifying an inflection point at $y/(W/2)=0.80$, inferring two secondary flow cells in agreement with the isovels, but at different location. With respect to the glue sand curves (figure 79), two runs have a common behaviour, *i.e.* $H1S5$ and $H1S6$ with a change at $y/(W/2)=0.48$; however, half of $H1S4$ is within the error limits of the other curves, with an inflection point at and $y/(W/2)=0.64$, as the experiments on PVC surface. When both types of graphs are contrasted, two shapes can be easily spotted, noticing that the rough surface runs present a higher relative velocity, U_d/V_{Pitot}, than the smooth surface counterpart does, and decreasing faster while the curves approach to the margin. This can be explain

due to the resistant friction factor, f, varies different respect to the depth, h, depending on the boundary surface, as figure 54 illustrates due to the gradient $\Delta(1/h_c)/\Delta f$ for rough and smooth boundary surfaces.

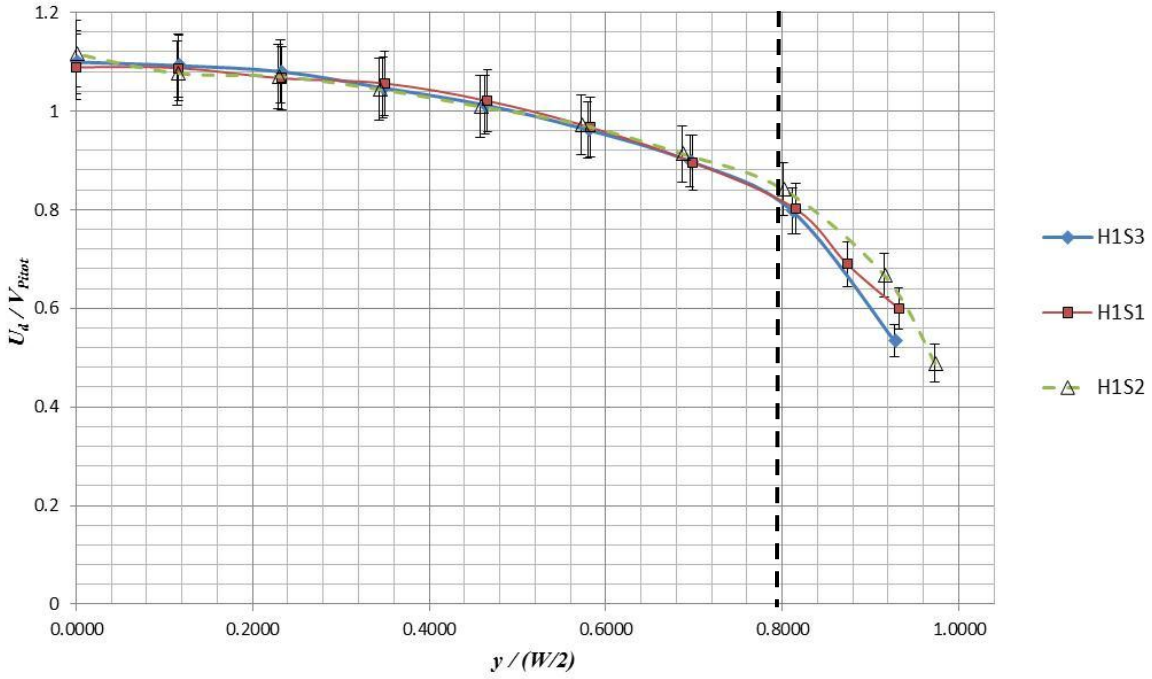

Figure 78. Dimensionless variation of the experimental depth average velocity, U_d, with respect to the main velocity measured of the channel, V_{Pitot}, along the dimensionless half cross section, $y/(W/2)$. The plot corresponds to the H1 experiments (h_c≈3.5cm). Three series are shown, each one for a different slope ($S1$=0.001485, $S2$=0.001725 and $S3$=0.005044). The uncertainty bars indicate that most of the data are within the limits. The dashes represent the divides between secondary flow cells proposed.

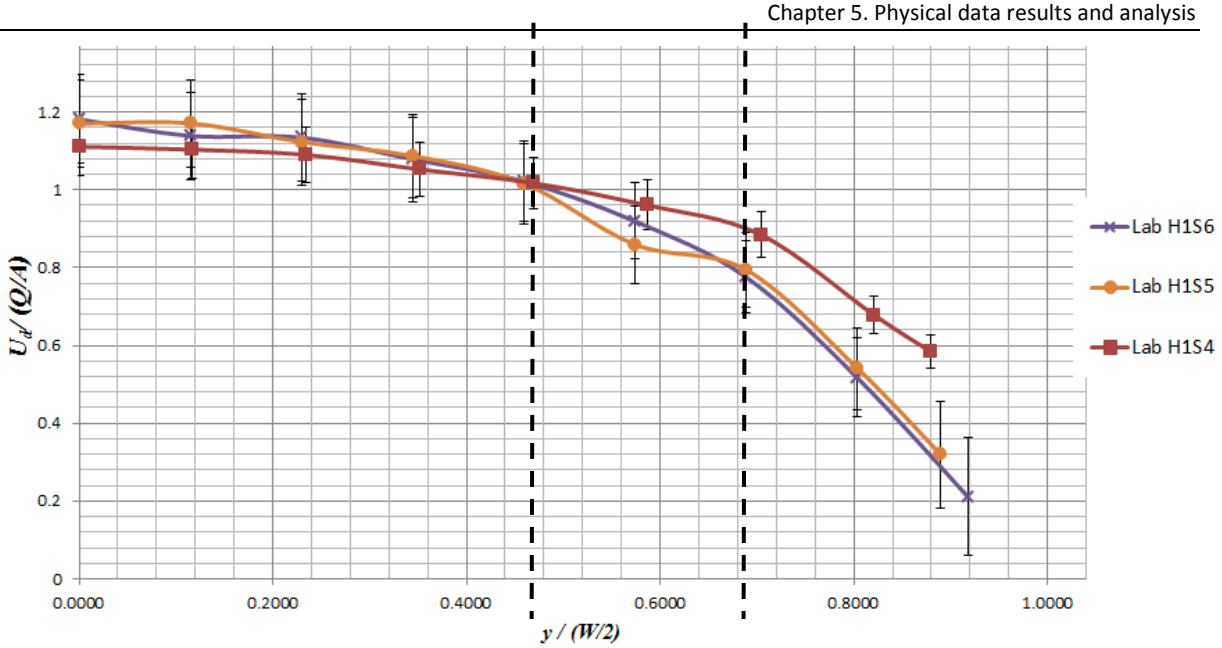

Figure 79. Dimensionless velocity distribution of the H1 experiments carried out on rough surface (d_{50}=1.46mm). Three sets are shown along with their uncertainty bars. It can be observed that two series are following the same pattern (H1S5 and H1S6), and that two thirds of H1S4 are within the uncertainty limits of the other two sets. The dashes represent the divides between secondary flow cells proposed.

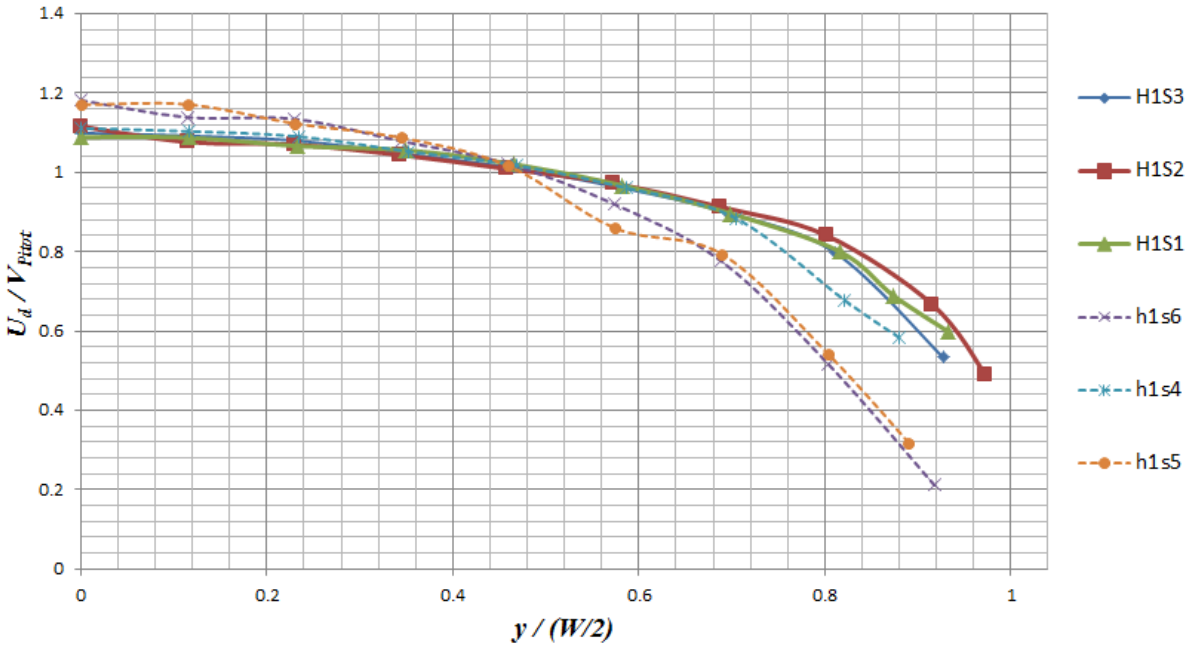

Figure 80.Summary of the six H1 experiments (h_c≈3.5cm), corresponding to the dimensionless transversal velocity variation. Two behaivours can be indentified, one for the smooth surface experiments (PVC), *i.e.* H1S1, H1S2 and H1S3; and another one for the rough surface sets (d_{50}=1.46mm), *i.e.* H1S4, H1S5 and H1S6.

With respect to $H2$ experiments (figures 81, 82 and 83), similar observations to $H1$ are found. That is, a different pattern of curves was identified per surface, being the relative velocity, U_d/V_{Pitot}, of the glue sand sets higher at the centre line ($y/(W/2)=0$) than the PVC ones, decreasing faster while they approaches to the margin ($y/(W/2)=1$). Additionally, kinks in the curves were observed at $y/(W/2)=0.24$, 0.36 and 0.74d for smooth surface experiments (figure 81), and at $y/(W/2)=0.24$ and 0.70 for rough surface sets (figure 82). These inflexion points correspond to the divides found on the isovelocity contours (figures 66 to 71, section 5.2.2), indicating secondary flow cells. However, additional twist were observed on the velocity profiles.

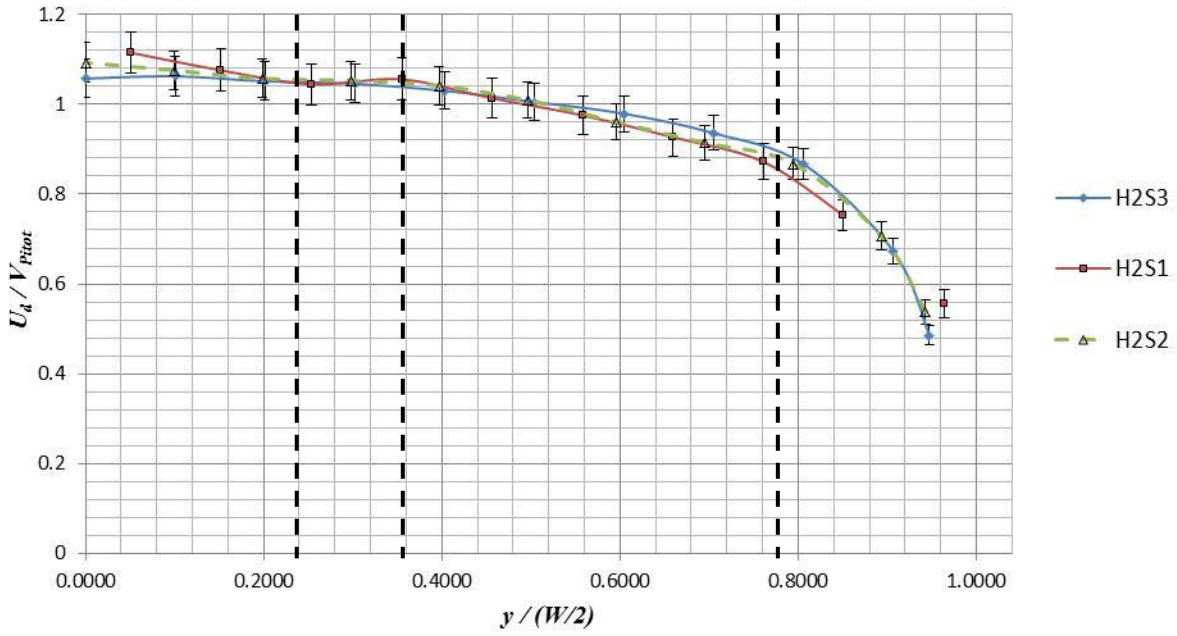

Figure 81. Dimensionless variation of the experimental depth average velocity, U_d, with respect to the main velocity measured of the channel, V_{Pitot}, along the dimensionless half cross section, $y/(W/2)$. The plot corresponds to the H2 experiments (h_c≈5.0cm). Three series are shown, each one for a different slope ($S1$=0.001485, $S2$=0.001725 and $S3$=0.005044). The uncertainty bars indicate that most of the data are within the limits. The dashes represent the divides between secondary flow cells proposed.

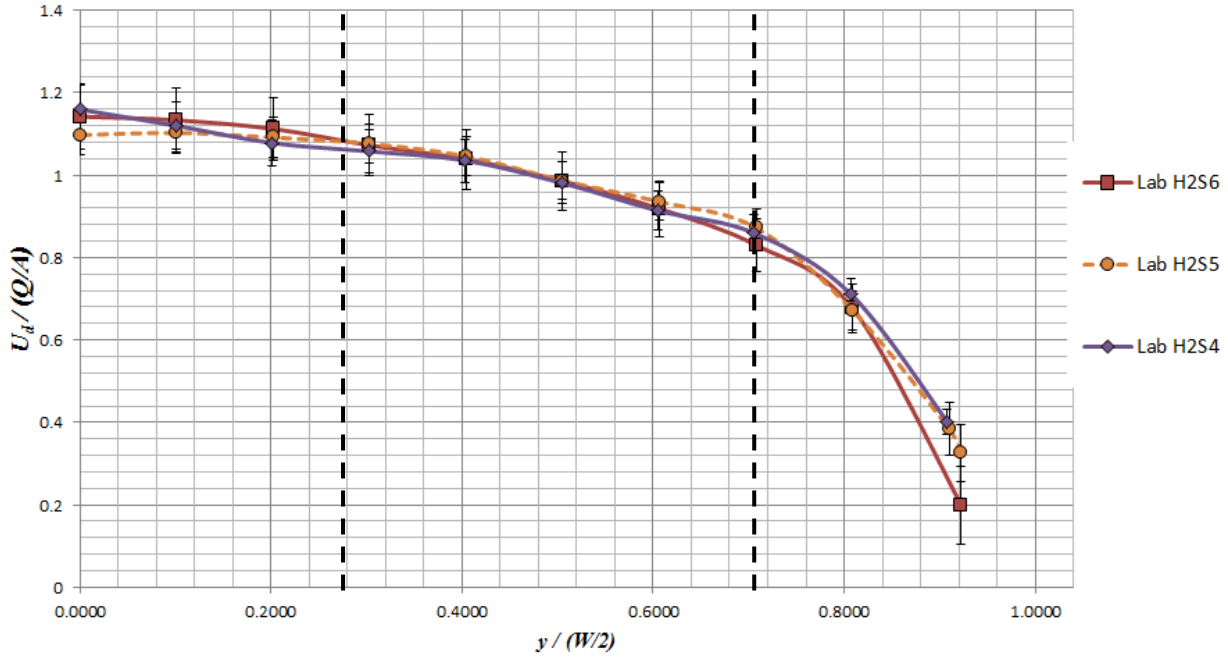

Figure 82. Dimensionless velocity distribution of the H2 experiments carried out on rough surface (d_{50}=1.46mm). Three sets are shown along with their uncertainty bars. It can be observed that the series are following the same pattern. The dashes represent the divides between secondary flow cells proposed.

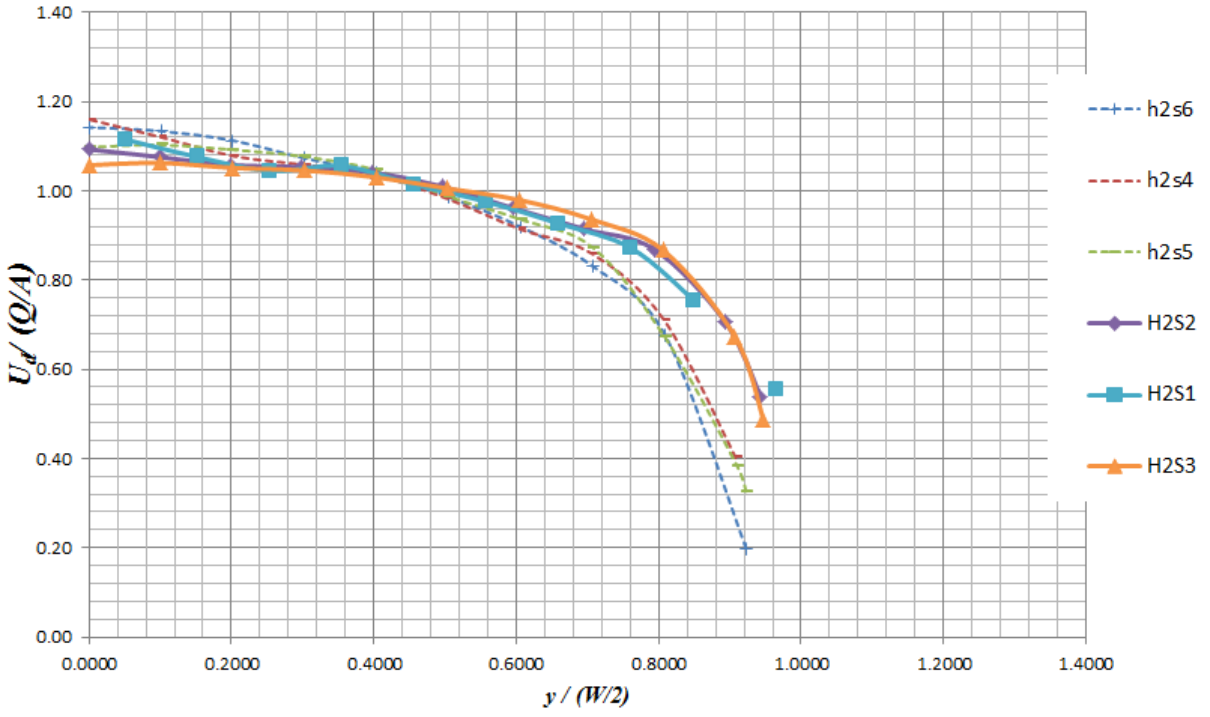

Figure 83. Summary of the six H2 experiments (h_c≈5.00cm), corresponding to the dimensionless transversal velocity variation. Two behaviours can be identified, one for the smooth surface experiments (PVC), *i.e.* H2S1, H2S2 and H2S3; and another one for the rough surface sets (d_{50}=1.46mm), *i.e.* H2S4, H2S5 and H2S6.

Finally, in the *H*3 experiments (figures 84, 85 and 86), two different shapes can be identified as well, depending on the boundary surface. With respect to the PVC sets (figure 84), inflection points were found at $y/(W/2)$=0.20, 0.44 and 0.80. While for the glue sand surface curves, three drastic changes were identified at $y/(W/2)$=0.40, 0.60 and 0.80. Both cases are in agreement with their corresponding isovels of section 5.2.2 (figures 72 to 77). This last confirms the existence of secondary flow cells, that the boundary modifies their behaviour, and that at higher depths the impact is more evident. Additionally, the difference in the divide location is explained due to the boundary material, affecting different the flow. In the case of the rough surface sets, the glue sand boundary provokes a faster decrement on U_d/V_{Pitot}, and a milder vertical velocity gradient due to a higher friction.

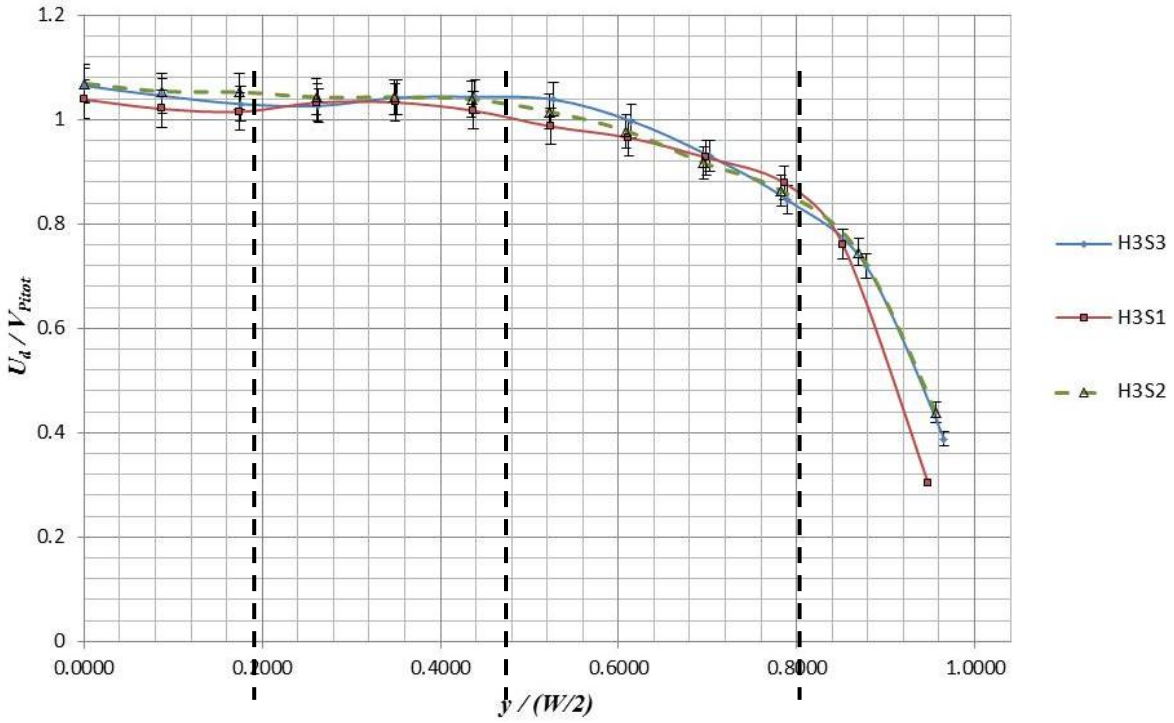

Figure 84. Dimensionless variation of the experimental depth average velocity, U_d, with respect to the main velocity measured of the channel, V_{Pitot}, along the dimensionless half cross section, $y/(W/2)$. The plot corresponds to the H3 experiments (h_c≈7.0cm). Three series are shown, each one for a different slope ($S1$=0.001485, $S2$=0.001725 and $S3$=0.005044).

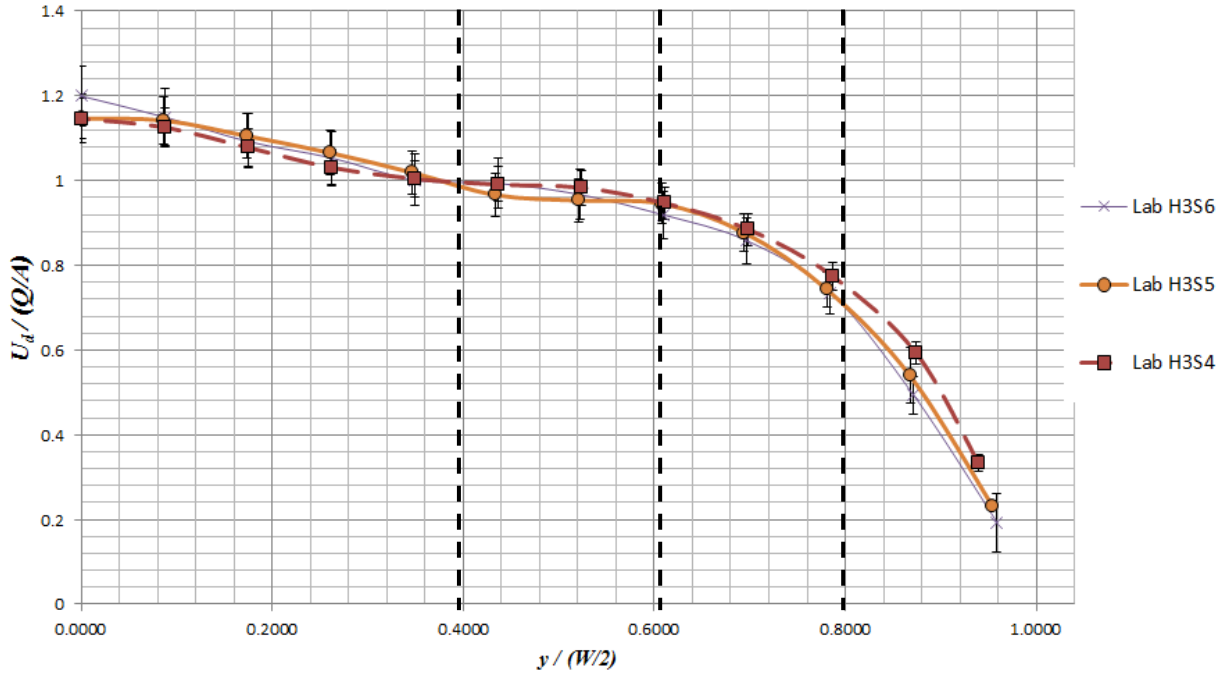

Figure 85. Dimensionless velocity distribution of the H1 experiments carried out on rough surface (d_{50}=1.46mm). Three sets are shown along with their uncertainty bars. It can be observed that the series are following the same pattern.

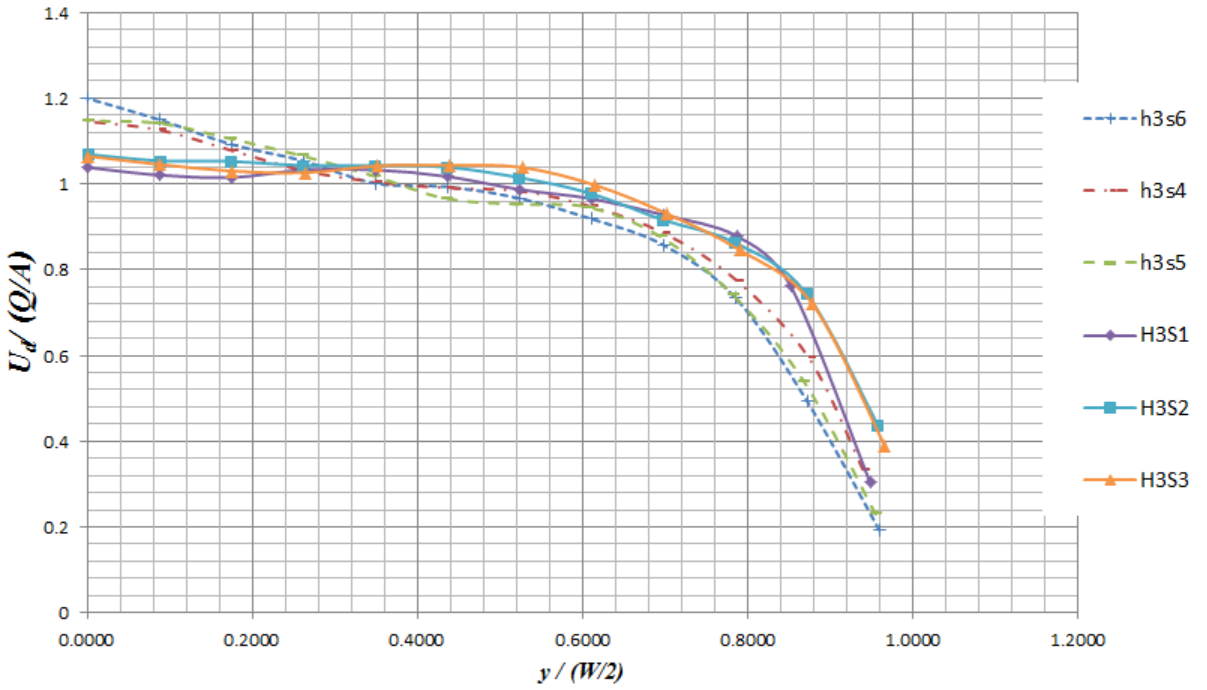

Figure 86. Summary of the six H3 experiments (h_c≈7.00cm), corresponding to the dimensionless transversal velocity variation. Two behaivours can be indentified, one for the smooth surface experiments (PVC), *i.e.* H3S1, H3S2 and H3S3; and another one for the rough surface sets (d_{50}=1.46mm), *i.e.* H3S4, H3S5 and H3S6.

5.3 Boundary shear stress results

The summary of the results related to the boundary shear stress measurements, τ_0, is shown on table 25. On it the geometrical characteristics (h_c, A, P, R, S) of each run are mentioned, as well as the Preston tube used, the number of points taken, the average boundary shear stress measured, τ_{Preston}:

$$\tau_{Preston} = \frac{1}{P}\int_0^P \tau_0 \, dp \tag{83}$$

its relative uncertainty, $\Delta\tau_{Preston}/\tau_{Preston}$, the theoretical average boundary shear stress, $\tau=\rho gRS$, and the error, E_τ, between τ_{Preston} and τ :

$$E_\tau\% = \left|\frac{\tau - \tau_{\text{Preston}}}{\tau_{\text{Preston}}}\right| 100 \tag{84}$$

E_τ is between 1.58% and 12.5%, considering acceptable since the average measured shear stress uncertainty, Δ_{Preston}, is between 2.51% and 10.98%. The corresponding uncertainty analysis is shown on the section 0.

With respect to E_τ, it is noted that it reduces when h_c increases. This can be explained due to the accuracy of the Preston tube improves when the pressure difference between the total and the static, P_T-P_S, increases. Such a subtraction depends mainly on the increment of P_T, due to P_S is only affected by the depth. While P_T is directly proportional to the flow velocity. Hence, a higher depth increases the velocity, also P_T-P_S does as well, and E_τ decreases. The corresponding uncertainty analysis is shown on the section 0.

Table 25. A summary of the runs carried out is shown below, presenting the results related to the measured boundary shear stress on smooth surface. The geometrical and experimental variables can be appreciated.

Smooth surface (PVC)

	S1			*S2*			*S3*		
	H1	*H2*	*H3*	*H1*	*H2*	*H3*	*H1*	*H2*	*H3*
S=	0.001485	0.001485	0.001485	0.001725	0.001725	0.001725	0.005044	0.005044	0.005044
h_c (cm)=	3.34	4.97	7.02	3.53	5.27	7.08	3.40	5.07	6.95
A (cm^2)=	84.00	144.69	228.77	87.82	154.51	234.99	85.41	147.39	227.85
P (cm)=	35.59	41.72	48.69	36.04	42.59	49.17	35.76	42.01	48.66
R (cm)=	2.36	3.47	4.70	2.44	3.63	4.78	2.39	3.51	4.68
Preston tube diameter (mm)=	3.00	4.80	4.80	3.00	3.00	3.00	3.00	3.00	3.00
No.of τ_0 readings=	20	20	23	19	11	23	17	21	23
$\tau_{Preston}$ (N/m^2)=	0.3753	0.5410	0.6957	0.3482	0.5425	0.8462	1.2667	1.8694	2.2760
$\tau=\rho gRS$ (N/m^2)=	0.3438	0.5053	0.6846	0.3864	0.6102	0.8037	1.1818	1.7357	2.3170
E_τ%=	8.39%	6.60%	1.58%	10.99%	**12.47%**	5.02%	**6.70%**	**7.15%**	1.80%
$\Delta\ \tau_{Preston}/\ \tau_{Preston}$ =	10.00%	7.44%	7.58%	10.98%	**8.44%**	6.48%	**2.56%**	**2.51%**	2.68%

As mentioned previously, the boundary shear stress was not measured for the glue sand surface experiments, but it was obtained indirectly by $\tau_0 = \rho f U_d^2/8$. The summary of the results is shown in table 26. However, the error obtained is higher than the uncertainty determined, suggesting a review of the friction factor used and its distribution along the cross section.

Table 26. A summary of the boundary shear stress obtained for the experiments on glue sand surface (d_{50}=1.46mm). It should be noted that τ_0 was not measured, it was obtained indirectly based on the velocity measurements.

	S4			*S5*			*S6*		
	H1	*H2*	*H3*	*H1*	*H2*	*H3*	*H1*	*H2*	*H3*
S	0.00494	0.00494	0.00494	0.00174	0.00174	0.00174	0.00148	0.00148	0.00148
h_c (cm)	3.27	5.05	7.02	3.49	5.02	7.115	3.495	5.021667	7.09
A (cm^2)	79.32	144.49	228.27	86.32	142.51	232.57	86.67	143.30	231.43
P (cm)	34.83	41.86	48.47	35.82	41.52	48.79	35.86	41.76	48.70
R (cm)	2.28	3.45	4.71	2.41	3.43	4.77	2.42	3.43	4.75
$\tau_0 = \rho f U_d^2 / 8$ (N/m^2)	1.45	1.54	2.25	0.31	0.49	0.65	0.25	0.46	0.53
$\tau = \rho g R S$ (N/m^2)	1.10	1.67	2.28	0.41	0.59	0.81	0.35	0.50	0.69
E_τ%	**23.78%**	**8.86%**	**1.35%**	**33.74%**	**18.84%**	**24.40%**	**40.03%**	**9.23%**	**29.91%**
$\Delta\tau_0 / \tau_0$	6.33%	6.25%	6.09%	10.65%	7.84%	7.85%	10.66%	7.92%	8.25%

5.3.1 Uncertainty analysis of τ_{Preston}

In order to determine the reliability of τ_{Preston}, an uncertainty analysis was required. The systematic assumptions related to the manometer and to the channel were considered in common with the ones of ΔQ_{Pitot} (section 5.2.1). While the systematic relative shear stress uncertainty attributed to the Preston tube, $\Delta\tau_{sys}/\tau_{\text{Preston}}$, was taken as 2%.

The procedure started propagating the uncertainty related to the manometer heads, ΔT and ΔS, to the total and static pressure uncertainties, ΔP_T and ΔP_S:

$$\frac{\Delta P_T}{P_T} = \sqrt{\left(\frac{\Delta T}{T}\right)^2 + \left(\frac{\Delta \sin(\alpha')}{\sin(\alpha')}\right)^2} \tag{85}$$

$$\frac{\Delta P_S}{P_S} = \sqrt{\left(\frac{\Delta S}{S}\right)^2 + \left(\frac{\Delta \sin(\alpha')}{\sin(\alpha')}\right)^2} \tag{86}$$

Later ΔP_T and ΔP_S were transmitted to Δx^* derived from equation 55, and subsequently to Δy^* from equation 57 (section 4.5.e) as:

$$\frac{\Delta x^*}{x^*} = \frac{1}{x^*} \frac{\sqrt{(\Delta P_T)^2 + (\Delta P_S)^2}}{(P_T - P_S)\ln(10)} \tag{87}$$

$$\frac{\Delta y^*}{y^*} = \frac{\Delta x^*}{y^*}\left|-0.1381 + 0.2874x^* - 0.018(x^*)^2\right| \tag{88}$$

Once Δx^* and Δy^* where known, the next step was to find the uncertainty of the boundary shear stress, $\Delta\tau_0$, by spreading the error of τ_0, that is defined as:

$$\tau_0 = 4\left(10^{y^*}\right)\frac{\rho v^2}{d^2} \tag{89}$$

proposing $\Delta\tau_0$ as the derivative of τ_0, with respect to y^*, affected by Δy^*:

$$\Delta\tau_0 = \left|\frac{d(\tau_0)}{d\,y^*}\right|\Delta y^* \tag{90}$$

$$\frac{d(\tau_0)}{d\,y^*} = 4(\ln 10)\left(10^{y^*}\right)\frac{\rho v^2}{d^2} \tag{91}$$

After $\Delta\tau_0$ was determined, the systematic shear stress uncertainty, $\Delta\tau_{sys}$, was taken into account, naming this variable $\Delta\tau_T$:

$$\Delta\tau_{T\,j} = \sqrt{\left(\Delta\tau_{0\,j}\right)^2 + \left(\Delta\tau_{sys\,j}\right)^2} \tag{92}$$

Finally, the average shear stress uncertainty of the whole cross section, $\Delta\tau_{\text{Preston}}$, was obtained by accumulating $\Delta\tau_T$ along the differential wetted perimeter, δp, and dividing the sum by the wetted perimeter of the channel, P:

$$\Delta\tau_{\text{Preston}} = \frac{1}{P}\sum_{j=1}^{M}\Delta\tau_{T\,j}\,\delta p_j \tag{93}$$

The corresponding results for each run are shown on table 25.

5.3.2 Shear stress profiles

The boundary shear stress measurements were plotted dimensionless for each run, obtaining transversal profiles. Later, they were grouped according to their depth, producing three graphs (figures 87, 88 and 89). The vertical axis corresponds to the relative shear stress, $\tau/\rho gRS$, and the horizontal axis to the relative distance from the centre line, $y/(W/2)$.

From each graph, it is observed that the curves are following the same pattern, varying for each depth, and that the data are falling within the common uncertainty, except for $H1S2$ and $H2S2$, but nearly half sections are between the limits. With respect to $H2S2$, it has the same shape that $H2S1$ and $H2S3$, just displaced, indicating a probable mistake during its measurements.

Due to the irregularity that the profiles presented, it is not possible to identify a divide, as was noticed on the isovelocity contours, and velocity profiles. Such an irregularity can be attributed to the large uncertainty yield by the Preston tube.

In general, the highest $\tau/\rho gRS$ is located at the centre line, in agreement with the velocity profiles, decreasing while approaching to the margin. By comparing the three figures, it can be appreciated that the curves are behaving differently. The gradient of $H1$ is higher than the $H2$ gradient, being these milder, and the $H3$ semi-constant during the first 60% of the section. These can be explained due to the

geometry affects the flow, although being the same channel, the margin slope varies for each depth. Hence, if the velocity and shear stress performs distinct for each channel shape, it is expected to find a particular secondary flow pattern per geometry.

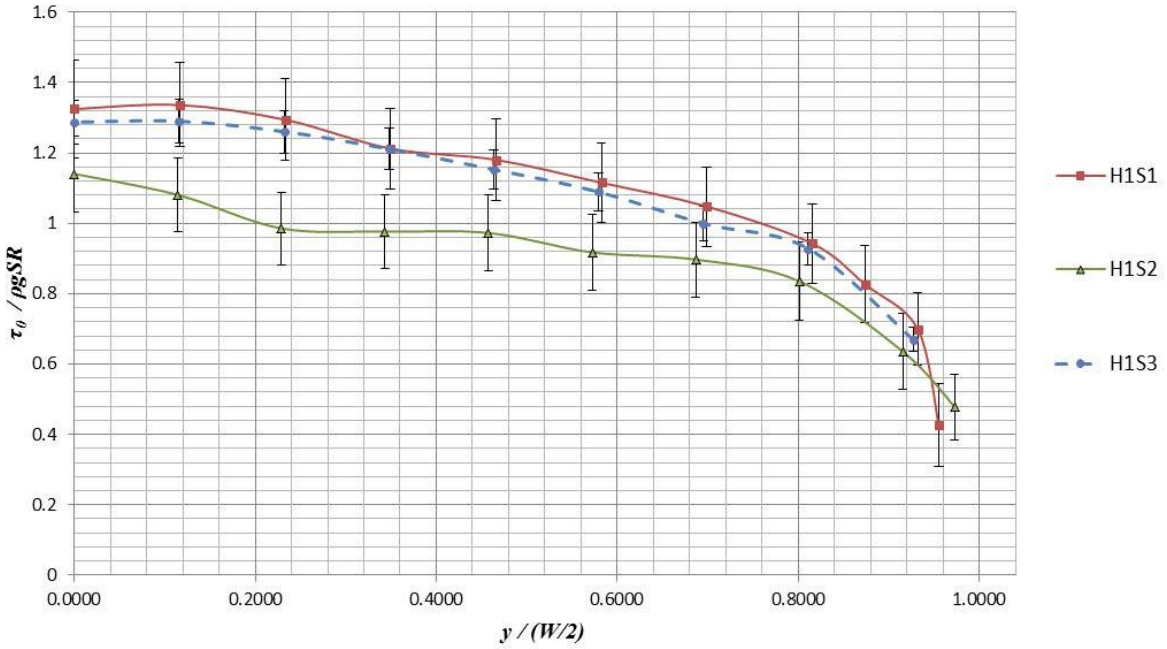

Figure 87. Dimensionless variation of the experimental boundary shear stress, τ_0, with respect to the average shear stress, ρgSR, along the dimensionless half cross section, $y/(W/2)$. The plot corresponds to the H2 experiments (h_c≈3.50cm). Three series are shown, each one for a different slope ($S1$=0.001485, $S2$=0.001725 and $S3$=0.005044). The uncertainty bars indicate that H1S1 and H1S3 are within the same limits, while H1S2 is not.

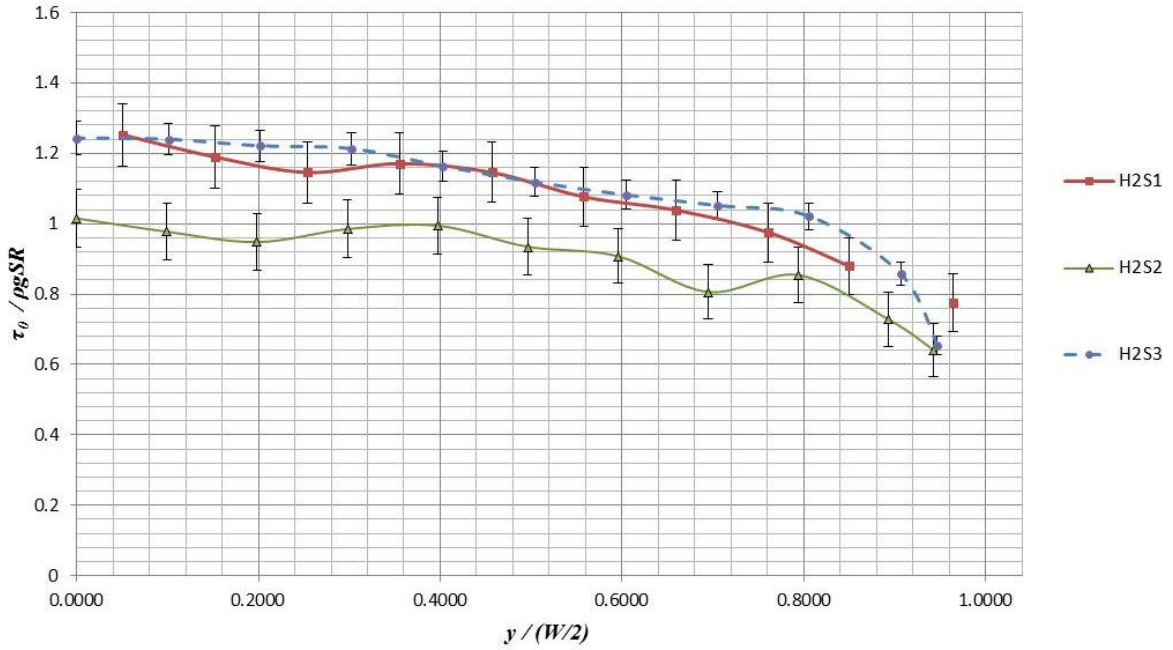

Figure 88. Dimensionless variation of the experimental boundary shear stress, τ_0, with respect to the average shear stress, ρgSR, along the dimensionless half cross section, $y/(W/2)$. The plot corresponds to the H3 experiments (h_c≈5.0cm). Three series are shown, each one for a different slope ($S1$=0.001485, $S2$=0.001725 and $S3$=0.005044). The uncertainty bars indicate that H2S1 and H2S3 are within the same limits, while H2S2 is not.

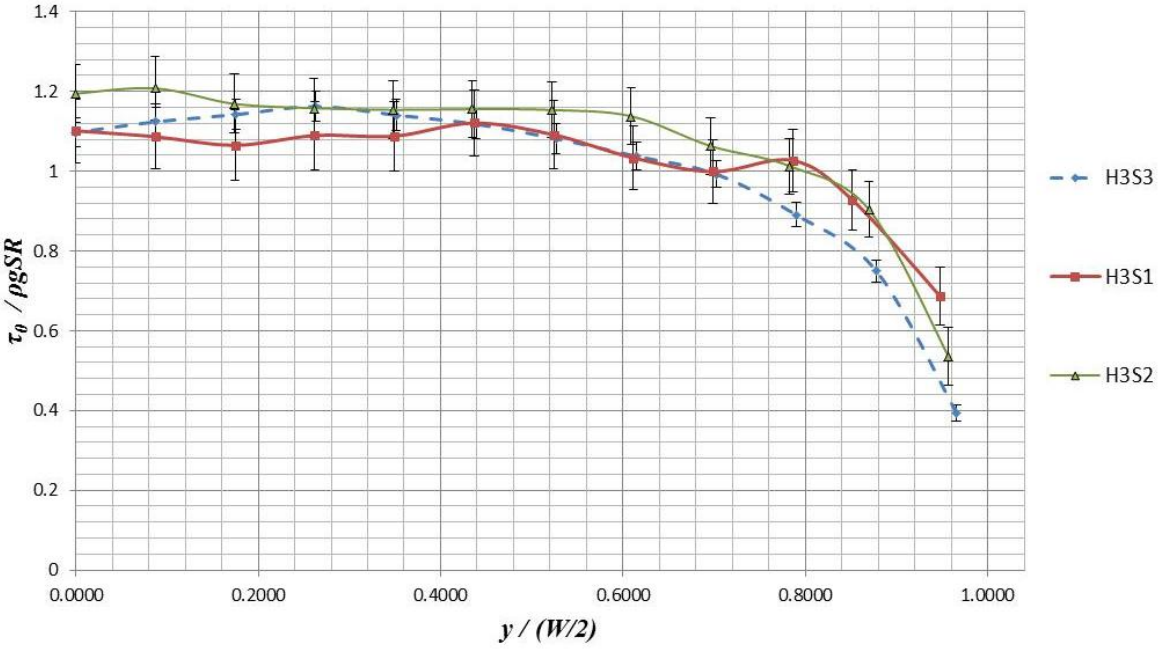

Figure 89. Dimensionless variation of the experimental boundary shear stress, τ_0,with respect to the average shear stress, ρgSR, along the dimensionless half cross section, $y/(W/2)$. The plot corresponds to the H3 experiments (h_c≈7.0cm). Three series are shown, each one for a different slope ($S1$=0.001485, $S2$=0.001725 and $S3$=0.005044). The uncertainty bars indicate that most of the data are within the limits.

With respect to the experiments on glue sand surface, due to technical difficulties, it was not possible to measure τ_0, but was it estimated by $\tau_0 = \rho f U_d^2/8$. Such results were plotted, since they are based on U_d, their patterns are quite similar to the velocity profiles on section 5.2.3., an as expected the uncertainty is quite high, over 20%

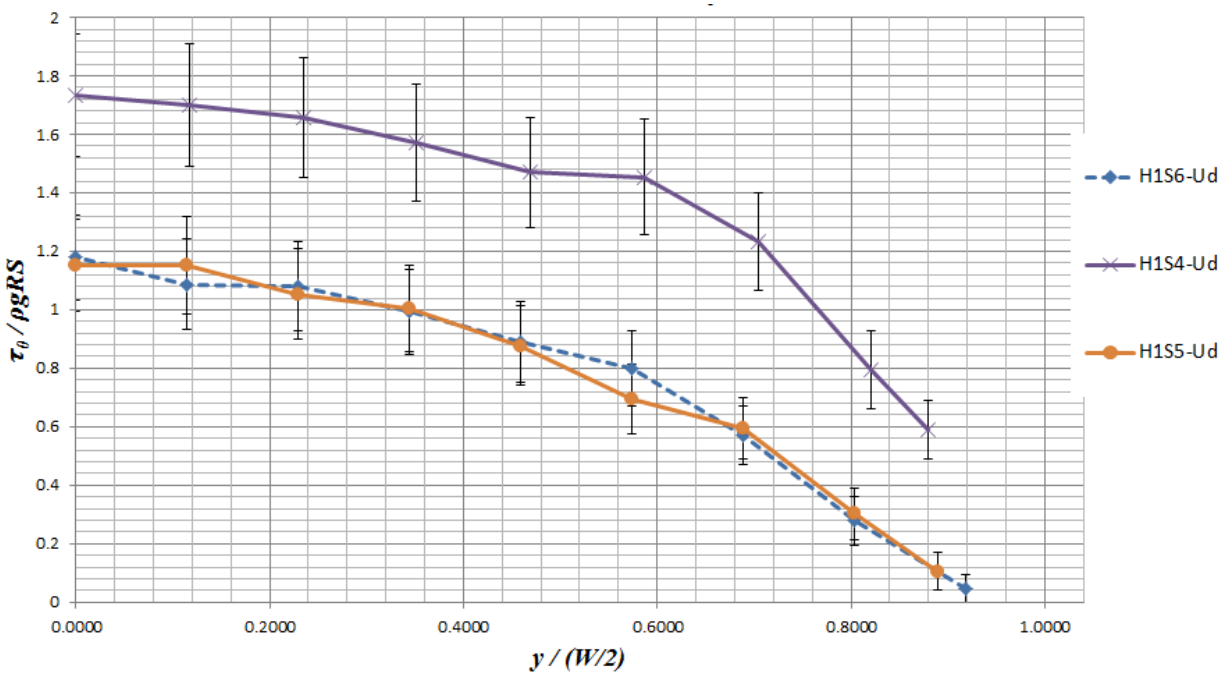

Figure 90. Dimensionless boundary shear stress distribution of the H1 experiments carried out on rough surface (d_{50}=1.46mm). Three sets are shown along with their uncertainty bars. It can be observed that the series H1S5 and H1S6 are following the same pattern.

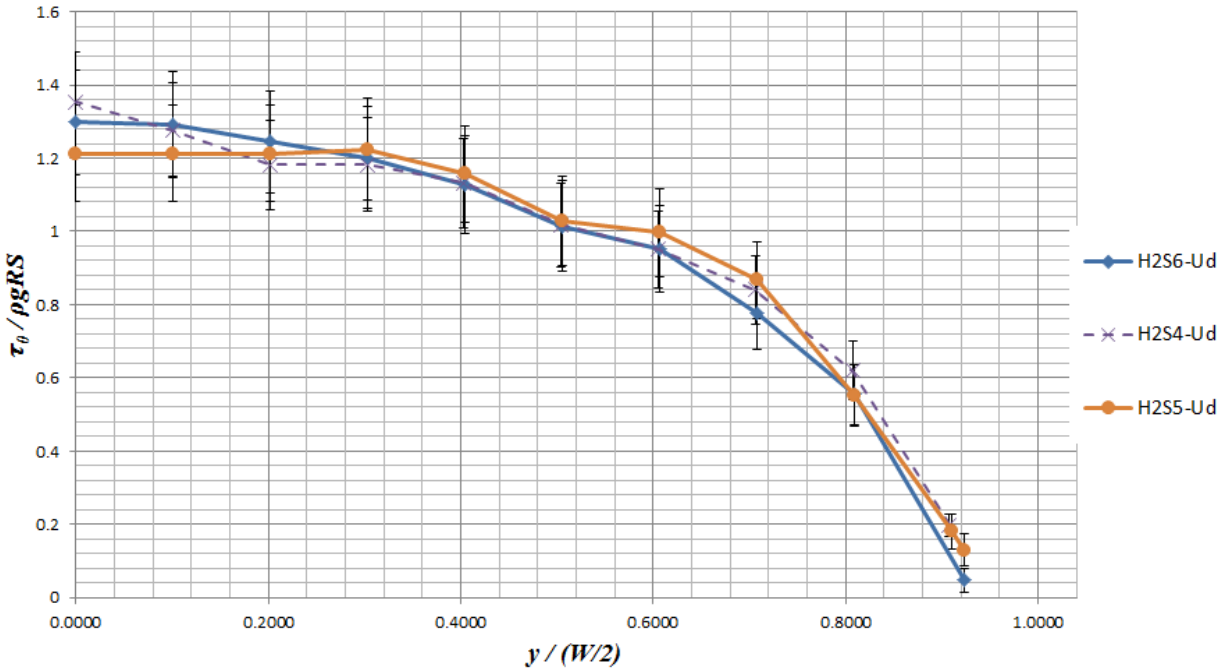

Figure 91. Dimensionless boundary shear stress distribution of the H2 experiments carried out on rough surface (d_{50}=1.46mm). Three sets are shown along with their uncertainty bars. It can be observed that the sets are following the same pattern with slightly variations.

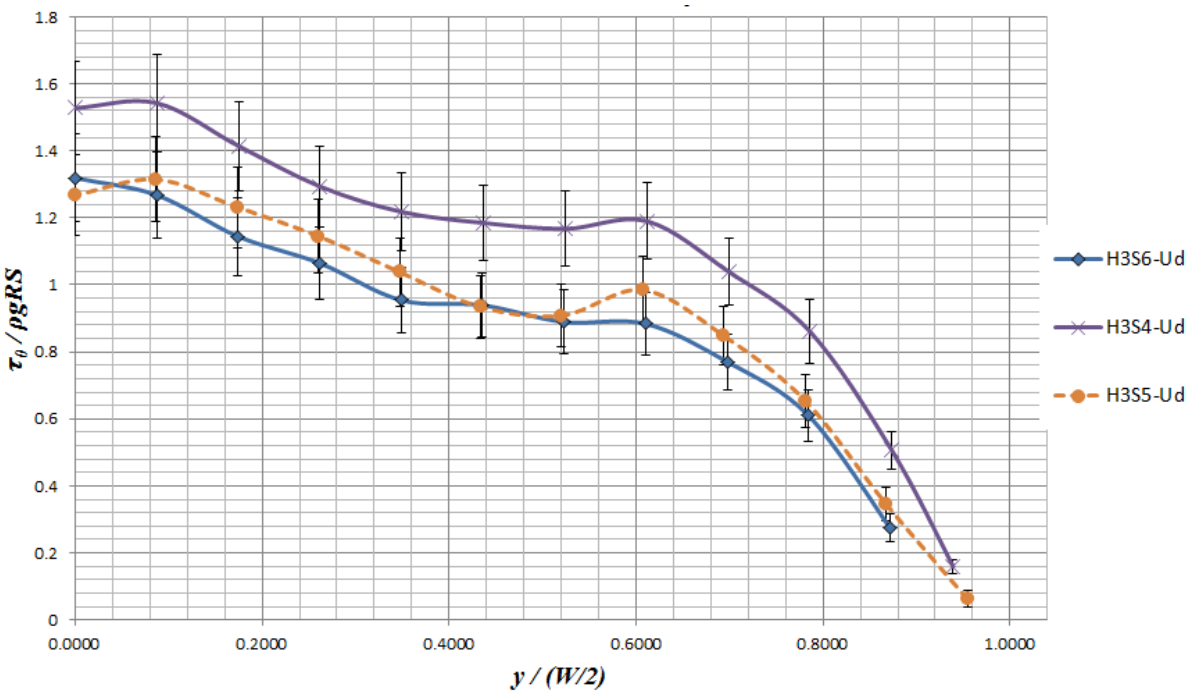

Figure 92. Dimensionless boundary shear stress distribution of the H3 experiments carried out on rough surface (d_{50}=1.46mm). Three sets are shown along with their uncertainty bars. It can be observed that the series H3S5 and H3S6 are following the same pattern, while only one third of H2S4 falls within the limits of the other two sets.

5.4 Main findings

After the uncertainty analysis carried out for discharge, velocity and shear stress, it is possible to say that are acceptable. They constitute an important piece of data that will allow modellers to calibrate their numerical models.

In general, with respect to the isovelocity curves, depth average velocity and shear stress profiles, similar patterns were found among the runs with equal depth and boundary condition. Specifically about the isovels, kinks were easily spotted, relating them to the presence of the secondary flow cells, in agreement with the observation of Tominaga et al (1989) and Wang and Cheng (2005). More kinks were found on rough surface experiments and on higher depths sets, implying more activity of secondary flow.

In order to analyse the isovelocity contours, depth average velocity profiles were produced. The previous observations were validated, finding inflection points on the curves, that are associated with the divide between secondary flow cells. However, it was not possible to observe such patterns in the shear stress profiles, due to the nature of the Preston tube.

The shape of the velocity and shear stress profiles are constants per channel geometry, without being affected by the slope. This confirms the observations on the numerical model simulations (table 6, section 3.4.2.2), whom states that the slope does not modify the ratio between bankside width, T, and central depth, hc.

CHAPTER 6

CALIBRATION AND VALIDATION OF THE NUMERICAL MODEL

6.1 Introduction

The current section presents the calibration process carried out for the quasi 2D flow model chosen, *i.e.* the SKM (Shiono and Knight, 1990), with an experimental cross section, representing a self-formed channel. By this, the ability of the numerical model to predict the water capacity of such geometries is explored. The behaviour of the flow in such geometries is particularly important due to it determines the stable cross section to be formed by the stream.

It should be noted that one of the advantages of the selected flow model (SKM) is its flexibility, permitting adjustments in: geometry, slope, S, lateral variation of the friction factor, f, and transversal flow (that is, the secondary flow gradient, Γ, and eddy viscosity, λ. Hence, it is feasible to reproduce numerically the results obtained from the physical experiment. The information related to the lab work is shown in chapters 5**.**

So far, there is a good understanding in predicting the flow lateral distribution for rectangular and trapezoidal cross sections(e.g. Knight, 2006), incorporating even the transversal flow. However the flow behaviour in self-formed stable geometries remains unclear, specifically the secondary flow terms (Γ and λ in the case of the

SKM). With respect to the geometry of the mentioned sections, many authors have noticed that the shape is quasi-parabolic(e.g. Ikeda, 1981, Macky, 1999, Stebbings, 1963, Babaeyan-Koopaei, 1997 , Diplas, 1990), being the side slope, next to the margin, equivalent to the angle of repose of the bed material. Hence, it is not a coincidence that some authors originally tried to represent natural sections as trapezoidal ones.

The calibration strategy consisted of proposing values for f based on the experiments, and λ from the method of Lundgren and Jonsson (1964), which depends on the section geometry only. Hence, Γ was the only unknown variable, being possible to identify it by calibrating each experiment. The following sections describe the methodology carried out for f, λ and Γ.

6.2 Friction factor

6.2.1 Determination of the friction factor for smooth surface

The friction factor, f, can be calculated from the lab work, by combining the depth average velocity, U_d, and the boundary shear stress, $\tau_0 = \rho f U_d^2/8$. This was achieved for each experiment on PVC surface, obtaining the lateral variation of f. Once it was known, the numerical model was feed with such results. But since the employed numerical model uses the SKM analytical solution, dividing the section in 6 panels, it was required to calculate an f average for each segment. The results for each case are shown in figures 93to 101, where the main values along the average can be observed. It should be noted that the dashed lines connecting the f values are

only showing the tendency. With respect to the panel next to the margin, only one point was considered, being the smaller one, due to it behaved better.

By analysing the figures with f results, it is observed that smaller values are obtained next to the centreline (y=0), increasing while are approaching to the margin, yielding a parabolic shape. This is in agreement with the general assumption that a small depth implies a high flow restriction due to the bed surface, and vice versa. It was noticed that the f values at centreline were close to the ones obtained from the stage discharge curves, varying with each longitudinal slope, S, as tables 11 to 16 are showing (section 5.1)

Due to f was determined from measurements, it was required to run a uncertainty analysis in order to assess the confidence of the results. The variables implied were U_d and τ_0, with their corresponding uncertainties ΔU_d a $\Delta\tau_0$, whom were obtained on sections 5.2.1 and 5.3.1 (equations 74 and 90). The uncertainty of f, Δf, is defined as:

$$\Delta f = \frac{8\tau_0}{\rho U_d^2}\left[\frac{\Delta\tau_0}{\tau_0} + 2\frac{\Delta U_d}{U_d}\right] \tag{94}$$

It was noted the great difference among uncertainties, being significant for some experiments, *e.g.* H1S1 (figure93), H1S2 (figure 96), and minimum for others, *i.e.* H1S3 (figure 99), H2S3 (figure 100) and H3S3 (figure 101). This can be explained due to small pressure differences produce high uncertainties, and in the case of S1 and S2 set of experiments, the flow pressures were smaller due to the flow velocity was small, yielding an small pressure difference. The pressure was measured by a manometer, and when the difference was small between the constant

and dynamic heads, the systematic errors meant an important percentage of the collected data, and subsequently a high uncertainty was produced.

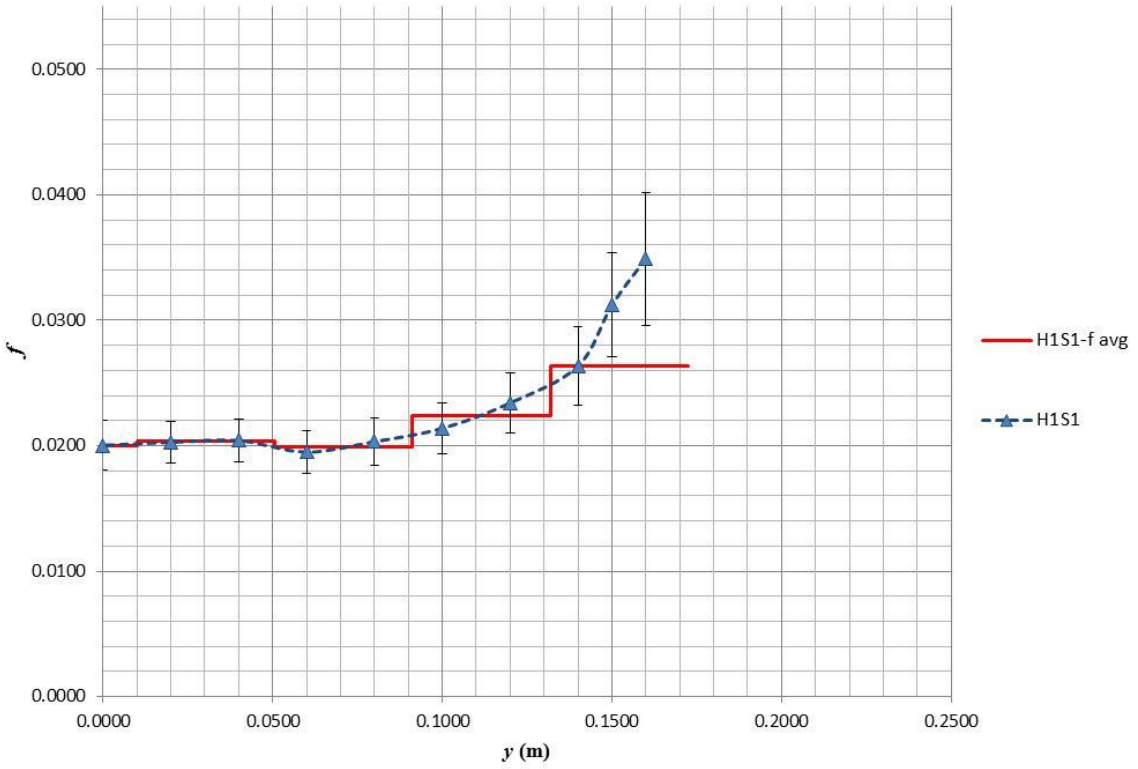

Figure 93. Friction factor, *f*, of the run H1S1. Two series are presented: H1S1 that was obtained based on velocity and boundary shear stress measurements (error bars are shown); and H1S1-favg that is the average value considered for calibration. This last was divided in five segments, corresponding to the SKM panels.

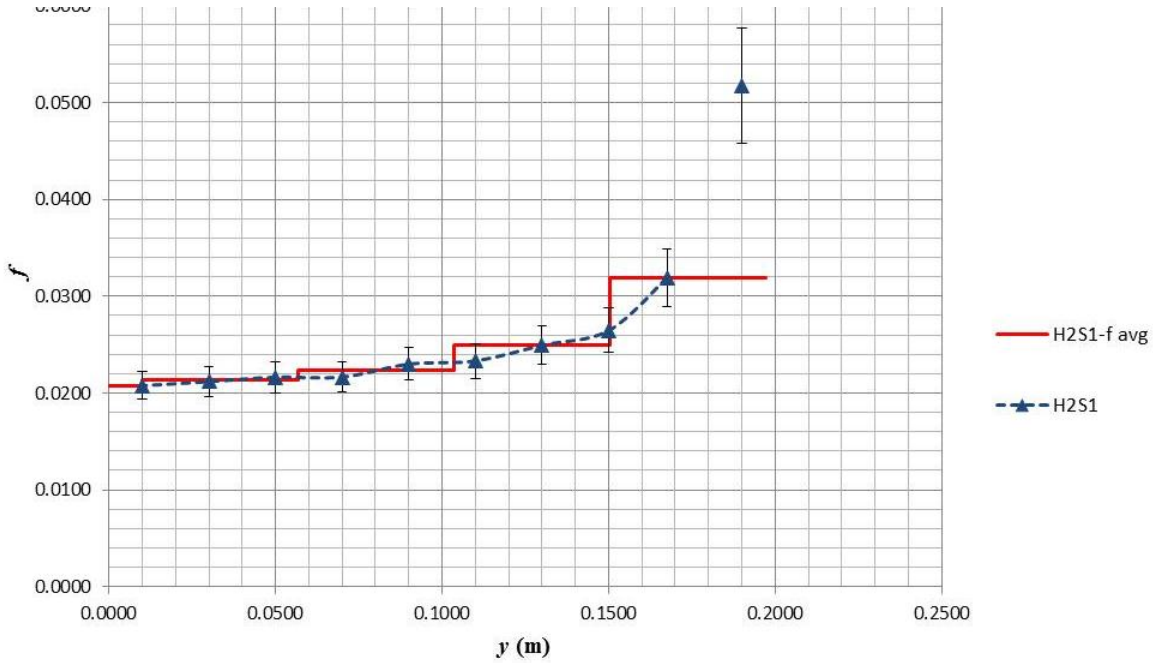

Figure 94. Friction factor, *f*, of the run H2S1. Two series are presented: H2S1 that was obtained based on velocity and boundary shear stress measurements (error bars are shown); and H2S1-favg that is the average value considered for calibration. This last was divided in five segments, corresponding to the SKM panels.

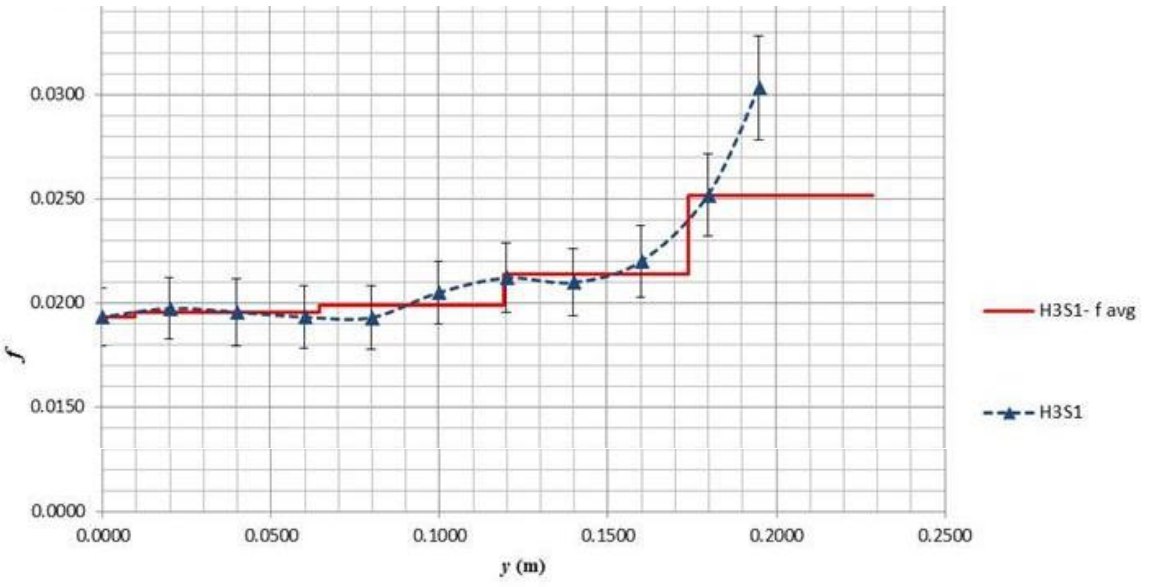

Figure 95. Friction factor, *f*, of the run H3S1. Two series are presented: H3S1 that was obtained based on velocity and boundary shear stress measurements (error bars are shown); and H3S1-favg that is the average value considered for calibration. This last was divided in five segments, corresponding to the SKM panels.

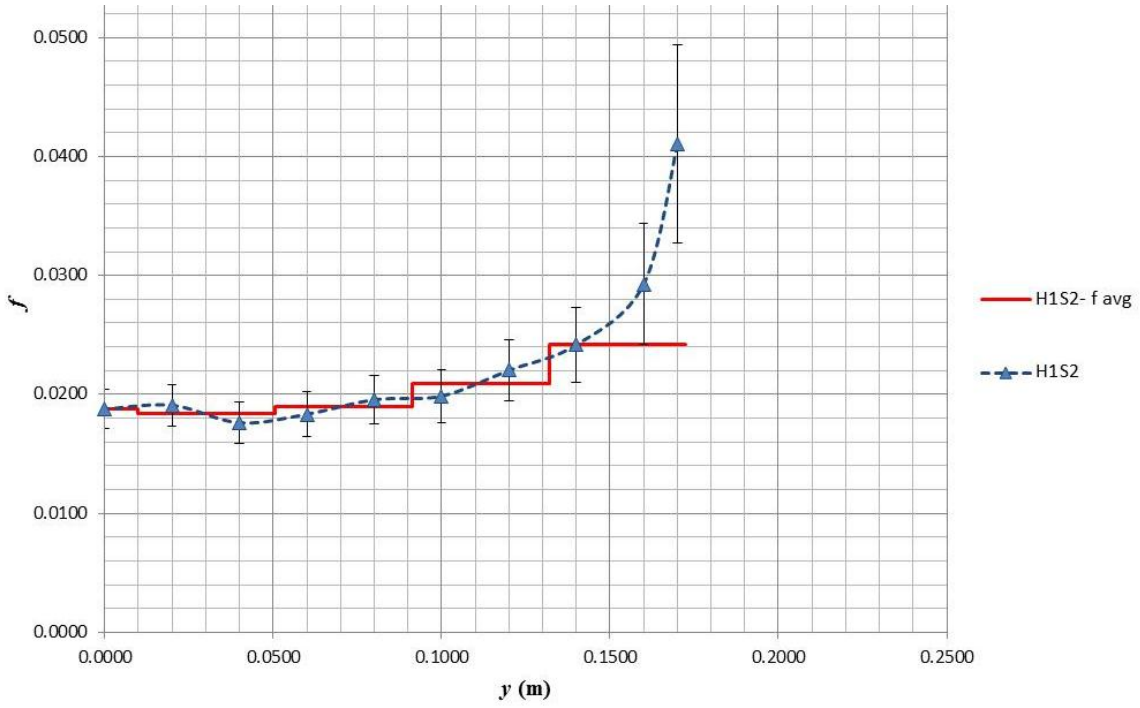

Figure 96. Friction factor, *f*, of the run H1S2. Two series are presented: H1S2 that was obtained based on velocity and boundary shear stress measurements (error bars are shown); and H1S2-favg that is the average value considered for calibration. This last was divided in five segments, corresponding to the SKM panels.

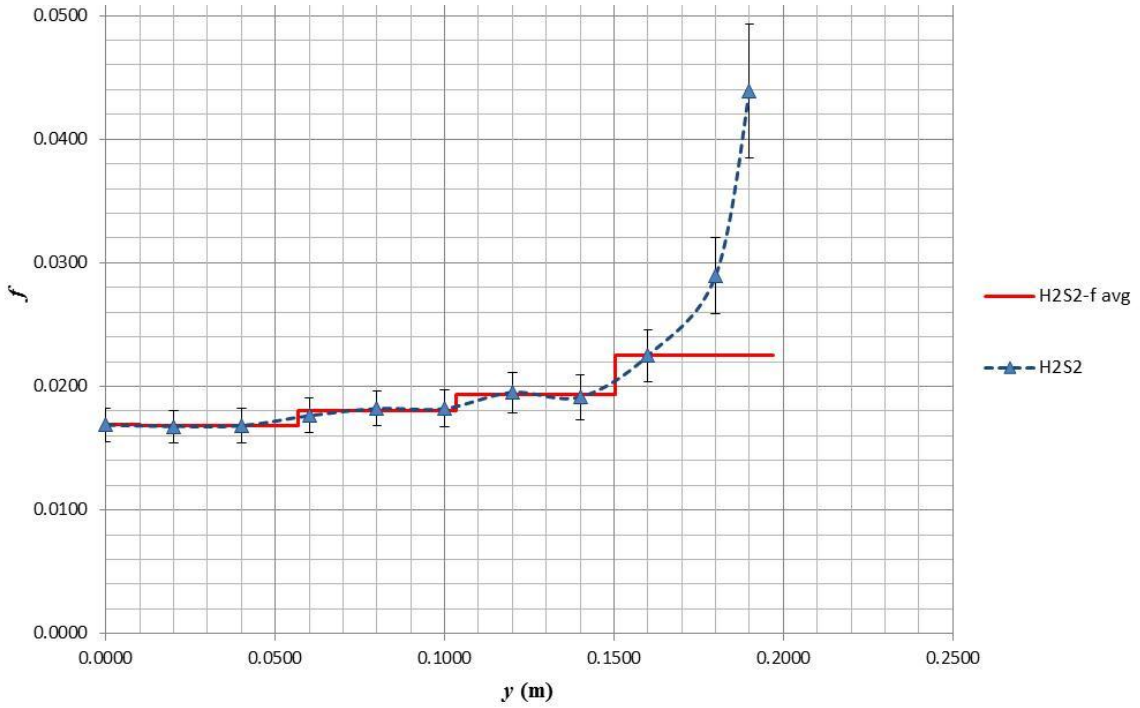

Figure 97. Friction factor, *f*, of the run H2S2. Two series are presented: H2S2 that was obtained based on velocity and boundary shear stress measurements (error bars are shown); and H2S2-favg that is the average value considered for calibration. This last was divided in five segments, corresponding to the SKM panels.

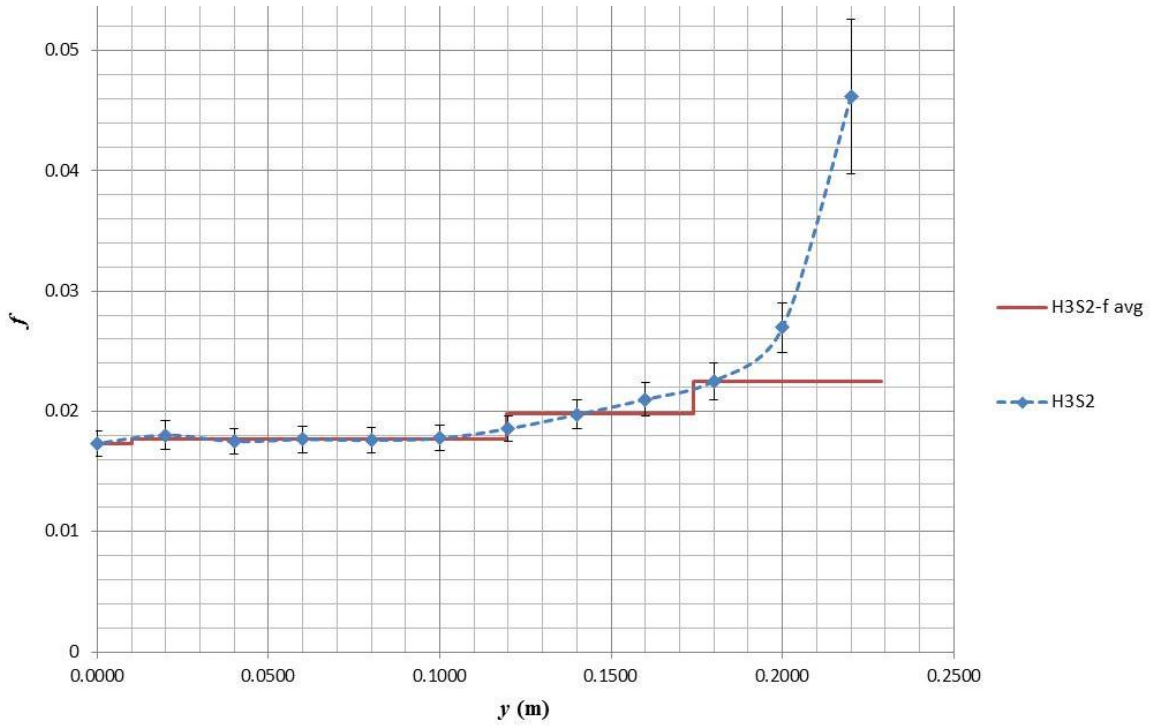

Figure 98. Friction factor, *f*, of the run H3S2. Two series are presented: H3S2 that was obtained based on velocity and boundary shear stress measurements (error bars are shown); and H3S2-favg that is the average value considered for calibration. This last was divided in five segments, corresponding to the SKM panels.

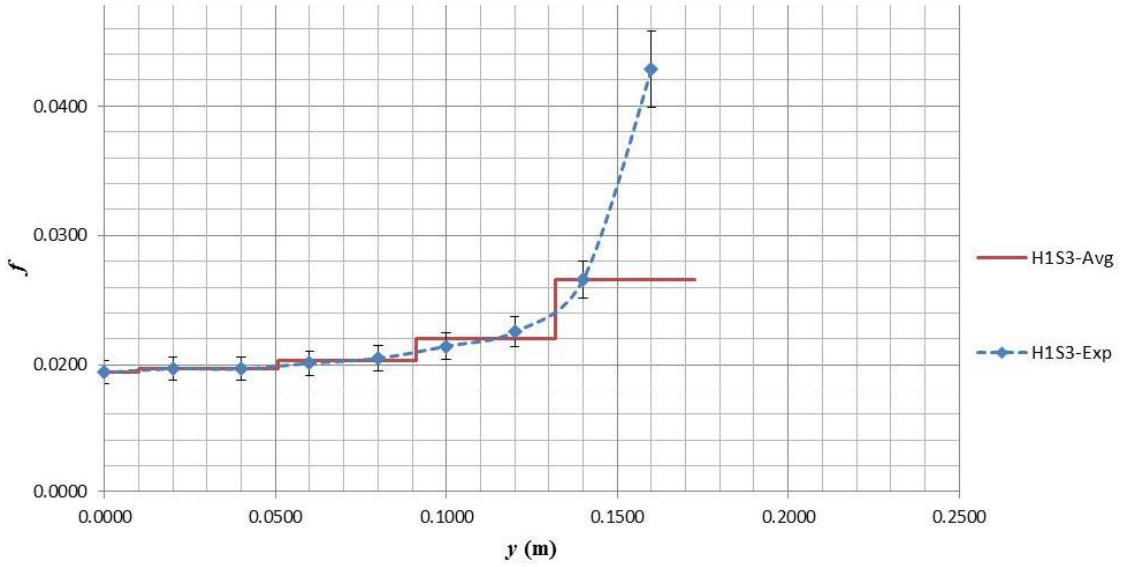

Figure 99. Friction factor, *f*, of the run H1S3. Two series are presented: H1S3 that was obtained based on velocity and boundary shear stress measurements (error bars are shown); and H1S3-favg that is the average value considered for calibration. This last was divided in five segments, corresponding to the SKM panels.

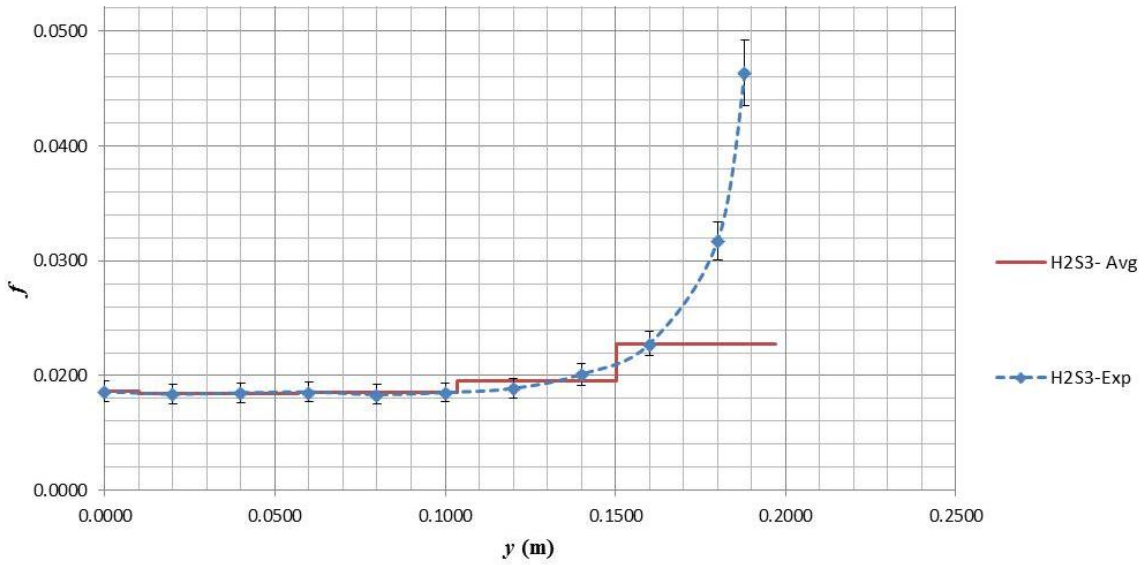

Figure 100. Friction factor, *f*, of the run H2S3. Two series are presented: H2S3 that was obtained based on velocity and boundary shear stress measurements (error bars are shown); and H2S3-favg that is the average value considered for calibration. This last was divided in five segments, corresponding to the SKM panels.

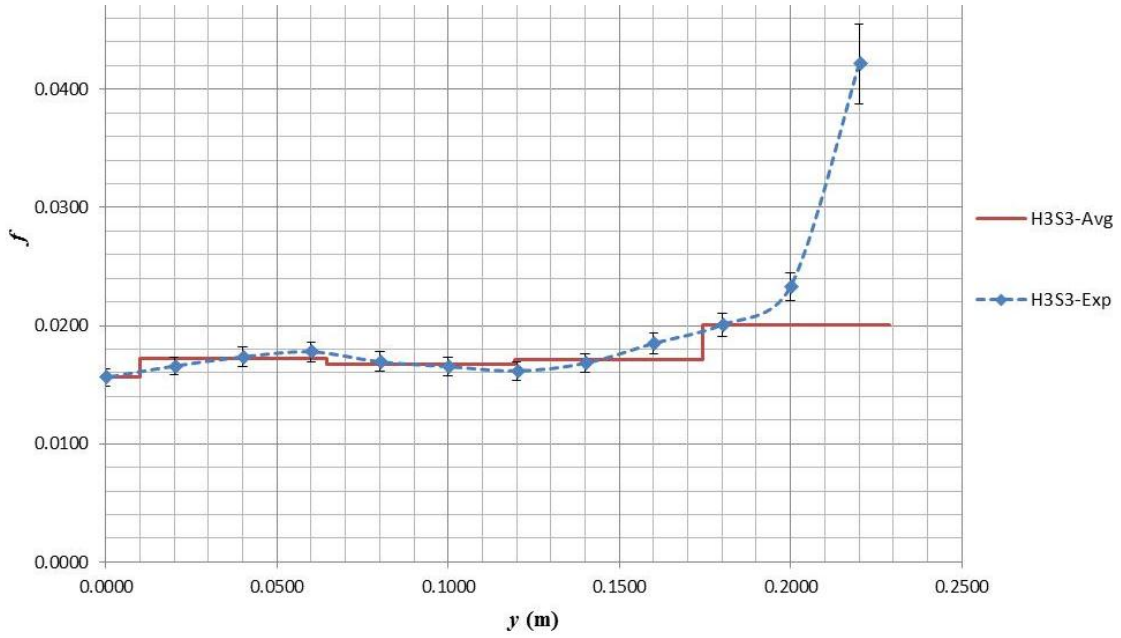

Figure 101. Friction factor, *f*, of the run H3S3. Two series are presented: H3S3 that was obtained based on velocity and boundary shear stress measurements (error bars are shown); and H3S3-favg that is the average value considered for calibration. This last was divided in five segments, corresponding to the SKM panels.

6.2.2 Determination of the friction factor for rough surface

With respect to the calibration of the glue sand experiments, it was not possible to obtain the friction factor based on measurements. This because the boundary shear stress,τ_0, was not taken, due to the Preston tube technique, same that was used for PVC, is not valid for rough surface (*e.g.* Barlow et al., 1999). Hence, an ingenious methodology was proposed. It was found by observing the behaviour of the lateral variation of the friction factor (figures 93 to 101).

As was mention on section 6.2.1, the distribution of f was parabolic, and it was noticed that the values were close for similar depths, *e,g,* H1S1, H1S2 and H1S3 (figures93, 96 and 99). Then, the next step was to compare the f curves having common depths (figures 102, 105 and 108). From such contrapositions, it was observed that f values were in the same order of magnitude, changing with the depth and slope. However, the parabolic shape was kept, identifying a pattern. Hence it was suggested to divide each curve by its central friction value, f_c, in the vertical, and by half width on the horizontal, $W/2$, comparing them (figures 103, 106 and 109). The graphs presented a remarkable coincidence, especially for small depths (H1, figure 103), subsequently an uncertainty analysis was carried out, being the curves within the limits.

In order to explain the similar pattern followed by the behaviour of f/f_c, the depth average velocity, U_d, and boundary shear stress, τ_0, distributions were plotted dimensionless, *i.e*. U_d divided by the average velocity measured by a Pitot tube, V_{Pitot}, τ_0 by the average shear stress, ρgRS, along with their corresponding uncertainty

analysis, and finally the horizontal, y, by half width, $W/2$. The velocity comparisons are shown in figures 78, 81 and 84, and the shear stress ones in figures 87, 88 and 89. With respect to U_d/V_{Pitot}, the curves are in agreement, particularly those of H1 (figure 78), being slightly wider in H2 and H3 (figures 81 and 84), but within the uncertainty limits. This was explained in chapter 3, where it was found that the shape of the lateral U_d distribution is constant, and independent of the slope, and demonstrated here.

On the other hand, the $\tau_0/\rho gRS$ curves present higher irregularities, being most of them in agreement and satisfying the uncertainty, except for H1S2 and H2S2 (figures 87 and 88). Then, it was recommended to remove such experiments from the calibration process. This pattern can be explained due to τ_0 is directly proportional to U_d, and both lateral variation shapes are non-related to the longitudinal slope, S. Hence, it is expected a narrow lateral distribution for f curves, which are affected by S but its influence reduced when f is affected by f_c, yielding compact curves (figures 103, 106 and 109).

Once the relationship f/f_c was accepted as constant for each depth of the experiments, a best fit polynomial equation was obtained of the type $f/f_c = g\left(y/(W/2)\right)$ (figures 104, 107 and 110). As mentioned above, f_c was taken from the friction factor obtained from the stage discharge curves previously done (section 5.1), and $W/2$ was already given for each cross section. Then, the rough surface experiments considered the lateral distribution of f during the calibration process.

Table 27. Summary of the values of f found during the calibration per experiment, and per panel.

1	2	3	9	10	11	12	13
			f				
	Material	**Exp.**	**P1 and P2**	**P3**	**P4**	**P5**	**P6**
H1	PVC	h1s3	0.0194	0.0197	0.0203	0.0220	0.0266
	PVC	h1s1	0.0200	0.0203	0.0199	0.0224	0.0263
	Glue Sand	h1s4	0.0628	0.0617	0.0628	0.0696	0.0764
	Glue Sand	h1s6	0.0567	0.0557	0.0567	0.0629	0.0690
	Glue Sand	h1s5	0.0601	0.0591	0.0601	0.0667	0.0731
	PVC	h1s2	0.0188	0.0184	0.0190	0.0210	0.0242
H2	Glue Sand	h2s4	0.0529	0.0538	0.0559	0.0602	0.0647
	Glue Sand	h2s6	0.0490	0.0498	0.0517	0.0558	0.0599
	Glue Sand	h2s5	0.0519	0.0528	0.0548	0.0591	0.0635
	PVC	h2s3	0.0186	0.0185	0.0185	0.0195	0.0228
	PVC	h2s1	0.0208	0.0214	0.0223	0.0249	0.0319
	PVC	h2s2	0.0169	0.0168	0.0180	0.0193	0.0225
H3	Glue Sand	h3s5	0.0472	0.0494	0.0490	0.0539	0.0581
	Glue Sand	h3s6	0.0447	0.0467	0.0464	0.0510	0.0550
	PVC	h3s2	0.0173	0.0177	0.0177	0.0198	0.0225
	Glue Sand	h3s4	0.0484	0.0506	0.0502	0.0553	0.0596
	PVC	h3s3	0.0156	0.0172	0.0167	0.0172	0.0201
	PVC	h3s1	0.0193	0.0196	0.0199	0.0214	0.0252

6.3 H1 experiments

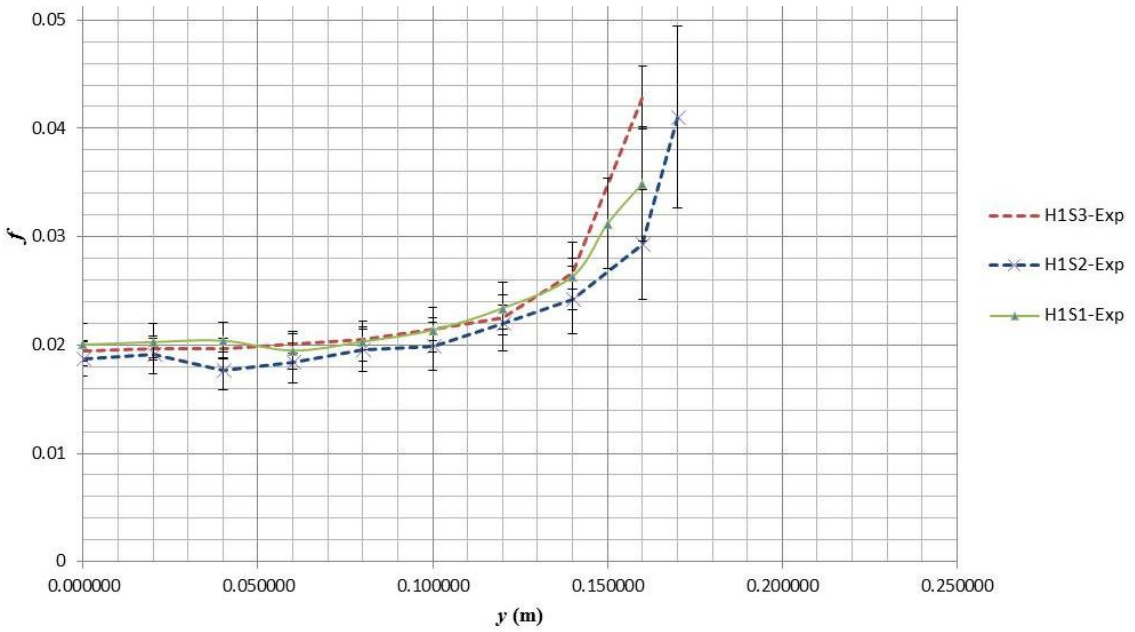

Figure 102.Variation of the friction factor, f, along half cross section of the H1 experiments (*i.e.*h_c≈3.5cm).Three series are presented, with their error bars, corresponding to the three slopes employed ($S1$=0.001485, $S2$=0.001725 and $S3$=0.005044).

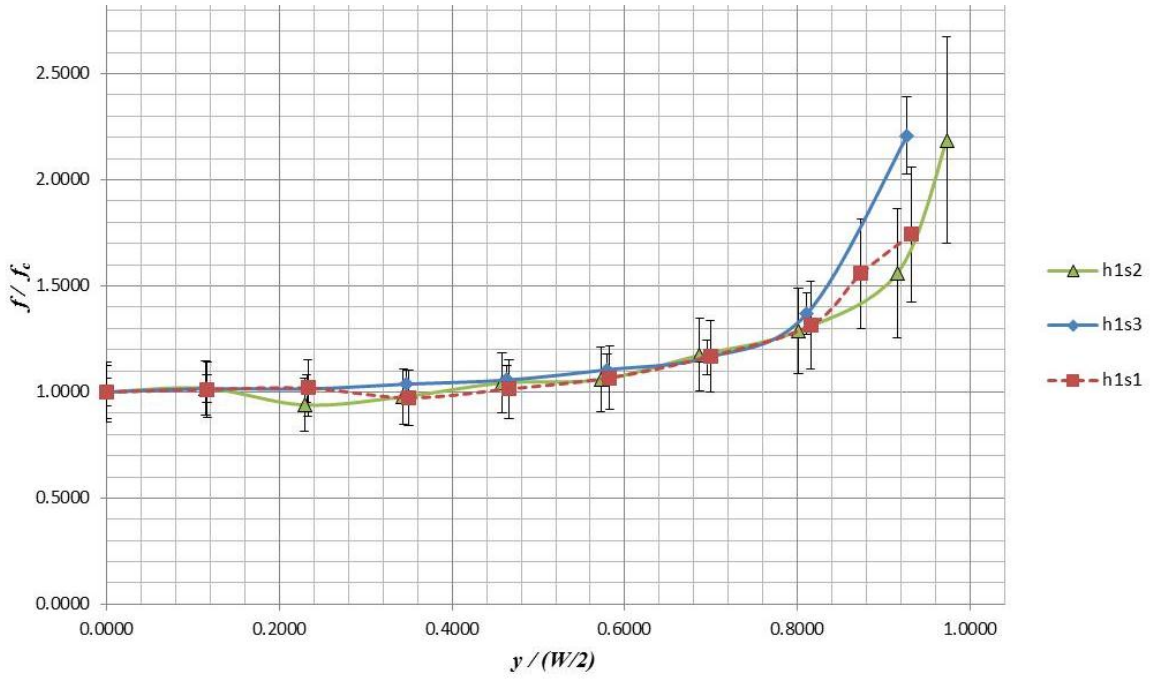

Figure 103. Friction factor variation of the H1 experiments (*i.e.*h_c≈3.5cm) with respect to the central friction value, f_c, along half dimensionless cross section, $y/(w/2)$. Three series are presented, with their error bars, corresponding to the three slopes employed ($S1$=0.001485, $S2$=0.001725 and $S3$=0.005044).

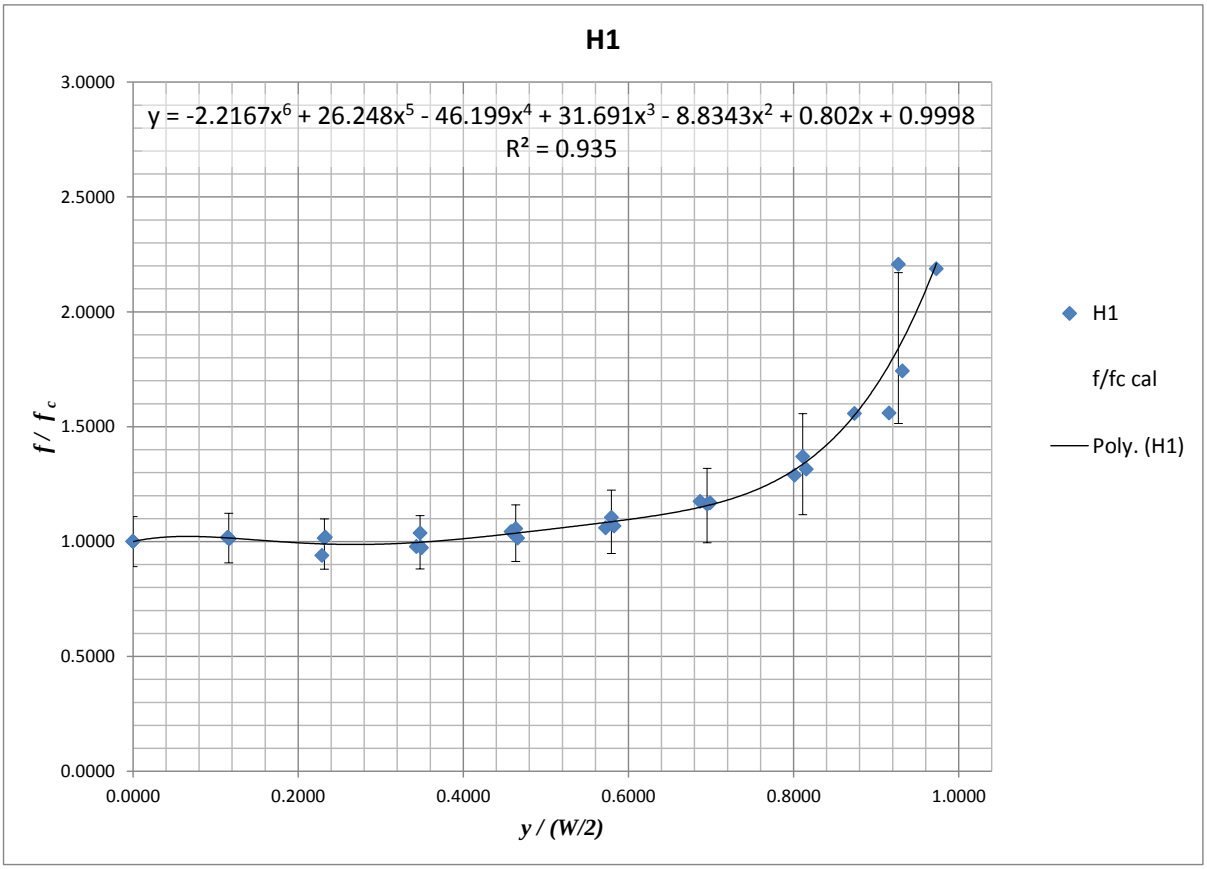

Figure 104. B**est fit polynomial equation corresponding to the variation of the friction factor, f, with respect to the central value, f_c, for H1 experiments (*i.e.* H1S1, H1S2, H1S3, with h_c≈3.5cm). The uncertainty bars are showing that most of the points are within the limits.**

6.4 H2 experiments

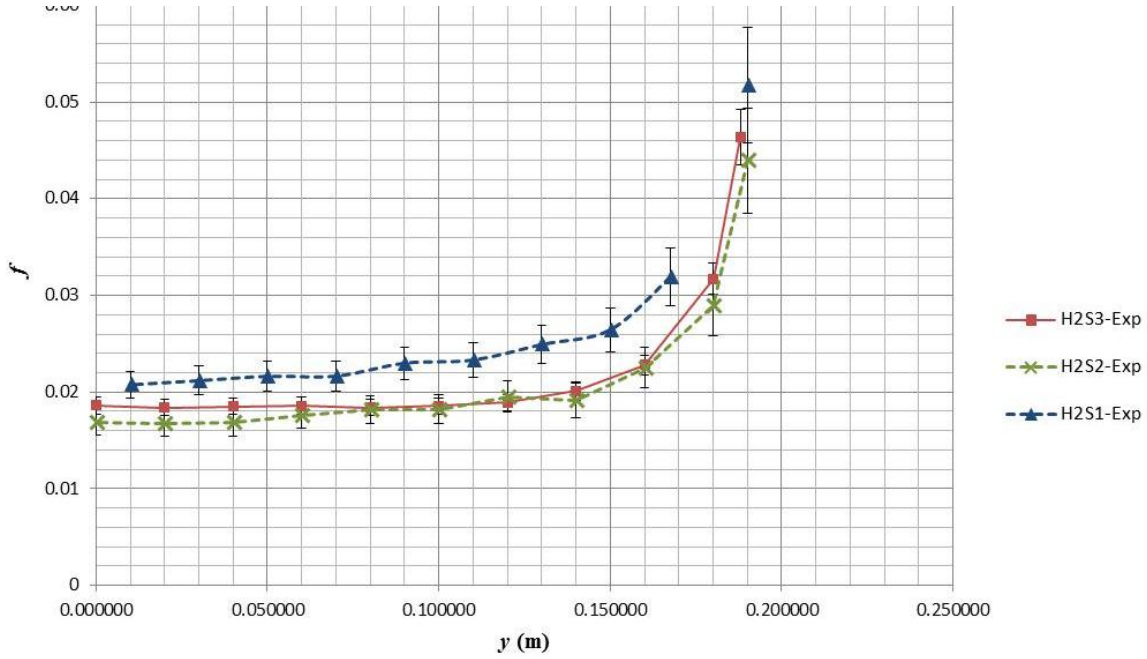

Figure 105. Variation of the friction factor, *f*, along half cross section of the H2 experiments (*i.e.*h_c≈5.0cm). Three series are presented, with their error bars, corresponding to the three slopes employed (*S1*=0.001485, *S2*=0.001725 and *S3*=0.005044)

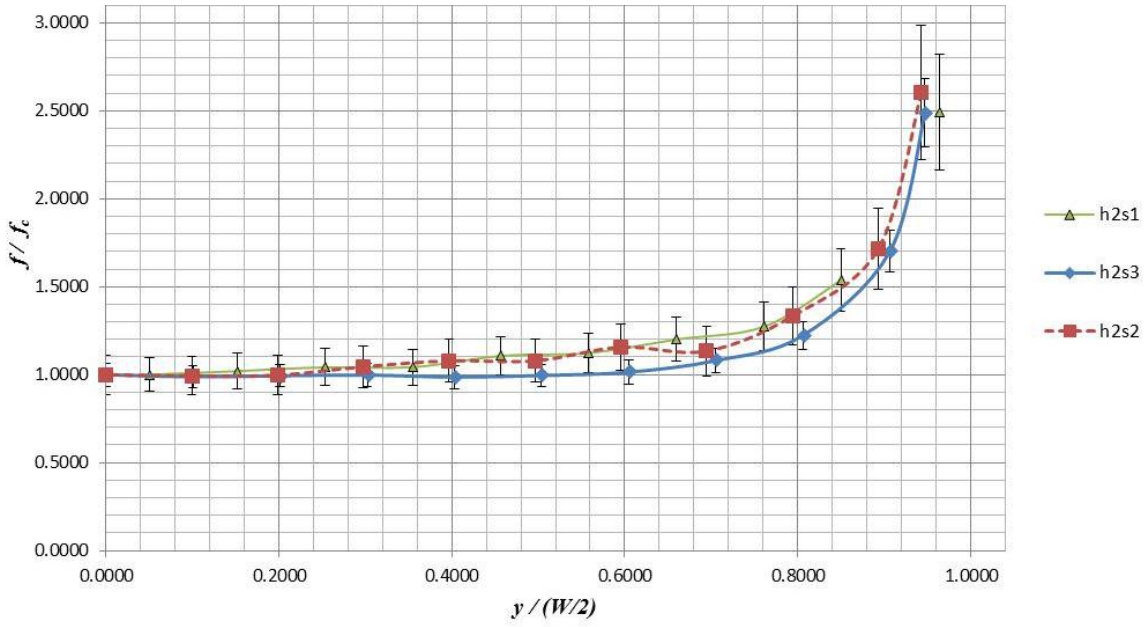

Figure 106. Friction factor variation of the H2 experiments (*i.e.*h_c≈5.0cm) with respect to the central friction value, f_c, along half dimensionless cross section, *y/(w/2)*. Three series are presented, with their error bars, corresponding to the three slopes employed (*S1*=0.001485, *S2*=0.001725 and *S3*=0.005044).

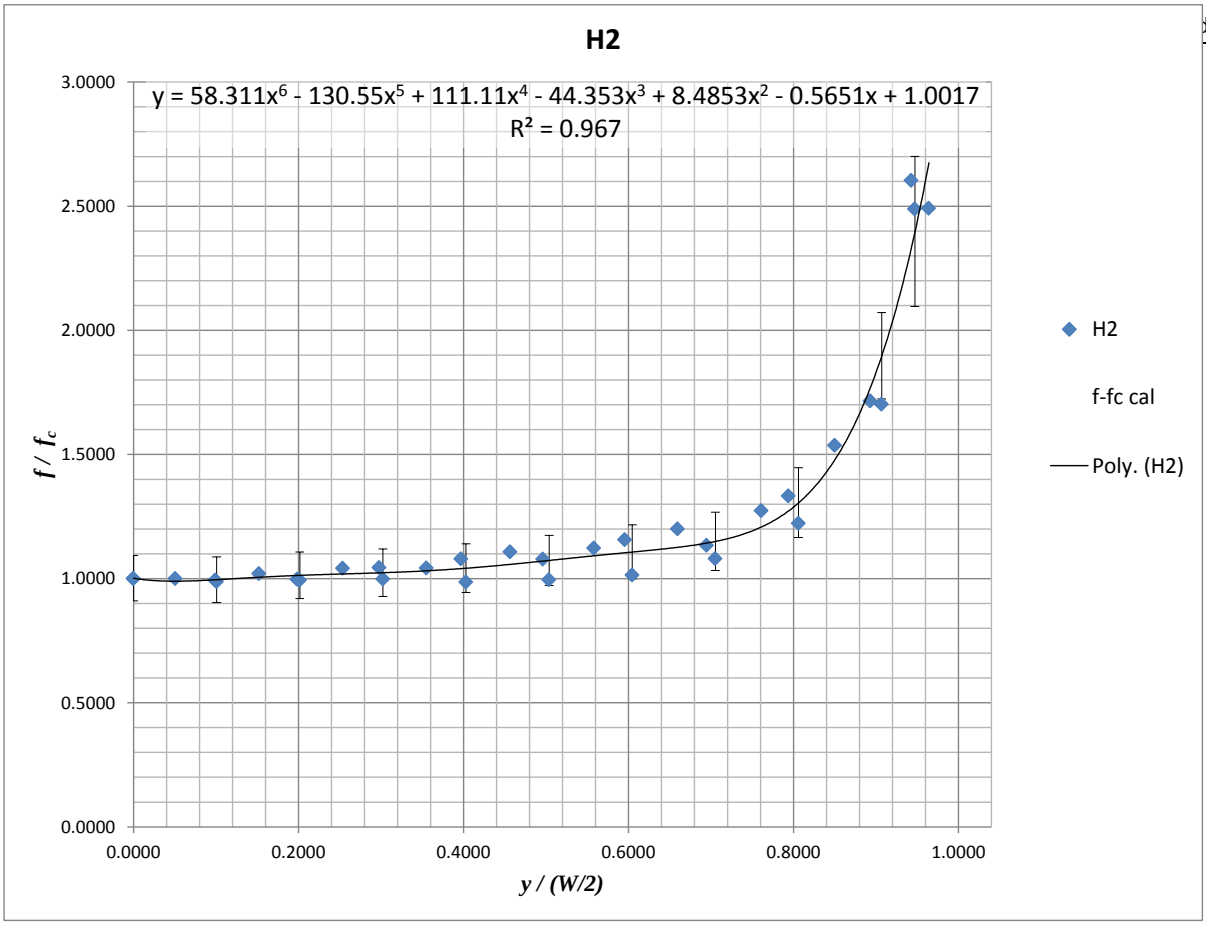

Figure 107.Best fit polynomial equation corresponding to the variation of the friction factor, f, with respect to the central value, f_c, for H2 experiments (*i.e.* H2S1, H2S2, H2S3, with h_c≈5.0cm). The uncertainty bars are showing that most of the points are within the limits.

6.5 H3 experiments

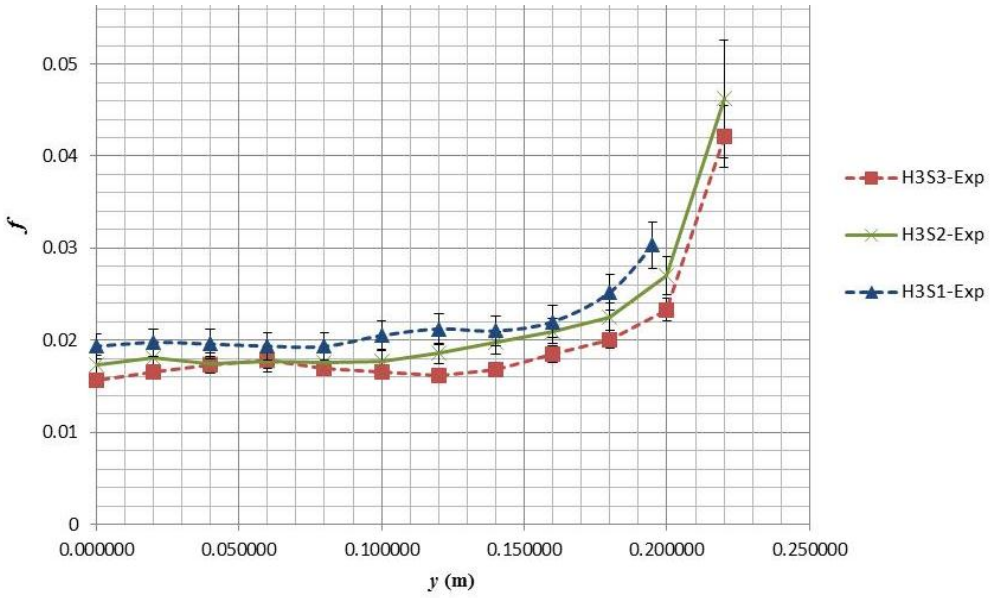

Figure 108.Variation of the friction factor, *f*, along half cross section of the H3 experiments (*i.e.*h_c≈7.00cm). Three series are presented, with their error bars, corresponding to the three slopes employed (*S1*=0.001485, *S2*=0.001725 and *S3*=0.005044)

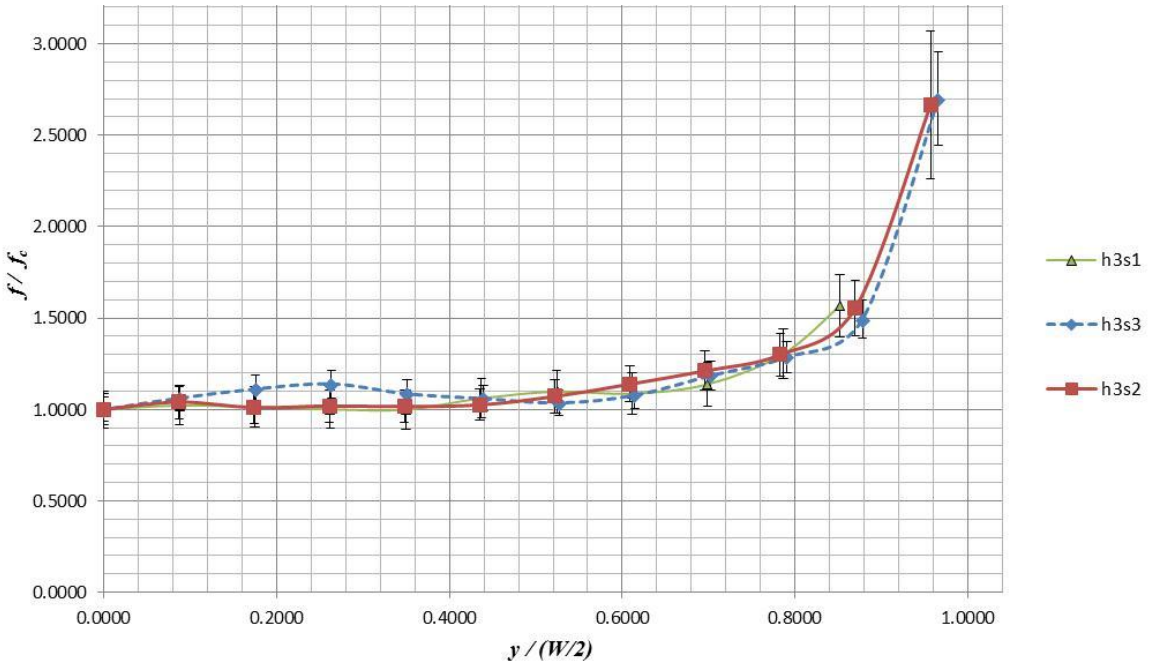

Figure 109. Friction factor variation of the H3 experiments (*i.e.*h_c≈7.0cm) with respect to the central friction value, f_c, along half dimensionless cross section, *y/(w/2)*. Three series are presented, with their error bars, corresponding to the three slopes employed (*S1*=0.001485, *S2*=0.001725 and *S3*=0.005044).

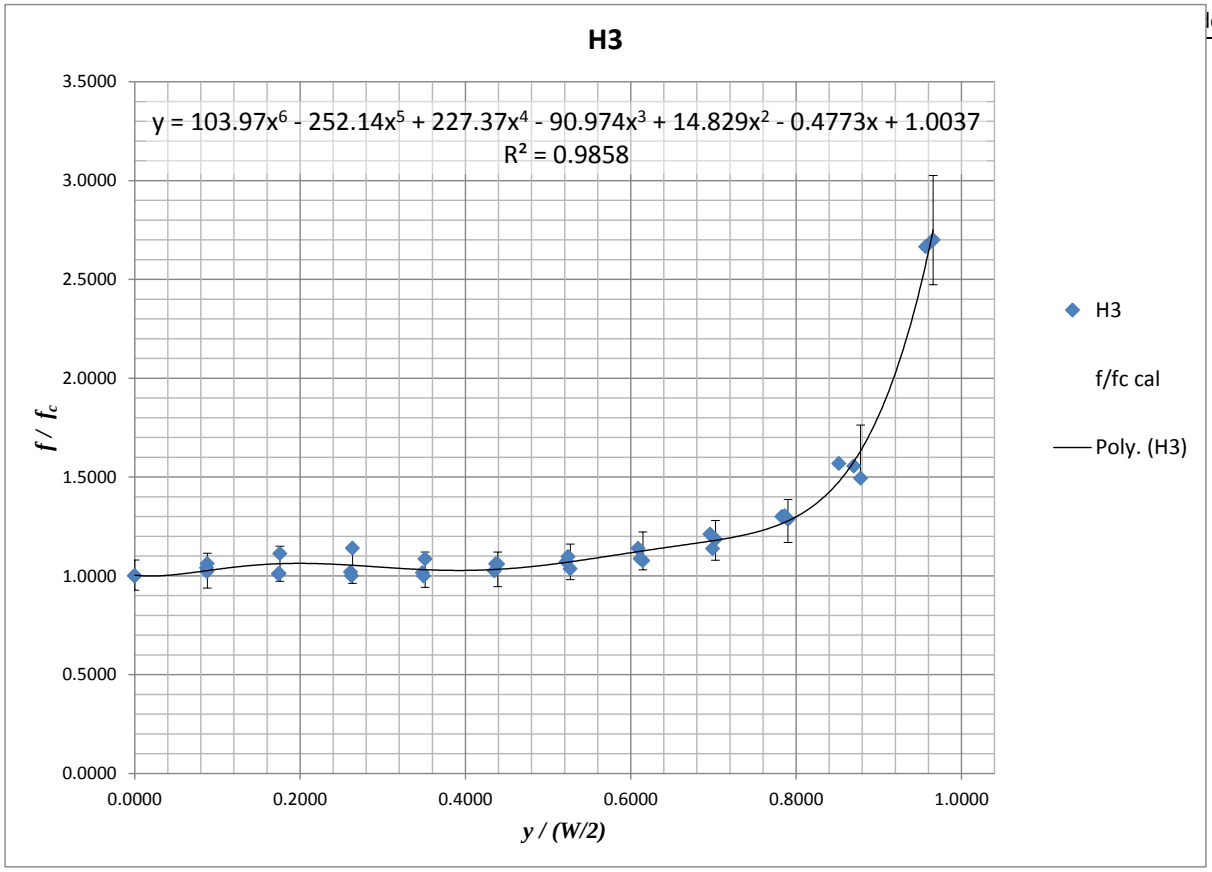

Figure 110.Best fit polynomial equation corresponding to the variation of the friction factor, f, with respect to the central value, f_c, for H3 experiments (*i.e.* H3S1, H3S2, H3S3, with h_c≈7.0cm). The uncertainty bars are showing that most of the points are within the limits.

6.6 Determination of λ

In order to determine the dimensionless eddy viscosity, λ, to be used by the numerical model for a self-formed cross section, it was proposed to use a methodology first used by Lundgren and Jonsson (1964). The approach consisted of relating λ completely to the geometry of the section, being this an advantage due to the difficulty to measure the depth average eddy viscosity, $\overline{\varepsilon_{yx}}$. It should be noted that the method was developed for curve shapes. The definition of λ is expressed as:

$$\lambda = \frac{\overline{\varepsilon_{yx}}}{U_* h} \tag{95}$$

where U_* is the shear friction velocity, and h the local depth.

Lundgren and Jonsson (1964) obtained the local eddy viscosity, ε_{yx}, based on U_*, the local curvature, c, the perpendicular depth, d, and the perpendicular distance with respect to the bottom, z':

$$\varepsilon_{yx} = 0.4U^* z\left(1-\frac{z'}{d}\right)\frac{\left(1-\frac{c}{2}(d+z')\right)}{\left(1-\frac{cd}{2}\right)(1-cz')} \tag{96}$$

$$U^* = \sqrt{\frac{\tau_0}{\rho}} \tag{97}$$

Since ε_{yx} was determined for each point within the cross section, an average was required in order to obtain λ with equation95. It was solved by integrating equation with respect to z':

$$\varepsilon_{yx\,Avg} = \frac{1}{d}\int_0^d \varepsilon_{yx}\, dz' \tag{98}$$

$$\varepsilon_{yx\,Avg} = \left(\frac{0.4U^*}{d}\right)\left(\frac{cd\left[cd\left(9-4cd\right)-6\right]-6\left(cd-1\right)^2\log\left(1-cd\right)}{6c^3d\left(cd-2\right)}\right) \tag{99}$$

$$\text{for}\quad \mathrm{Re}\left(\frac{1}{cd}\right)>1 \;\vee\; \mathrm{Re}\left(\frac{1}{cd}\right)<0 \;\vee\; \frac{1}{cd}\notin \mathbf{R}$$

The results are shown in figure 111. It is observed that the λ values of the three depths are in the same order of magnitude, increasing with depth. Due to the methodology is valid for curve shapes, λ was not calculated for $0 \leq y < 0.01$ and $0.20 < y < 0.23$, because such segments had none curvature ($c=0$). Subsequently a λ average was obtained for each type of section, shown in table 28, noticing that three of them are around 0.070. This is in agreement with other authors, *e.g*. Ikeda (1981),

Nezu and Nakagawa (1993). For practical reasons, λ was taken as 0.070 during the calibration, because it has been observed that the variation of λ has a minor impact on the SKM results (Knight *et al.*, 1996).

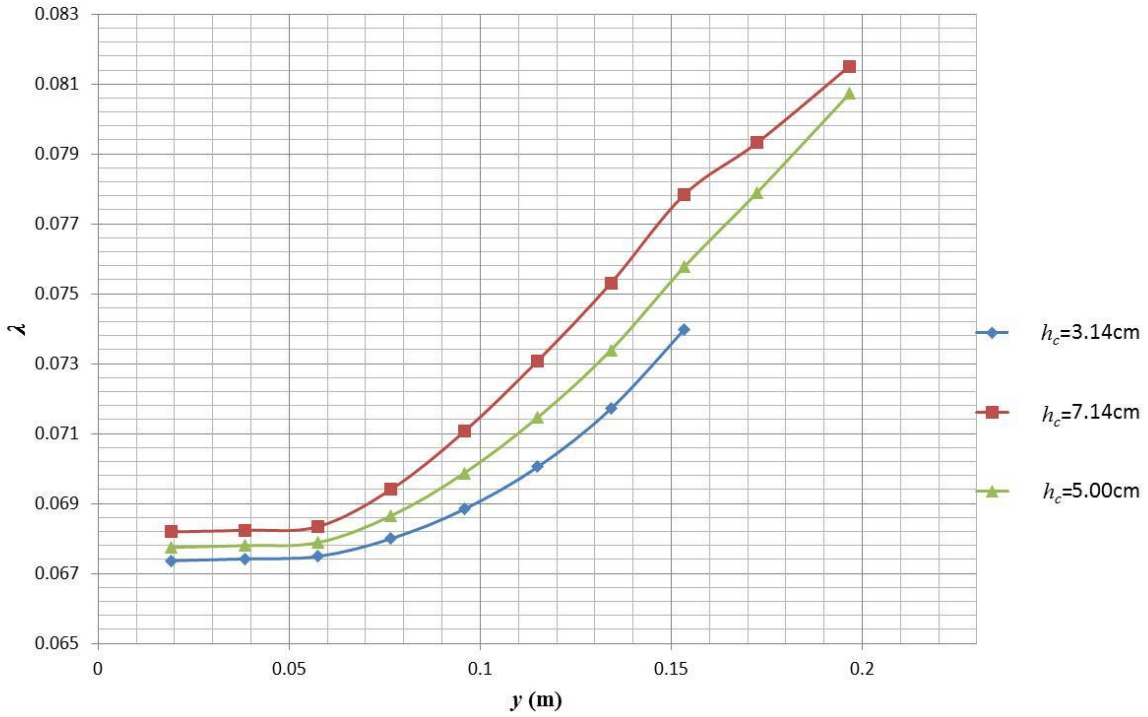

Figure 111. Variation of λ along half cross section obtained by Lundgren and Jonsson (1964)

Table 28. Average values obtained for each cross sectional geometry based on the results of figure 111.

h_c	$\lambda = \overline{\varepsilon_{yx}} / U * h$
3.14	0.06936
5.00	0.07212
7.14	0.07323

6.7 Γ calibration

Once f and λ were obtained, the only unknown variable was Γ. In order to determine it, a calibration process was required. It consisted of matching the numerical model with the experimental data, for depth average velocity, U_d, and boundary shear stress, τ_0, in the case of smooth surface (PVC), and only U_d for glue sand experiments (d_{50}=1.46mm). However, due to τ_0 can be calculated from U_d, τ_0 was considered as well for rough surface. The procedure evaluated different Γ values for the six different SKM panels, summing the differences between the calculated and the experimental results, Σ, choosing the Γ yielding the smaller sum. In order to give confidence to the calibration, an uncertainty analysis was run.

The calibrated results plotted along the physical data were attached in the Appendix C. On it, all the runs are found, for smooth and rough surface, for velocity and shear stress. A summary was plotted in this section, grouping them by depth and surface (figures 112 to 135, section 6.7.1). For comparison purposes the graphs were presented dimensionless, *i.e.* $U_d/(Q/A)$ and $\tau_0/\rho gRS$, where Q is the discharge of the corresponding run, that was measured by an electromagnetic flowmeter; A, the cross sectional area; and ρgRS, being the average shear stress. It is possible to say that all the calibrations reached an acceptable level, due to all the cases are falling within the uncertainty bars of the physical data.

6.7.1 Calibrated plots

The section is showing first the runs on smooth surface, starting with the H1 simulated data profiles, and subsequently graph showing both sets of data: calculated and physical data. Then, following the same logic the shear stress profiles for H1 are presented. Later, the same order for H2 runs is taken, and finally for H3. The process is repeated for rough surface experiments.

From the 18 sets of data calibrated (9 in PVC surface and 9 in glue sand surface), four of them seem to be out of the pattern. These are H1S2, failing on its τ_0 curve (figures 114 and 115); H1S4, on U_d and τ_0 (figures 79, 90 and 127); H2S2, on τ_0 (figures 118 and 119); and H3S4, on τ_0 as well (figure 92). Those calibrations were not taken into account for the conclusions, due to their inconsistency.

The steps that can be appreciated on the shear stress graphs correspond to the friction factor variation. This due to it is not changing smoothly, it is varying drastically at the SKM panels. However, the impact of f on U_d is not as dramatic.

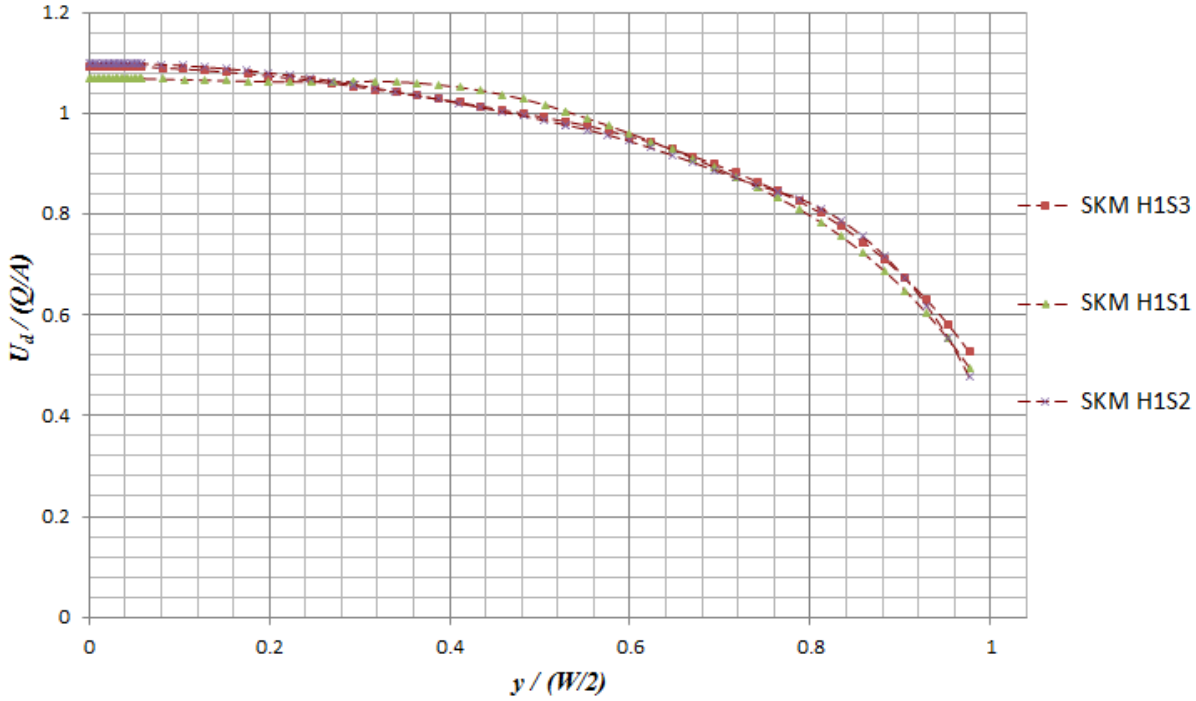

Figure 112. Dimensionless calibrated velocity distribution of the H1 experiments carried out on smooth surface (PVC). It can be observed that the series are following the same pattern with slightly variations.

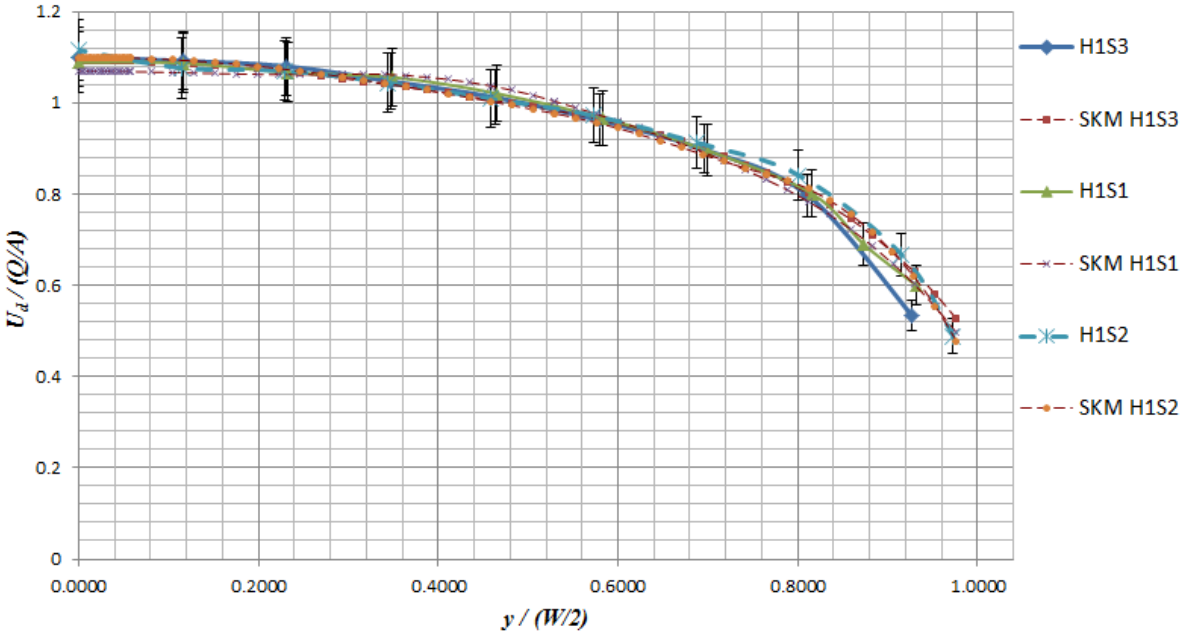

Figure 113. Dimensionless calibrated velocity distributions along the experimental data with their uncertainty bars, corresponding to the H1 sets on smooth surface (PVC). It can be observed that the calibrated simulations fall within the limits.

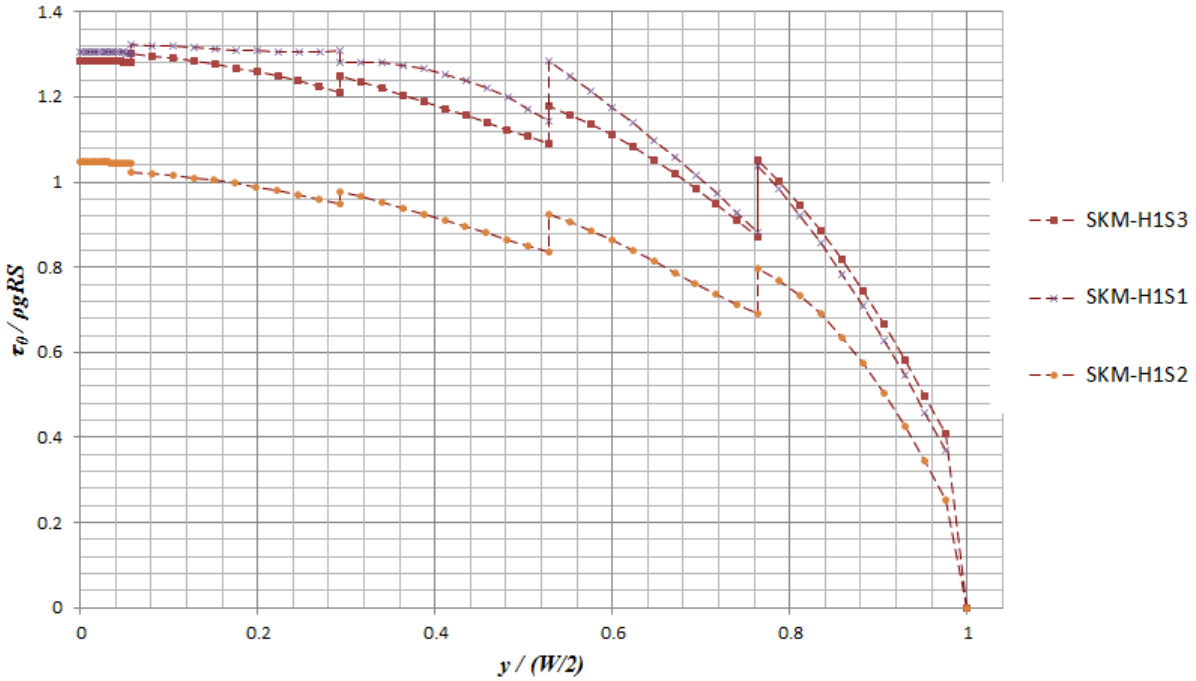

Figure 114. Dimensionless calibrated boundary shear stress distribution of the H1 experiments carried out on smooth surface (PVC). Two patterns can be observed, one for H1S3 and H1S1, and another one for H1S2.

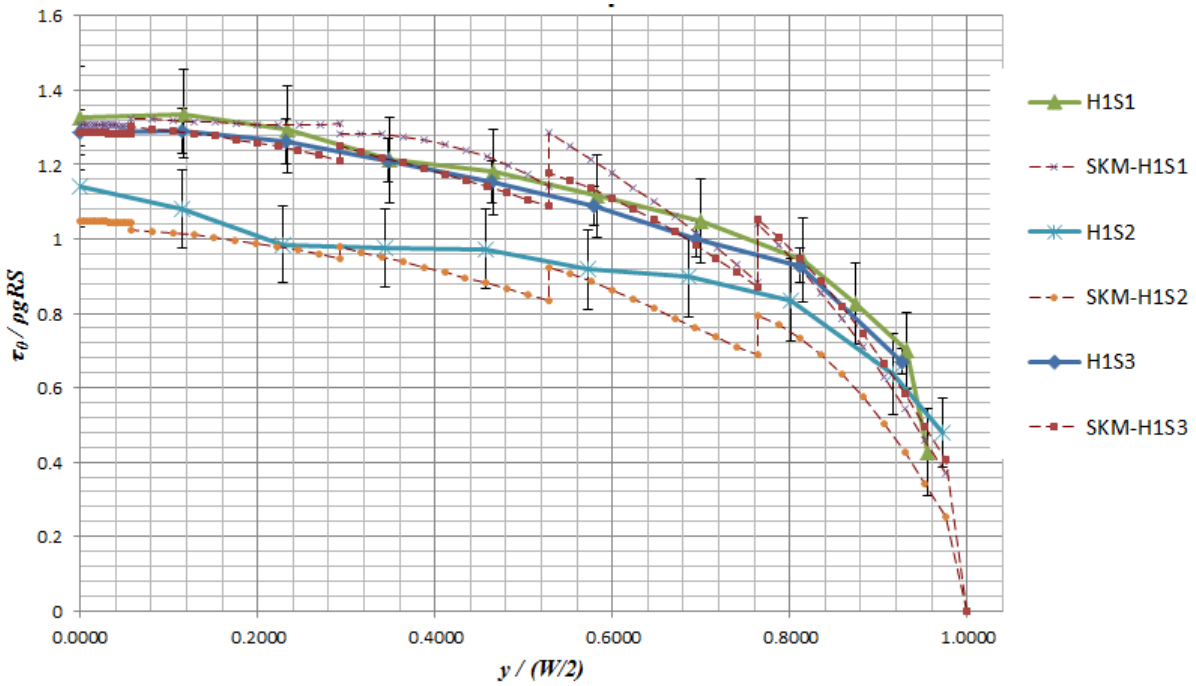

Figure 115. Dimensionless calibrated boundary shear stress distributions along the experimental data with their uncertainty bars, corresponding to the H1 sets on smooth surface (PVC). It can be observed that the calibrated simulations fall within the error limits.

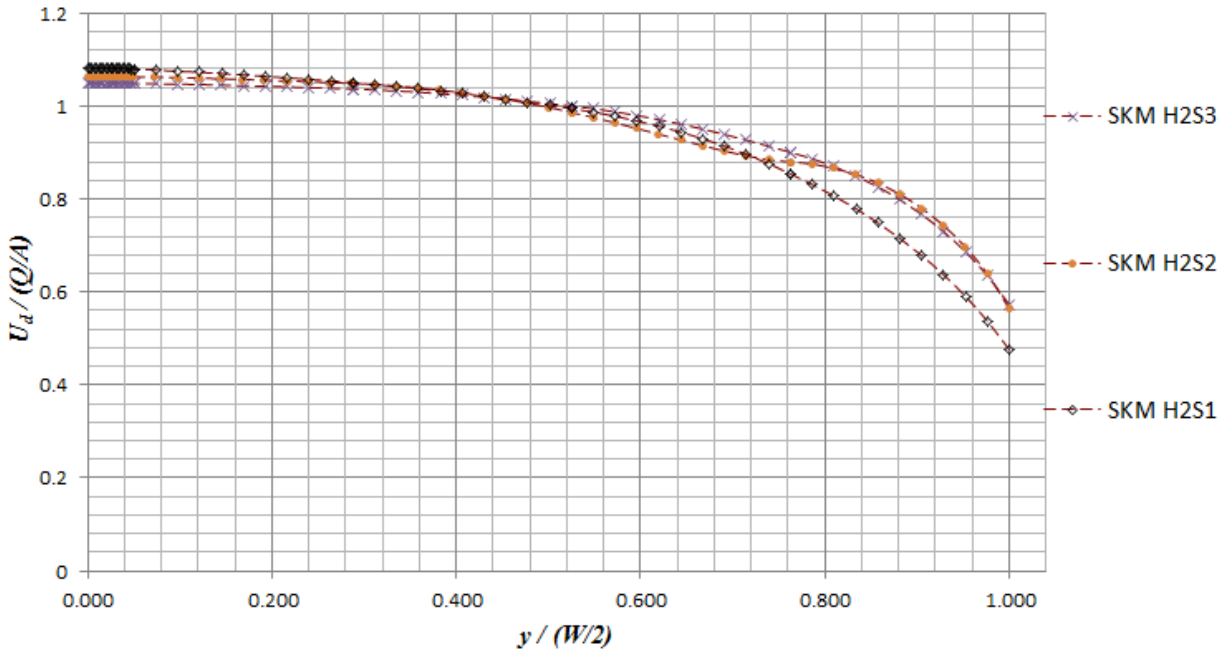

Figure 116. Dimensionless calibrated velocity distribution of the H2 experiments carried out on smooth surface (PVC). It can be observed that the series are following the same pattern with slightly variations.

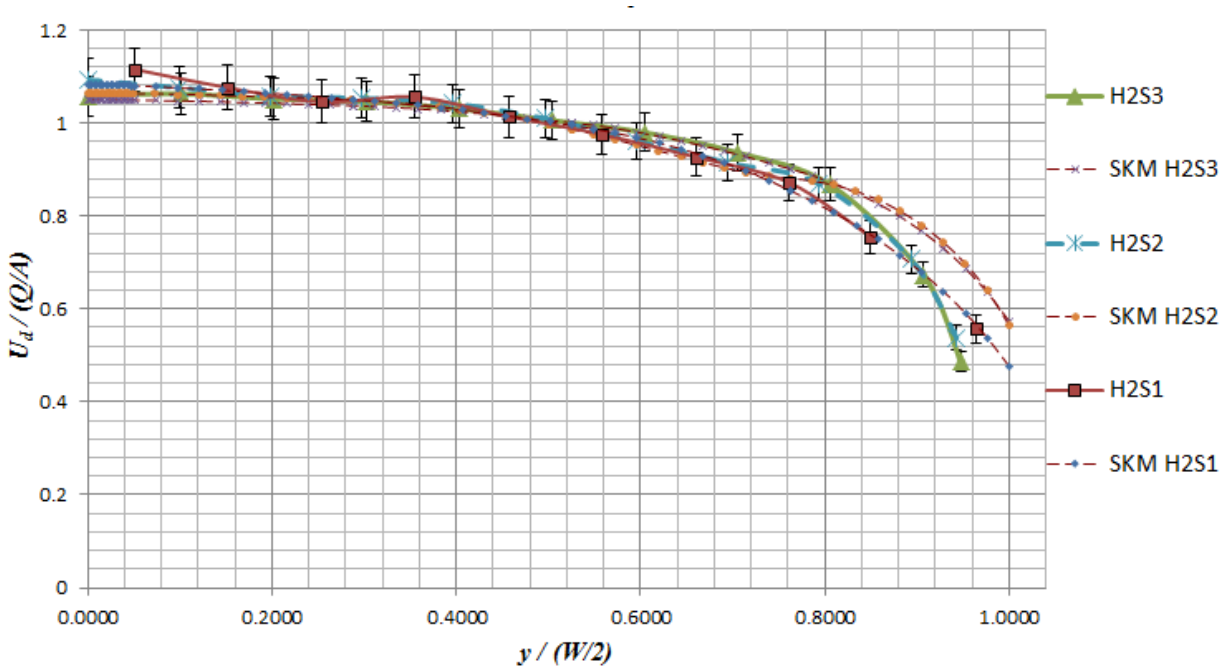

Figure 117. Dimensionless calibrated velocity distributions along the experimental data with their uncertainty bars, corresponding to the H2 sets on smooth surface (PVC). It can be observed that the calibrated simulations fall within the limits.

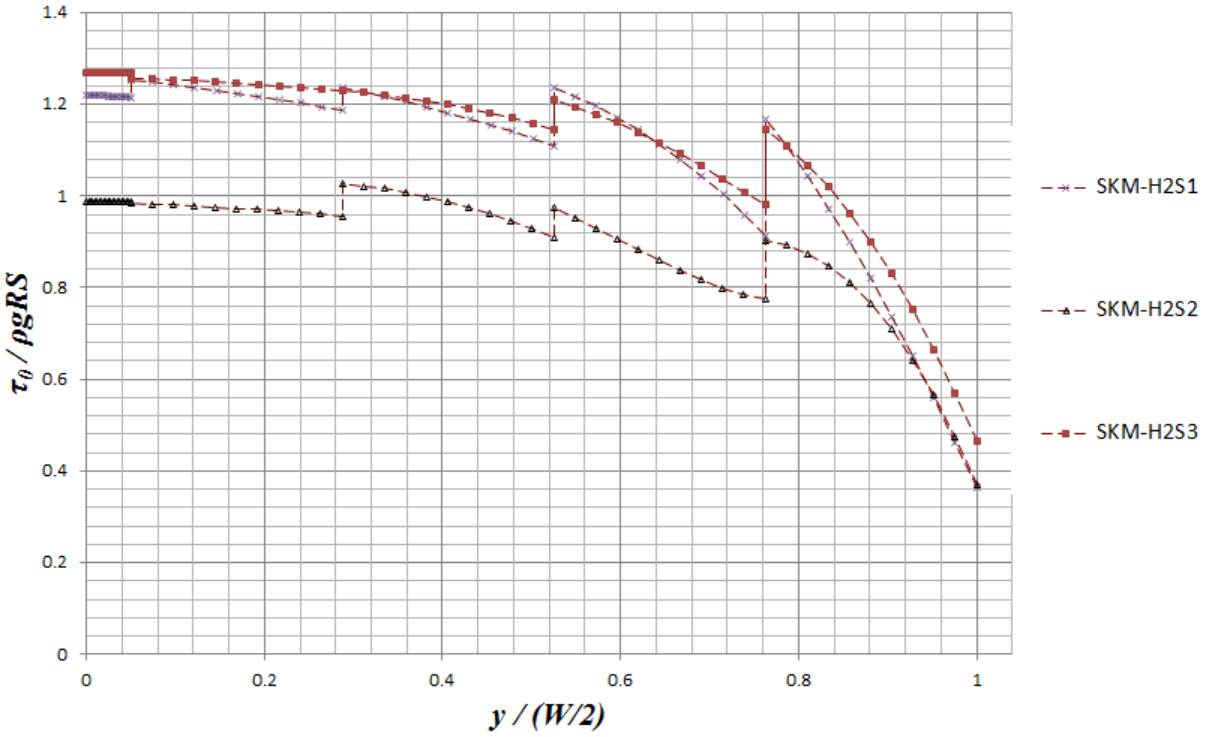

Figure 118. Dimensionless calibrated boundary shear stress distribution of the H2 experiments carried out on smooth surface (PVC). Two patterns can be observed, one for H2S3 and H2S1, and another one for H2S2.

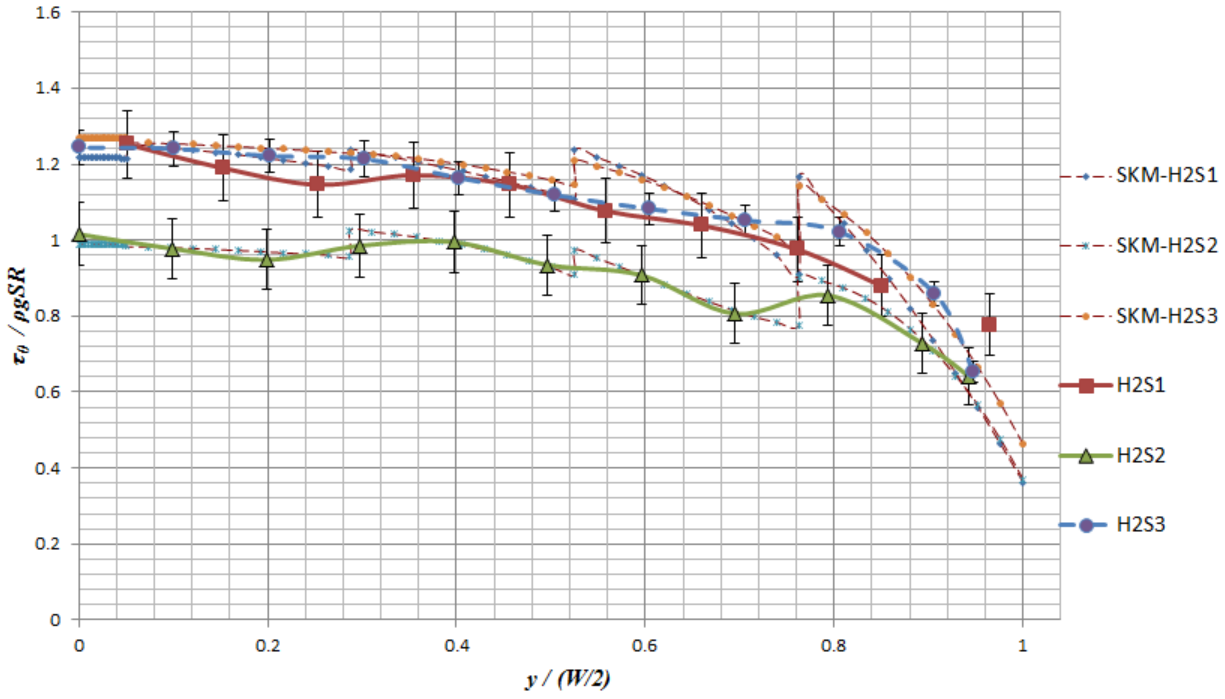

Figure 119. Dimensionless calibrated boundary shear stress distributions along the experimental data with their uncertainty bars, corresponding to the H2 sets on smooth surface (PVC). It can be observed that the calibrated simulations fall within the error limits.

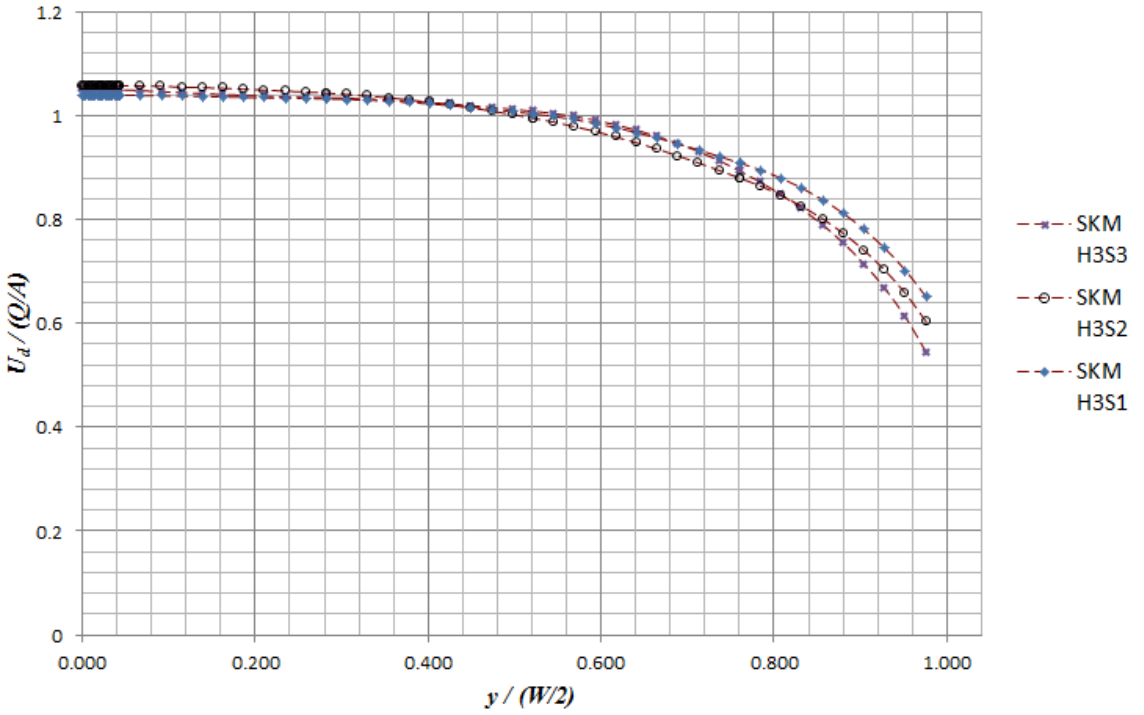

Figure 120. Dimensionless calibrated velocity distribution of the H3 experiments carried out on smooth surface (PVC). It can be observed that the series are following the same pattern with slightly variations.

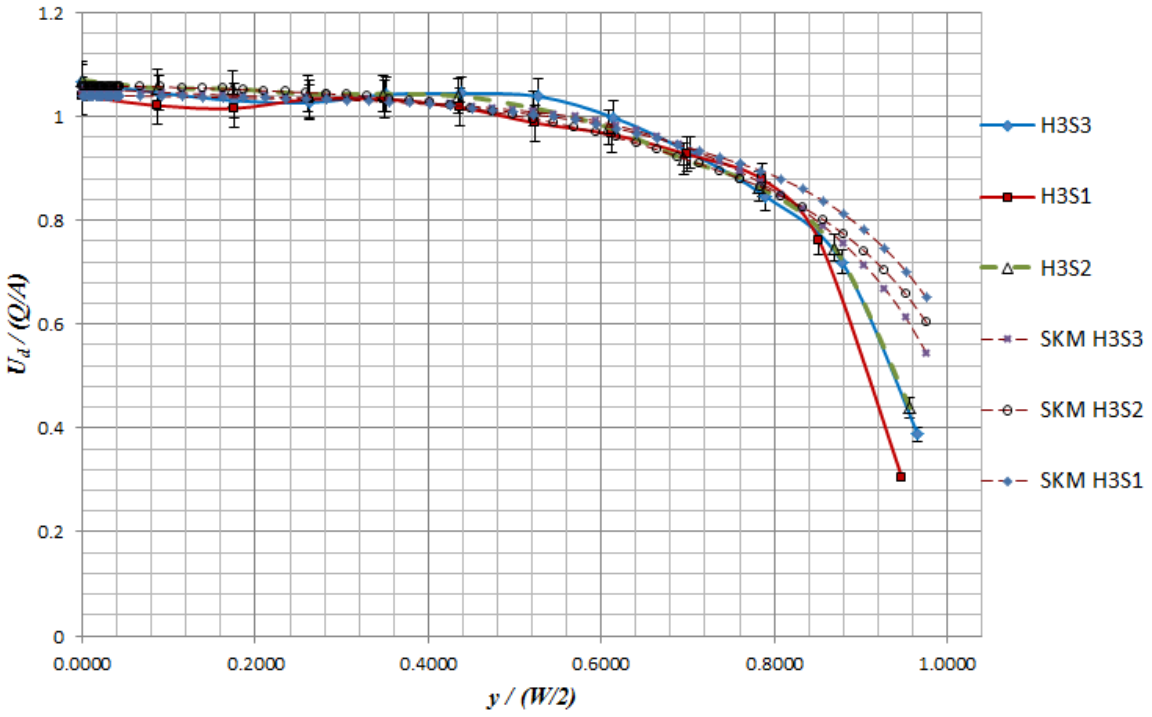

Figure 121. Dimensionless calibrated velocity distributions along the experimental data with their uncertainty bars, corresponding to the H3 sets on smooth surface (PVC). It can be observed that the calibrated simulations fall within the limits.

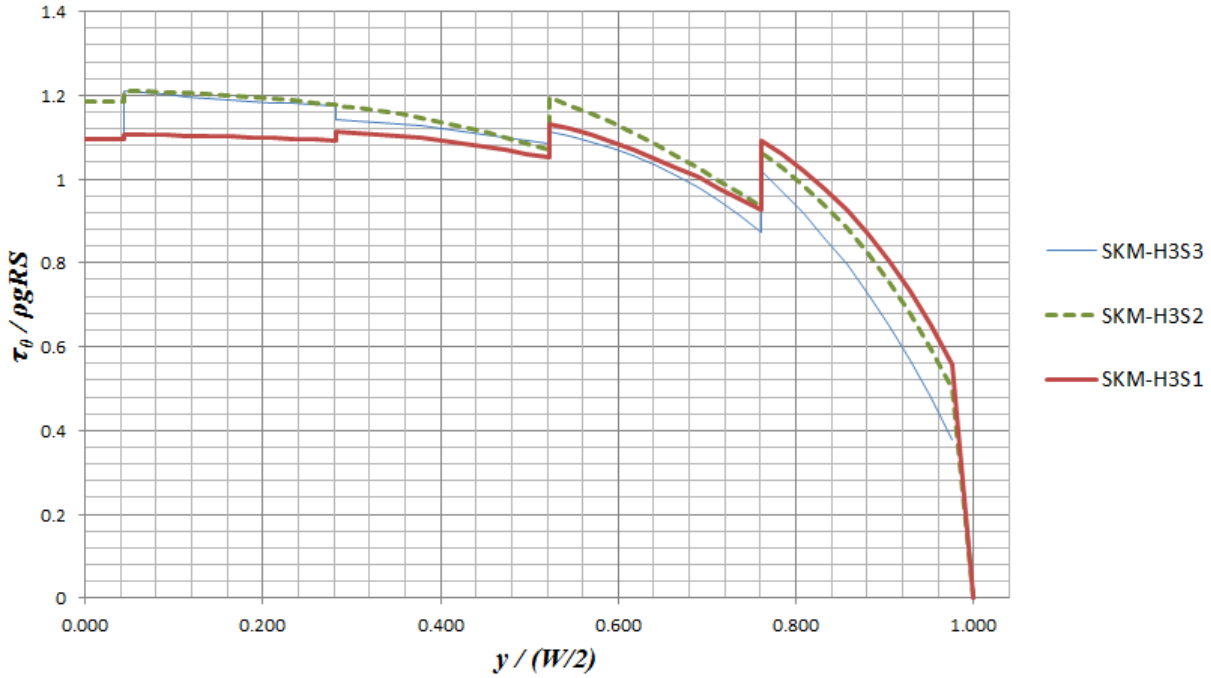

Figure 122. Dimensionless calibrated boundary shear stress distribution of the H3 experiments carried out on smooth surface (PVC). It can be observed that the series are following the same pattern with variations.

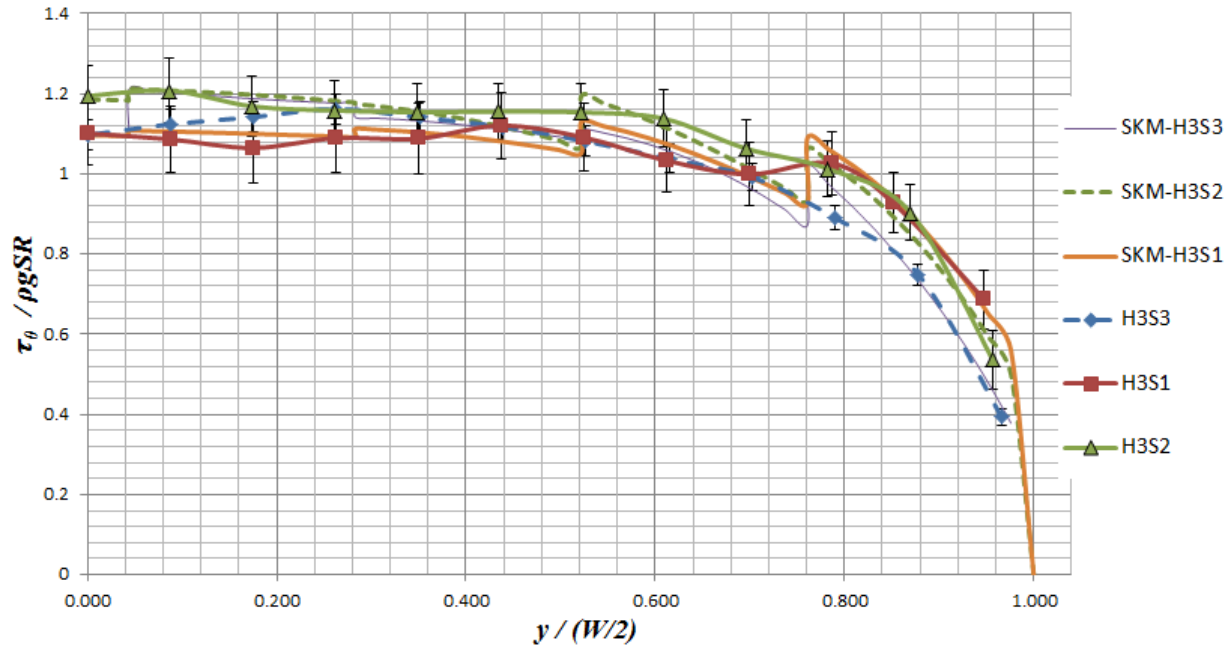

Figure 123. Dimensionless calibrated boundary shear stress distributions along the experimental data with their uncertainty bars, corresponding to the H3 sets on smooth surface (PVC). It can be observed that the calibrated simulations fall within the error limits.

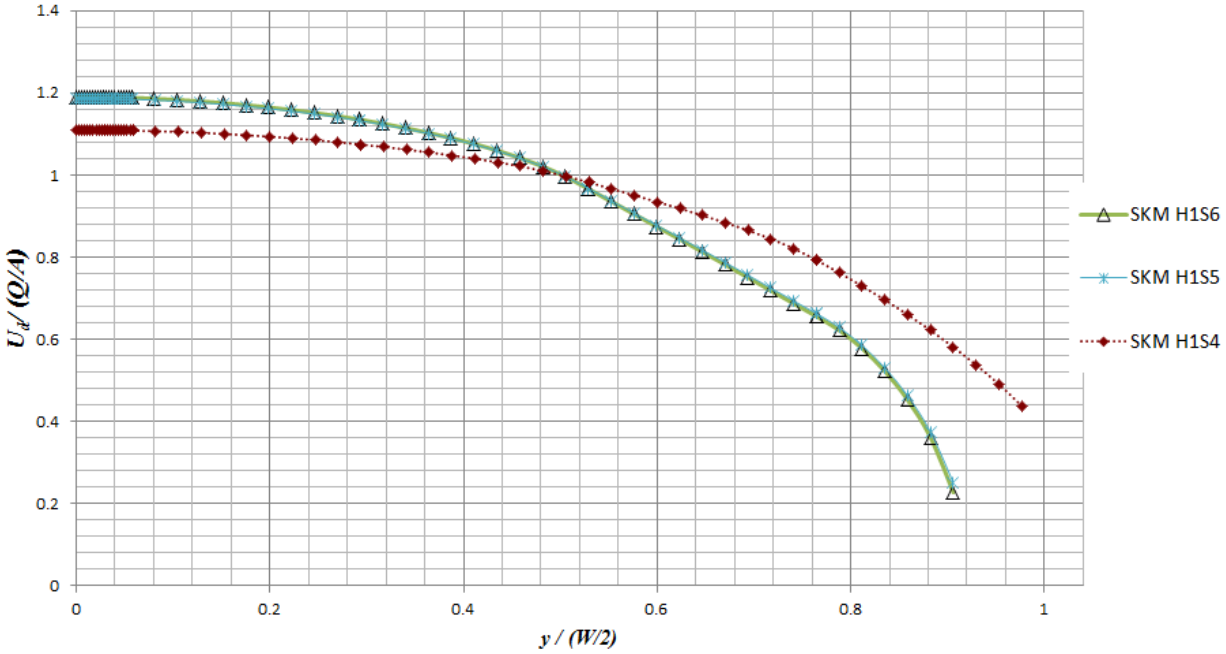

Figure 124. Dimensionless calibrated velocity distribution of the H2 experiments carried out on rough surface (d_{50}=1.46mm). Two different patterns can be observed.

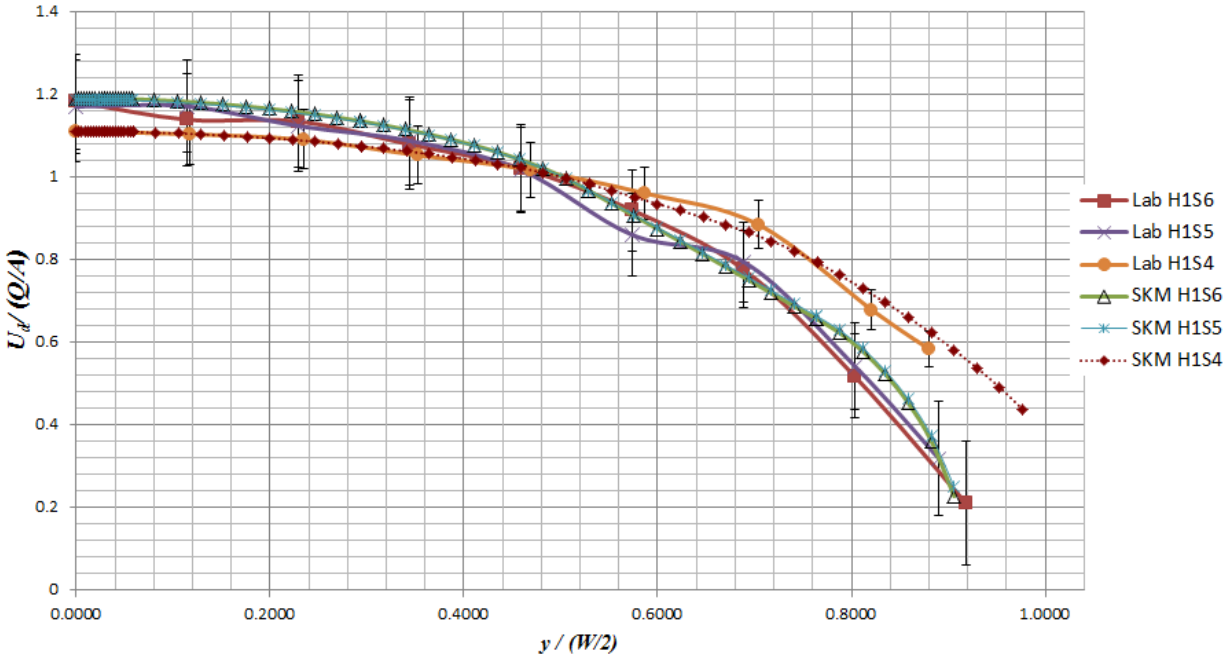

Figure 125. Dimensionless calibrated velocity distributions along the experimental data with their uncertainty bars, corresponding to the H1 sets onrough surface (d_{50}=1.46mm). It can be observed that the calibrated simulations fall within the limits.

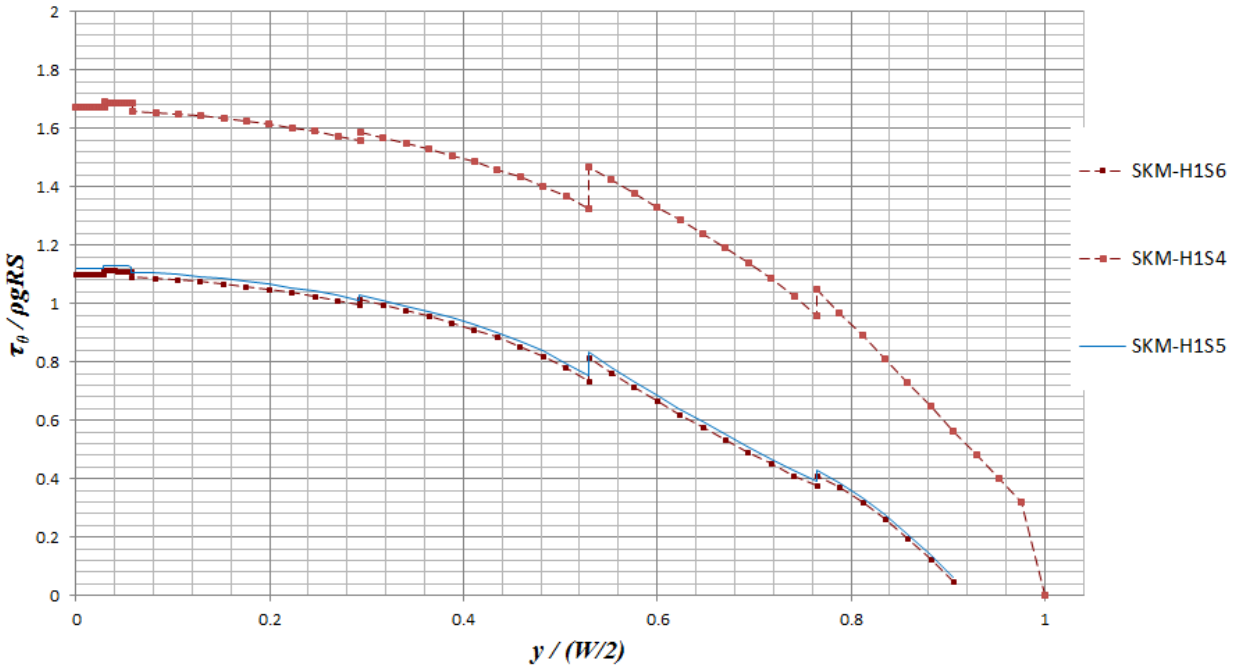

Figure 126. Dimensionless calibrated boundary shear stress distribution of the H1 experiments carried out on rough surface (d_{50}=1.46mm). Two patterns can be observed, one for H1S5 and H1S6, and another one for H1S4.

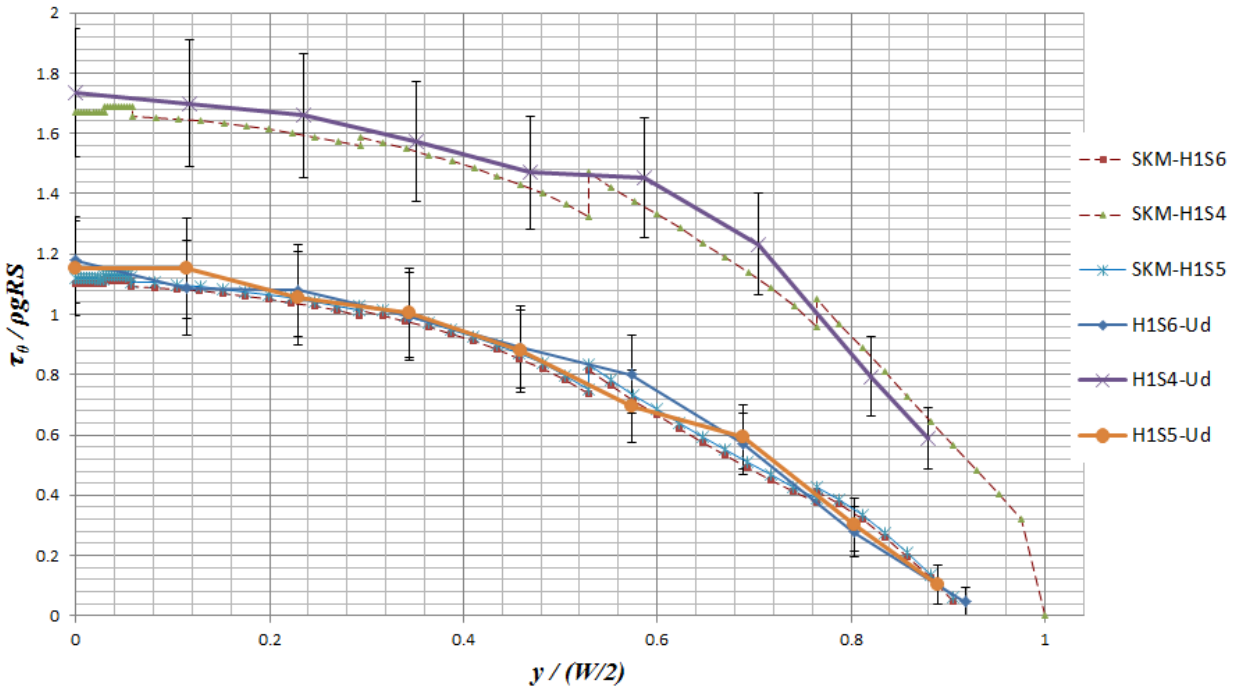

Figure 127. Dimensionless calibrated boundary shear stress distributions along the experimental data with their uncertainty bars, corresponding to the H1 sets on rough surface (d_{50}=1.46mm). It can be observed that the calibrated simulations fall within the error limits.

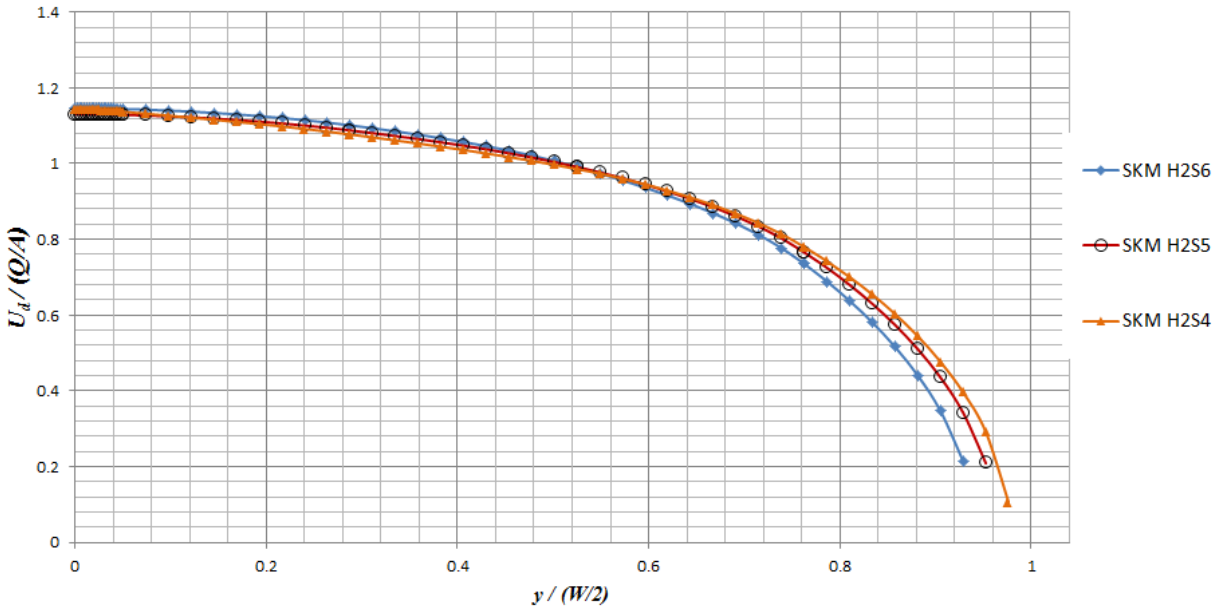

Figure 128. Dimensionless calibrated velocity distribution of the H2 experiments carried out on rough surface (d_{50}=1.46mm). It can be observed that the series are following the same pattern with slightly variations.

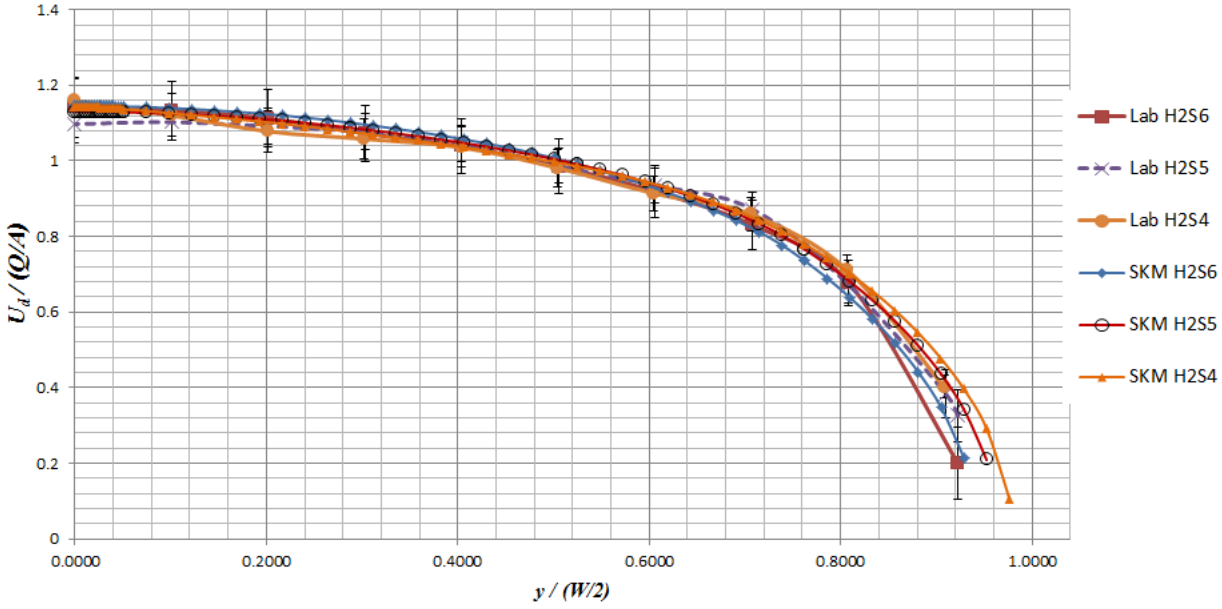

Figure 129. Dimensionless calibrated velocity distributions along the experimental data with their uncertainty bars, corresponding to the H2 sets onrough surface (d_{50}=1.46mm). It can be observed that the calibrated simulations fall within the limits.

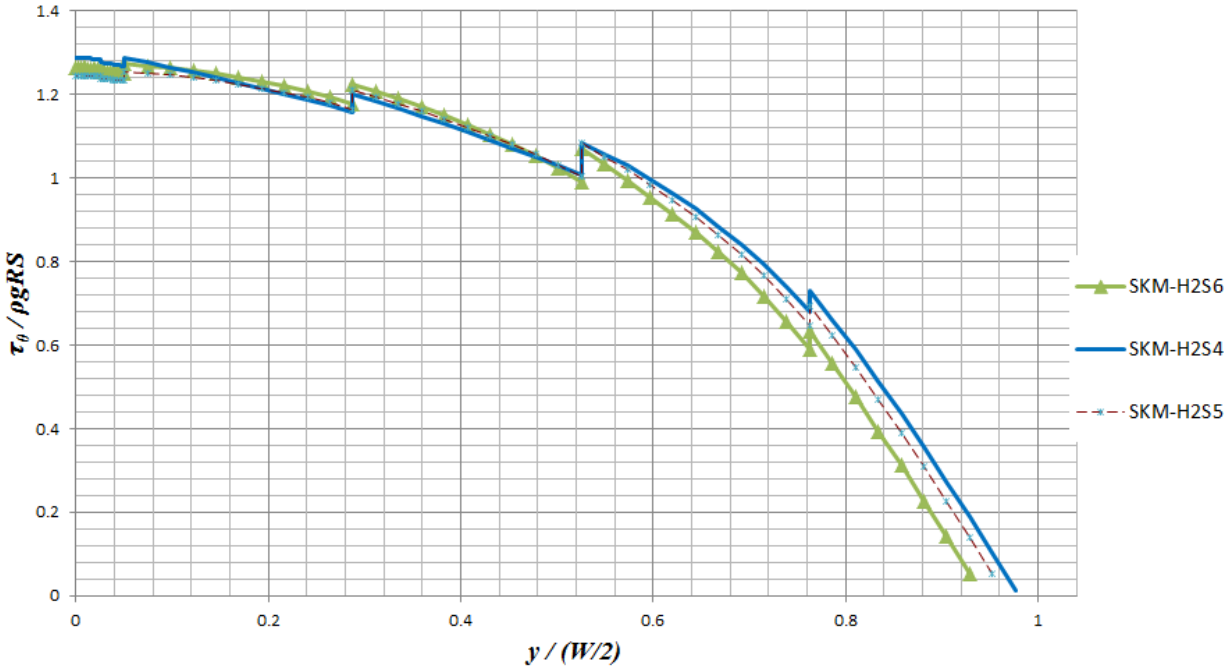

Figure 130. Dimensionless calibrated boundary shear stress distribution of the H3 experiments carried out on rough surface (d_{50}=1.46mm). It can be observed that the series are following the same pattern with small variations.

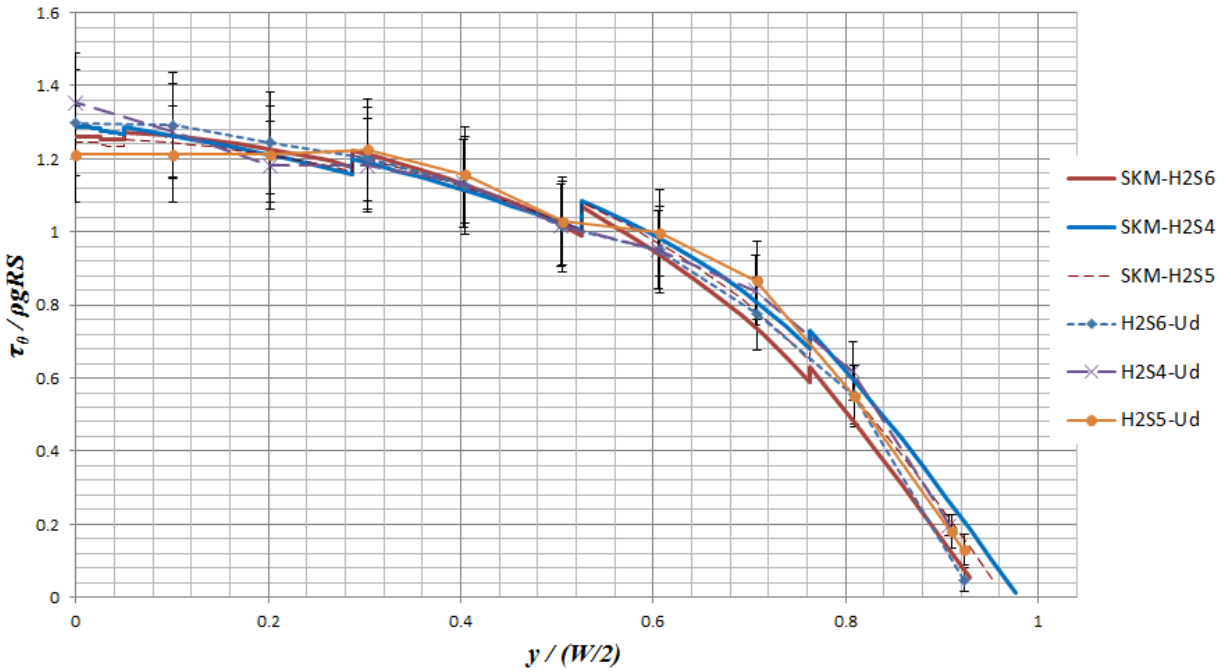

Figure 131. Dimensionless calibrated boundary shear stress distributions along the experimental data with their uncertainty bars, corresponding to the H2 sets on rough surface (d_{50}=1.46mm). It can be observed that the calibrated simulations fall within the error limits.

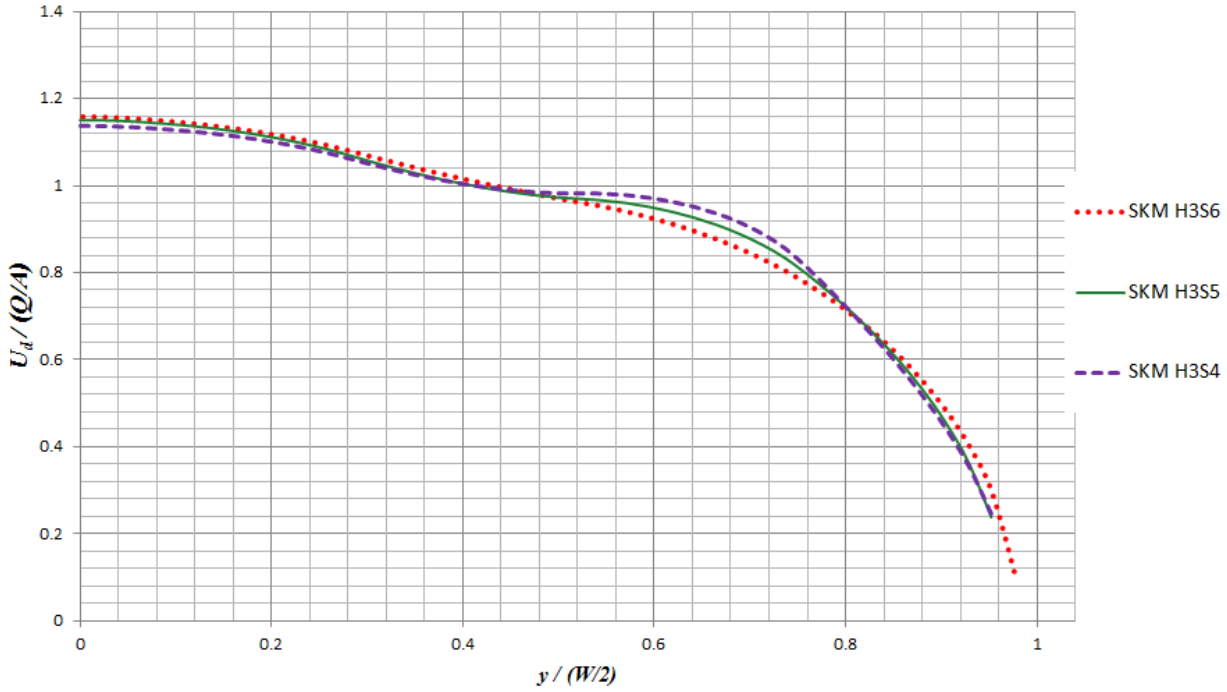

Figure 132. Dimensionless calibrated velocity distribution of the H3 experiments carried out on rough surface (d_{50}=1.46mm). It can be observed that the series are following the same pattern with slightly variations.

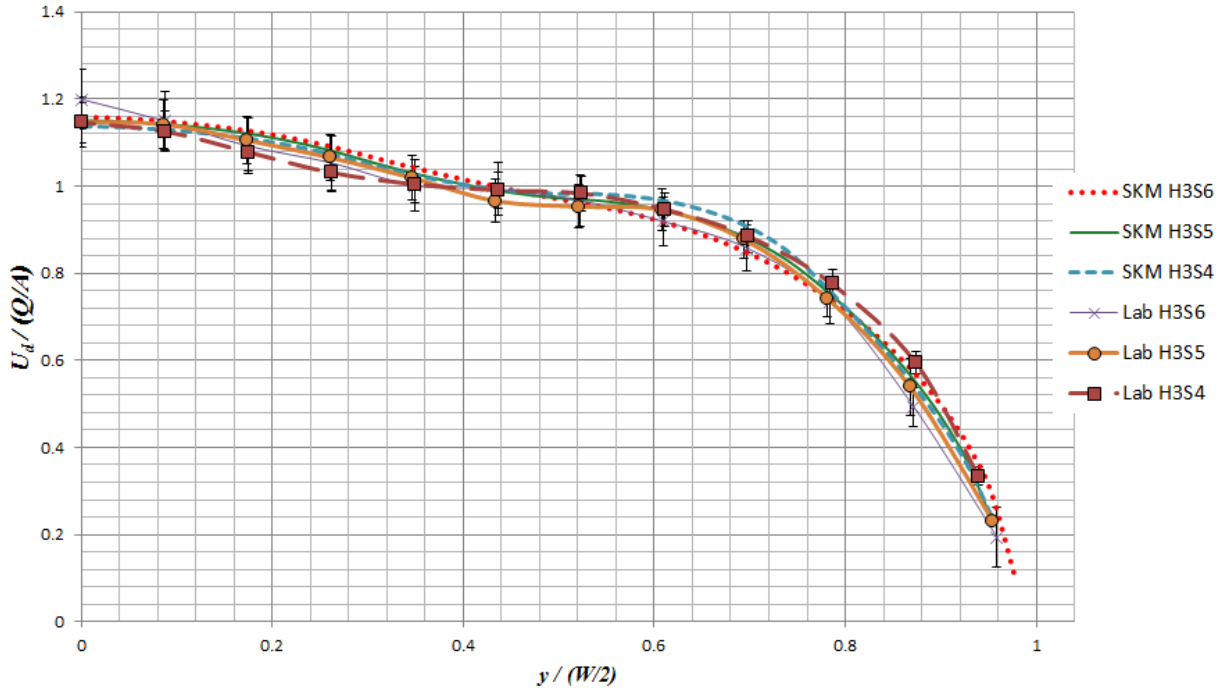

Figure 133. Dimensionless calibrated velocity distributions along the experimental data with their uncertainty bars, corresponding to the H3 sets onrough surface (d_{50}=1.46mm). It can be observed that the calibrated simulations fall within the limits.

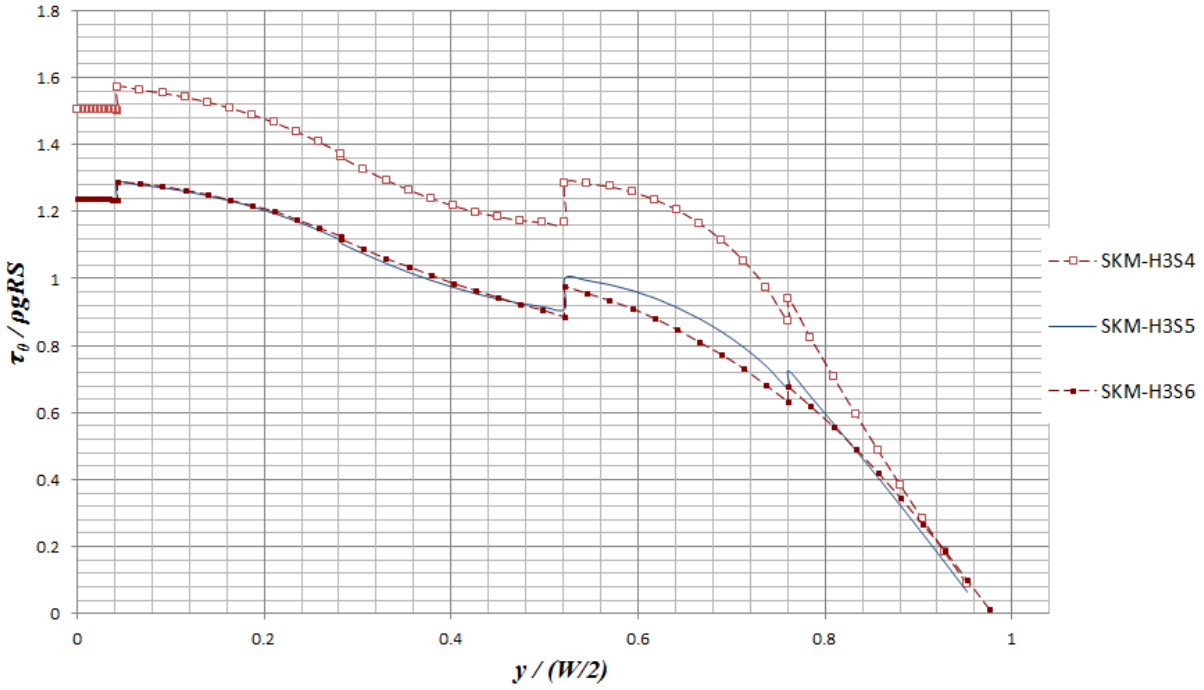

Figure 134. Dimensionless calibrated boundary shear stress distribution of the H3 experiments carried out on rough surface (d_{50}=1.46mm). Two patterns can be observed, one for H3S5 and H3S6, and another one for H3S4.

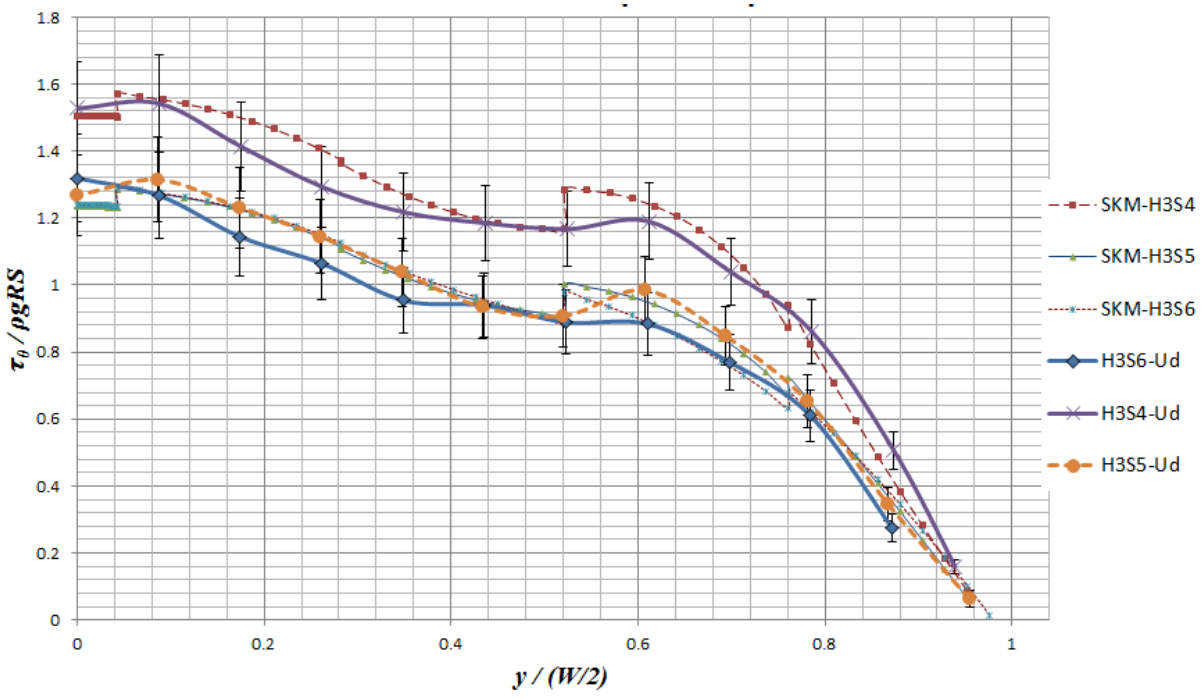

Figure 135. Dimensionless calibrated boundary shear stress distributions along the experimental data with their uncertainty bars, corresponding to the H3 sets on rough surface (d_{50}=1.46mm). It can be observed that the calibrated simulations fall within the error limits.

6.7.2 Γ results

The calibrated values of Γ are shown in table 29, for the 18 experiments. The first column notes the depth key (H1, H2 or H3), the second one the type of surface material (glue sand or PVC), the third one the code of the experiment, composed by a depth and slope (*e.g.* h1s1). From the 4th to the 8th columns, multiples of:

$$p=\Gamma/C\rho gSh_c \quad (100)$$

are shown for each SKM panel, where p is the secondary flow factor per panel, and C the coefficient of secondary flow for self-formed bankside. The 9th to the 13th columns are indicating the value used for f per panel. On the 14th the value of C is shown (equation 100). With respect to the 15th and 16th, the sum of the differences between experimental and simulated values is indicated for velocity and shear stress. From the 17th to the 20th, geometrical values are presented, *i.e.* central depth, h_c, longitudinal slope, S, and hydraulic radius, R, as well as the average shear stress, τ_{aveg}. Finally, the 21st to 25th are showing the actual Γ data.

Table 29. Results obtained and data used to calibration $\Gamma/\rho gRS$. The experiment key is shown in column 3; the geometrical characteristics on columns 17-19; the surface material on column 2; the panel coefficients on columns 4-8; the friction factor used in each panel, on columns 9-13; calibrated $\Gamma/\rho gRS$, column 14; velocity errors on column 15; boundary shear stress error on column 16; actual value of Γ on columns 21-25.

1	2	3	4	5	6	7	8	9	10	11	12	13	14	15	16	17	18	19	20	21	22	23	24	25
			p					f												Γ				
	Material	Exp.	P1 and P2	P3	P4	P5	P6	P1 and P2	P3	P4	P5	P6	C	$\Sigma=\lvert U_{dPitot} - U_{dSKM}\rvert$	$\Sigma=\lvert \tau_m - \tau_{SKM}\rvert$	h	S	R	τ_{aveg}	P1 and P2	P3	P4	P5	P6
H1	PVC	h1s3	1	1	1	-2	-4	0.0194	0.0197	0.0203	0.0220	0.0266	0.055	0.1036	0.3183	0.034	0.00504	2.39	1.6798	0.0924	0.0924	0.0924	-0.1848	-0.3696
	PVC	h1s1	1	1	-1	-1	-3	0.0200	0.0203	0.0199	0.0224	0.0263	0.070	0.0401	0.2170	0.033	0.00149	2.36	0.4866	0.0341	0.0341	-0.0341	-0.0341	-0.1022
	Glue Sand	h1s4	-1	-1	-1	-1	-1	0.0628	0.0617	0.0628	0.0696	0.0764	0.175	0.0597	0.3676	0.033	0.00494	2.28	1.5857	-0.2775	-0.2775	-0.2775	-0.2775	-0.2775
	Glue Sand	h1s6	1	1	1	1.25	1	0.0567	0.0557	0.0567	0.0629	0.0690	0.195	0.0710	0.0867	0.035	0.00148	2.42	0.5081	0.0991	0.0991	0.0991	0.1239	0.0991
	Glue Sand	h1s5	1	1	1	1.5	1	0.0601	0.0591	0.0601	0.0667	0.0731	0.200	0.0446	0.1172	0.035	0.00174	2.41	0.5964	0.1193	0.1193	0.1193	0.1789	0.1193
	PVC	h1s2	1	1	1	0.5	-0.5	0.0188	0.0184	0.0190	0.0210	0.0242	0.245	0.0491	0.2421	0.035	0.00172	2.44	0.5964	0.1461	0.1461	0.1461	0.0731	-0.0731
H2	Glue Sand	h2s4	-1	2	2	0.5	1	0.0529	0.0538	0.0559	0.0602	0.0647	0.060	0.1004	0.5760	0.051	0.00494	3.45	2.4488	-0.1469	0.2939	0.2939	0.0735	0.1469
	Glue Sand	h2s6	1	1	1	1	2	0.0490	0.0498	0.0517	0.0558	0.0599	0.085	0.0389	0.1196	0.050	0.00148	3.43	0.7301	0.0621	0.0621	0.0621	0.0621	0.1241
	Glue Sand	h2s5	1	1	1	0.5	1	0.0519	0.0528	0.0548	0.0591	0.0635	0.100	0.0499	0.1654	0.050	0.00174	3.43	0.8579	0.0858	0.0858	0.0858	0.0429	0.0858
	PVC	h2s3	1	1	0.333	-1	-3.5	0.0186	0.0185	0.0185	0.0195	0.0228	0.105	0.3381	0.4034	0.051	0.00504	3.51	2.5061	0.2631	0.2631	0.0877	-0.2631	-0.9210
	PVC	h2s1	0.5	1	0.5	-1	-2.5	0.0208	0.0214	0.0223	0.0249	0.0319	0.115	0.0824	0.2778	0.050	0.00149	3.47	0.7240	0.0416	0.0833	0.0416	-0.0833	-0.2082
	PVC	h2s2	1	1	0.5	0.5	-1	0.0169	0.0168	0.0180	0.0193	0.0225	0.295	0.1568	0.1744	0.053	0.00172	3.63	0.8909	0.2628	0.2628	0.1314	0.1314	-0.2628
H3	Glue Sand	h3s5	1	1	8	-1	2	0.0472	0.0494	0.0490	0.0539	0.0581	0.045	0.0594	0.2465	0.071	0.00174	4.77	1.2159	0.0547	0.0547	0.4377	-0.0547	0.1094
	Glue Sand	h3s6	1	2	4	1	1	0.0447	0.0467	0.0464	0.0510	0.0550	0.050	0.1695	0.5378	0.071	0.00148	4.75	1.0308	0.0515	0.1031	0.2062	0.0515	0.0515
	PVC	h3s2	1	1	0.5	-0.5	-2	0.0173	0.0177	0.0177	0.0198	0.0225	0.155	0.2205	0.3887	0.071	0.00172	4.78	1.1980	0.1857	0.1857	0.0928	-0.0928	-0.3714
	Glue Sand	h3s4	-1	-1	1.5	-2	0.5	0.0484	0.0506	0.0502	0.0553	0.0596	0.155	0.1831	1.3333	0.070	0.00494	4.71	3.4041	-0.5276	-0.5276	0.7914	-1.0553	0.2638
	PVC	h3s3	0.25	1	0.5	-2	-1	0.0156	0.0172	0.0167	0.0172	0.0201	0.226	0.4230	0.8018	0.070	0.00504	4.68	3.4387	0.1943	0.7772	0.3886	-1.5543	-0.7772
	PVC	h3s1	1	1	0.5	-0.333	-1.5	0.0193	0.0196	0.0199	0.0214	0.0252	0.240	0.3059	0.2107	0.070	0.00149	4.70	1.0227	0.2454	0.2454	0.1227	-0.0818	-0.3682

In order to appreciate better the behaviour of the secondary flow gradient, Γ, the Γ calibrated (table 29) values were plotted, dividing the results in three graphs according to their depths (figures 136, 137 and 138). Additionally, the coefficient $p=\Gamma/C\rho gSh_c$ were sketched in the same way (figures 139, 140 and 141). From such figures and table 29, it was possible to identify the patterns followed by Γ for their corresponding surface and depth, summarizing it on table 30. It should be noted that while Γ is increasing along with the depth, for PVC surface, the opposite is happening for glue sand surface. Additionally, $p=\Gamma/C\rho gSh_c$ was in agreement for the cases with equal surface and depth, also the p was close as well, except for H2S4 and H3S2. Hence, it was possible to propose an average for p and its multiples for each depth and surface material, shown in table 31. The differences between p values can be attributed to the cross sectional variation, in spite of being the same section, the hydraulic radius and side slope are changing, altering Γ. Finally, for the prediction of self-formed cross sections, it is recommended to use $C=\Gamma/\rho gpSh_c=0.093$, and the panel multiples as $p1=p2=1$, $p3=1$, $p4=1$, $p5=0.75$, and $p6=1.50$.

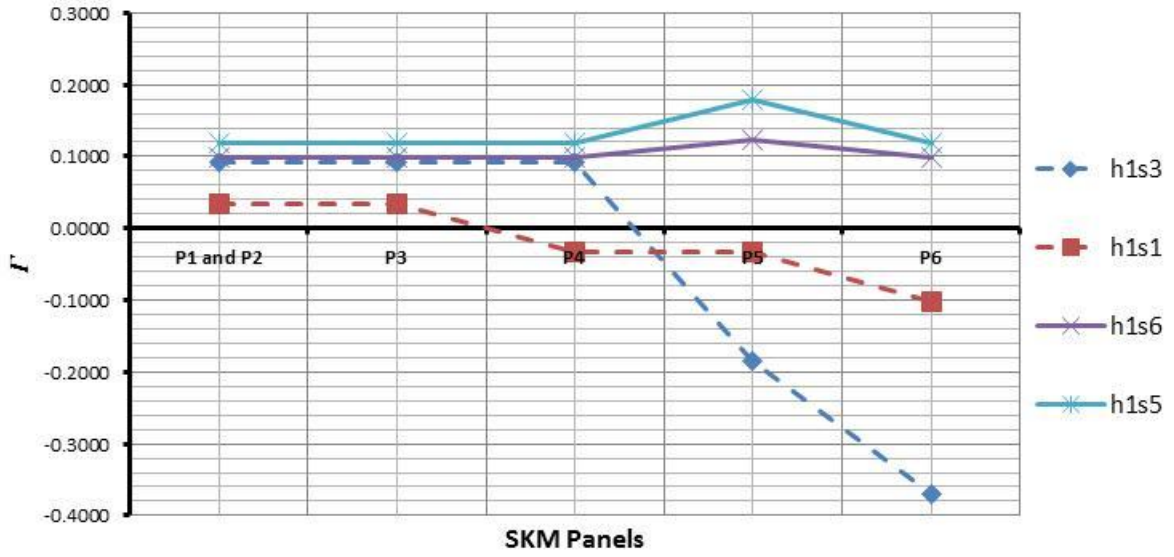

Figure 136. Actual value of Γ obtained after a calibration process for each panel (*e.g.* P1 and P2). Four series are presented, corresponding to the H1 experiments. Similar behaviour can be observed for h1s6 and h1s5, whom used rough surface (d_{50}=1.46mm).

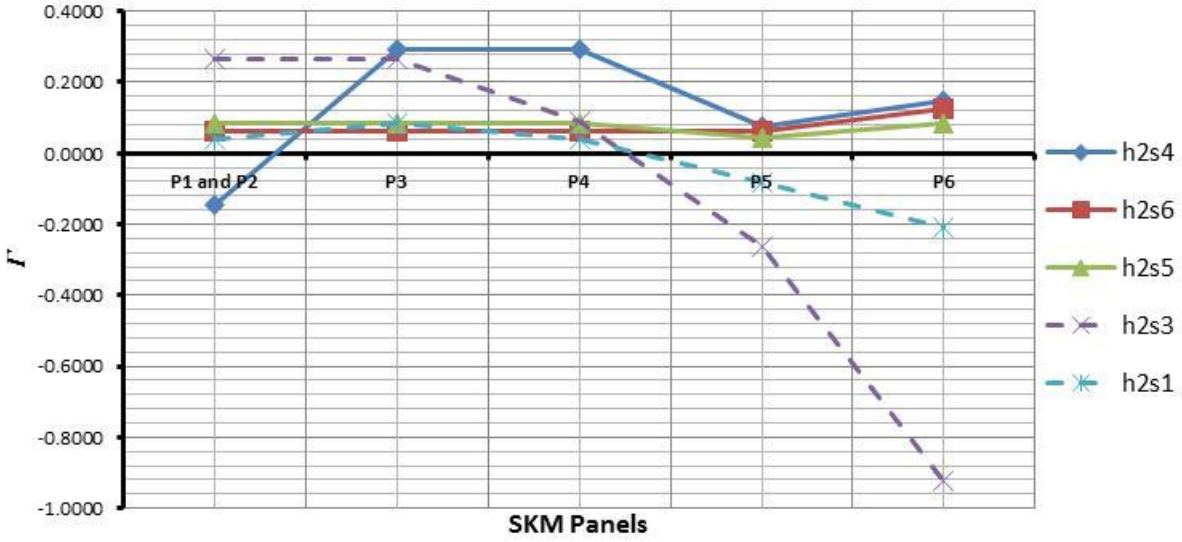

Figure 137. Actual value of Γ obtained after a calibration process for each panel (*e.g.* P1 and P2). Five series are presented, corresponding to the H2 experiments. Similar behaviour can be observed forh2s5 and h2s6, whom used rough surface (d_{50}=1.46mm), and for h2s3 and h2s1, whom used smooth surface (PVC).

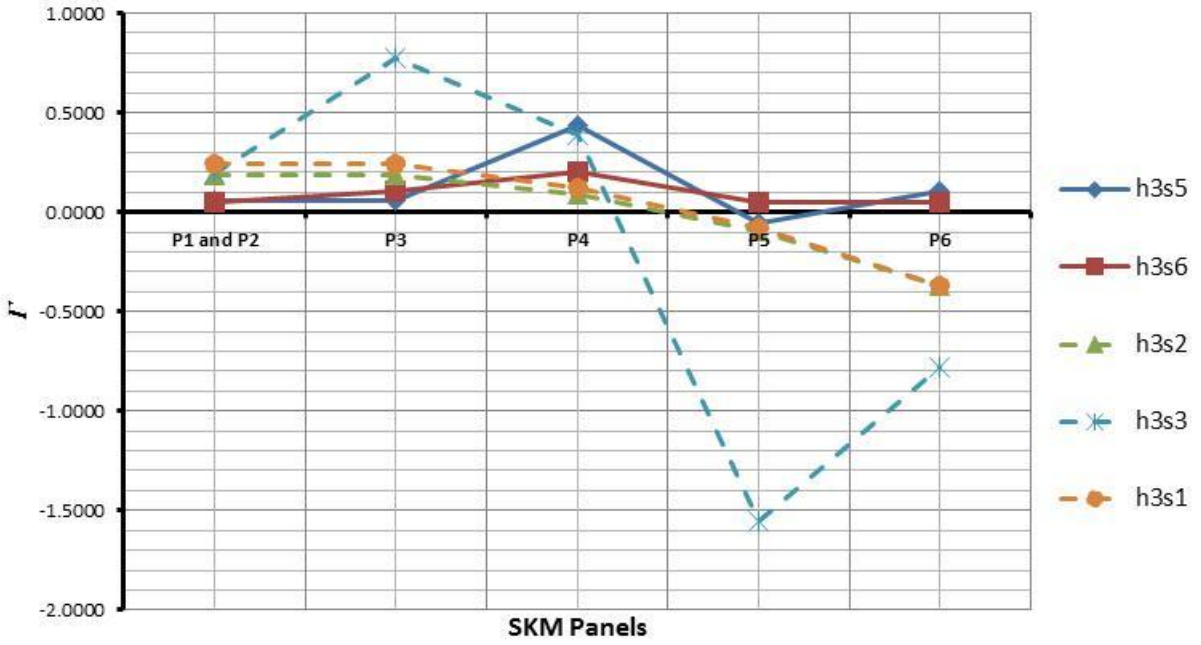

Figure 138. Actual value of Γ obtained after a calibration process for each panel (*e.g.* P1 and P2). Five series are presented, corresponding to the H3 experiments. Similar behaviour can be observed for h3s5 and h3s6, whom used rough surface (d_{50}=1.46mm), and for h3s1 and h3s2, whom used smooth surface (PVC).

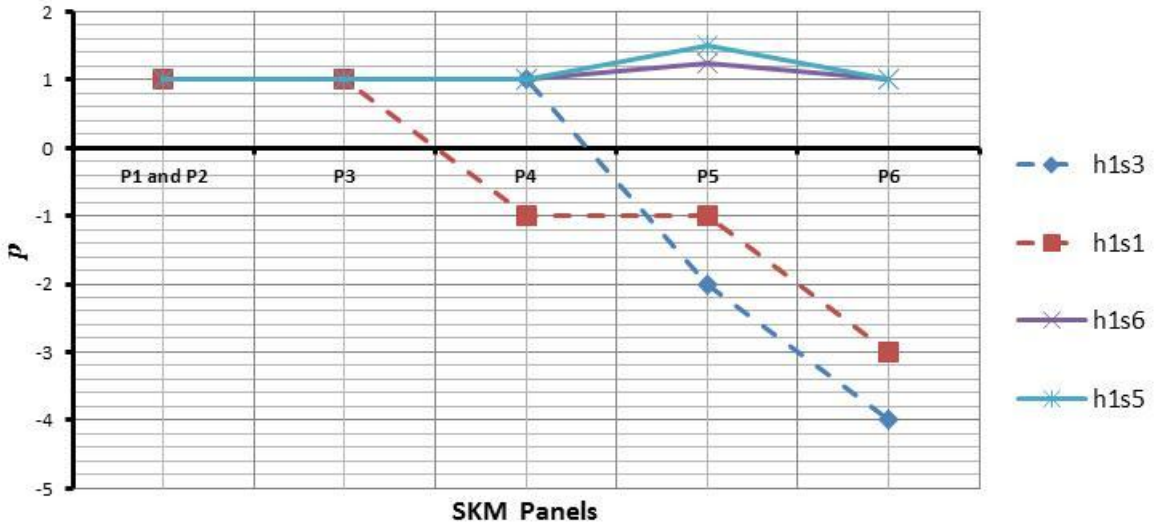

Figure 139. Values obtained for p per panel. Four series are presented, corresponding to the H1 experiments. Similar behaviour can be observed for h1s5 and h1s6, whom used rough surface (d_{50}=1.46mm), and for h1s1 and h1s3, whom used smooth surface (PVC).

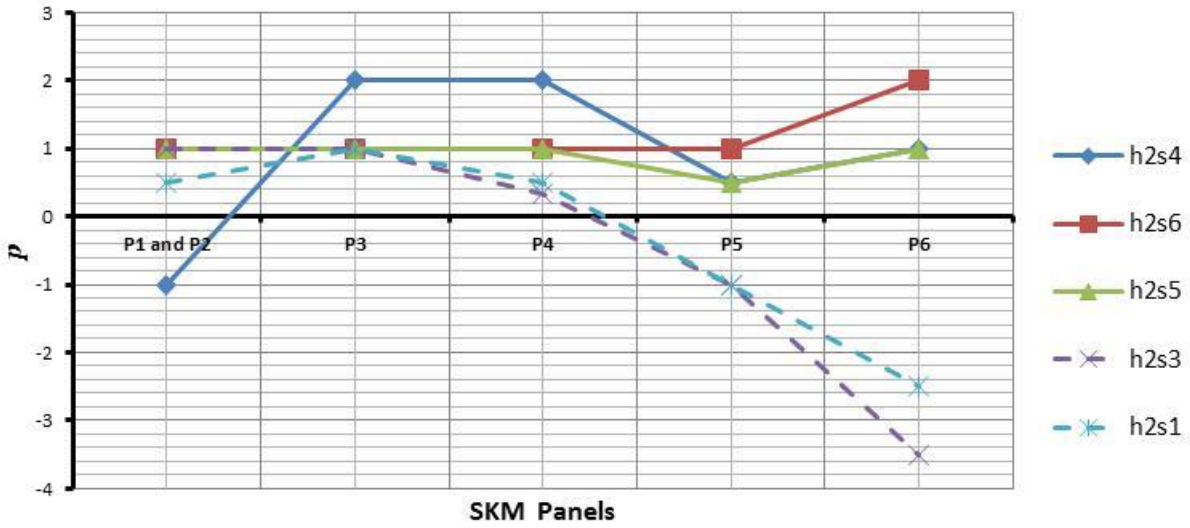

Figure 140. Values obtained for p per panel. Five series are presented, corresponding to the H2 experiments. Similar behaviour can be observed for h2s4, h2s5 and h2s6, whom used rough surface (d_{50}=1.46mm), and for h2s1 and h2s3, whom used smooth surface (PVC).

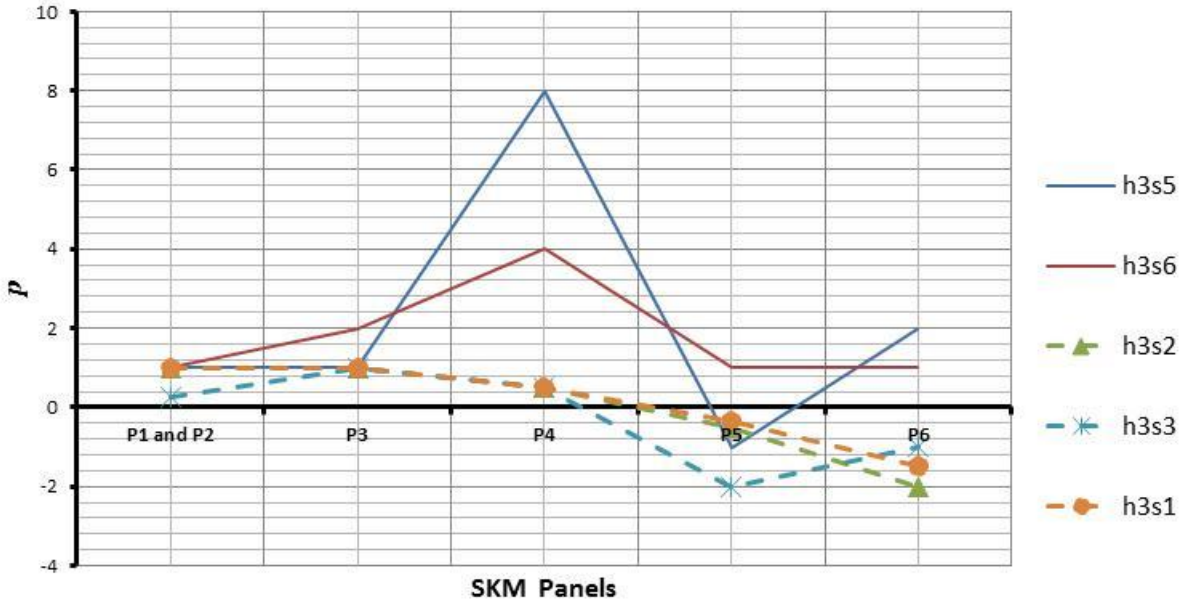

Figure 141. Values obtained for p per panel. Five series are presented, corresponding to the H3 experiments. Similar behaviour can be observed for h3s5 and h3s6, whom used rough surface (d_{50}=1.46mm), and for h3s1, h3s2 and h3s3, whom used smooth surface (PVC).

Table 30. Summary of the calibrated values found for p and C, per experiment and panel.

1	2	3	4	5	6	7	8	9
			p					
	Material	**Exp.**	**p1 and p2**	**p3**	**p4**	**p5**	**p6**	C
H1	PVC	h1s3	1	1	1	-2	-4	0.055
	PVC	h1s1	1	1	-1	-1	-3	0.070
	Glue Sand	h1s6	1	1	1	1.25	1	0.195
	Glue Sand	h1s5	1	1	1	1.5	1	0.200
H2	Glue Sand	h2s4	-1	2	2	0.5	1	0.060
	Glue Sand	h2s6	1	1	1	1	2	0.085
	Glue Sand	h2s5	1	1	1	0.5	1	0.100
	PVC	h2s3	1	1	0.3333	-1	-3.5	0.105
	PVC	h2s1	0.5	1	0.5	-1	-2.5	0.115
H3	Glue Sand	h3s5	1	1	8	-1	2	0.045
	Glue Sand	h3s6	1	2	4	1	1	0.050
	PVC	h3s2	1	1	0.5	-0.5	-2	0.155
	PVC	h3s3	0.25	1	0.5	-2	-1	0.226
	PVC	h3s1	1	1	0.5	-0.3333	-1.5	0.240

Table 31. Summary of the calibrated values found for p and C, per depth, surface material and panel.

1	2	3	4	5	6	7	8
		p					
	Material	**P1 and p2**	**p3**	**p4**	**p5**	**p6**	C
H1	Glue Sand	1	1	1	1.375	1	0.198
	PVC	1	1	0	-1.5	-3.5	0.063
H2	Glue Sand	1	1	1	0.75	1.5	0.093
	PVC	0.75	1	0.4167	-1	-3	0.110
H3	Glue Sand	1	2	6	0	1.5	0.048
	PVC	0.625	1	0.5	-1.1667	-1.3	0.233

6.8 Validation

In order to corroborate the results obtained in the previous section, where $C=\Gamma/\rho gpSh_c=0.093$,using six SKM panels, and the methodology for the variation of f, it was required to try them on the Yu and Knight (1998) model for the prediction of self-formed channels and compare the products with experimental data, *i.e.* Babaeyan-Koopaei (1997) and Macky (1999). The model was described in chapter 3and analysed in section 3.4, employing six SKM panels, two for the central flatbed and four equidistant on the bankside, affecting Γ on each panel by the following factors, p1=p2=1, p3=1, p4=1, p5=0.75, and p6=1.50 (p*i*, panel *i*).

With respect to the set of experimental data selected to compare the proposed factors, they were the experiments of Babaeyan-Koopaei (1997) (table 35) and Macky (1999) (table 32), whom produced self-formed sections in the laboratory, using d_{50}=1mm and d_{50}=3.42mm. The advantage of these experiments was that they were alternative to the ones carried out by Ikeda (1981), and in the case of Babaeyan-Koopaei (1997), more information was provided, *e.g.* hydraulic area, A, carved slope, S_{bed}, water surface slope, S_w, and the transversal geometry.

Table 32. Experimental results for self-formed cross sections provided by Macky (1999). The material used was uniform sand d_{50}=3.42, α=36.5º and μ=0.74.

Run	S	Q (L/s)	W (m)	h_c (m)	Q_s ml/s
2	0.00958	51.00	1.86	0.0409	2.20
3	0.00800	92.20	3.27	0.0455	6.20
4	0.00681	176.20	4.47	0.0523	22.00
5	**0.00638**	**12.10**	**0.50**	**0.0476**	**0.00**
6	**0.00535**	**72.40**	**2.19**	**0.0657**	**0.70**
7	0.00529	159.40	3.48	0.0692	6.10
8	0.00593	257.20	5.06	0.0724	25.60
9	**0.00350**	**111.40**	**2.38**	**0.0964**	**0.60**

The validation process consisted of compare the results of the numerical model employing $\Gamma/\rho gpSh_c$=0, as was originally proposed by Yu and Knight (1998), and $\Gamma/\rho gpSh_c$=0.093, value found in this research, against the experimental data (tables 33 and 34). Then, the numerical model was fed by the corresponding longitudinal slope, S, sand diameter, d, and discharge, Q, of each lab test, obtaining two sets of results per run with the geometrical information of the cross section, *i.e.* centre line depth, h_c, top with, W, and half central flatbed, $b/2$. Later the errors between the calculated and the lab data were obtained and reported in percentage, being ΔQ, Δh_c, ΔW and ΔA. Such results are shown in tables 33 and 34, for Macky (1999), and tables 36 and 37, for the data of Babaeyan-Koopaei (1997).

Table 33. The results of the simulations trying to reproduce the experiments of Macky (1999) (table 32). The numerical model employed was the one of Yu and Knight (1998), using $\Gamma/\rho gpSh_c$=0.10 and the variation of f for the bank side, f/f_c. The errors with respect to the lab data are provided as well (ΔQ, ΔW and Δh_c).

	Yu and Knight Model, $\Gamma/\rho gpSh_c$ =0.10								Errors		
Run	Q_s ml/s	Q (L/s)	W (m)	h_c (m)	A (m^2)	$b/2$ (m)	$T/2$	$(T/2)/h_c$	ΔQ (%)	ΔW (%)	Δh_c (%)
9	**0.00**	**111.40**	**2.1887**	**0.0868**	**0.1724**	**0.8882**	**0.2061**	**2.3753**	**0.00%**	**8.04%**	**9.99%**
6	**0.60**	**72.40**	**2.2774**	**0.0566**	**0.1203**	**1.0049**	**0.1338**	**2.3624**	**0.00%**	**4.09%**	**13.79%**
5	**0.70**	**12.10**	**0.5600**	**0.0474**	**0.0221**	**0.1681**	**0.1119**	**2.3572**	**0.00%**	**12.67%**	**0.32%**
7	2.20	159.40	4.7839	0.0573	0.2616	2.2566	0.1353	2.3627	0.00%	37.31%	17.22%
3	6.10	92.20	4.5459	0.0378	0.1651	2.1841	0.0888	2.3495	0.00%	39.10%	16.93%
4	6.20	176.20	7.0916	0.0444	0.3039	3.4412	0.1046	2.3547	0.00%	58.58%	15.03%
2	22.00	51.00	3.1566	0.0315	0.0954	1.5044	0.0739	2.3435	0.00%	69.71%	22.91%
8	25.60	257.20	8.7332	0.0511	0.4304	4.2461	0.1205	2.3591	0.00%	72.46%	29.46%
									Average:	**37.74%**	**15.71%**

Table 34. The results of the simulations trying to reproduce the experiments of Macky (1999) (table 32). The numerical model employed was the one of Yu and Knight (1998), using $\Gamma/\rho gSh_c$=0 and the variation of f on the bank side, f/f_c. The errors with respect to the lab data are provided as well (ΔQ, ΔW and Δh_c).

	Yu and Knight, Γ=0								Errors		
	Q_s	Q	W	h_c	A	$b/2$	$T/2$	$(T/2)/h_c$	ΔQ	ΔW	Δh_c
Run	ml/s	(L/s)	(m)	(m)	(m^2)	(m)			(%)	(%)	(%)
9	**0.00**	**111.40**	**2.4619**	**0.0812**	**0.1830**	**1.0181**	**0.2129**	**2.6204**	**0.00%**	**3.44%**	**15.73%**
6	**0.60**	**72.40**	**2.5877**	**0.0530**	**0.1287**	**1.1555**	**0.1383**	**2.6087**	**0.00%**	**18.27%**	**19.29%**
5	**0.70**	**12.10**	**0.6196**	**0.0444**	**0.0233**	**0.1941**	**0.1157**	**2.6039**	**0.00%**	**24.66%**	**6.67%**
7	2.20	159.40	5.4670	0.0536	0.2807	2.5936	0.1399	2.6090	0.00%	56.92%	22.50%
3	6.10	92.20	5.2260	0.0354	0.1780	2.5211	0.0919	2.5971	0.00%	59.92%	22.24%
4	6.20	176.20	8.1453	0.0416	0.3273	3.9644	0.1082	2.6018	0.00%	82.14%	20.45%
2	22.00	51.00	3.6341	0.0295	0.1030	1.7406	0.0765	2.5916	0.00%	95.38%	27.84%
8	25.60	257.20	10.0185	0.0478	0.4629	4.8847	0.1246	2.6058	0.00%	97.84%	33.96%
									Average:	**54.82%**	**21.09%**

While comparing the errors between tables 38 and 39, it is observed that in average, and in all the cases, the simulated results are closer to the experimental data when $\Gamma/\rho gpSh_c$=0.10 than $\Gamma/\rho gpSh_c$=0, decreasing the error significantly when the sediment discharge, Q_s, trends to cero. This confirms the stable channel paradox of Parker (1978b, and 1979), that predicts stable banksides in threshold condition with a central bed carrying material. However, it is inferred that when Q_s is higher the accuracy of the geometry estimation decreases, perhaps due to the channel bottom is moving, altering slightly its hydraulic capacity.

Table 35. The results of the experiments carried out by Babaeyan-Koopaei (1997) for self-formed cross sections. The used uniform sand material with d_{50}=1mm.

Test No	S_{bed} Carved channel	S_w	Q (L/s)	W (m)	h_c (m)	A (m^2)	S_w	Q_s (mg/l)	V m/s	ΔS
1	0.0028	0.00254	4.0	0.4961	0.0248	0.01227	0.00254	527.90	0.33	10.28%
2	0.0028	0.00298	4.0	0.6065	0.0216	0.01309	0.00298	709.90	0.31	5.88%
3	0.0028	0.00270	4.0	0.5507	0.0233	0.01278	0.00270	222.20	0.31	3.67%
4	0.0028	0.00256	4.0	0.5114	0.0239	0.01219	0.00256	105.50	0.33	9.29%
5	0.0027	0.00268	4.0	0.5111	0.0225	0.01146	0.00268	91.40	0.35	0.63%
6	0.0027	0.00283	3.0	0.4354	0.0199	0.00867	0.00283	-	0.35	4.59%
7	0.0028	0.00293	3.0	0.4218	0.0208	0.00875	0.00293	159.00	0.34	4.37%
8	0.0027	0.00302	2.0	0.3061	0.0185	0.00567	0.00302	-	0.35	10.68%
9	0.0029	0.00293	2.5	0.3549	0.0203	0.00720	0.00293	101.30	0.35	1.06%
10	0.0028	0.00281	3.5	0.4569	0.0229	0.01046	0.00281	150.60	0.33	0.28%
11	0.0030	0.00284	3.5	0.4703	0.0218	0.01024	0.00284	130.80	0.34	5.63%
12	0.0029	0.00276	3.5	0.4644	0.0228	0.01059	0.00276	130.90	0.33	4.96%
13	0.0030	0.00280	3.5	0.4730	0.0222	0.01048	0.00280	115.70	0.33	7.30%
14	0.0028	0.00274	4.0	0.5038	0.0239	0.01204	0.00274	112.70	0.33	2.23%
15	0.0029	0.00287	4.0	0.5141	0.0232	0.01187	0.00287	87.60	0.34	1.08%
16	0.0028	0.00272	4.0	0.5294	0.0226	0.01190	0.00272	-	0.34	2.94%
17	0.0030	0.00288	4.0	0.5663	0.0212	0.01198	0.00288	-	0.33	4.35%
18	0.0029	0.00310	4.0	0.5787	0.021	0.01210	0.00310	125.80	0.33	6.45%
19A	0.0024	0.00275	2.5	0.3670	0.0208	0.00766	0.00275	334.60	0.33	12.73%
20A	0.0024	0.00269	2.5	0.3560	0.0213	0.00760	0.00269	246.40	0.33	10.78%
21A	0.0024	0.00254	3.0	0.4060	0.0218	0.00886	0.00254	176.80	0.34	5.51%
22A	0.0025	0.00254	3.5	0.4550	0.0228	0.01041	0.00254	145.90	0.34	1.57%
23A	0.0026	0.00236	4.0	0.5270	0.0255	0.01190	0.00236	37.10	0.34	10.17%
24A	0.0027	0.00230	4.0	0.5320	0.0228	0.01219	0.00230	25.80	0.33	17.39%
25A	0.0026	0.00219	4.0	0.5260	0.0232	0.01223	0.00219	15.60	0.33	18.72%
26A	0.0025	0.00265	2.5	0.3550	0.0219	0.00779	0.00265	188.10	0.32	5.66%
27A	0.0026	0.00254	2.5	0.3500	0.0217	0.00761	0.00254	152.00	0.33	2.36%
28A	0.0024	0.00223	4.0	0.4840	0.0247	0.01199	0.00223	104.80	0.33	7.62%
29A	0.0024	0.00221	4.0	0.4900	0.0244	0.01201	0.00221	67.60	0.33	8.60%
30A	0.0025	0.00234	4.0	0.4990	0.0239	0.01191	0.00234	91.70	0.34	6.84%
31A	0.0026	0.00218	4.0	0.5030	0.0245	0.01235	0.00218	17.70	0.32	19.27%
32A	0.0026	0.00251	2.5	0.3600	0.022	0.00791	0.00251	119.80	0.32	3.59%
33A	0.0026	0.00240	2.5	0.3380	0.0225	0.00763	0.00240	124.50	0.33	8.33%
34A	0.0021	0.00227	2.5	0.3300	0.025	0.00825	0.00227	39.90	0.30	7.49%
35A	0.0020	0.00223	2.5	0.3050	0.0261	0.00799	0.00223	54.90	0.31	10.31%
36A	0.0019	0.00210	2.5	0.3050	0.0268	0.00818	0.00210	53.40	0.31	9.52%
37A	0.0016	0.00202	2.5	0.3050	0.0269	0.00821	0.00202	41.50	0.30	20.79%
38A	0.0017	0.00199	2.5	0.3070	0.0269	0.00824	0.00199	37.40	0.30	14.57%
39A	0.0018	0.00203	2.5	0.3160	0.0263	0.00832	0.00203	36.50	0.30	11.33%

With respect to the experiments of Babaeyan-Koopaei (1997), simulations were obtained and presented on tables 36 and 37. The summary of the errors is shown in tables 38 and 39, respectively for $\Gamma/\rho gpSh_c$=0.10 and $\Gamma/\rho gpSh_c$=0. It was noticed that the uniform flow condition was not satisfied for every test, differing the longitudinal bed slope, S_{bed}, with the water surface slope, S_w, up to 20.79% (test 37A). Based on this, it was inferred that simulation errors (ΔQ, Δh_c, ΔW and ΔA) trends to increase when the difference between slopes, $\Delta S=|S_{bed}-S_w|/S_w$, was higher. Then, the results were ordered from the largest to the smallest ΔS for each set, obtaining averages for ΔQ, Δh_c, ΔW and ΔA for several ΔS ranges. This last were varying from cero, increasing the top limits of ΔS, *e.g.* $0<\Delta S<2\%$ and $0<\Delta S<4\%$ (tables 38 and 39); additionally the bottom limit was increasing as well, *e.g.* $0<\Delta S<2\%$ and $2<\Delta S<4\%$ (tables 40 and 41).

Hence, by comparing tables 38 and 39, it was observed that ΔW is smaller when $\Gamma/\rho gpSh_c$=0.10, improving ΔW from 13.89% to 5.54%, meanwhile Δh_c is in the same order of magnitude for both sets, and ΔA trends to be higher for $\Gamma/\rho gpSh_c$=0.10. Such tendencies did not change for the ranges analysed. With respect to the comparison of tables 40 and 41, a similar behaviour was detected, reducing ΔW significantly when $\Gamma/\rho gSh_c$=0.10, being both Δh_c sets close, and ΔA was smaller for $\Gamma/\rho gSh_c$=0. Then, it can be said that $\Gamma/\rho gSh_c$=0.10 improves the top width estimation, W, while Δh_c and ΔA attributed to the active bed, expressed as sediment discharge, Q_s.

From the analysis of both comparisons, *i.e.* experiments and simulations for Macky (1999) and Babaeyan-Koopaei (1997), it is possible to say that by using $\Gamma/\rho gSh_c$=0.10, the numerical model of Yu and Knight (1998) enhances the top width

estimation, W, and does not affect the prediction of the central depth, h_c.

Table 36. The results of the simulations attempting to reproduce the experiments of Babaeyan-Koopaei (1997) (table 35), employing the numerical model of Yu and Knight (1998) are shown below. The value for $\Gamma/\rho g S h_c$ was 0.10, and the lateral variation of f for the bank side, f/f_c, was used. Additionally, the errors with respect to the lab data are provided (ΔQ, ΔW and Δh_c).

		Yu and Knight model , Γ= 0.10						Errors			
Test No	ΔS	Q (L/s)	W (m)	h_c (m)	A (m^2)	$b/2$ (m)	$T/2$	ΔQ (%)	ΔW (%)	Δh_c (%)	ΔA (%)
37A	20.79%	2.50	0.3026	0.0307	0.00723	0.0690	0.0823	0.02%	0.79%	14.16%	11.95%
31A	19.27%	4.00	0.4593	0.0285	0.01118	0.1535	0.0762	0.04%	8.68%	16.12%	9.52%
25A	18.72%	4.00	0.4609	0.0283	0.01117	0.1546	0.0758	0.00%	12.38%	22.08%	8.61%
24A	17.39%	4.00	0.4799	0.0270	0.01121	0.1678	0.0721	0.00%	9.79%	18.25%	8.05%
38A	14.57%	2.50	0.2999	0.0312	0.00724	0.0663	0.0837	0.00%	2.32%	15.99%	12.22%
19A	12.73%	2.50	0.3759	0.0225	0.00728	0.1278	0.0602	0.00%	2.43%	8.32%	4.97%
39A	11.33%	2.50	0.3033	0.0306	0.00723	0.0697	0.0820	0.00%	4.01%	16.24%	13.07%
20A	10.78%	2.50	0.3692	0.0230	0.00727	0.1231	0.0615	0.00%	3.70%	8.15%	4.35%
8	**10.68%**	**2.00**	**0.3377**	**0.0205**	**0.00593**	**0.1142**	**0.0546**	**0.01%**	**10.31%**	**10.74%**	**4.60%**
35A	10.31%	2.50	0.3216	0.0278	0.00722	0.0864	0.0744	0.03%	5.45%	6.51%	9.56%
1	10.28%	4.00	0.5235	0.0244	0.01131	0.1965	0.0652	0.03%	5.52%	1.56%	7.80%
23A	10.17%	4.00	0.4906	0.0263	0.01123	0.1750	0.0703	0.00%	6.91%	3.03%	5.60%
36A	9.52%	2.50	0.3095	0.0296	0.00722	0.0756	0.0792	0.02%	1.46%	10.26%	11.66%
4	9.29%	4.01	0.5283	0.0242	0.01134	0.1995	0.0647	0.20%	3.31%	1.27%	7.03%
29A	8.60%	4.00	0.4643	0.0281	0.01118	0.1570	0.0751	0.00%	5.25%	15.03%	6.87%
33A	8.33%	2.50	0.3381	0.0259	0.00723	0.0999	0.0691	0.02%	0.02%	14.89%	5.23%
28A	7.62%	4.00	0.4677	0.0278	0.01119	0.1594	0.0744	0.00%	3.36%	12.60%	6.72%
34A	7.49%	2.50	0.3251	0.0273	0.00722	0.0894	0.0731	0.04%	1.49%	9.32%	12.46%
13	7.30%	3.50	0.5088	0.0222	0.01004	0.1953	0.0591	0.00%	7.57%	0.19%	4.15%
30A	6.84%	4.01	0.4878	0.0265	0.01124	0.1730	0.0709	0.19%	2.25%	10.88%	5.61%
18	6.45%	4.00	0.6344	0.0200	0.01157	0.2640	0.0532	0.05%	9.62%	5.00%	4.35%
2	5.88%	4.00	0.6090	0.0208	0.01151	0.2490	0.0555	0.02%	0.40%	3.70%	12.03%
26A	5.66%	2.50	0.3646	0.0234	0.00726	0.1198	0.0625	0.03%	2.71%	6.85%	6.80%
11	5.63%	3.50	0.5166	0.0218	0.01006	0.2001	0.0582	0.00%	9.83%	0.00%	1.77%
21A	5.51%	3.01	0.4104	0.0244	0.00861	0.1400	0.0652	0.19%	1.09%	11.93%	2.75%
12	4.96%	3.50	0.5038	0.0224	0.01003	0.1921	0.0598	0.01%	8.48%	1.75%	5.21%
6	**4.59%**	**3.00**	**0.4499**	**0.0219**	**0.00868**	**0.1665**	**0.0584**	**0.08%**	**3.33%**	**10.05%**	**0.10%**
7	4.37%	3.00	0.4646	0.0211	0.00870	0.1760	0.0563	0.13%	10.14%	1.44%	0.61%
17	**4.35%**	**3.99**	**0.5870**	**0.0216**	**0.01144**	**0.2360**	**0.0575**	**0.21%**	**3.66%**	**1.65%**	**4.50%**
3	3.67%	4.01	0.5546	0.0230	0.01139	0.2160	0.0613	0.14%	0.70%	1.50%	10.88%
32A	3.59%	2.50	0.3494	0.0247	0.00724	0.1087	0.0660	0.04%	2.93%	12.27%	8.49%
16	**2.94%**	**4.00**	**0.5578**	**0.0228**	**0.01139**	**0.2180**	**0.0609**	**0.09%**	**5.36%**	**0.88%**	**4.23%**
27A	2.36%	2.50	0.3524	0.0244	0.00723	0.1110	0.0652	0.14%	0.69%	12.44%	4.94%
14	2.23%	4.01	0.5627	0.0226	0.01141	0.2210	0.0603	0.13%	11.69%	5.44%	5.19%
22A	1.57%	3.50	0.4668	0.0244	0.00995	0.1682	0.0652	0.04%	2.60%	7.02%	4.36%
15	1.08%	4.00	0.5873	0.0216	0.01147	0.2360	0.0576	0.09%	14.23%	6.90%	3.40%
9	1.06%	2.50	0.3976	0.0211	0.00732	0.1425	0.0563	0.06%	12.03%	3.94%	1.61%
5	0.63%	4.01	0.5514	0.0231	0.01139	0.2140	0.0617	0.17%	7.88%	2.67%	0.65%
10	0.28%	3.50	0.5100	0.0221	0.01005	0.1960	0.0590	0.00%	11.61%	3.49%	3.97%

Table 37. The results of the simulations attempting to reproduce the experiments of Babaeyan-Koopaei (1997) (table 35), employing the numerical model of Yu and Knight (1998) are shown below. The value for $\Gamma/\rho g S h_c$ was 0, and the lateral variation of f for the bank side, f/f_c, was used. Additionally, the errors with respect to the lab data are provided (ΔQ, ΔW and Δh_c).

		Yu and Knight Model, Γ=0						Errors			
Test No	ΔS	Q (L/s)	W (m)	h_c (m)	A (m^2)	$b/2$ (m)	$T/2$	ΔQ (%)	ΔW (%)	Δh_c (%)	ΔA (%)
37A	20.79%	2.50	0.3280	0.0288	0.0075	0.0790	0.0850	0.00%	7.55%	7.01%	8.71%
31A	19.27%	4.00	0.5082	0.0267	0.0117	0.1755	0.0786	0.00%	1.04%	8.81%	4.89%
25A	18.72%	4.00	0.5102	0.0265	0.0118	0.1769	0.0783	0.00%	2.99%	14.38%	3.88%
24A	17.39%	4.00	0.5330	0.0253	0.0118	0.1920	0.0745	0.00%	0.18%	10.79%	3.10%
38A	14.57%	2.50	0.3249	0.0292	0.0075	0.0761	0.0863	0.00%	5.82%	8.63%	9.07%
19A	12.73%	2.50	0.4171	0.0211	0.0077	0.1464	0.0621	0.00%	13.66%	1.48%	0.16%
39A	11.33%	2.50	0.3291	0.0286	0.0075	0.0800	0.0845	0.00%	4.14%	8.90%	9.83%
20A	10.78%	2.50	0.4091	0.0216	0.0077	0.1410	0.0635	0.00%	14.91%	1.32%	0.71%
8	**10.68%**	**2.00**	**0.3748**	**0.0192**	**0.0063**	**0.1310**	**0.0564**	**0.00%**	**22.44%**	**3.74%**	**10.28%**
35A	10.31%	2.50	0.3514	0.0261	0.0075	0.0989	0.0768	0.00%	15.22%	0.16%	5.69%
1	10.28%	4.00	0.5844	0.0229	0.0120	0.2248	0.0674	0.00%	17.80%	7.78%	2.51%
23A	10.17%	4.00	0.5456	0.0246	0.0118	0.2003	0.0725	0.00%	3.53%	3.47%	0.42%
36A	9.52%	2.50	0.3367	0.0277	0.0075	0.0867	0.0817	0.00%	10.38%	3.29%	8.19%
4	9.29%	4.00	0.5895	0.0227	0.0120	0.2280	0.0667	0.00%	15.27%	5.17%	1.81%
29A	8.60%	4.00	0.5143	0.0263	0.0118	0.1796	0.0775	0.00%	4.97%	7.76%	2.02%
33A	8.33%	2.50	0.3718	0.0242	0.0076	0.1146	0.0713	0.00%	10.00%	7.57%	0.77%
28A	7.62%	4.00	0.5184	0.0261	0.0118	0.1824	0.0768	0.00%	7.11%	5.50%	1.82%
34A	7.49%	2.50	0.3561	0.0256	0.0075	0.1026	0.0755	0.00%	7.91%	2.39%	8.57%
13	7.30%	3.50	0.5694	0.0208	0.0106	0.2236	0.0611	0.00%	20.39%	6.49%	1.54%
30A	6.84%	4.00	0.5414	0.0248	0.0118	0.1975	0.0732	0.00%	8.49%	3.88%	0.64%
18	6.45%	4.00	0.7143	0.0187	0.0123	0.3022	0.0550	0.00%	23.44%	10.89%	1.79%
2	5.88%	4.00	0.6844	0.0195	0.0122	0.2849	0.0573	0.00%	12.85%	9.71%	6.54%
26A	5.66%	2.50	0.4038	0.0219	0.0076	0.1374	0.0645	0.00%	13.73%	0.04%	1.95%
11	5.63%	3.50	0.5783	0.0204	0.0107	0.2290	0.0601	0.00%	22.95%	6.26%	4.11%
21A	5.51%	3.00	0.4545	0.0229	0.0091	0.1599	0.0673	0.00%	11.95%	4.87%	2.26%
12	4.96%	3.50	0.5629	0.0210	0.0106	0.2196	0.0618	0.00%	21.21%	7.86%	0.35%
6	**4.59%**	**3.00**	**0.5021**	**0.0205**	**0.0092**	**0.1907**	**0.0603**	**0.00%**	**15.33%**	**3.06%**	**5.83%**
7	4.37%	3.00	0.5188	0.0198	0.0092	0.2011	0.0583	0.00%	23.01%	4.72%	5.35%
17	**4.35%**	**4.00**	**0.6608**	**0.0202**	**0.0122**	**0.2710**	**0.0594**	**0.00%**	**16.70%**	**4.79%**	**1.61%**
3	3.67%	4.00	0.6207	0.0215	0.0121	0.2471	0.0633	0.00%	12.71%	7.76%	5.67%
32A	3.59%	2.50	0.3856	0.0231	0.0076	0.1246	0.0681	0.00%	7.11%	5.17%	3.92%
16	**2.94%**	**4.00**	**0.6250**	**0.0213**	**0.0121**	**0.2497**	**0.0628**	**0.00%**	**18.07%**	**5.57%**	**1.44%**
27A	2.36%	2.50	0.3894	0.0229	0.0076	0.1274	0.0673	0.00%	11.26%	5.36%	0.04%
14	2.23%	4.00	0.6294	0.0212	0.0121	0.2523	0.0624	0.00%	24.93%	11.33%	0.38%
22A	1.57%	3.50	0.5196	0.0229	0.0105	0.1925	0.0673	0.00%	14.19%	0.27%	0.94%
15	1.08%	4.00	0.6594	0.0202	0.0122	0.2702	0.0595	0.00%	28.27%	12.81%	2.48%
9	1.06%	2.50	0.4420	0.0198	0.0077	0.1628	0.0582	0.00%	24.55%	2.47%	7.28%
5	0.63%	4.00	0.6166	0.0216	0.0120	0.2446	0.0637	0.00%	20.65%	3.83%	5.10%
10	0.28%	3.50	0.5718	0.0207	0.0106	0.2251	0.0608	0.00%	25.16%	9.74%	1.77%

Table 38. The ranges of error average analysed, corresponding to different ΔS of table 36, where $\Gamma/\rho gpSh_c$=0.10 was used.

	Average		
ΔS	ΔW (%)	Δh_c (%)	ΔA (%)
0<ΔS<2%	9.67%	4.80%	2.80%
0<ΔS<4%	6.97%	5.66%	4.77%
0<ΔS<5%	6.81%	5.10%	4.15%
0<ΔS<6%	6.08%	5.22%	4.53%
0<ΔS<8%	5.81%	5.74%	4.99%
0<ΔS<10%	5.32%	6.42%	5.39%
0<ΔS<11%	5.49%	6.35%	5.55%
0<ΔS<15%	5.27%	6.97%	5.94%
0<ΔS<21%	5.54%	8.06%	6.31%

Table 39. The ranges of error average analysed, corresponding to different ΔS of table 37, where $\Gamma/\rho gpSh_c$=0 was used.

	Average		
ΔS	ΔW (%)	Δh_c (%)	ΔA (%)
0<ΔS<2%	22.56%	5.83%	3.51%
0<ΔS<4%	18.69%	6.43%	2.90%
0<ΔS<5%	18.80%	6.05%	3.01%
0<ΔS<6%	18.03%	5.87%	3.17%
0<ΔS<8%	17.04%	5.86%	3.10%
0<ΔS<10%	16.02%	5.87%	3.12%
0<ΔS<11%	15.83%	5.47%	3.24%
0<ΔS<15%	15.15%	5.54%	3.51%
0<ΔS<21%	13.89%	6.03%	3.68%

Table 40. The ranges of error average analysed, corresponding to different ΔS of table 36, where $\Gamma/\rho g S h_c$=0.10 was used.

	Average		
ΔS	ΔW (%)	Δh_c (%)	ΔA (%)
0<ΔS<2%	9.67%	4.80%	2.80%
2<ΔS<4%	4.27%	6.51%	6.75%
4<ΔS<5%	6.40%	3.72%	2.61%
5<ΔS<6%	3.51%	5.62%	5.84%
6<ΔS<8%	4.86%	7.60%	6.66%
8<ΔS<10%	2.51%	10.36%	7.70%
10<ΔS<11%	6.38%	6.00%	6.38%
11<ΔS<15%	2.92%	13.51%	10.09%
15<ΔS<21%	7.91%	17.65%	9.53%

Table 41. The ranges of error average analysed, corresponding to different ΔS of table 37, where $\Gamma/\rho g S h_c$=0 was used.

	Average		
ΔS	ΔW (%)	Δh_c (%)	ΔA (%)
0<ΔS<2%	22.56%	5.83%	3.51%
2<ΔS<4%	14.82%	7.04%	2.29%
4<ΔS<5%	19.06%	5.11%	3.28%
5<ΔS<6%	15.37%	5.22%	3.71%
6<ΔS<8%	13.47%	5.83%	2.87%
8<ΔS<10%	10.15%	5.95%	3.20%
10<ΔS<11%	14.78%	3.29%	3.92%
11<ΔS<15%	7.87%	6.34%	6.35%
15<ΔS<21%	2.94%	10.25%	5.15%

6.9 Discussion and findings

With respect to the findings obtained in this chapter, it is possible to summarize them as:

- A good approximation was found by using the experimental friction factor, f, for the PVC surface experiments, and by employing the variation of f with respect to the centreline friction factor, f_c, f/f_c, for the rough surface set.
- The use of the methodology of Lundgren and Jonsson (1964) to determine λ for self-formed banksides yields approximately 0.070, being in agreement with other authors that obtained such result experimentally, *i.e.* Nezu and Nakagawa (1993). Hence it is recommended to use λ=0.07 for practical purposes.
- It was confirmed experimentally that the dimensionless shape of the depth average velocity, $U_d/Q/A$, and shear stress lateral distributions, $\tau_0/\rho gRS$, are not affected by the slope. Such an observation was spotted on chapter 3.
- Different dimensionless velocity, $U_d/(Q/A)$, and shear stress, $\tau_0/\rho gRS$, lateral distribution shapes were found, changing for each bed surface. This alteration was attributed by the influence of the secondary flow, being corroborated by obtaining a distinct $\Gamma/\rho gSR$ per surface (Table 31).

$$\frac{V}{U*} = \frac{6\delta}{\kappa\pi^2}\sin\left(\frac{\pi y}{H}\right)\left[2\cos\left(\frac{\pi z}{H}\right) - \pi\left(2\frac{z}{H} - 1\right)\sin\left(\frac{\pi z}{H}\right)\right] \quad (101)$$

Additionally the equation 101 proposed by Ikeda(1981) is in agreement with the previous observation. It expresses the relationship between transversal velocity, V, shear velocity, $U*$, and subsequently to boundary shear stress, τ_0, same variable that changes according to the bed surface.

- $\Gamma/\rho gSR=pC$ values for smooth and rough surfaces were proposed in table 31, for the three depths analysed, recommending $C=0.093$, or 0.10 for practical purposes, for the prediction of self-formed cross sections, with panel factors as $p1=p2=1$, $p3=1$, $p4=1$, $p5=0.75$, and $p6=1.50$. The rest of the $\Gamma/\rho gSR=pC$ can be used to assess existing sections, i.e. the discharge, velocity and shear stress distribution when the section does not work at bankfull.

- With respect to the flow cells identified on section 5.2.2. They followed the same Γ signal variation for the smooth surface experiments only. This last in agreement with the research of Omran (2005), whom used glass surface and obtained p3>0, p4>0, p5<0 and p6<0. However, for rough surface, the same pattern was not confirmed, finding p3>0, p4>0, p5>0 and p6>0.

- This variation in the flow pattern is attributed to the boundary surface.

CHAPTER 7

CONCLUSIONS

The aim of this research was to investigate the capacity of a simple quasi 2D flow model, *i.e.* the SKM (Shiono and Knight, 1990), in combination with bank side equations, *i.e.* the Yu and Knight model (1998), to determine the bed profile of an alluvial channel, incorporating the secondary flow variables. In order to accomplish this purpose, the numerical model was build and analysed, a physical model was constructed, representing a self-formed channel, and 18 lab experiments were ran. Later a calibration-validation process was carried out.

The document is organized in 7 chapters, being the first one the introduction stating the problematic, the aim and objectives of the thesis. The second one consists of the literature review, where the different bank profile equations were described and the knowledge gap identified. With this respect, it was found that the central bed of a self-formed cross section is not flat, as some numerical models try to represent. Also it was not clear which value of dimensionless eddy viscosity, λ, was appropriate for self-formed geometries. Additionally the lateral variation of the friction factor, f, on the bankside was unknown and the effect of Γ on the formation of cross sections had not been evaluated. On the other hand the numerical model studied (*i.e.* Yu and Knight, 1998) was developed for granular, uniform material and without vegetation. Such model has the potential to develop a graphical solution, similar to the one of Diplas and Vigilar (1998) and to propose a deformation of a channel along

time, in the same way than Paquier and Khodashenas (2002).

From the previous findings it was decided to explore the dimensionless eddy viscosity, λ, the lateral variation of the friction factor, f, and the secondary flow gradient, Γ. Subsequently the behaviour of the numerical model was analysed in chapter 3, discovering that the bank side width, T, is affected by the central bed width, b. This last, due to the lateral geometry of the section is related to the boundary shear stress, τ_0, distribution, being affected by b, and it is inversely proportional to T, but reaching an stable limit, sl, when $b/2h_c$>2 approximately, being this the case of wide channels ($B/h>15$). Additionally, the impact of Γ, λ, φ and S on the numerical model were identified, finding the following relationships:

If λ, φ and S are constants, then:

$$\Gamma \propto f,\ A,\ Q,\ \frac{1}{U_d},\ \tau_{max},\ T,\ h_c \tag{102}$$

If Γ, φ and S are constants, then:

$$\lambda \propto f,\ A,\ Q,\ \frac{1}{U_d},\ \frac{1}{\tau_{max}},\ T,\ h_c,\ \frac{T}{h_c} \tag{103}$$

If Γ, λ and S are constants, then:

$$\varphi \propto \frac{1}{A}, \frac{1}{Q}, V,\ \tau_{max},\ \frac{1}{T},\ h_c,\ \left(\frac{T}{h_c}\right)^{-1} \tag{104}$$

If Γ, λ and φ are constants, then:

$$S \propto f,\ \frac{1}{A}, \frac{1}{Q},\ \frac{1}{V}, \frac{1}{U_d},\ \frac{1}{T},\ \frac{1}{h_c} \tag{105}$$

From the relationships above, it is noted the impact of Γ and λ, on the estimation of the transversal geometry, the hydraulic area and subsequently the

water capacity of the section.

Based on the experimental work, validation and calibration (chapters 5 and 6), where a relationship was proposed for the lateral variation of the friction factor, f, values found for Γ and λ obtained from the methodology of Lundgren and Jonsson (1964). It was observed a good performance for the numerical model , improving the estimation of the top width, W, significantly, without affecting the central depth, h_c.

With respect to the friction factor variation, it was determined from the PVC surface experiments, relating f to the central friction factor, f/f_c, that was assumed as the global one obtained from the corresponding stage discharge curves. In the future it is recommended to use the global f of the section for f_c and then carry on with the variation of f per SKM panels.

About the dimensionless eddy viscosity, λ, the proposal of Lundgren and Jonsson (1964) was applied obtaining values close to 0.070, as other researchers determined based on experiments, *i.e.* Nezu and Nakagawa (1993). Hence, for practical reasons λ=0.07 is recommended. The advantage of this methodology is that it is based on the geometry of the section, and it is valid for curved shapes.

As was noted during the numerical model behaviour (section 3.4), it was confirmed during the experiments, that, the dimensionless shape of the velocity, $U_d/Q/A$, and shear stress, $\tau_0/\rho gRS$, distributions are not affected by the slope. However, they are highly affected by the bed surface, obtaining a characteristic profile per depth and per surface. This difference is attributed to boundary shear stress, τ_0, affecting the lateral distribution. Such observations are in agreement with the work of Ikeda (1981), whom proposed a relationship for the transversal velocity,

V.

With respect to the secondary flow, values were obtained for $\Gamma/\rho gSR$ per depth and surface, reaching a good approximation during the calibration. The range of values can be observed on table 31. There can be observed that the experiments on smooth surface are producing the following variation of secondary flow factors: $p3>0$, $p4>0$ and $p5<0$, $p6<0$. On the other hand, the sets carried out on rough surface are showing: $p3>0$, $p4>0$, $p5>0$, and $p6>0$. It is evident that the PVC experiments are following the same signal variation that a trapezoidal bankside, as Omran and Knight (2006) shown, using the data of Tominaga *et al.*(1989), proposing two flow cells, but they did experiments in glass surface.

For practical purposes, during the estimation of self-formed cross sections, it is recommended the use of $C=0.010$, with the following panel factors: $p1=p2=1$, $p3=1$, $p4=1$, $p5=0.75$, and $p6=1.50$, where $\Gamma/\rho gSR=pC$ Also in combination with the relationship f/fc for the bank side friction factor, and using λ=0.070.

However, there is still work to do in this area, since the behaviour of the secondary flow cells on the central belt were not taken into account, and evidence show us that the depth is not constant, making room for a further research.

It should be mentioned that this research was founded by the National Council of Science and Technology (CONACYT, Mexico) in combination with a PGTA. A conference paper was produced from this research and presented in a symposium organized by CONACYT in Strasburg, November 2012.

References

ABRIL, J. B. & KNIGHT, D. W. 2004. Stage-discharge prediction for rivers in flood applying a depth-averaged model. *Journal of Hydraulic Research,* 42**,** 616-629.

ACKERS, P. & WHITE, W. R. 1975. SEDIMENT TRANSPORT - NEW APPROACH AND ANALYSIS. *Journal of the Hydraulics Division-Asce,* 101**,** 621-625.

AKAN, A. O. 2006. *Open channel hydraulics*, Butterworth-Heinemann.

BABAEYAN-KOOPAEI, K. 1997 *A study of straight stable channels and their interactions with bridge structures. .* PhD, University of Newcastle upon Tyne

BABAEYAN-KOOPAEI, K. & VALENTINE, E. M. 1998. Bank Profiles of Self-formed Straight Stable Channels. *Third International Conference on Hydroscience and Engineering.* Cottbus, Germany.

BABAEYAN-KOOPAEI, K., VALENTINE, E. M. & SWAILES, D. C. 2000. Optimal design of parabolic-bottomed triangle canals. *Journal of Irrigation and Drainage Engineering,* 126**,** 408-411.

BARLOW, J. B., RAE, W. H. & POPE, A. 1999. *Low-speed wind tunnel testing,* New York, USA, John Wiley and Sons, Inc.

CAO, S. & KNIGHT, D. W. 1996a. Regime theory of alluvial channels based upon the concepts of stream power and probability. *Proceedings of the Institution of Civil Engineers-Water Maritime and Energy,* 118**,** 160-167.

CAO, S. Y. & KNIGHT, D. W. 1996b. *Shannon's entropy-based bank profile equation of threshold channels,* Rotterdam, A a Balkema.

CAO, S. Y. & KNIGHT, D. W. 1997. Entropy-based design approach of threshold alluvial channels. *Journal of Hydraulic Research,* 35**,** 505-524.

CAO, S. Y. & KNIGHT, D. W. 1998. Design for hydraulic geometry of alluvial channels. *Journal of Hydraulic Engineering-Asce,* 124**,** 484-492.

CHOW, V. T. 1959. *Open-channel hydraulics,* Tokyo; London, McGraw-Hill.

DEY, S. 2001. Bank profile of threshold channels: A simplified approach. *Journal of Irrigation and Drainage Engineering-Asce,* 127**,** 184-187.

DIPLAS, P. 1990. Characteristics of Self-Formed Straight Channels. *Journal of Hydraulic Engineering,* 116**,** 707-728.

DIPLAS, P. & VIGILAR, G. 1992. HYDRAULIC GEOMETRY OF THRESHOLD CHANNELS. *Journal of Hydraulic Engineering-Asce,* 118**,** 597-614.

DIPLAS, P. & VIGILAR, G. 1998. Hydraulic Geometry of Stable Channels with Active Beds Designed for Maximum Flow Conveyance. *Third International Conference on Hydroscience and Engineering.* Cottbus, Berlin, Germany.

GLOVER, R. E. & FLOREY, Q. L. 1951. *Stable channel profiles,* Denver, U.S. Dept. of the Interior, Bureau of Reclamation, Design and Construction Division.

GRIFFITHS, G. A. 1981. Stable-channel design in gravel-bed rivers. *Journal of Hydrology,* 52**,** 291-305.

HENDERSON, F. M. 1961. Stability of alluvial channels. *ASCE -- Proceedings -- Journal of the Hydraulics Division,* 87**,** 109-138.

HUANG, H. Q., NANSON, G. C. & FAGAN, S. D. 2002. Hydraulic geometry of straight alluvial channels and the principle of least action. *Journal of Hydraulic Research,* 40**,** 153-160.

IKEDA, S. 1981. SELFFORMED STRAIGHT CHANNELS IN SANDY BEDS. *Journal of the Hydraulics Division-Asce,* 107**,** 389-406.

IKEDA, S. 1982. INCIPIENT MOTION OF SAND PARTICLES ON SIDE SLOPES. 108**,** 95-114.

IKEDA, S., PARKER, G. & KIMURA, Y. 1988. STABLE WIDTH AND DEPTH OF STRAIGHT GRAVEL RIVERS WITH HETEROGENEOUS BED MATERIALS. *Water Resources Research,* 24**,** 713-722.

JIN, M. 1995. Boundary shear stress measurements by two tubes. *Journal of Hydraulic Research,* 33**,** 385-395.

JULIEN, P. Y. & WARGADALAM, J. 1995. ALLUVIAL CHANNEL GEOMETRY - THEORY AND APPLICATIONS. *Journal of Hydraulic Engineering-Asce,* 121**,** 312-325.

KENNEDY, R. G. 1895. The Prevention of Silting in Irrigation Canals. *: Minutes of the Proceedings,* 119**,** 281-290.

KHODASHENAS, S. R. & PAQUIER, A. 1999. A geometrical method for computing the distribution of boundary shear stress across irregular straight open channels. *Journal of Hydraulic Research,* 37**,** 381-388.

KNIGHT, D. W. 2006. *River flood hydraulics: theoretical issues and stage-discharge relationships*.

KNIGHT, D. W., C, J. B. A. & STOKES, N. 1996. REFINED CALIBRATION OF A DEPTH-AVERAGED MODEL FOR TURBULENT FLOW IN A COMPOUND CHANNEL. *Proceedings of the ICE - Water Maritime and Energy* [Online], 118.

KNIGHT, D. W., C. MCGAHEY, R. LAMB & SAMUELS, P. 2010. *Practical channel hydraulics : roughness, conveyance and afflux,* Boca Raton [Fla.]; London, CRC Press.

KNIGHT, D. W., OMRAN, M. & TANG, X. N. 2007. Modeling depth-averaged velocity and boundary shear in trapezoidal channels with secondary flows. *Journal of Hydraulic Engineering-Asce,* 133**,** 39-47.

LACEY, G. 1930. Stable channels in alluvium. *Institution of Civil Engineers -- Minutes of Proceedings,* 22**,** 36.

LEE, J. S. & JULIEN, P. Y. 2006. Downstream hydraulic geometry of alluvial channels. *Journal of Hydraulic Engineering-Asce,* 132**,** 1347-1352.

LEOPOLD, L. & MADDOCK, T. 1953. The Hydraulic Geometry of Stream Channels and Some Physiographic Implications. *US Geological Survey*.

LUNDGREN, H. & JONSSON, I. G. 1964. Shear and velocity distribution in shallow channels. *ASCE -- Proceedings, Journal of the Hydraulics Division,* 90**,** 1-21.

MACKY, G. H. 1999. Large flume experiments on the stable straight gravel bed channel. *Water Resour. Res.,* 35**,** 2601-2603.

MIRONENKO, A. P., WILLARDSON, L. S. & JENAB, S. A. 1984. Parabolic Canal Design and Analysis. *Journal of Irrigation and Drainage Engineering,* 110**,** 241-246.

NEZU, I. & NAKAGAWA, H. 1993. *Turbulence in open-channel flows,* Rotterdam, Balkema.

NEZU, I., ONITSUKA, K., SAGARA, Y. & IKETANI, K. Year. Secondary currents and bed shear stress in compound open-channel flows with shallow flood plain. *In:* XXVIII Congress IAHR, 1999 Graz , Austria.

OMRAN, M. 2005. *Modelling stage-discharge curves, velocity and boundary shear stress distributions in natural and artificial channels using a depth-averaged approach.* PhD Thesis, The University of Birmingham, England, UK.

OMRAN, M. & KNIGHT, D. 2006. Modelling the distribution of boundary shear stress in open channel flows. *In:* ELSA C. T. L. ALVES, ANTÓNIO H. CARDOSO, JOÃO G. A. B. LEAL & FERREIRA, R. M. L. (eds.) *River Flow 2006.* Lisbon, Portugal: Taylor & Francis.

PAQUIER, A. & KHODASHENAS, S. R. 2002. River bed deformation calculated from boundary shear stress. *Journal of Hydraulic Research,* 40**,** 603-609.

PARKER, G. 1978a. SELF-FORMED STRAIGHT RIVERS WITH EQUILIBRIUM BANKS AND MOBILE BED .1. SAND-SILT RIVER. *Journal of Fluid Mechanics,* 89**,** 109-125.

PARKER, G. 1978b. SELF-FORMED STRAIGHT RIVERS WITH EQUILIBRIUM BANKS AND MOBILE BED .2. GRAVEL RIVER. *Journal of Fluid Mechanics,* 89**,** 127-&.

PARKER, G. 1979. HYDRAULIC GEOMETRY OF ACTIVE GRAVEL RIVERS. *Journal of the Hydraulics Division-Asce,* 105**,** 1185-1201.

PATEL, V. C. 1965. Calibration of the Preston tube and limitations on its use in pressure gradients. *Journal of Fluid Mechanics,* 23**,** 185-208.

PRESTON, J. H. 1954. The determination of turbulent skin friction by means of Pitot tubes. *J . Roy. Aero. Soc.,* 58**,** 109.

SHANNON, C. E. 1951. PREDICTION AND ENTROPY OF PRINTED ENGLISH. *Bell System Technical Journal,* 30**,** 50-64.

SHIONO, K. & KNIGHT, D. W. 1990. Mathematical models of flow in two or multi stage straight channels. *International conference on river flood hydraulics. Wallingford, 1990***,** 229-238.

SHIONO, K. & KNIGHT, D. W. 1991. Turbulent open-channel flows with variable depth across the channel. *Journal of Fluid Mechanics,* 222**,** 617-46.

SIMONS, D. B. & SENTURK, F. 1992. *Sediment transport technology : water and sediment dynamics,* Littleton, Colo., Water Resources Publications.

STEBBINGS, J. 1963. Shapes of self-formed model alluvial channels. *Institution of Civil Engineers -- Proceedings,* 25**,** 485-510.

STERLING, M. 1998. *A study of boundary shear stress, flow resistance and the free overfall in open channels with a circular cross-section.* . PhD, University of Birmingham.

TOMINAGA, A., NEZU, I., EZAKI, K. & NAKAGAWA, H. 1989. *Three-dimensional turbulent structure in straight open channel flows,* Delft, PAYS-BAS, International Association for Hydraulic Research.

VIGILAR, G. G. & DIPLAS, P. 1997. Stable channels with mobile bed: Formulation and numerical solution. *Journal of Hydraulic Engineering-Asce,* 123**,** 189-199.

VIGILAR, G. G. & DIPLAS, P. 1998. Stable channels with mobile bed: Model verification and graphical solution. *Journal of Hydraulic Engineering-Asce,* 124**,** 1097-1108.

WANG, Z. Q. & CHENG, N. S. 2005. Secondary flows over artificial bed strips. *Advances in Water Resources,* 28**,** 441-450.

WHITE, W. R., PARIS, E. & BETTESS, R. 1980. THE FRICTIONAL CHARACTERISTICS OF ALLUVIAL STREAMS - A NEW APPROACH. *Proceedings of the Institution of Civil Engineers Part 2-Research and Theory,* 69**,** 737-750.

YALIN, M. S. & DA SILVA, A. M. F. 1999. Regime channels in cohesionless alluvium. *Journal of Hydraulic Research,* 37**,** 725-742.

YU, G. & KNIGHT, D. W. 1998. Geometry of self-formed straight threshold channels in uniform material. *Proceedings of the Institution of Civil Engineers-Water and Maritime Engineering,* 130**,** 31-41.

YUEN, K. W. H. 1989. *A study of boundary shear stress, flow resistance and momentum transfer in open channels with simple and compound trapezoidal cross sections.* PhD, University of Birmingham.

Appendix A

Table 42. Data from Yu and Knight (1998), it is observed that T/h_c is constant per method, d=0.88mm

Q (L/s)	Authors	S_0 / 1000	T (cm)	h_c (cm)	T / h_c
50.00	USBR	0.412	**110.60**	17.70	6.2486
200.50	USBR	0.217	**209.80**	33.50	6.2627
150.10	USBR	0.248	**183.60**	29.30	6.2662
101.00	USBR	0.298	**152.90**	24.40	6.2664
24.40	The model	0.412	**90.60**	11.90	7.6134
72.40	The model	0.248	**151.00**	19.80	7.6263
18.80	The model	0.466	**80.10**	10.50	7.6286
75.60	The model	0.243	**154.10**	20.20	7.6287
136.90	The model	0.184	**203.80**	26.70	7.6330
150.40	The model	0.176	**213.00**	27.90	7.6344
90.80	The model	0.223	**168.00**	22.00	7.6364
181.80	The model	0.161	**233.00**	30.50	7.6393
45.60	The model	0.308	**121.50**	15.90	7.6415
96.20	The model	0.217	**172.70**	22.60	7.6416
50.00	The model	0.295	**126.90**	16.60	7.6446
100.10	The model	0.213	**175.90**	23.00	7.6478
37.60	The model	0.337	**110.90**	14.50	7.6483
56.80	The model	0.278	**134.70**	17.60	7.6534
48.90	The model	0.298	**125.60**	16.40	7.6585
199.90	The model	0.154	**243.60**	31.80	7.6604
100.00	Cao and Knight	0.337	**172.80**	21.60	8.0000
200.00	Cao and Knight	0.243	**239.30**	29.90	8.0033
50.00	Cao and Knight	0.466	**124.90**	15.60	8.0064
150.00	Cao and Knight	0.278	**209.10**	26.10	8.0115
50.00	Diplas	0.308	**135.10**	16.10	8.3913
150.00	Diplas	0.184	**226.20**	26.90	8.4089
100.00	Diplas	0.223	**187.00**	22.20	8.4234
200.00	Diplas	0.161	**259.10**	30.70	8.4397

Appendix B

The current appendix presents the cross sectional graphs, velocity and shear stress profiles for the cases I to III of the simulations of section 3.4.1. With respect to the vertical lines on the left hand side, they are representing the centreline of the channel. The origin the toe (junction between flatbed and bankside), and the margin is located at the right extreme.

About the cross sections, the inflection points on the bankside are due to they were plotted with four point only. But their effect cannot be appreciated on the velocity or shear stress distributions.

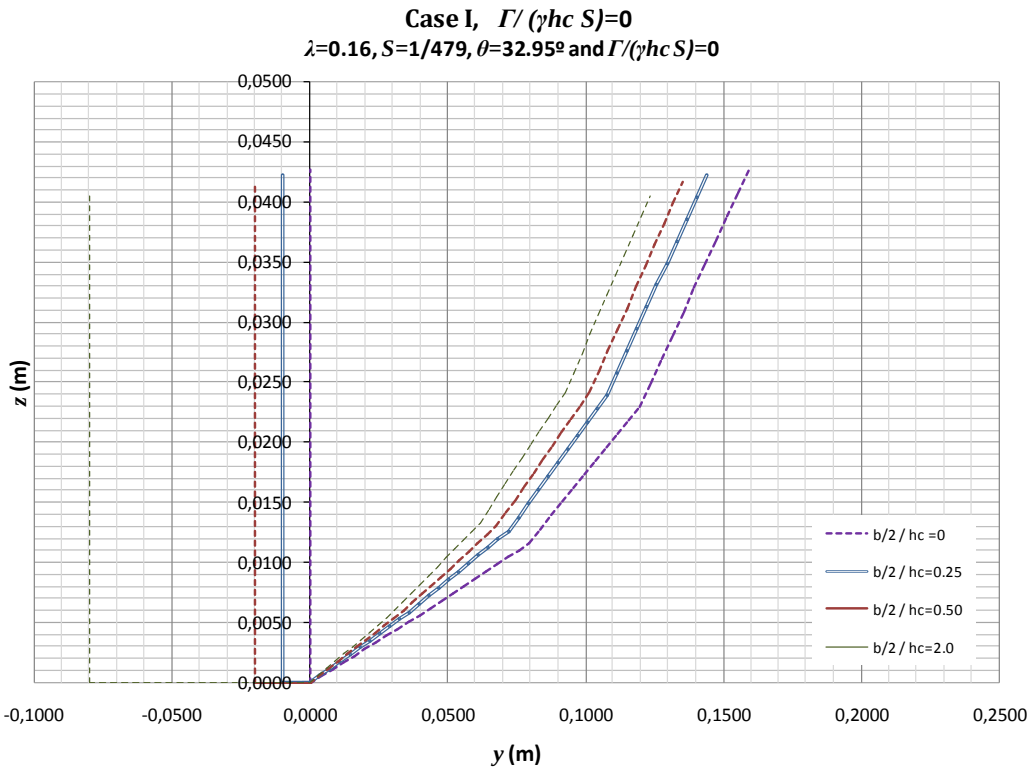

Figure B- 1. Cross sections obtained for λ=0.16,S=1/479, θ=32.95º, and $\Gamma/\gamma RS$=0, when $b/2h_c$=0, 0.25, 0.5 and 2.0. The origin (y,z) is placed at the toe.

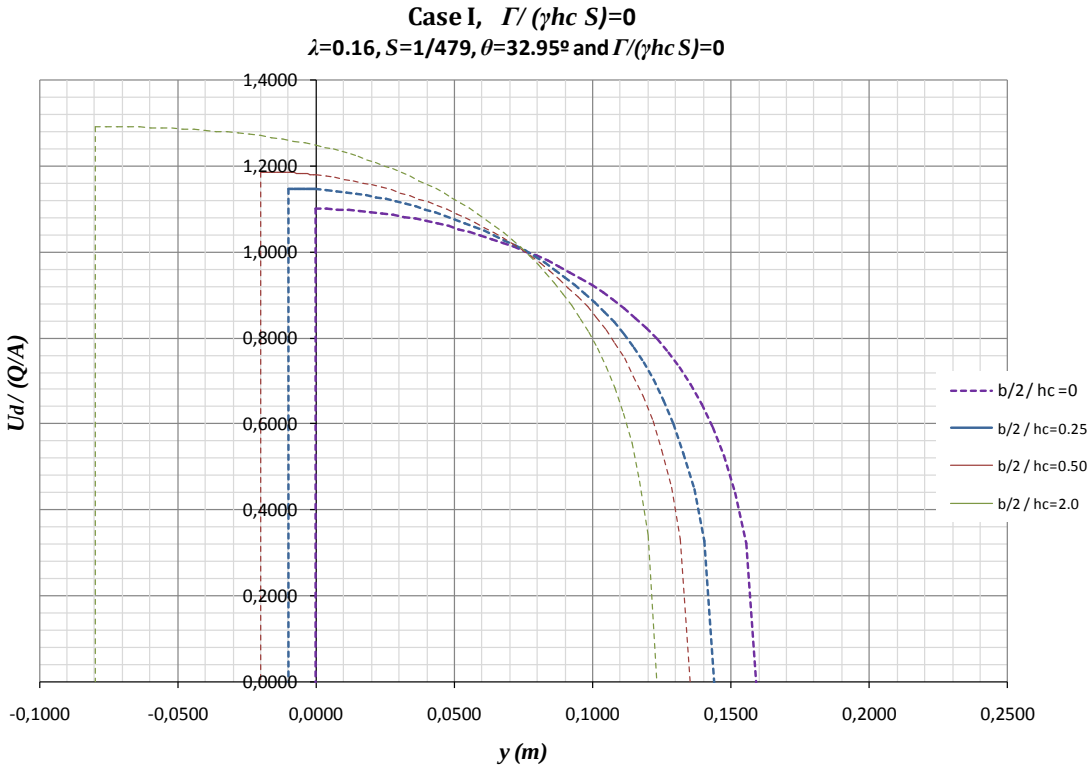

Figure B- 2. Velocity profiles obtained for λ=0.16,S=1/479, θ=32.95°, and $\Gamma/\gamma RS$=0, when $b/2h_c$=0, 0.25, 0.5 and 2.0. The origin (y,z) is placed at the toe.

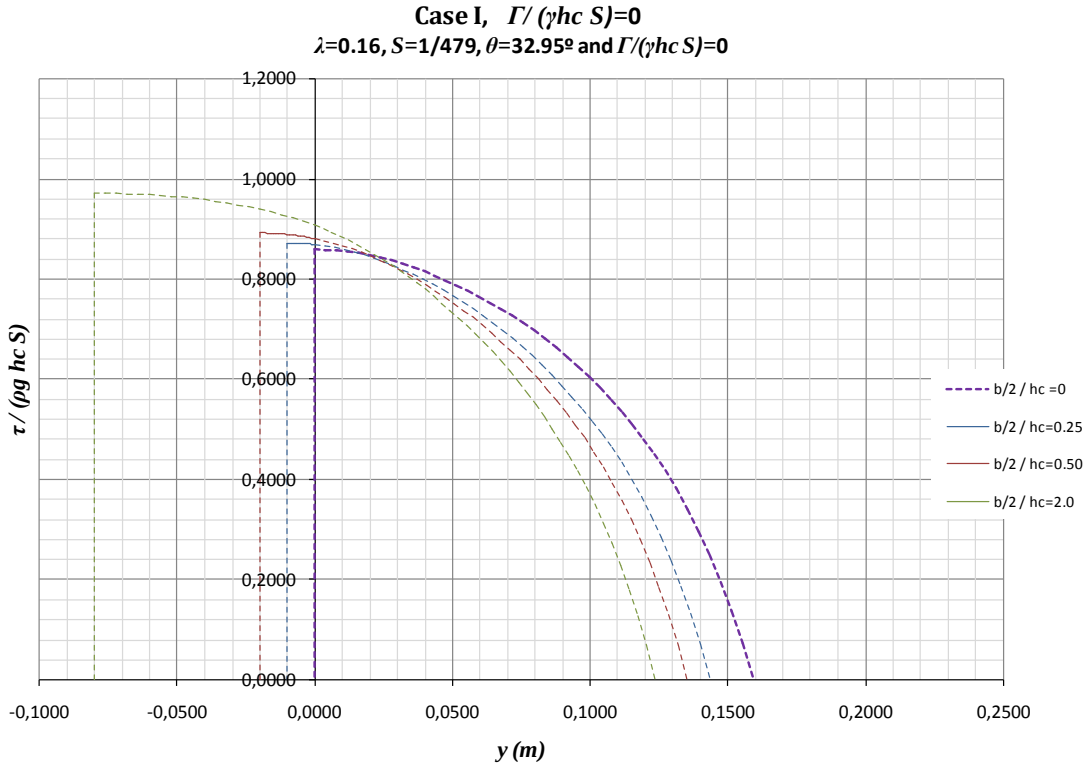

Figure B- 3. Shear profiles obtained for λ=0.16,S=1/479, θ=32.95°, and $\Gamma/\gamma RS$=0, when $b/2h_c$=0, 0.25, 0.5 and 2.0. The origin (y,z) is placed at the toe.

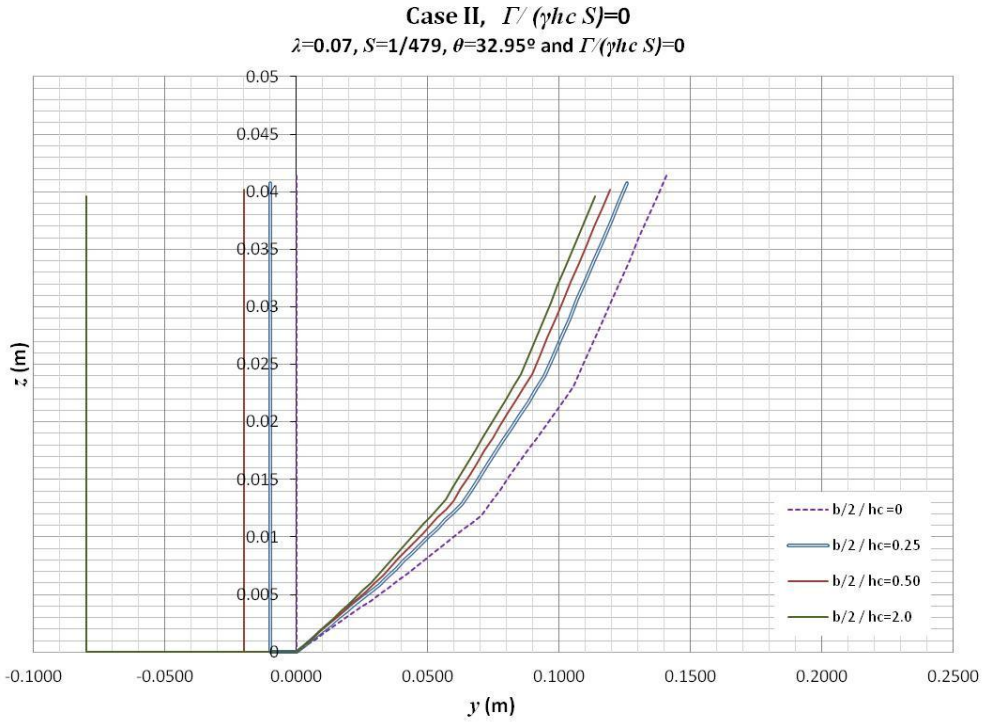

Figure B- 4. Cross sections obtained for λ=0.07,S=1/479, θ=32.95º, and $\Gamma/\gamma RS$=0, when $b/2h_c$=0, 0.25, 0.5 and 2.0. The origin (y,z) is placed at the toe.

Figure B- 5. Velocity profiles obtained for λ=0.07,S=1/479, θ=32.95º, and $\Gamma/\gamma RS$=0, when $b/2h_c$=0, 0.25, 0.5 and 2.0. The origin (y,z) is placed at the toe.

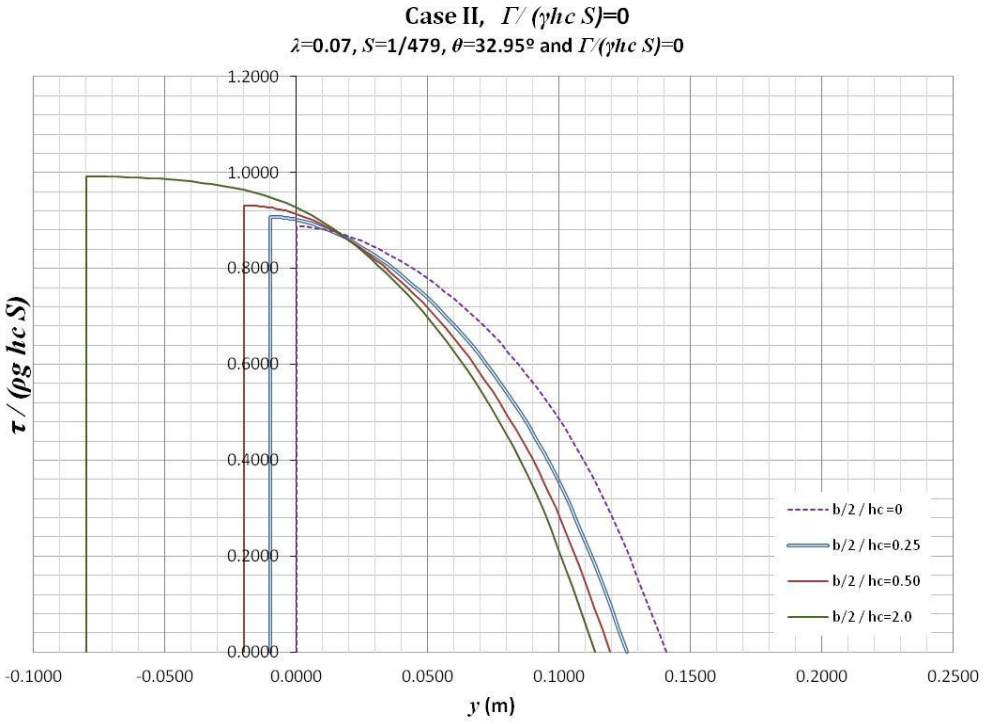

Figure B- 6. Shear stress profiles obtained for λ=0.07,S=1/479, θ=32.95º, and $\Gamma/\gamma RS$=0, when $b/2h_c$=0, 0.25, 0.5 and 2.0. The origin (y,z) is placed at the toe.

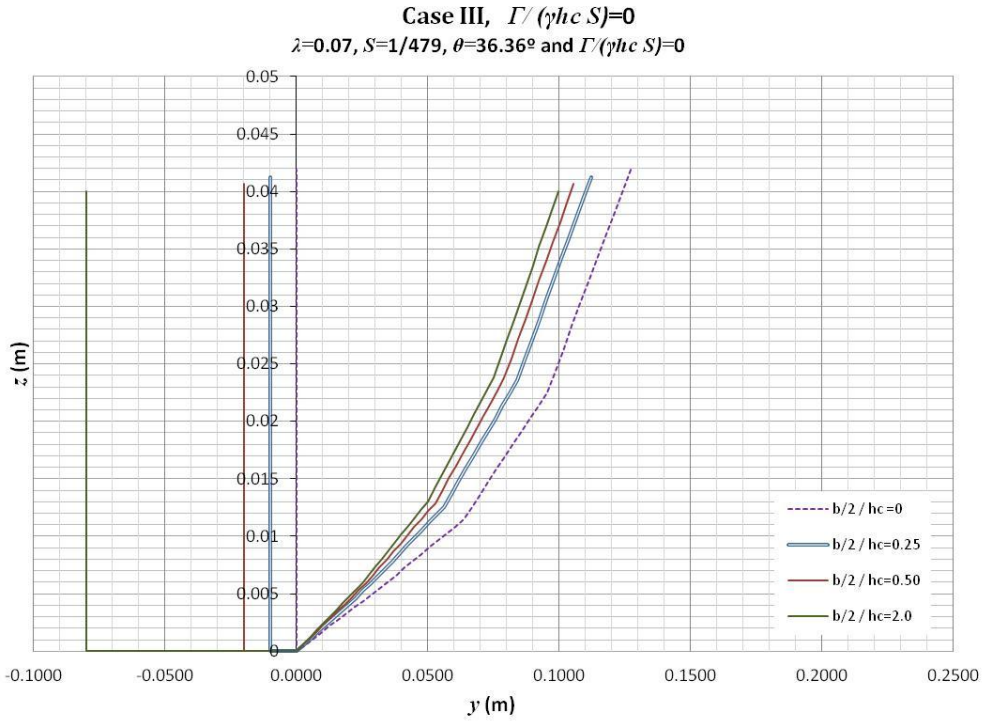

Figure B- 7. Cross sections obtained for λ=0.07,S=1/479, θ=36.36º, and $\Gamma/\gamma RS$=0, when $b/2h_c$=0, 0.25, 0.5 and 2.0. The origin (y,z) is placed at the toe.

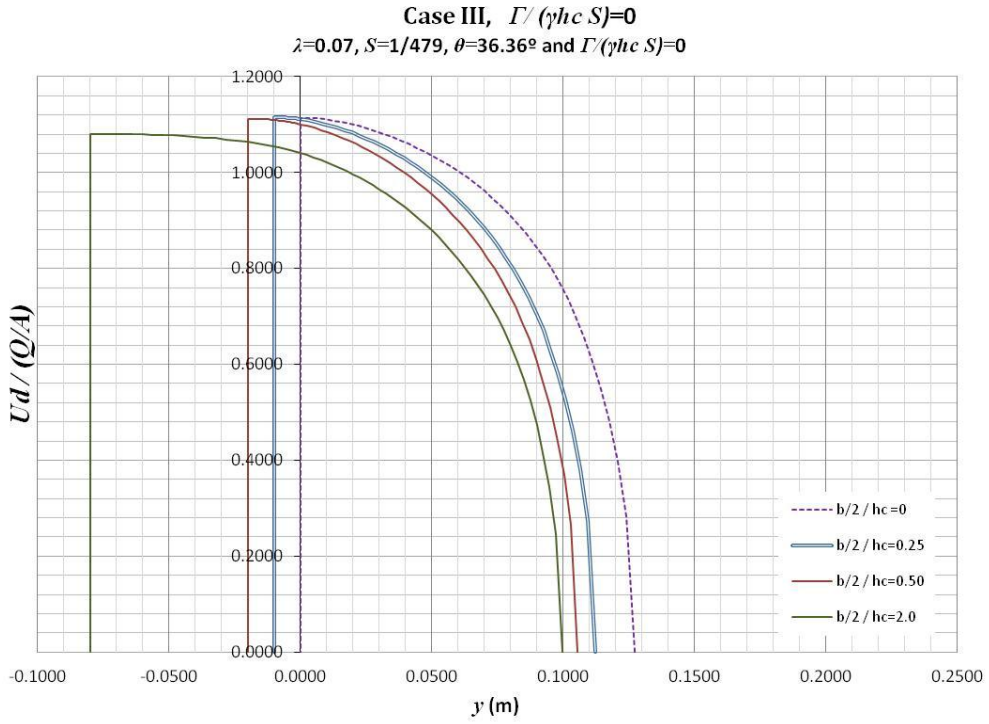

Figure B- 8. Velocity profiles obtained for λ=0.07, S=1/479, θ=36.36º, and $\Gamma/\gamma RS$=0, when $b/2h_c$=0, 0.25, 0.5 and 2.0. The origin (y,z) is placed at the toe.

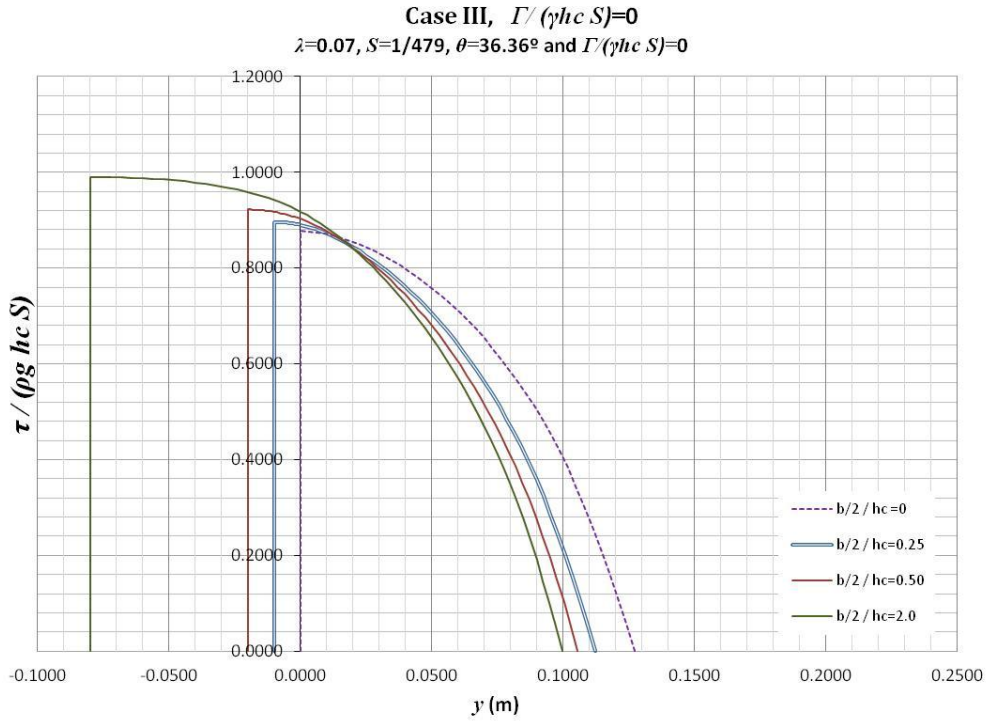

Figure B- 9. Shear stress profiles obtained for λ=0.07, S=1/479, θ=36.36º, and $\Gamma/\gamma RS$=0, when $b/2h_c$=0, 0.25, 0.5 and 2.0. The origin (y,z) is placed at the toe.

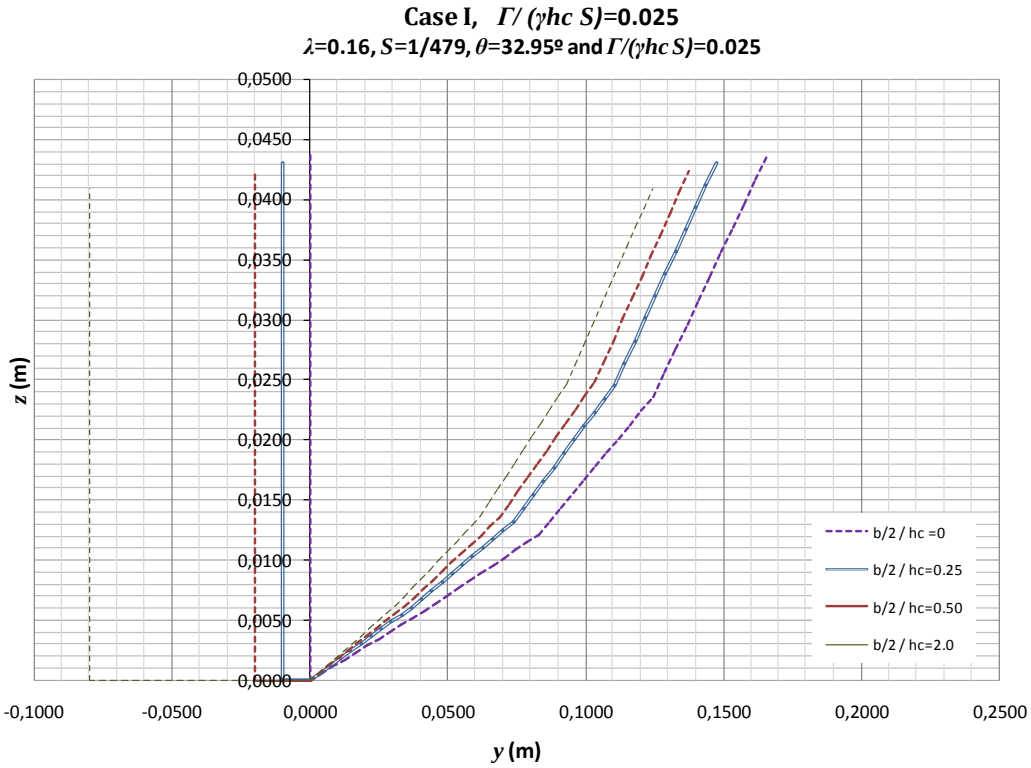

Figure B- 10. Cross sections obtained for λ=0.16, S=1/479, θ=32.95º, and $\Gamma/\gamma RS$=0.025, when $b/2h_c$=0, 0.25, 0.5 and 2.0. The origin (y,z) is placed at the toe.

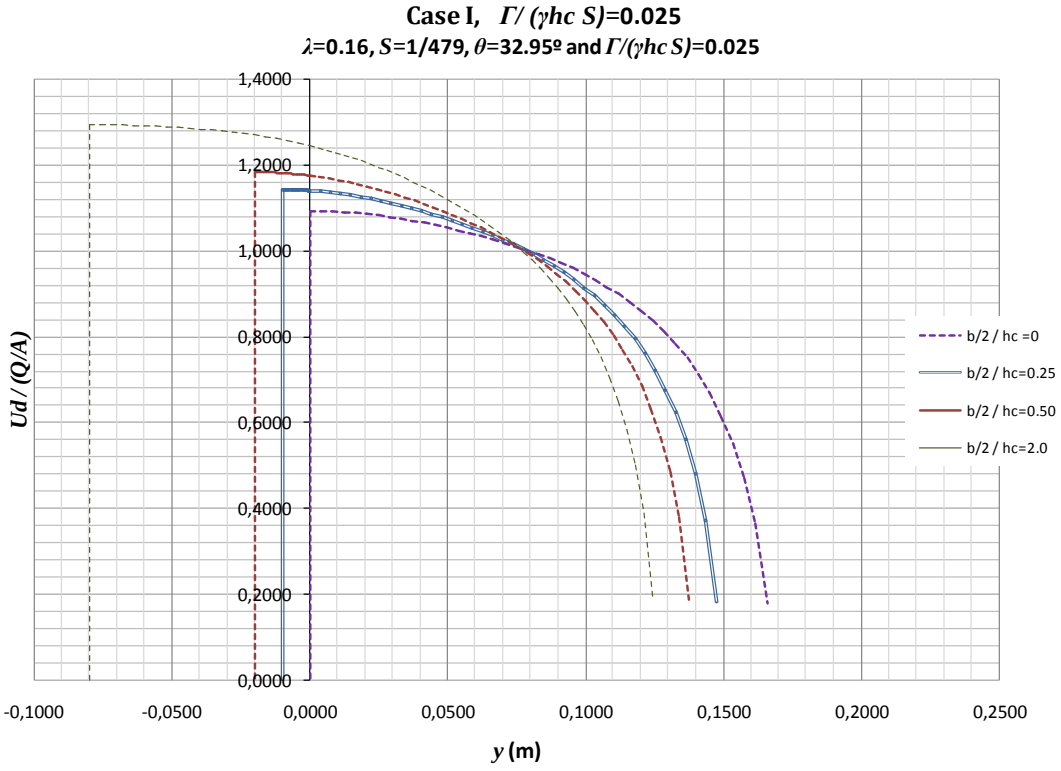

Figure B- 11. Velocity profiles obtained for λ=0.16, S=1/479, θ=32.95º, and $\Gamma/\gamma RS$=0.025, when $b/2h_c$=0, 0.25, 0.5 and 2.0. The origin (y,z) is placed at the toe

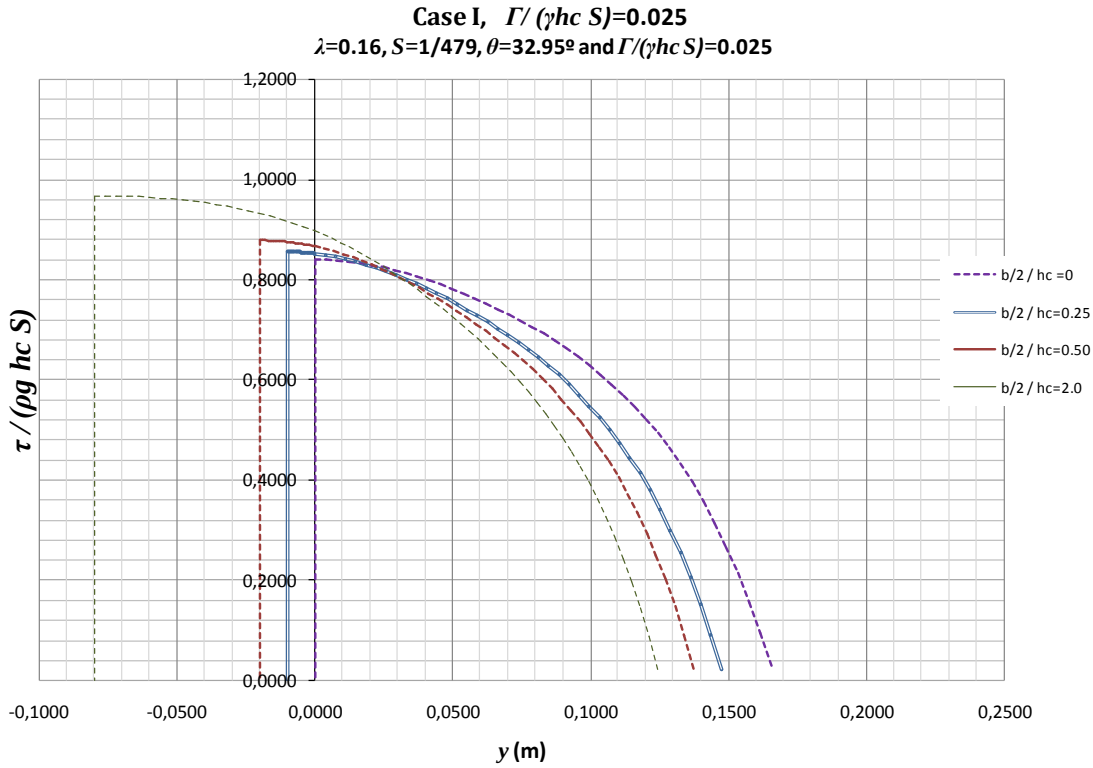

Figure B- 12. Shear stress profiles obtained for λ=0.16, S=1/479, θ=32.95º, and $\Gamma/\gamma RS$=0.025, when $b/2h_c$=0, 0.25, 0.5 and 2.0. The origin (y,z) is placed at the toe

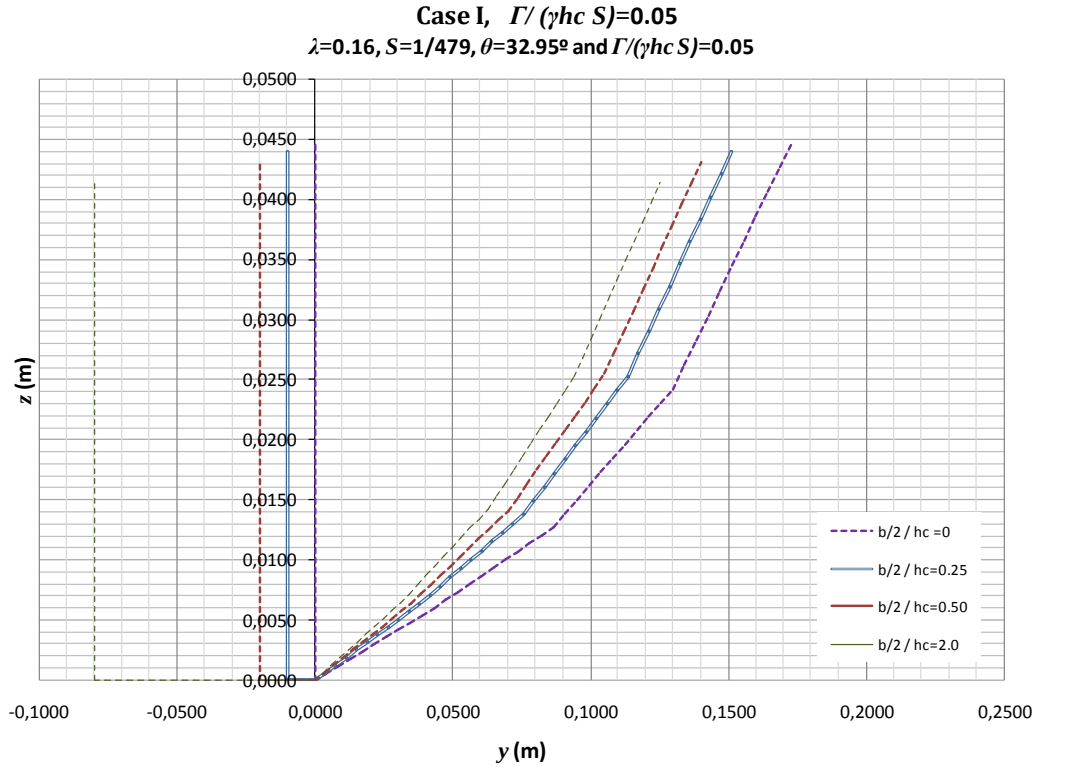

Figure B- 13. Cross sections obtained for λ=0.16, S=1/479, θ=32.95º, and$\Gamma/\gamma RS$=0.05, when$b/2h_c$=0, 0.25, 0.5 and 2.0. The origin (y,z) is placed at the toe

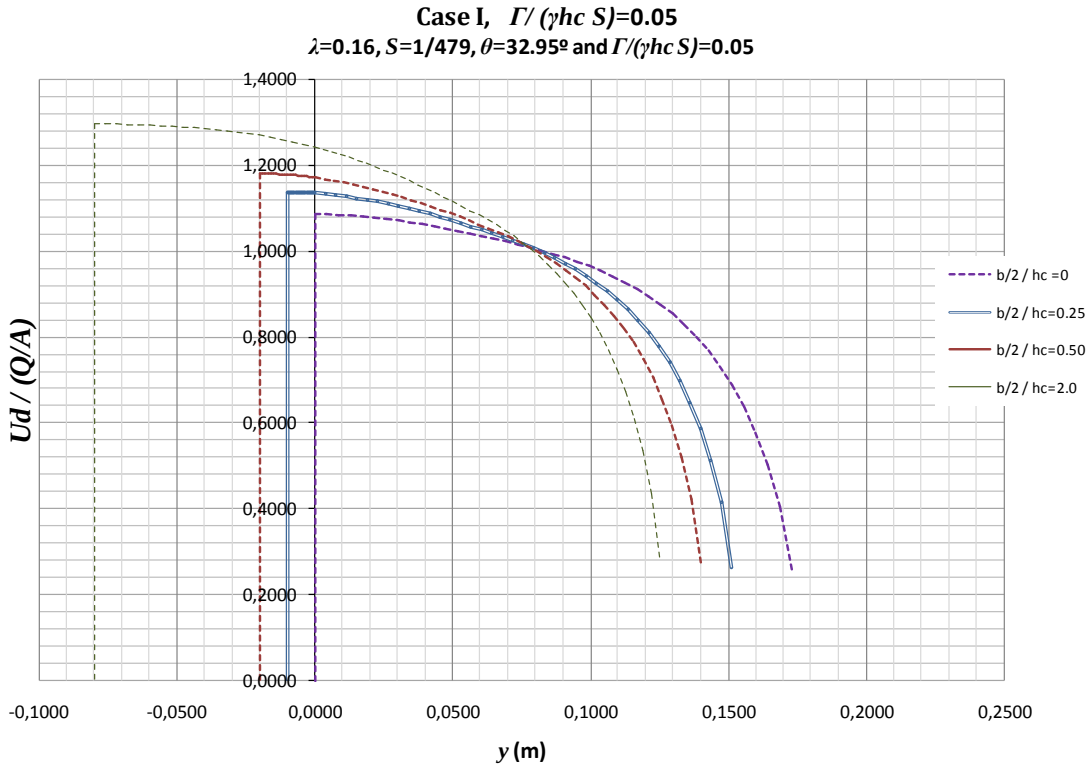

Figure B- 14. Velocity profiles obtained for λ=0.16, S=1/479, θ=32.95°, and $\Gamma/\gamma RS$=0.05, when$b/2h_c$=0, 0.25, 0.5 and 2.0. The origin (y,z) is placed at the toe.

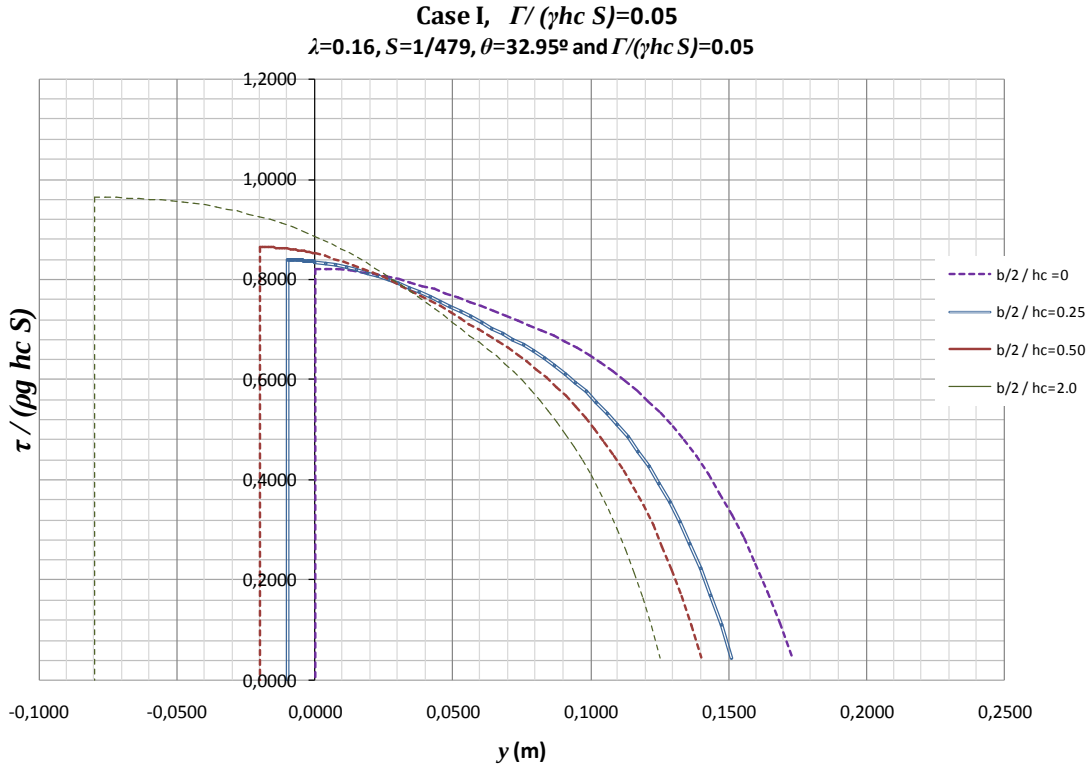

Figure B- 15. Shear stress profiles obtained for λ=0.16, S=1/479, θ=32.95°, and $\Gamma/\gamma RS$=0.05, when$b/2h_c$=0, 0.25, 0.5 and 2.0. The origin (y,z) is placed at the toe.

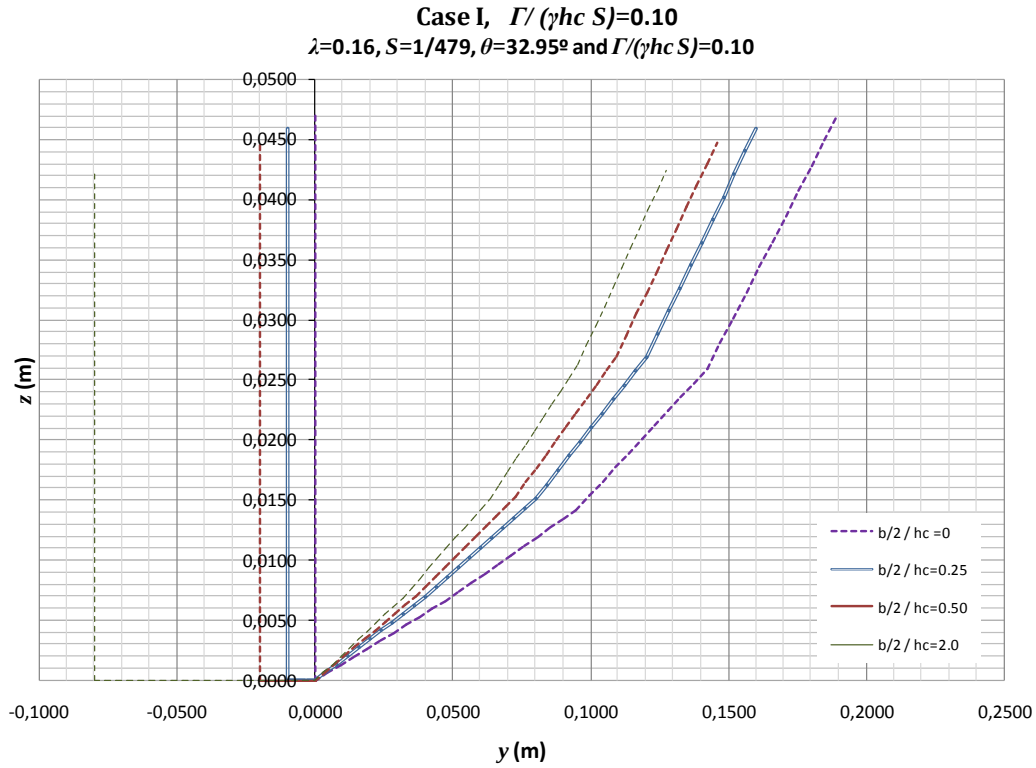

Figure B- 16. Cross sections obtained for λ=0.16, S=1/479, θ=32.95º, and $\Gamma/\gamma RS$=0.10, when$b/2h_c$=0, 0.25, 0.5 and 2.0. The origin (y,z) is placed at the toe.

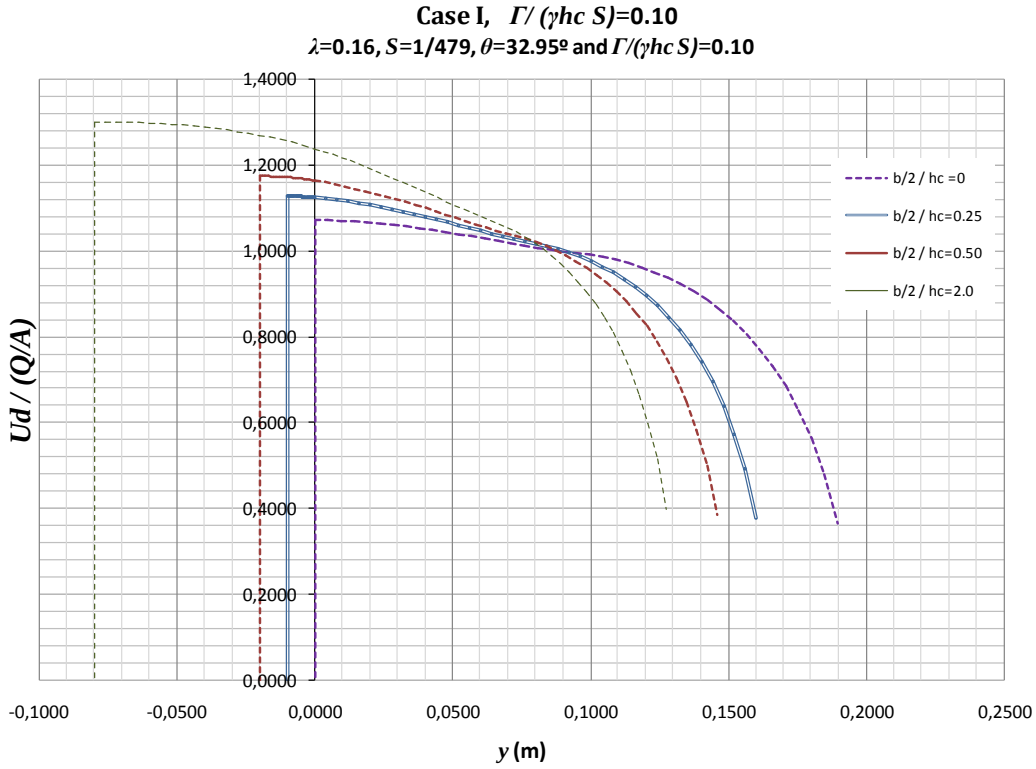

Figure B- 17. Velocity profiles obtained for λ=0.16, S=1/479, θ=32.95º, and $\Gamma/\gamma RS$=0.10, when$b/2h_c$=0, 0.25, 0.5 and 2.0. The origin (y,z) is placed at the toe.

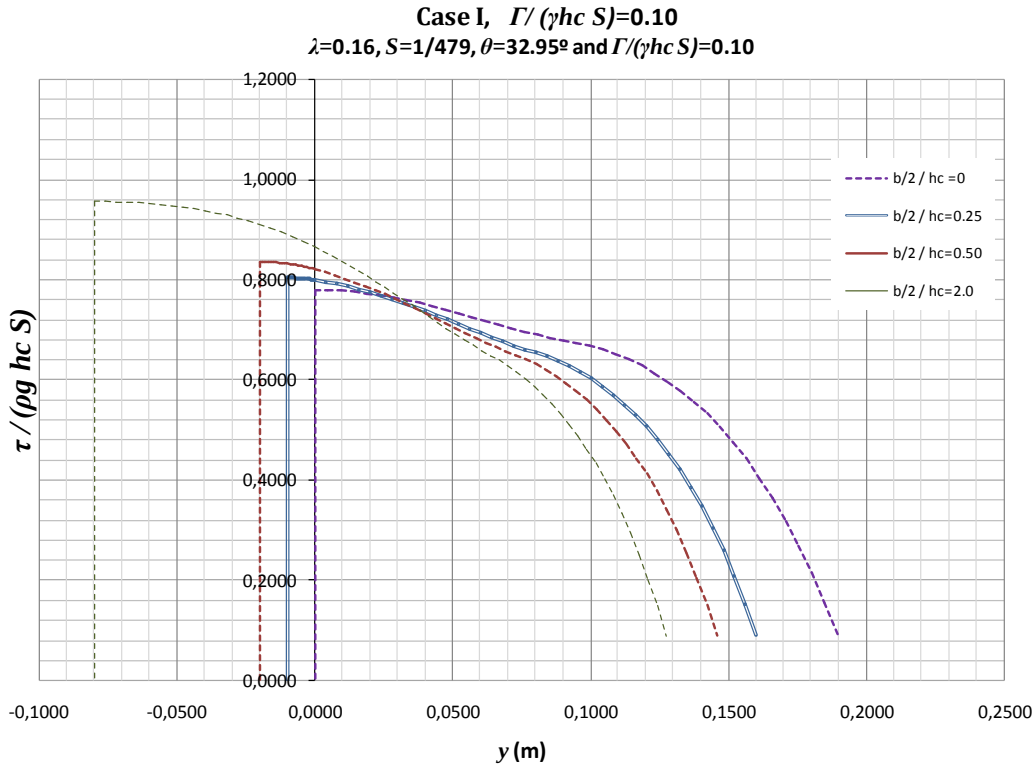

Figure B- 18. Shear stress profiles obtained for λ=0.16, S=1/479, θ=32.95°, and $\Gamma/\gamma RS$=0.10, when$b/2h_c$=0, 0.25, 0.5 and 2.0. The origin (y,z) is placed at the toe.

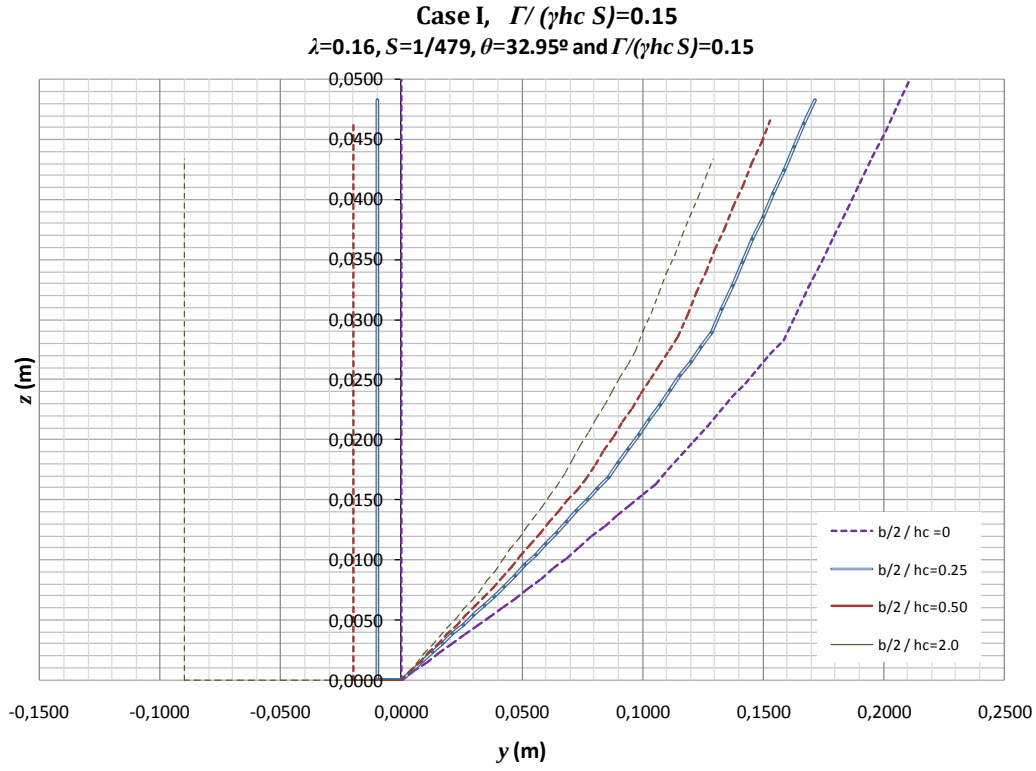

Figure B- 19. Cross sections obtained for λ=0.16, S=1/479, θ=32.95°, and $\Gamma/\gamma RS$=0.10, when$b/2h_c$=0, 0.25, 0.5 and 2.0. The origin (y,z) is placed at the toe.

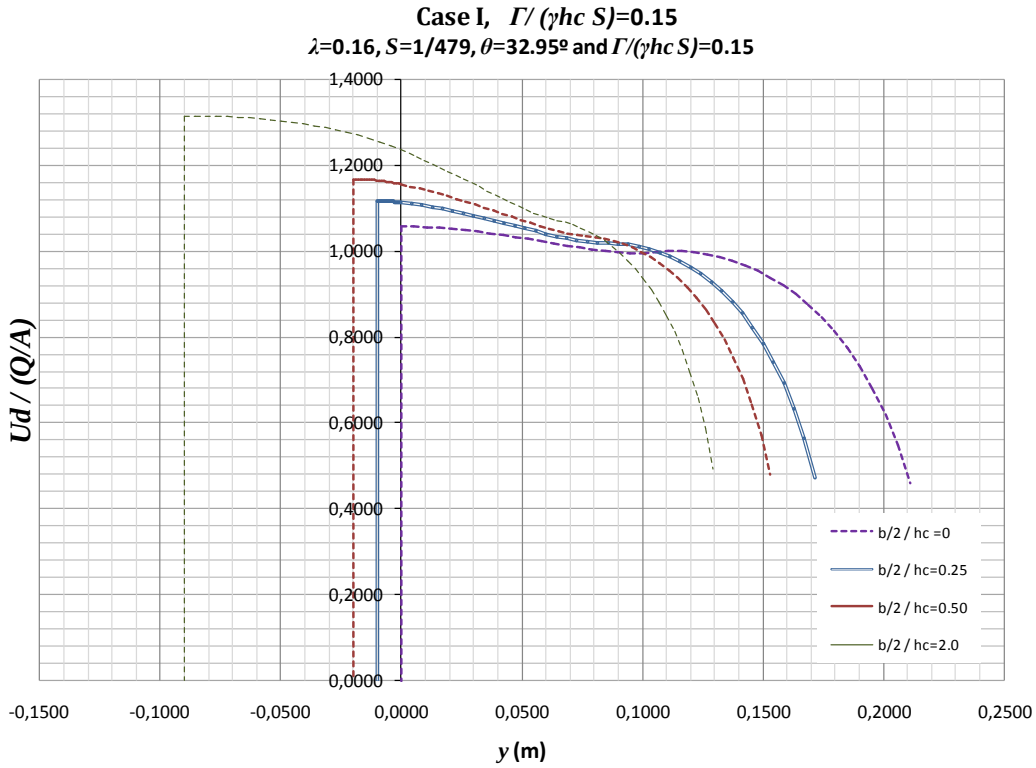

Figure B- 20. Velocity profiles obtained for λ=0.16, S=1/479, θ=32.95°, and $\Gamma/\gamma RS$=0.15, when$b/2h_c$=0, 0.25, 0.5 and 2.0. The origin (y,z) is placed at the toe.

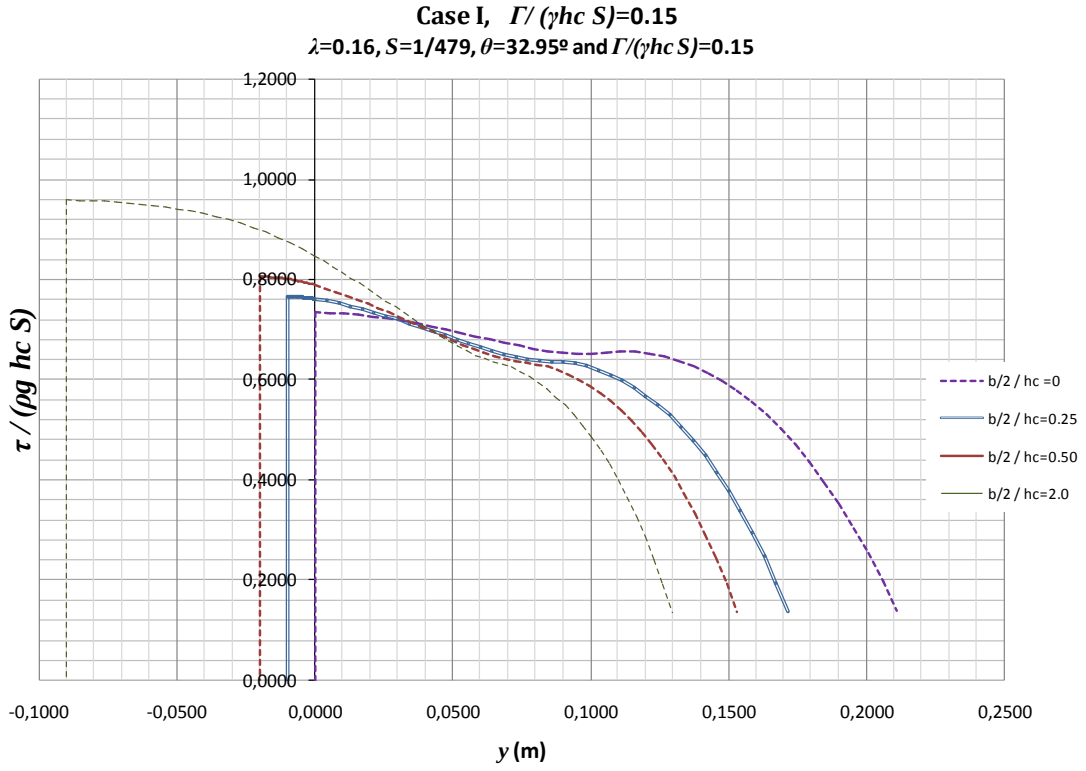

Figure B- 21. Shear stress profiles obtained for λ=0.16, S=1/479, θ=32.95°, and $\Gamma/\gamma RS$=0.15, when$b/2h_c$=0, 0.25, 0.5 and 2.0. The origin (y,z) is placed at the toe.

Appendix C

The current section presents the results of the calibrated simulations employing the numerical model (SKM) for the 18 experimental sets. Each set comes with two half sectional profiles, one for depth average velocity, U_d, and one for boundary shear stress, τ_0. Both graphs are displayed dimensionless, being U_d expressed with respect to the average velocity, V, obtained by $V=Q/A$; and τ_0, with respect to the average shear stress, $\tau_0=\rho gRS$. While the horizontal component, y, is expressed in terms of the half cross sectional width, $W/2$.

The experiments are divided in smooth and rough surface, being nine per surface. For each one, three depths were evaluated, corresponding to three slopes per depth.

With respect to the physical data, U_d was obtained based on Static Pitot tube measurements, while τ_0, from Preston tube. Velocity and shear stress graphs are provided for both types of surfaces. However, it was not possible to use the Pitot tube to measure τ_0 on rough surface, hence it was determined by $\tau_0 = \rho f U_d^2/8$ .The friction factor, f, was obtained by the methodology proposed on ta section 6.2.2, obtaining an average value per SKM panel. Such a values can be found on table 27.

About the rest of the variables used during the calibration process, they are found on table 29 with details. Additionally, each plot comes with its appropriate caption, mentioning the input data employed.

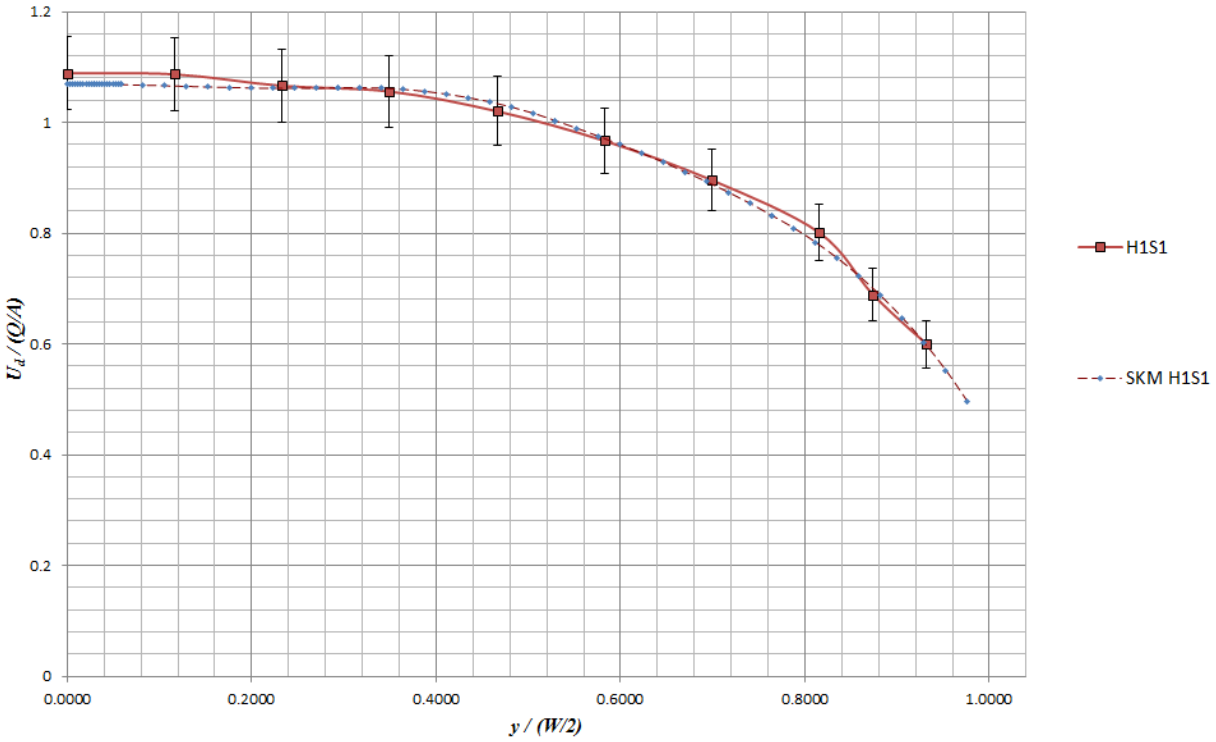

Figure C- 1. Dimensionless calibrated velocity distribution along the experimental data with their uncertainty bars, for H1S1 PVC, using h_c=3.34cm, S=0.001485, $f_{1,2}$= 0.0200, f_3= 0.0203, f_4= 0.0199, f_5= 0.0224, f_6= 0.0263, $p_{1,2}$=1, p_3=1, p_4=-1, p_5=-1, p_6=-3, C=0.070, and λ=0.07.

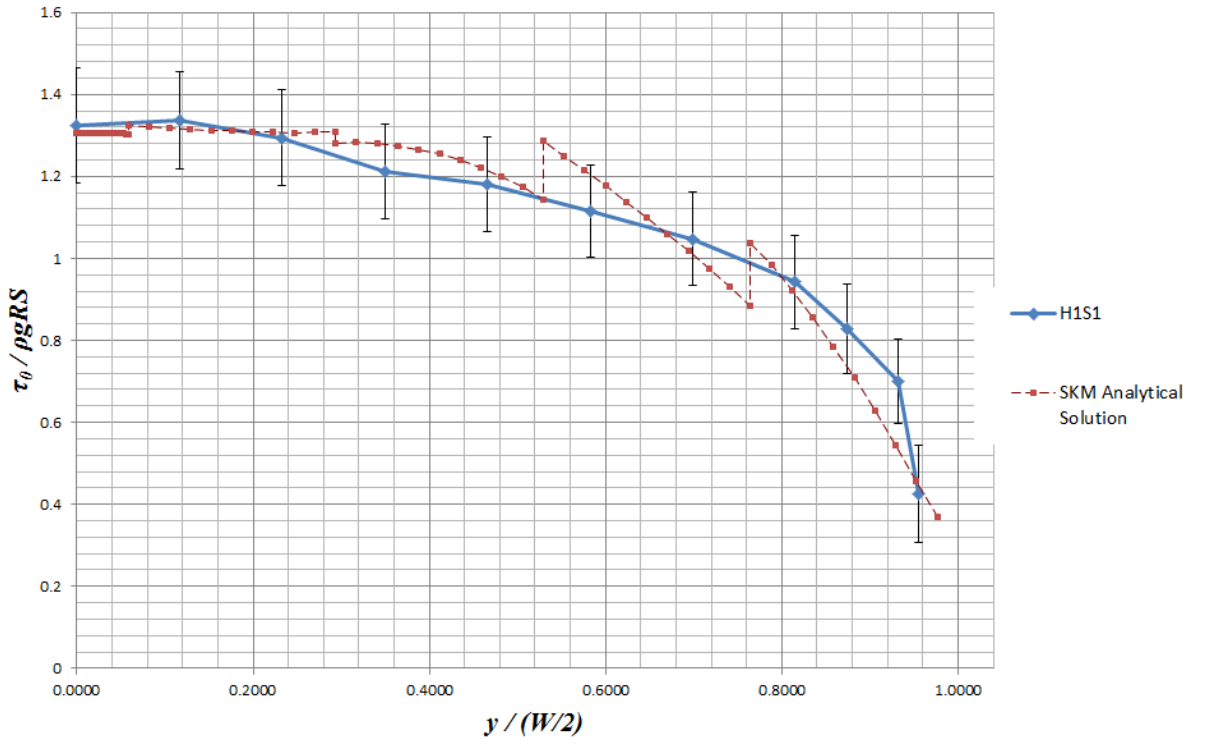

Figure C- 2. Dimensionless calibrated boundary shear stress distribution along the experimental data with uncertainty bars, for H1S1 on PVC, using h_c=3.34cm, S=0.001485, $f_{1,2}$= 0.0200, f_3= 0.0203, f_4= 0.0199, f_5= 0.0224, f_6= 0.0263, $p_{1,2}$=1, p_3=1, p_4=-1, p_5=-1, p_6=-3, C=0.070, and λ=0.07.

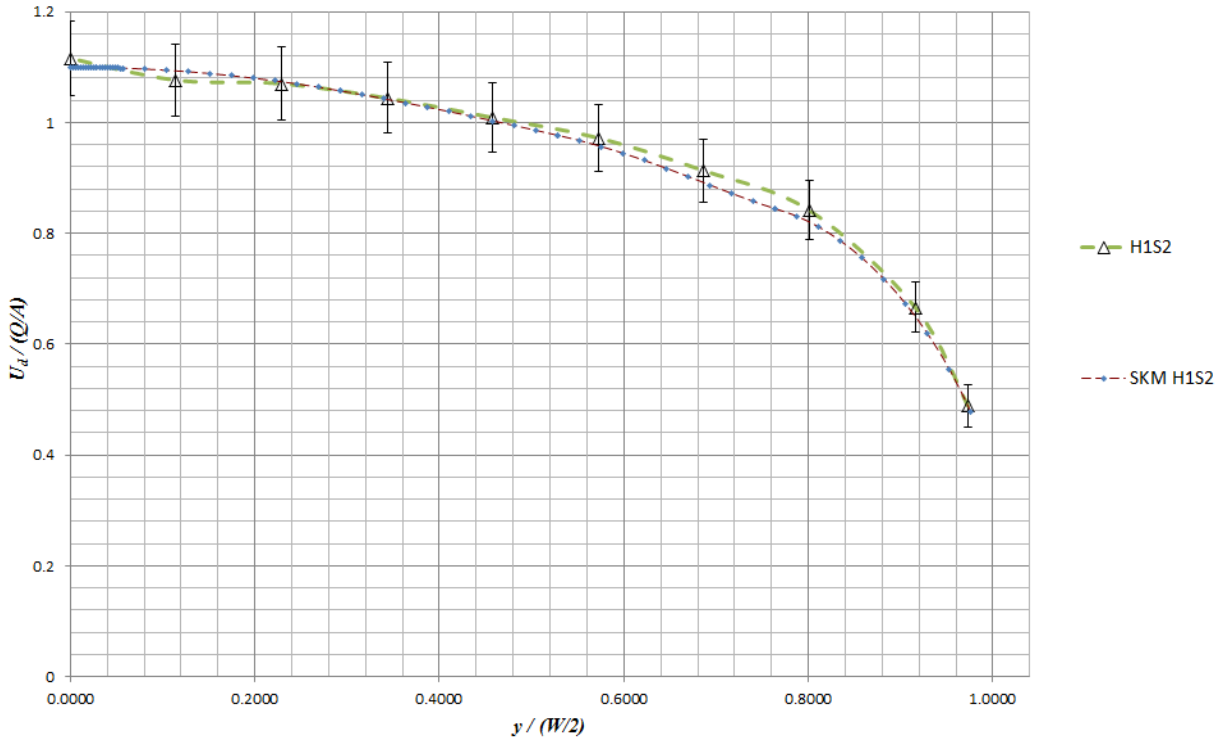

Figure C- 3. Dimensionless calibrated velocity distributions along the experimental data with their uncertainty bars, for H1S2 on PVC, using h_c=3.52cm, S=0.001725,$f_{1,2}$= 0.0188, f_3=0.0184, f_4= 0.0190, f_5= 0.0210, f_6= 0.0242, $p_{1,2}$=1, p_3=1, p_4=-1, p_5= 0.5, p_6=-0.5,C= 0.245, and λ=0.07.

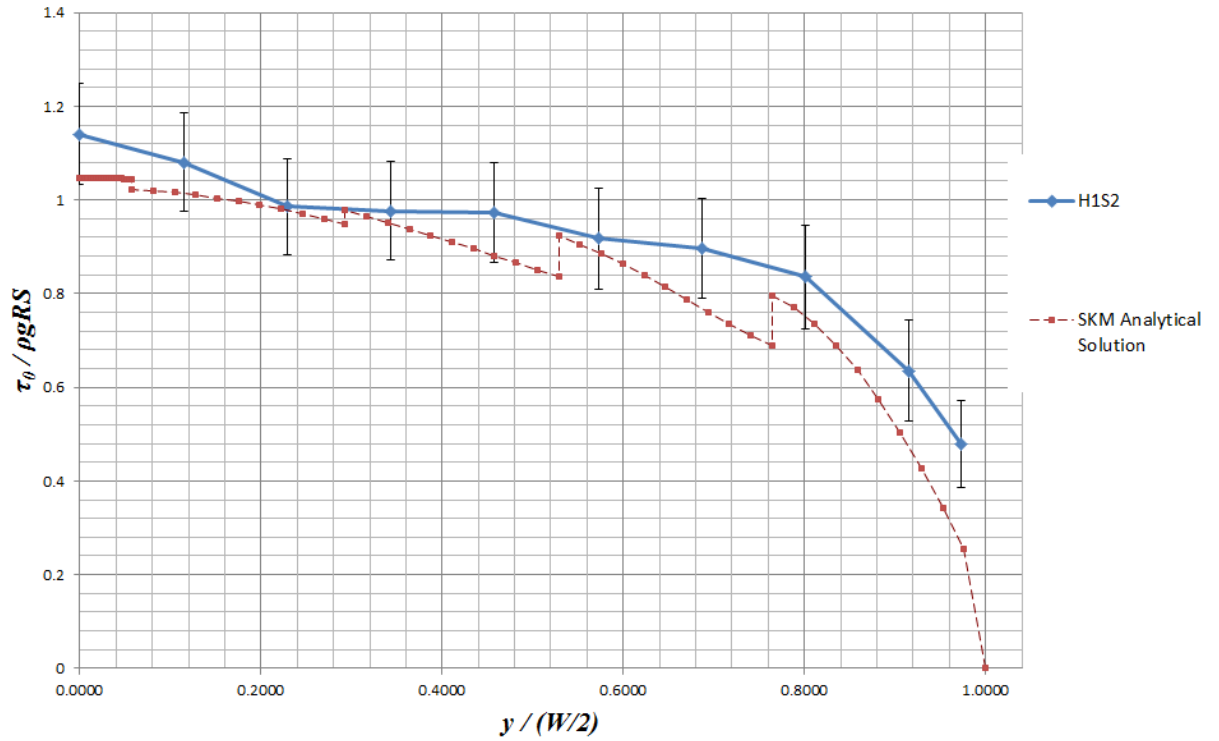

Figure C- 4. Dimensionless calibrated boundary shear stress distribution along the experimental data with their uncertainty bars, for H1S2 on PVC, using h_c=3.52cm, S=0.001725, $f_{1,2}$= 0.0188, f_3=0.0184, f_4= 0.0190, f_5= 0.0210, f_6= 0.0242, $p_{1,2}$=1, p_3=1, p_4=-1, p_5= 0.5, p_6=-0.5,C= 0.245, and λ=0.07.

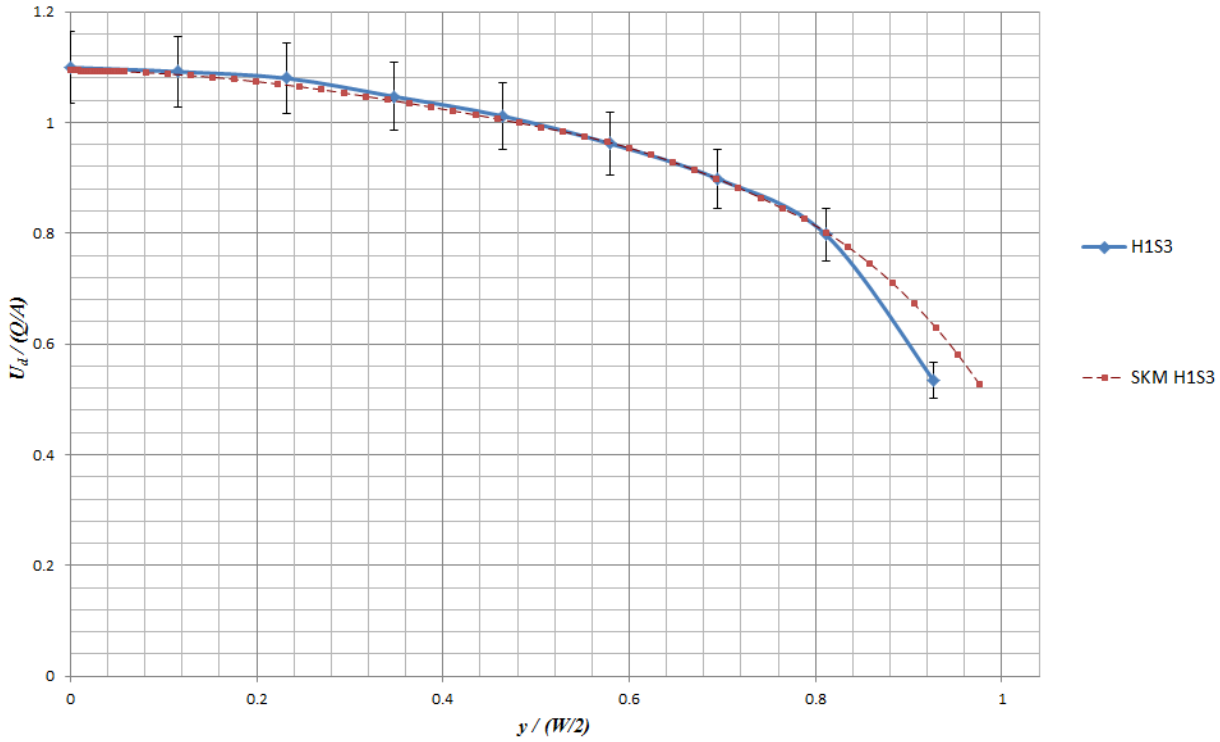

Figure C- 5. Dimensionless calibrated velocity distributions along the experimental data with their uncertainty bars, for H1S3 on PVC, using h_c=3.395cm, S=0.005044, $f_{1,2}$= 0.0194, f_3=0.0197, f_4= 0.0203, f_5= 0.0220, f_6= 0.0266, $p_{1,2}$=1, p_3=1,p_4=1, p_5=-2, p_6=-4, C= 0.055, and λ=0.07.

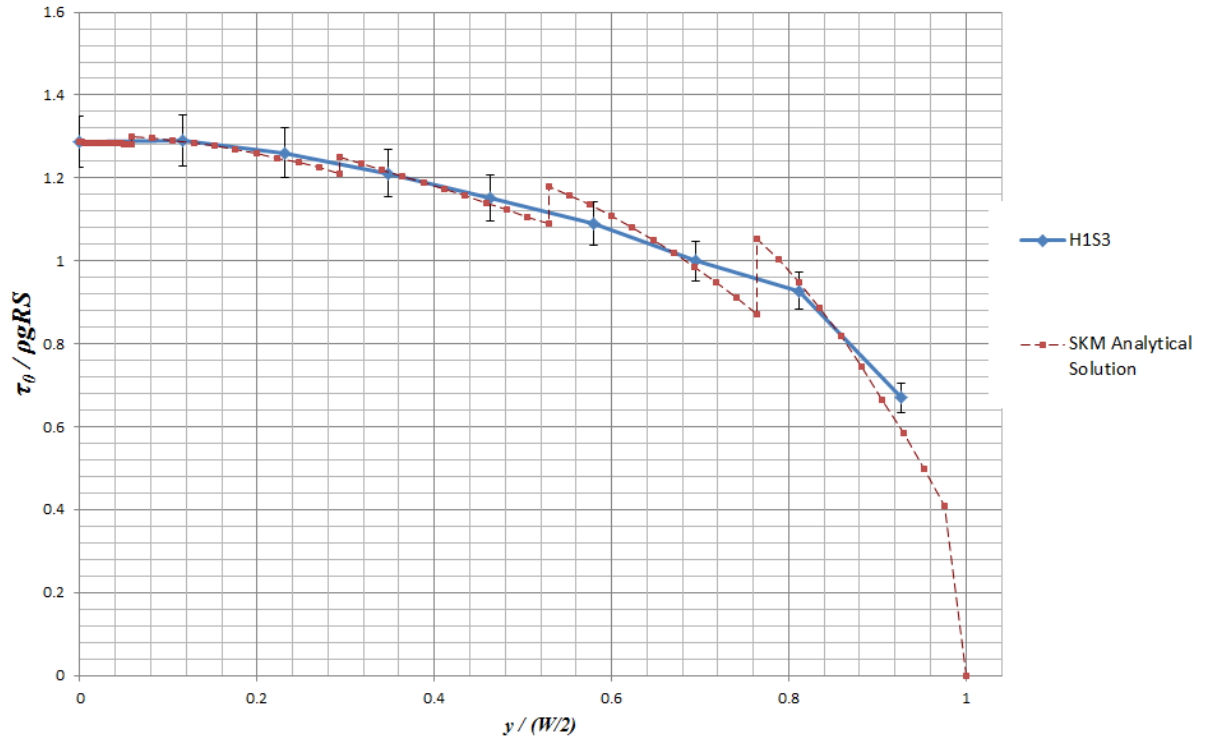

Figure C- 6. Dimensionless calibrated boundary shear stress distribution along the experimental data with their uncertainty bars, for H1S3 PVC, using h_c=3.395cm, S=0.005044, $f_{1,2}$= 0.0194, f_3=0.0197, f_4=0.0203, f_5= 0.0220, f_6= 0.0266, $p_{1,2}$=1, p_3=1, p_4=1, p_5=-2, p_6=-4, C= 0.055, and λ=0.07.

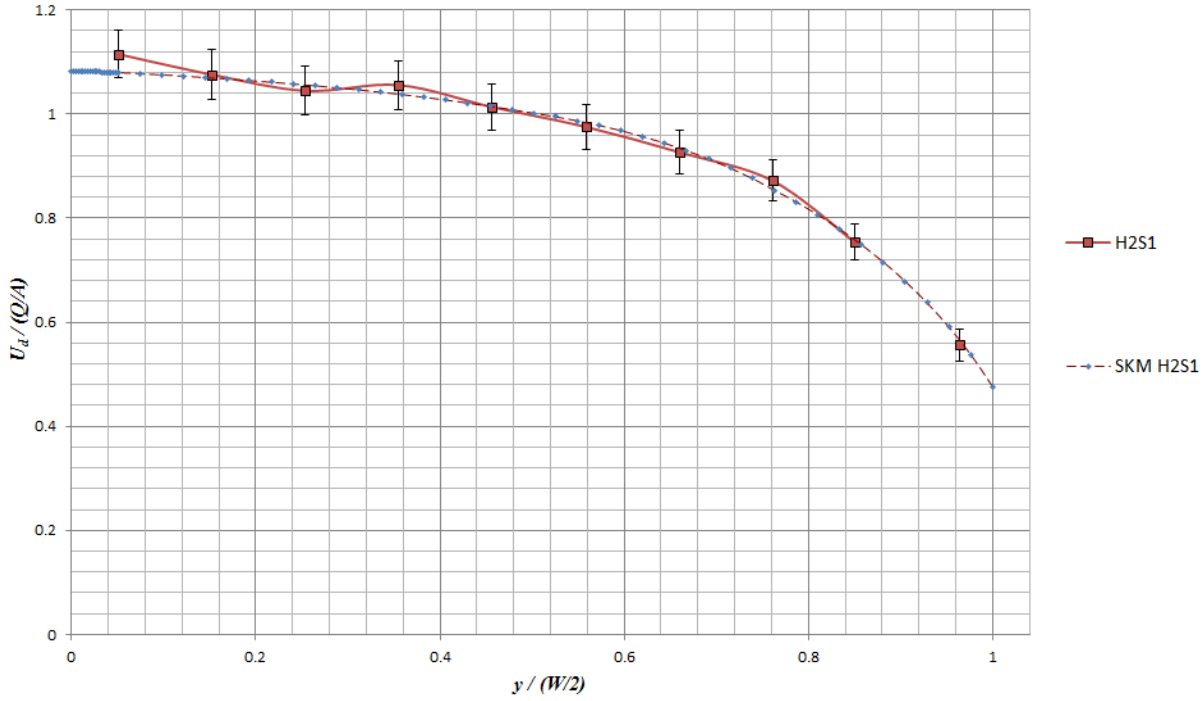

Figure C- 7. Dimensionless calibrated velocity distributions along the experimental data with their uncertainty bars, for H2S1 on PVC, using h_c=4.97cm, S=0.001485, $f_{1,2}$= 0.0208, f_3=0.0214, f_4= 0.0223, f_5= 0.0249, f_6= 0.0319, $p_{1,2}$=0.5, p_3=1, p_4=0.5, p_5=-1, p_6=-2.5, C=0.115, and λ=0.07.

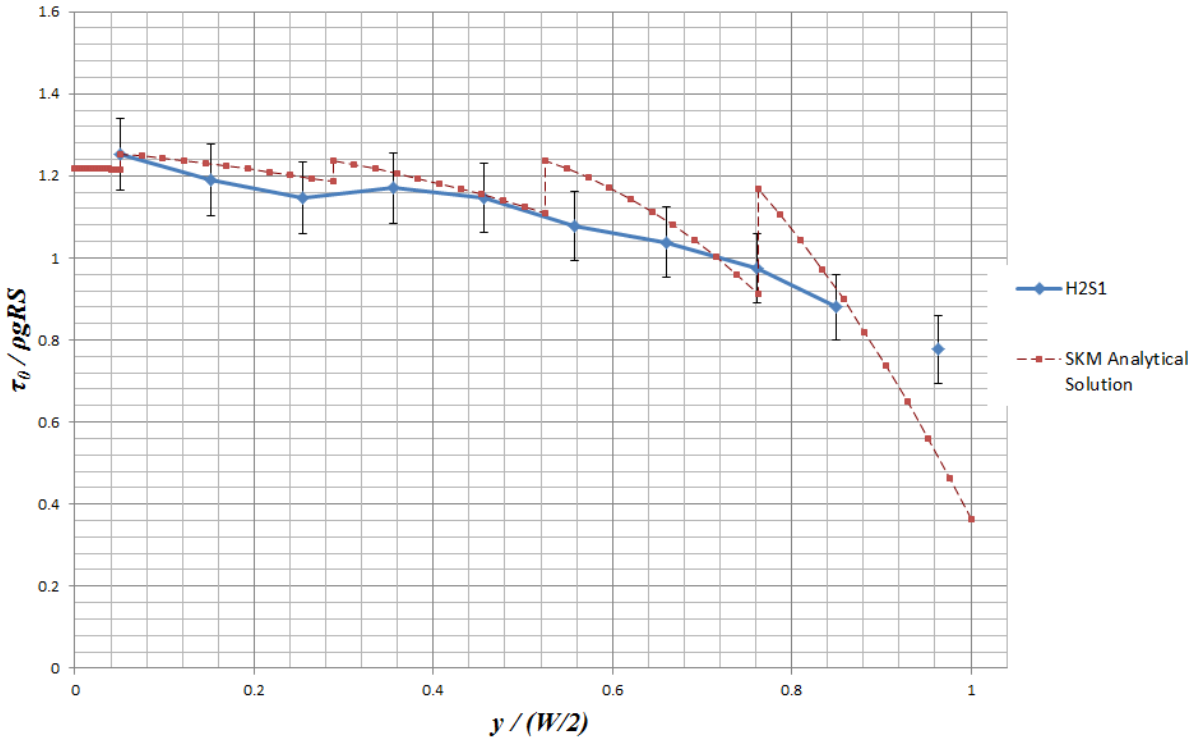

Figure C- 8. Dimensionless calibrated boundary shear stress distribution along the experimental data with their uncertainty bars, for H2S1 on PVC, using h_c=4.97cm, S=0.001485, $f_{1,2}$= 0.0208, f_3=0.0214, f_4= 0.0223, f_5= 0.0249, f_6= 0.0319, $p_{1,2}$=0.5, p_3=1, p_4=0.5, p_5=-1, p_6=-2.5, C=0.115, and λ=0.07.

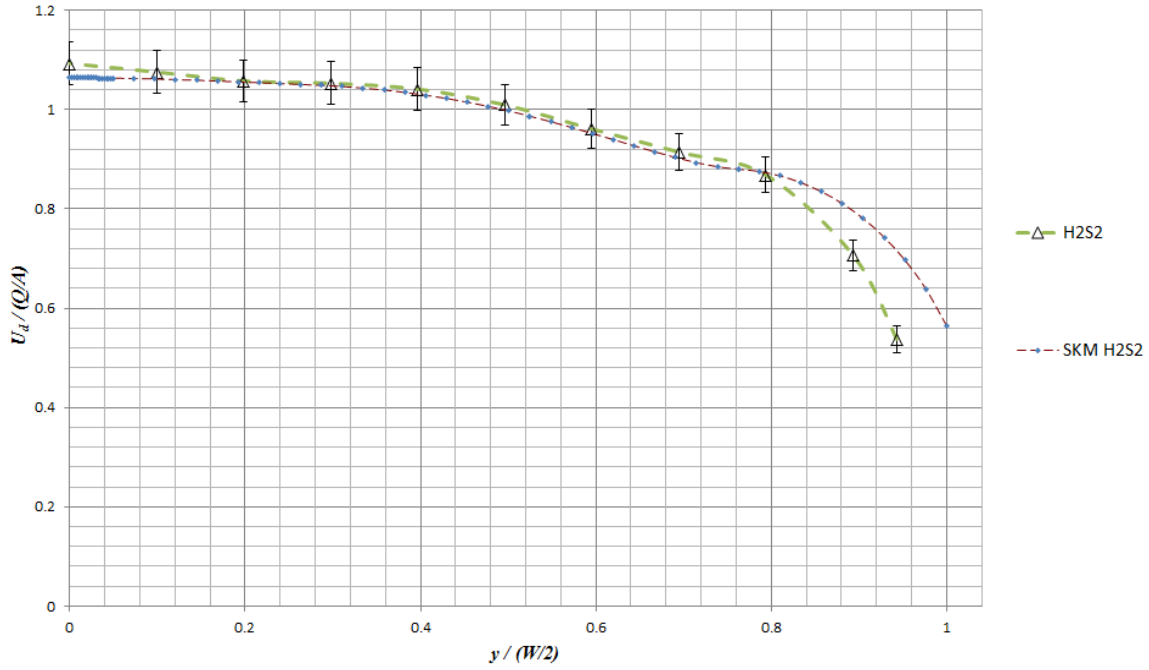

Figure C- 9. Dimensionless calibrated velocity distributions along the experimental data with their uncertainty bars, for H2S2 PVC, using h_c=5.265cm, S=0.001725, $f_{1,2}$= 0.0169, f_3=0.0168, f_4= 0.0180, f_5= 0.0193, f_6= 0.0225, $p_{1,2}$=1, p_3=1, p_4=0.5, p_5=0.5, p_6=-1, C=0.295, and λ=0.07.

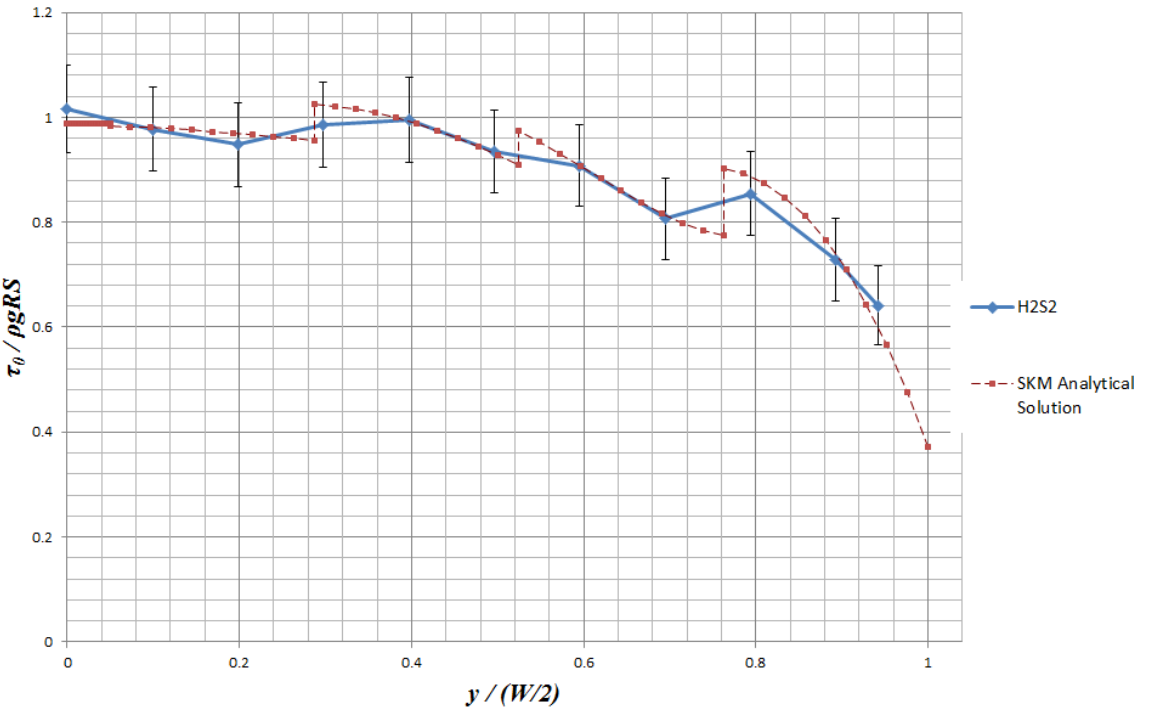

Figure C- 10. Dimensionless calibrated boundary shear stress distribution along the experimental data with their uncertainty bars, for H2S2 on PVC, using h_c=5.265cm, S=0.001725, $f_{1,2}$= 0.0169, f_3=0.0168, f_4= 0.0180, f_5= 0.0193, f_6= 0.0225, $p_{1,2}$=1, p_3=1, p_4=0.5, p_5=0.5, p_6=-1, C=0.295, and λ=0.07.

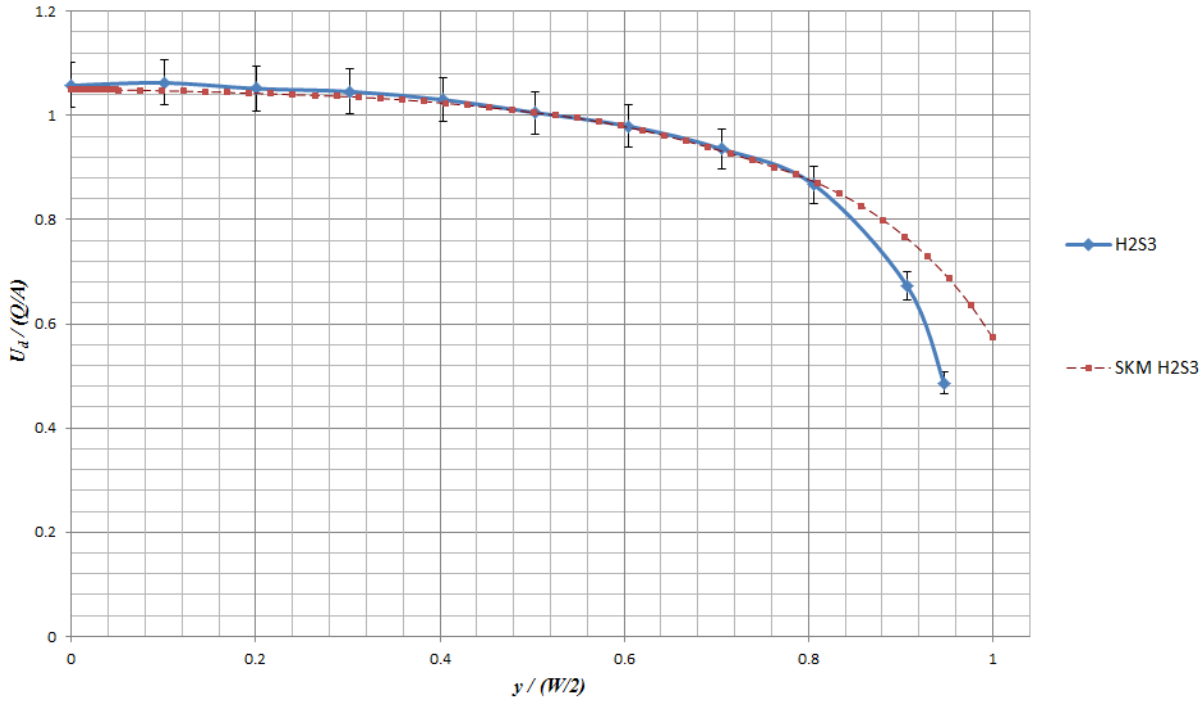

Figure C- 11. Dimensionless calibrated velocity distributions along the experimental data with their uncertainty bars, for H2S3 set on PVC, using h_c=5.065cm, S=0.005044, $f_{1,2}$= 0.0186, f_3=0.0185, f_4=0.0185, f_5=0.0195, f_6=0.0228, $p_{1,2}$=1, p_3=1, p_4=0.3333, p_5=-1, p_6=-3.5, C=0.105, and λ=0.07.

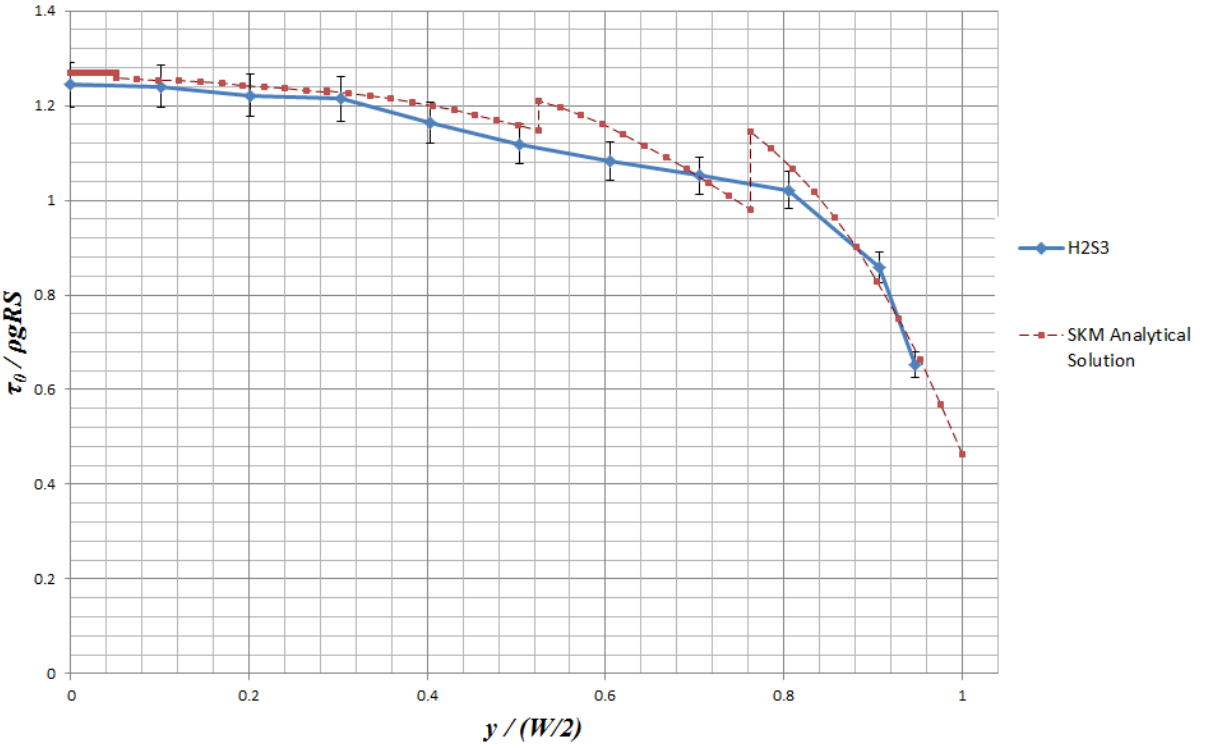

Figure C- 12. Dimensionless calibrated boundary shear stress distribution along the experimental data with their uncertainty bars, for H2S3 on PVC, using h_c=5.065cm, S=0.005044, $f_{1,2}$= 0.0186, f_3=0.0185, f_4=0.0185, f_5=0.0195, f_6=0.0228, $p_{1,2}$=1, p_3=1, p_4=0.3333, p_5=-1, p_6=-3.5, C=0.105, and λ=0.07.

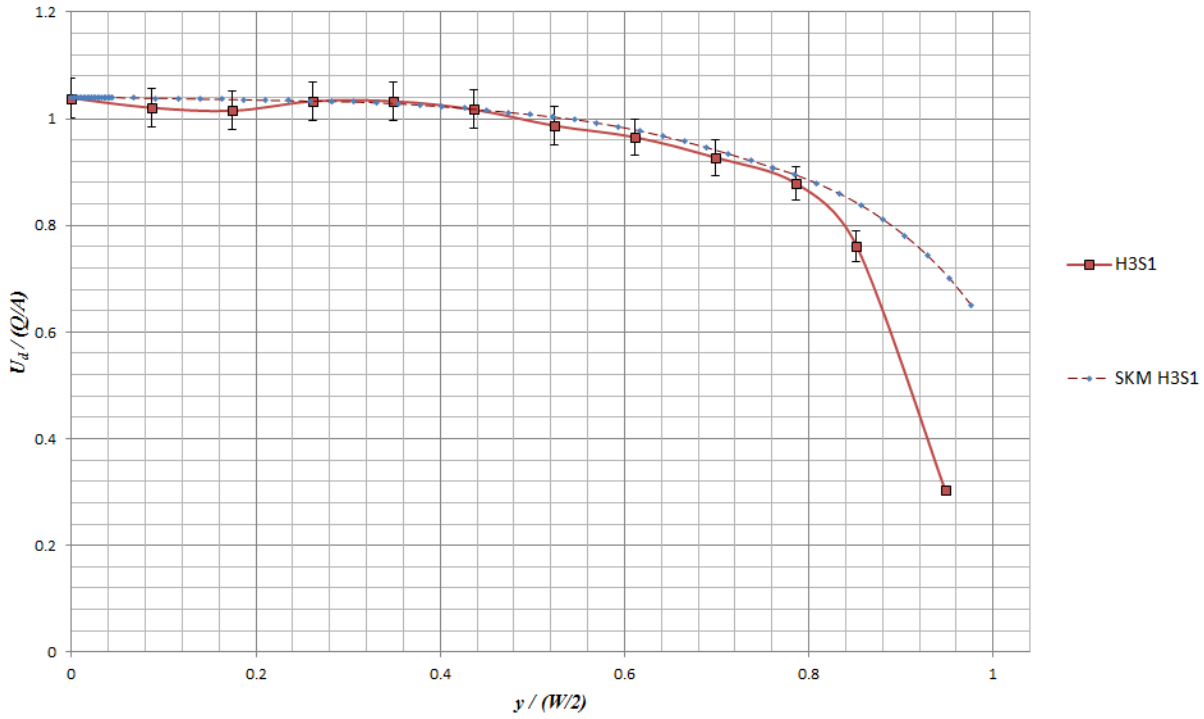

Figure C- 13. Dimensionless calibrated velocity distributions along the experimental data with their uncertainty bars, for H3S1 on PVC, using h_c=7.02cm, S=0.001485, $f_{1,2}$= 0.0193, f_3=0.0196, f_4=0.0199, f_5=0.0214, f_6=0.0252, $p_{1,2}$=1, p_3=1, p_4=0.5, p_5=-0.3333, p_6=-1.5, C=0.240, and λ=0.07.

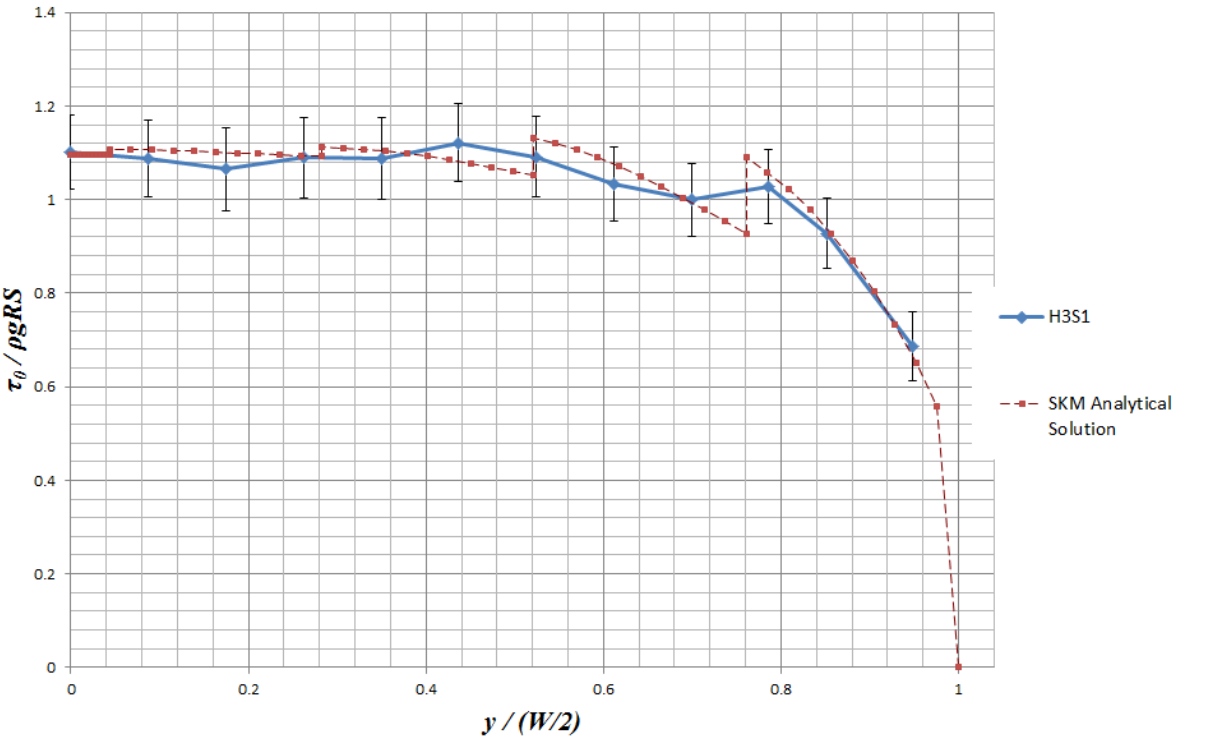

Figure C- 14. Dimensionless calibrated boundary shear stress distribution along the experimental data with their uncertainty bars, for H3S1 PVC, using h_c=7.02cm, S=0.001485, $f_{1,2}$= 0.0193, f_3=0.0196, f_4=0.0199, f_5=0.0214, f_6=0.0252, $p_{1,2}$=1, p_3=1, p_4=0.5, p_5=-0.3333, p_6=-1.5, C=0.240, and λ=0.07.

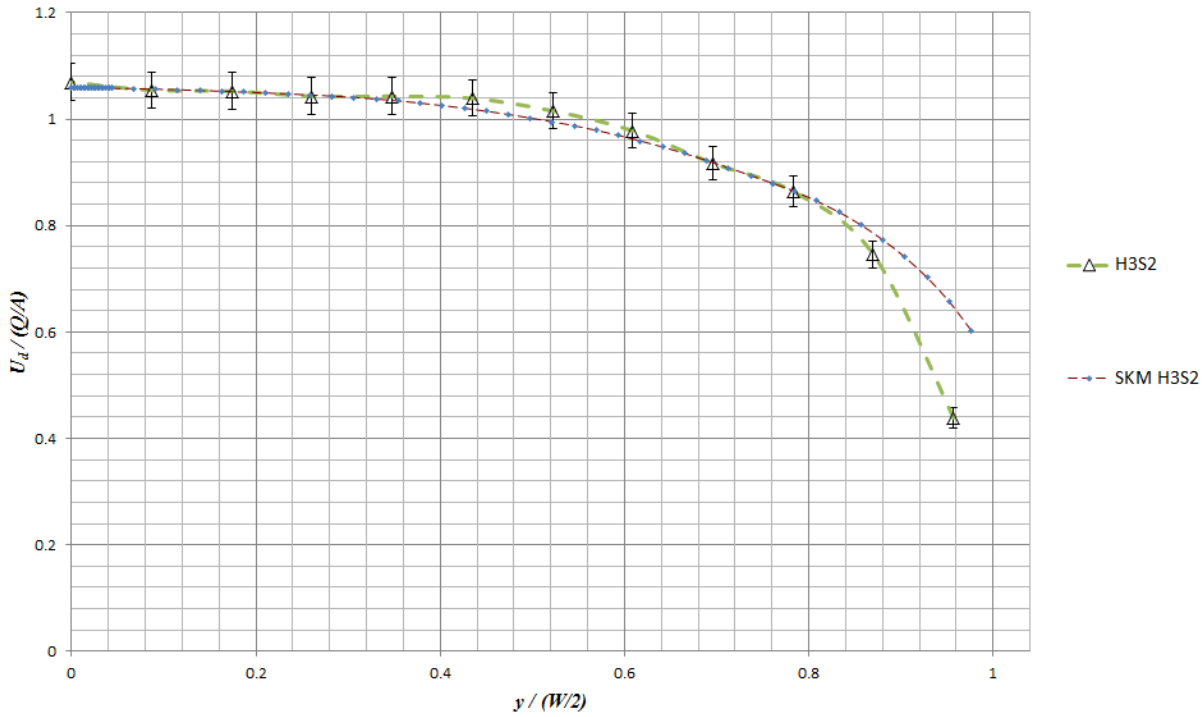

Figure C- 15. Dimensionless calibrated velocity distributions along the experimental data with their uncertainty bars, for H3S2 on PVC, using h_c=7.08cm, S=0.001725, $f_{1,2}$= 0.0173, f_3=0.0177, f_4=0.0177, f_5=0.0198, f_6=0.0225, $p_{1,2}$=1, p_3=1, p_4=0.5, p_5=-0.5, p_6=-2, C=0.155, and λ=0.07.

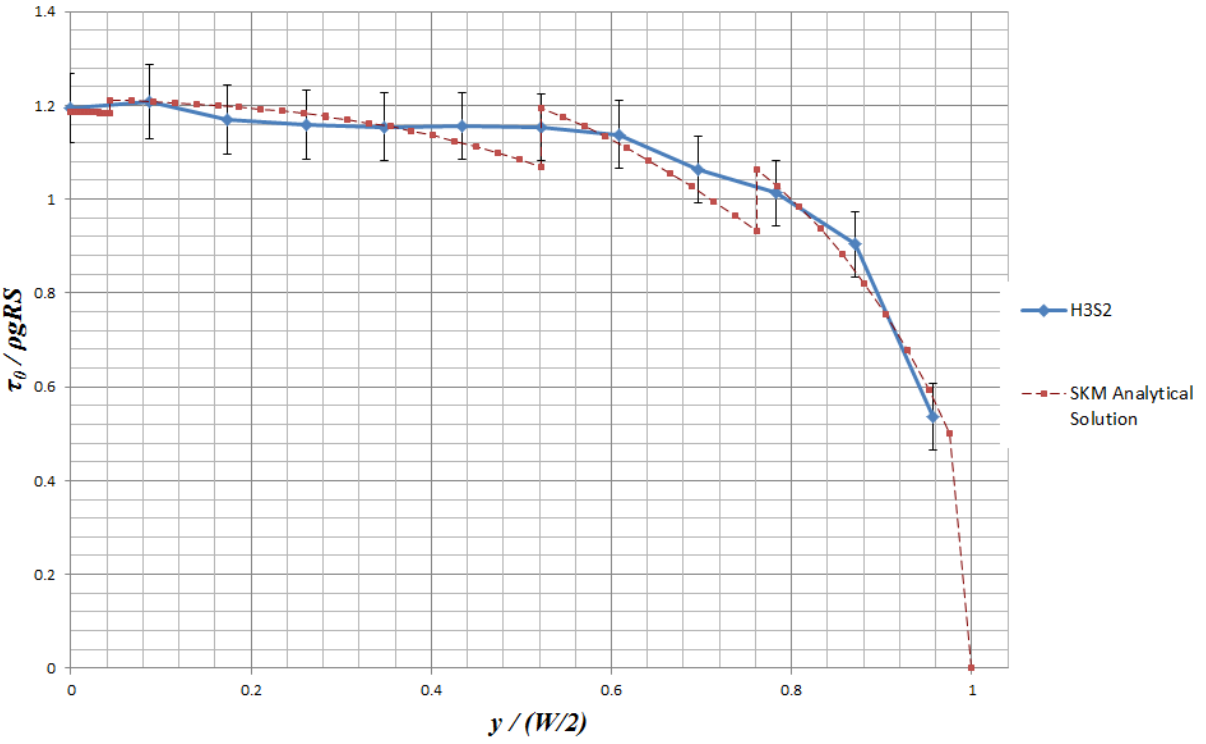

Figure C- 16. Dimensionless calibrated boundary shear stress distribution along the experimental data with their uncertainty bars, corresponding to the set H3S2 on smooth surface (PVC).

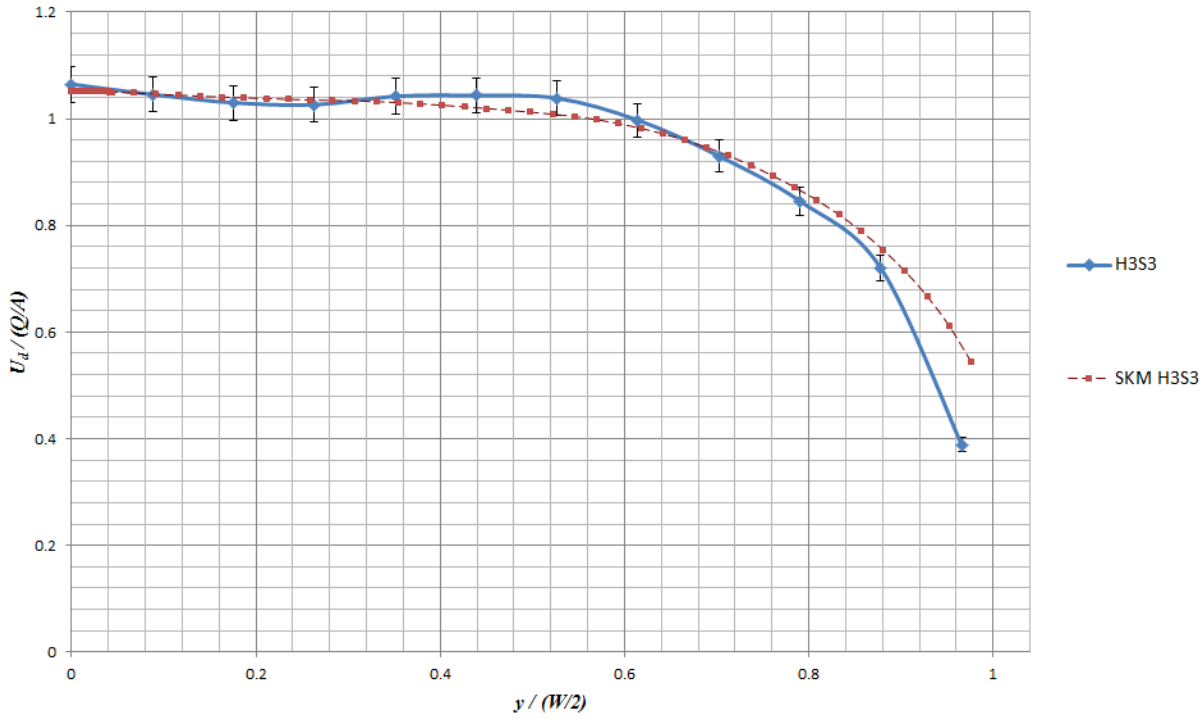

Figure C- 17. Dimensionless calibrated velocity distributions along the experimental data with their uncertainty bars, for H3S3 PVC, using h_c=6.95cm, S=0.005044, $f_{1,2}$= 0.0156, f_3=0.0172, f_4=0.0167, f_5=0.0172, f_6=0.0201, $p_{1,2}$=0.25, p_3=1, p_4=0.5, p_5=-2, p_6=-1, C=0.226, and λ=0.07.

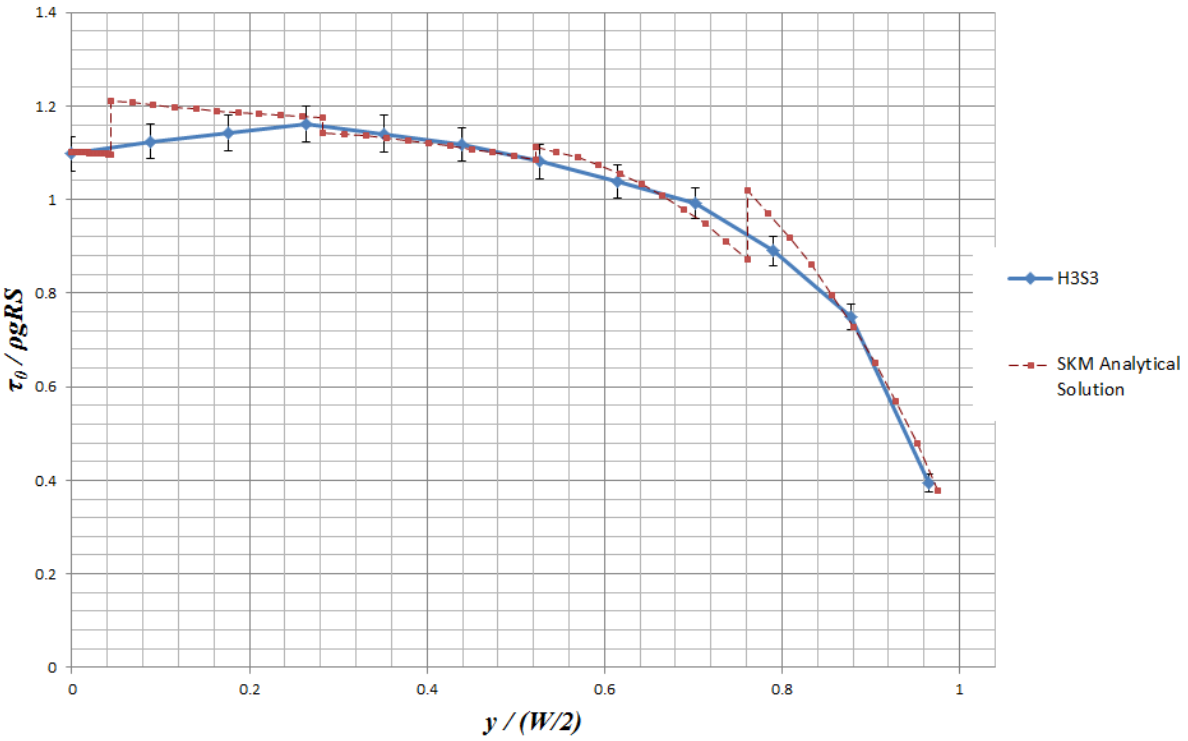

Figure C- 18. Dimensionless calibrated boundary shear stress distribution along the experimental data with their uncertainty bars, corresponding to the set H3S3 on smooth surface (PVC).

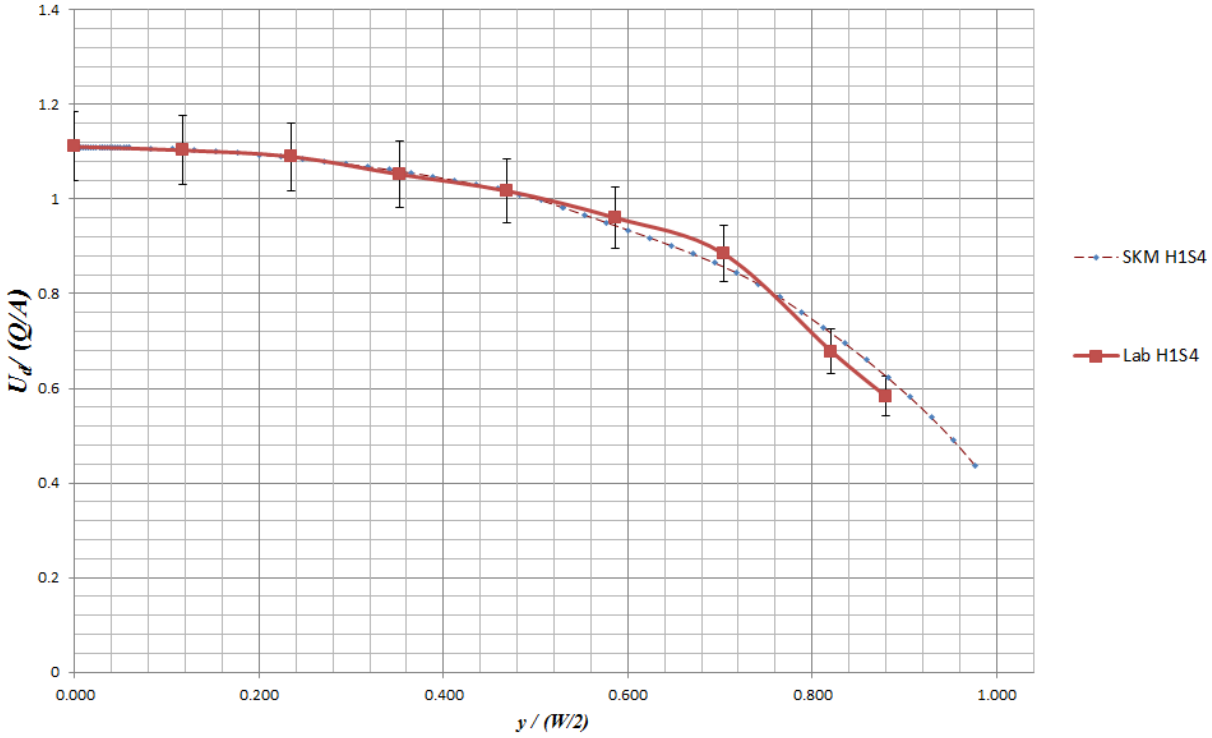

Figure C- 19. Dimensionless calibrated velocity distributions along the experimental data with their uncertainty bars, for H1S4 on rough surface, using h_c=3.27cm, S=0.004913, $f_{1,2}$= 0.0628,f_3=0.0617, f_4=0.0628, f_5=0.0696, f_6=0.0764, $p_{1,2}$=-1, p_3=-1, p_4=-1, p_5=-1, p_6=-1, C=0.175, and λ=0.07.

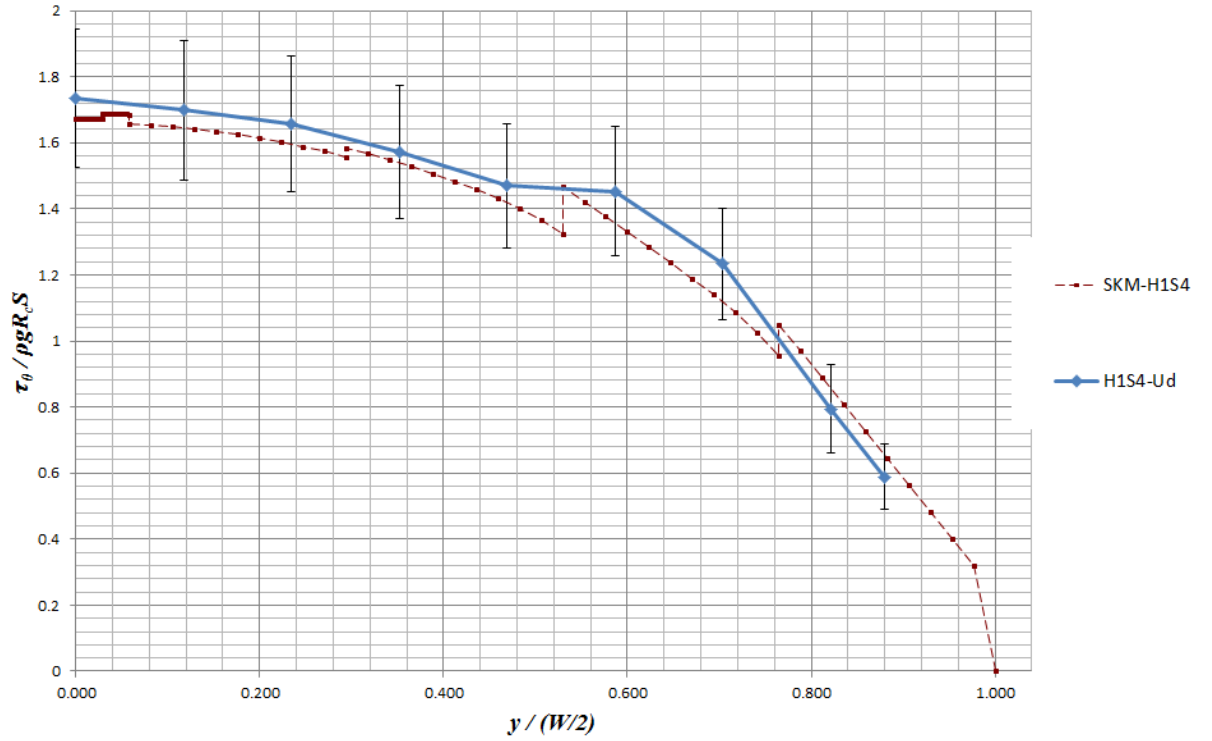

Figure C- 20. Dimensionless calibrated boundary shear stress distribution along the experimental data with error bars, for H1S4 on rough surface, using h_c=3.27cm, S=0.004913, $f_{1,2}$= 0.0628,f_3=0.0617, f_4=0.0628, f_5=0.0696, f_6=0.0764, $p_{1,2}$=-1, p_3=-1, p_4=-1, p_5=-1, p_6=-1, C=0.175, and λ=0.07.

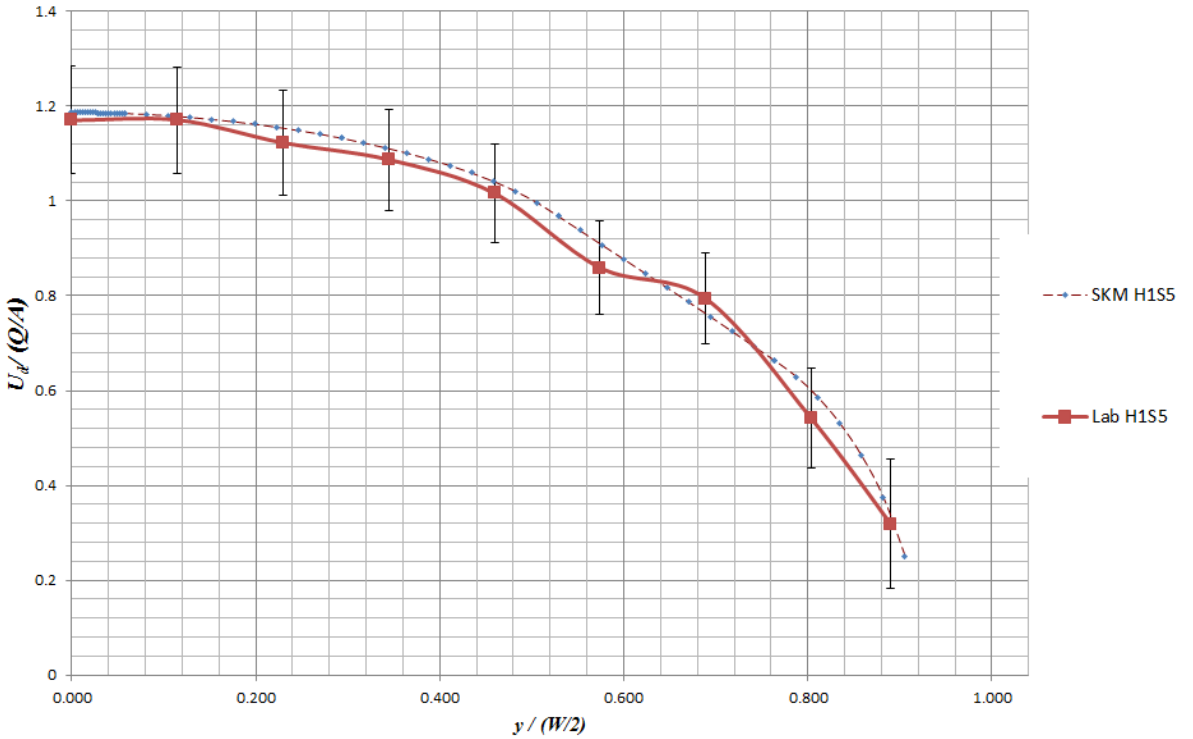

Figure C- 21. Dimensionless calibrated velocity distributions along the experimental data with their uncertainty bars, for H1S5 set on rough surface, using h_c=3.49cm, S=0.001742, $f_{1,2}$= 0.0601, f_3=0.0591, f_4=0.0601, f_5=0.0667, f_6=0.0731, $p_{1,2}$=1, p_3=1, p_4=1, p_5=1.5, p_6=1, C=0.200, and λ=0.07.

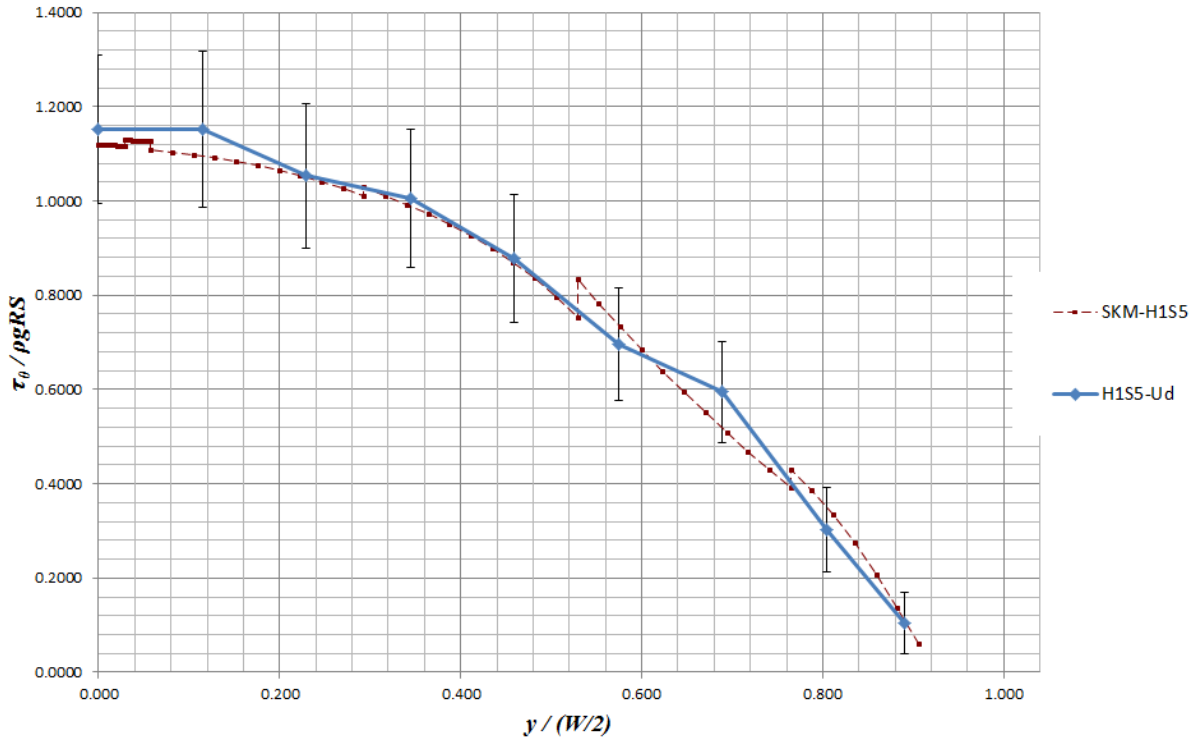

Figure C- 22. Dimensionless calibrated boundary shear stress distribution along the experimental data with their uncertainty bars, for H1S5 on rough surface, using h_c=3.49cm, S=0.001742, $f_{1,2}$= 0.0601, f_3=0.0591, f_4=0.0601, f_5=0.0667, f_6=0.0731, $p_{1,2}$=1, p_3=1, p_4=1, p_5=1.5, p_6=1, C=0.200, and λ=0.07.

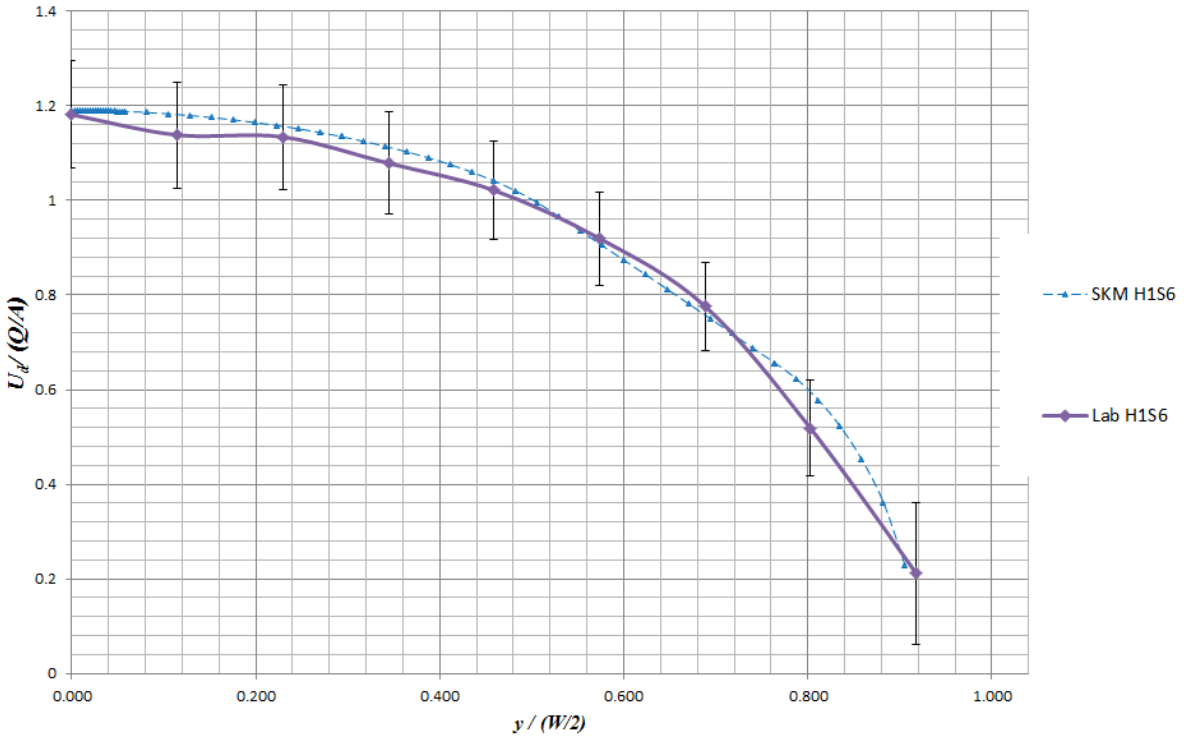

Figure C- 23. Dimensionless calibrated velocity distributions along the experimental data with their uncertainty bars, for H1S6 set on rough surface, using h_c=3.50cm, S=0.001482, $f_{1,2}$= 0.0567, f_3=0.0557, f_4=0.0567, f_5=0.0629, f_6=0.0690, $p_{1,2}$=1, p_3=1, p_4=1, p_5=1.25, p_6=1, C=0.195, and λ=0.07.

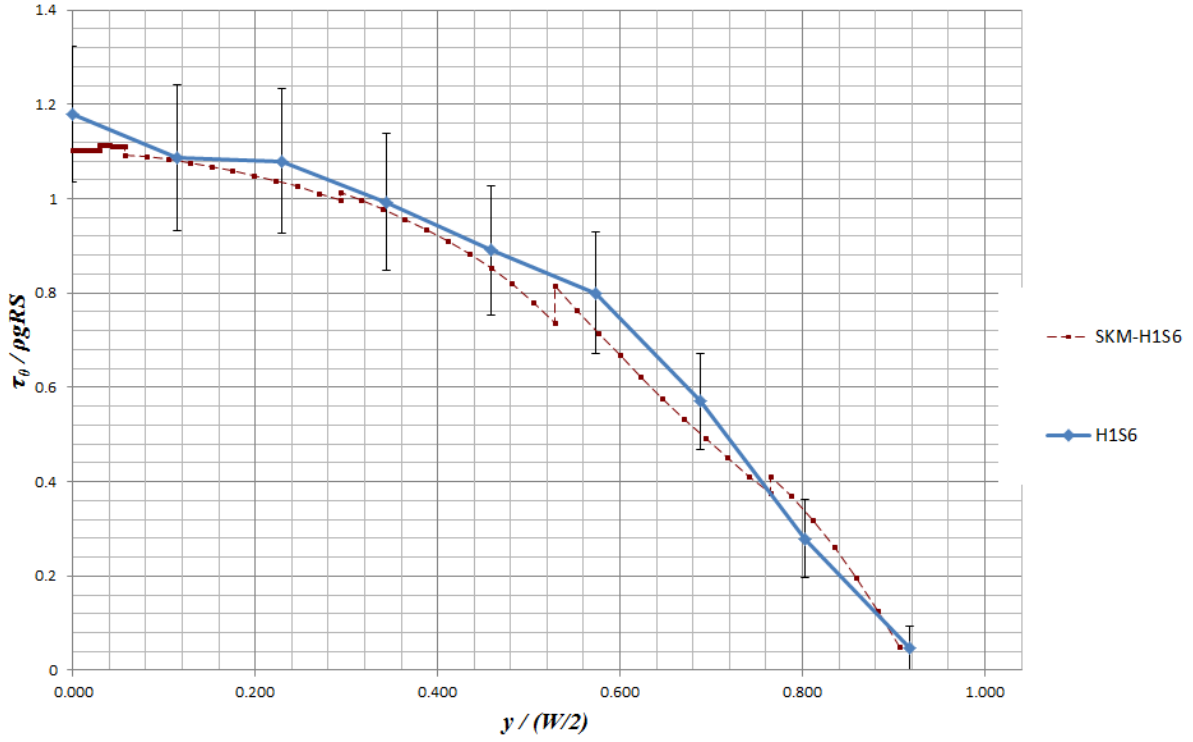

Figure C- 24. Dimensionless calibrated boundary shear stress distribution along the experimental data with their uncertainty bars, for H1S6 on rough surface, using h_c=3.50cm, S=0.001482, $f_{1,2}$= 0.0567, f_3=0.0557, f_4=0.0567, f_5=0.0629, f_6=0.0690, $p_{1,2}$=1, p_3=1, p_4=1, p_5=1.25, p_6=1, C=0.195, and λ=0.07.

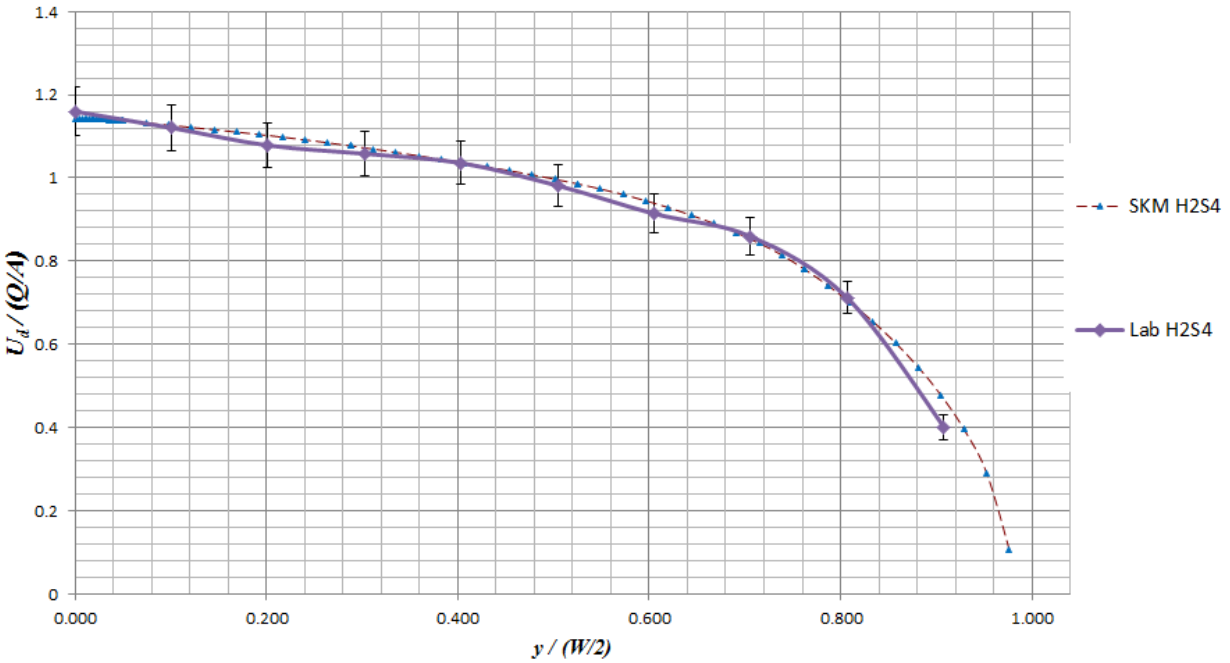

Figure C- 25. Dimensionless calibrated velocity distributions along the experimental data with their uncertainty bars, for H2S4 set on rough surface, using h_c=5.05cm, S=0.004943, $f_{1,2}$= 0.0529, f_3=0.0538, f_4=0.0559, f_5=0.0602, f_6=0.0647, $p_{1,2}$=-1, p_3=2, p_4=2, p_5=0.5, p_6=1, C=0.060, and λ=0.07.

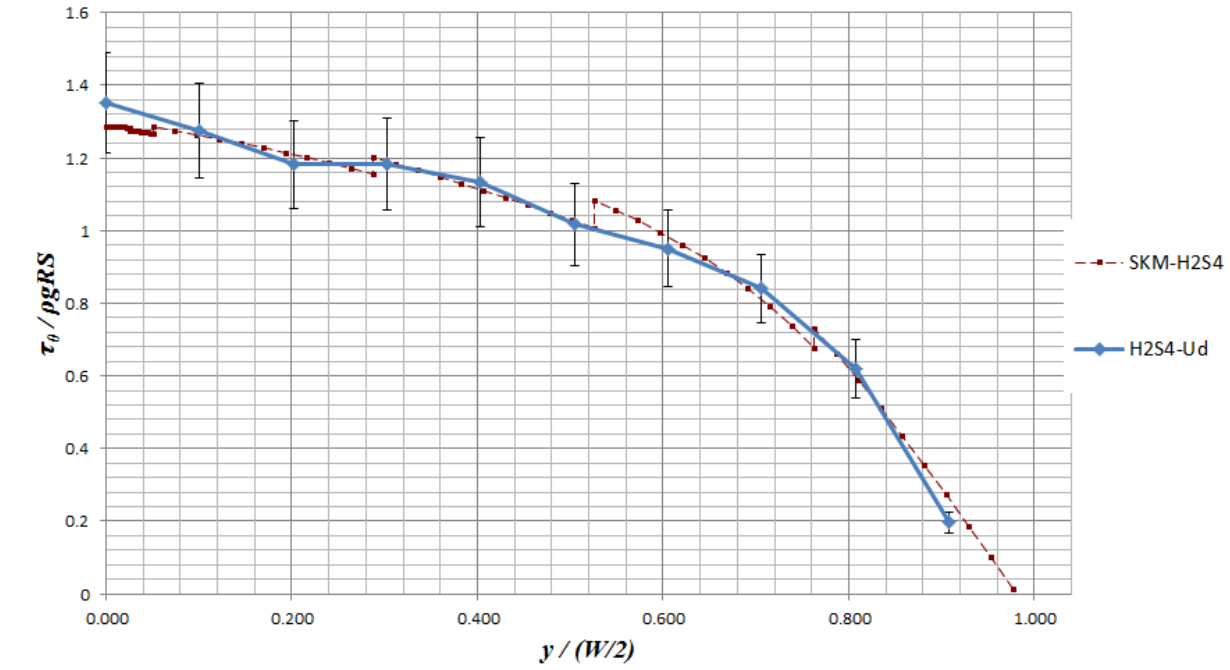

Figure C- 26. Dimensionless calibrated boundary shear stress distribution along the experimental data with their uncertainty bars, for H2S4 on rough surface, using h_c=5.05cm, S=0.004943, $f_{1,2}$= 0.0529, f_3=0.0538, f_4=0.0559, f_5=0.0602, f_6=0.0647, $p_{1,2}$=-1, p_3=2, p_4=2, p_5=0.5, p_6=1, C=0.060, and λ=0.07.

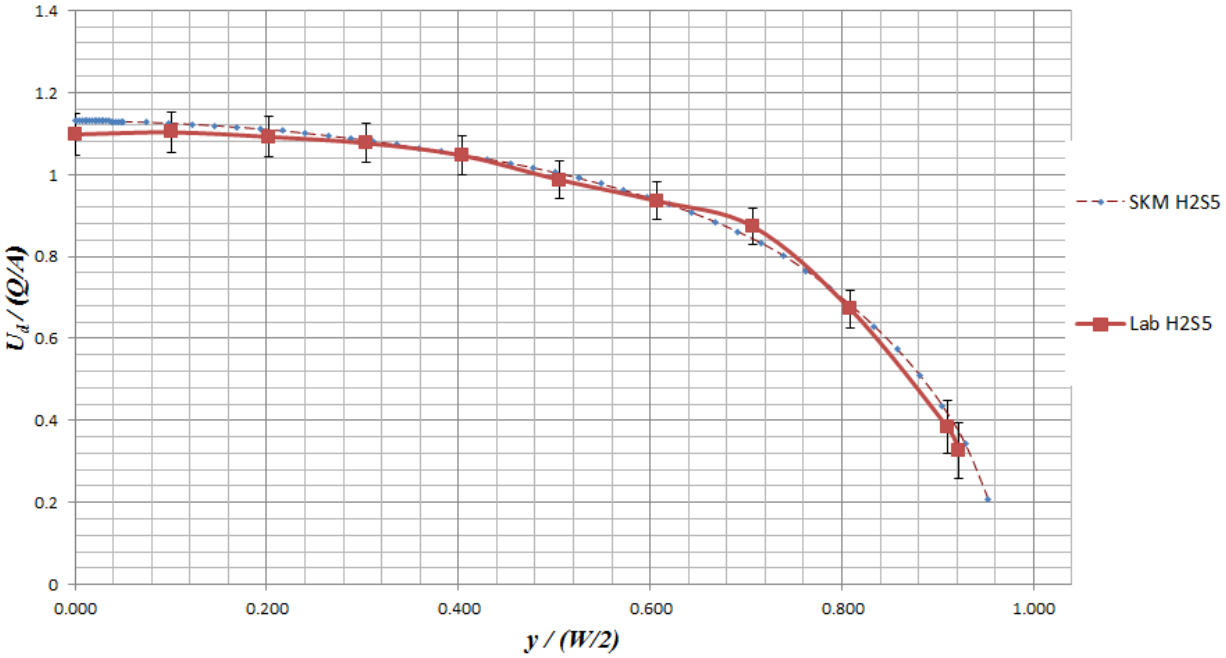

Figure C- 27. Dimensionless calibrated velocity distributions along the experimental data with their uncertainty bars, for H2S5 set on rough surface, using h_c=5.02cm, S=0.001742, $f_{1,2}$= 0.0519, f_3=0.0528, f_4=0.0548, f_5=0.0591, f_6=0.0635, $p_{1,2}$=1, p_3=1, p_4=1, p_5=0.5, p_6=1, C=0.100, and λ=0.07.

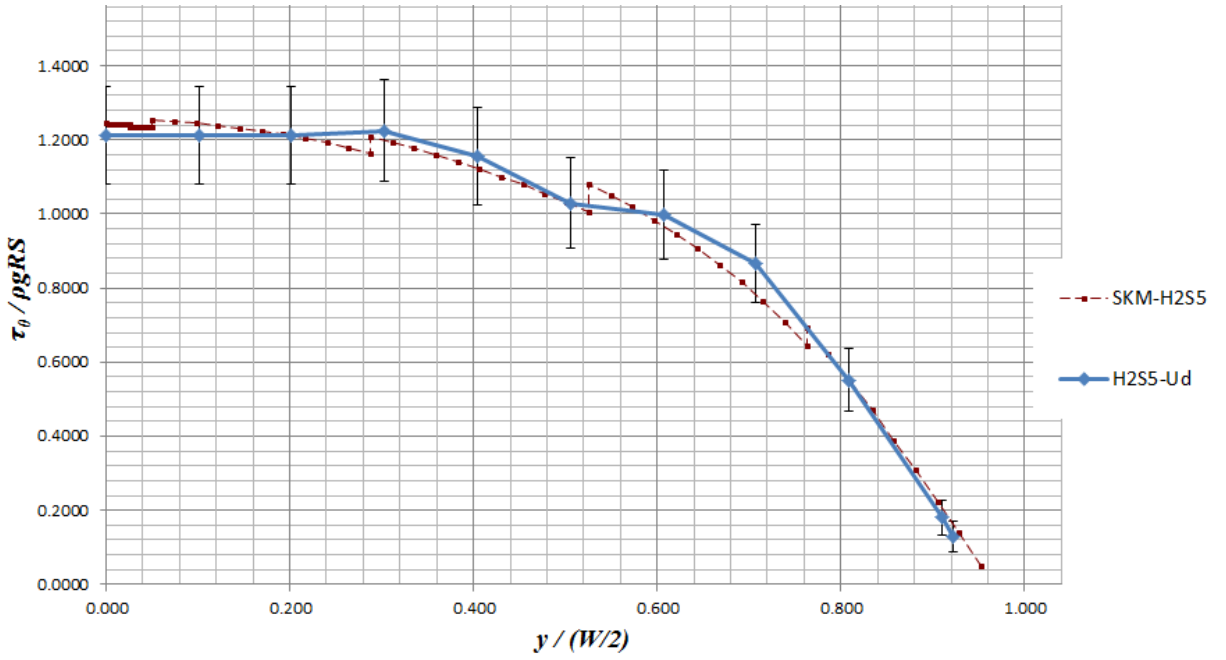

Figure C- 28. Dimensionless calibrated boundary shear stress distribution along the experimental data with their uncertainty bars, for H2S5 on rough surface, using h_c=5.02cm, S=0.001742, $f_{1,2}$= 0.0519, f_3=0.0528, f_4=0.0548, f_5=0.0591, f_6=0.0635, $p_{1,2}$=1, p_3=1, p_4=1, p_5=0.5, p_6=1, C=0.100, and λ=0.07.

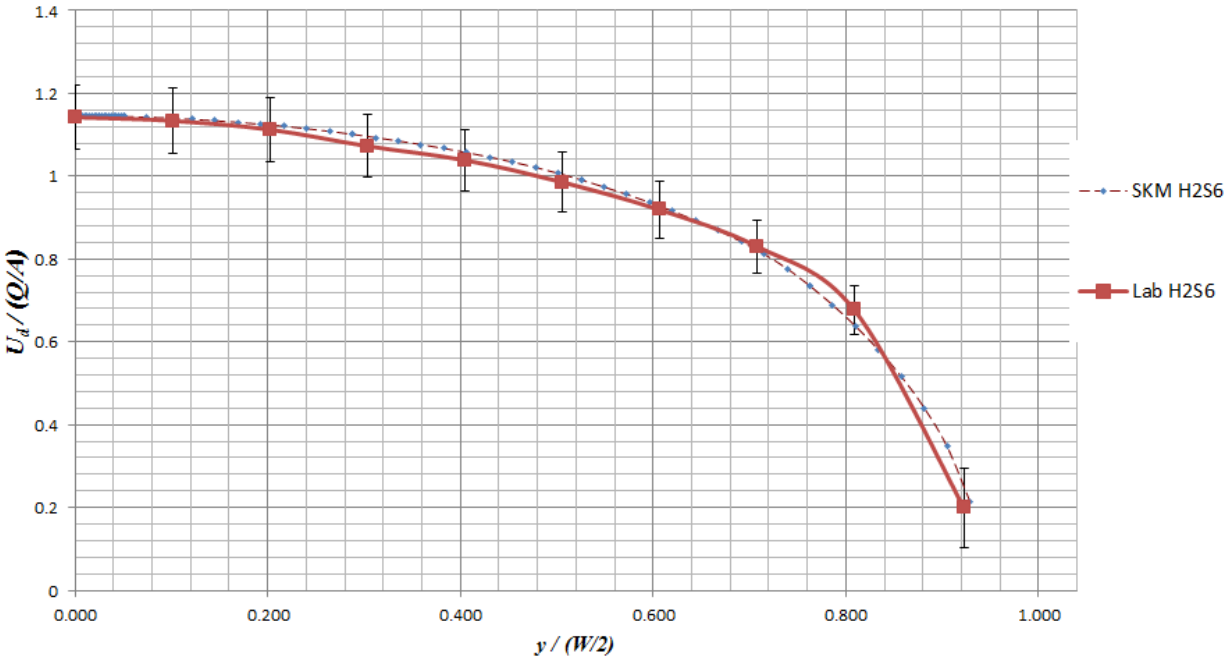

Figure C- 29. Dimensionless calibrated velocity distributions along the experimental data with their uncertainty bars, for H2S6 set on rough surface, using h_c=5.02cm, S=0.001482, $f_{1,2}$= 0.0490, f_3=0.0498, f_4=0.0517, f_5=0.0558, f_6=0.0599, $p_{1,2}$=1, p_3=1, p_4=1, p_5=1, p_6=2, C=0.085, and λ=0.07.

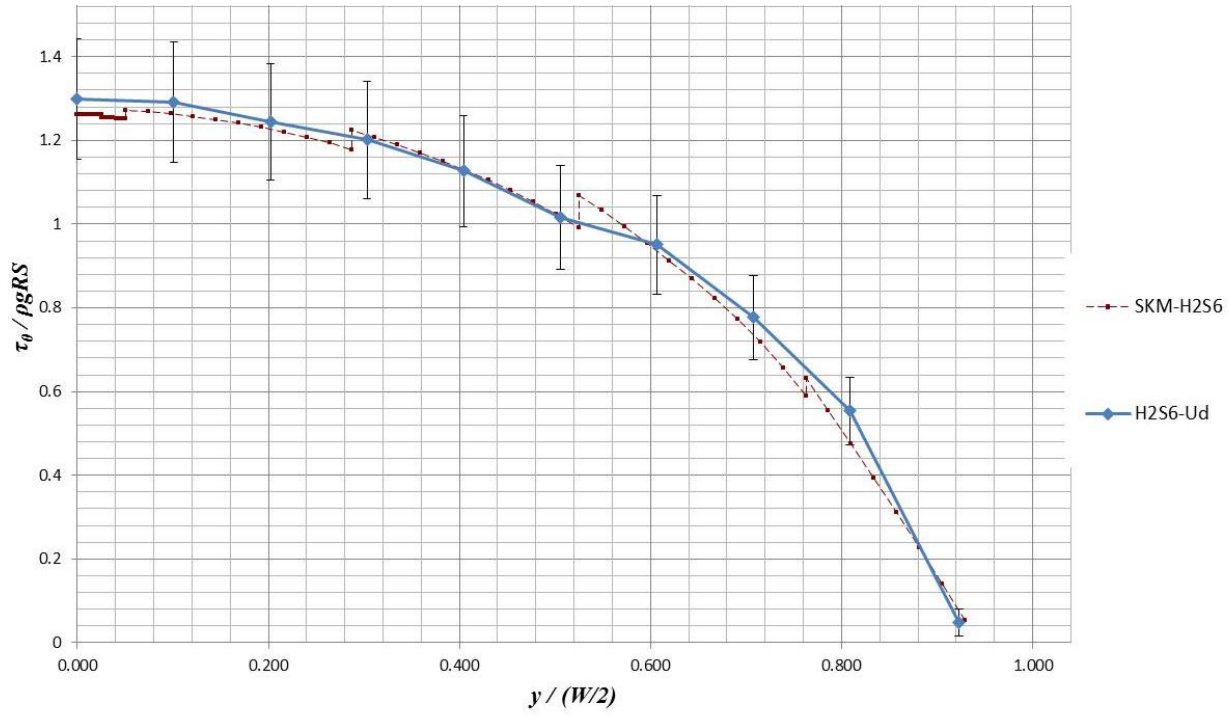

Figure C- 30. Dimensionless calibrated boundary shear stress distribution along the experimental data with their uncertainty bars, for H2S6 rough surface, using h_c=5.02cm, S=0.001482, $f_{1,2}$= 0.0490, f_3=0.0498, f_4=0.0517, f_5=0.0558, f_6=0.0599, $p_{1,2}$=1, p_3=1, p_4=1, p_5=1, p_6=2, C=0.085, and λ=0.07.

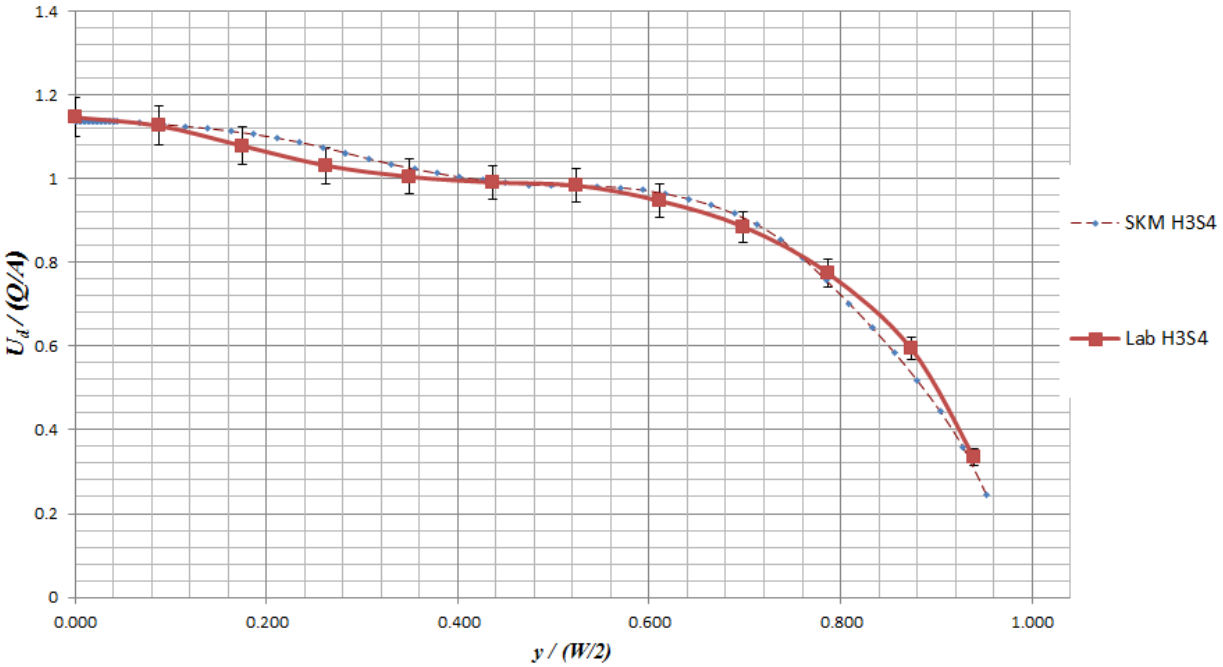

Figure C- 31. Dimensionless calibrated velocity distributions along the experimental data with their uncertainty bars, for H3S4 set on rough surface, using h_c=7.02cm, S=0.004943, $f_{1,2}$= 0.0484, f_3=0.0506, f_4=0.0502, f_5=0.0553, f_6=0.0596, $p_{1,2}$=-1, p_3=-1, p_4=1.5, p_5=-2, p_6=0.5, C=0.155, and λ=0.07.

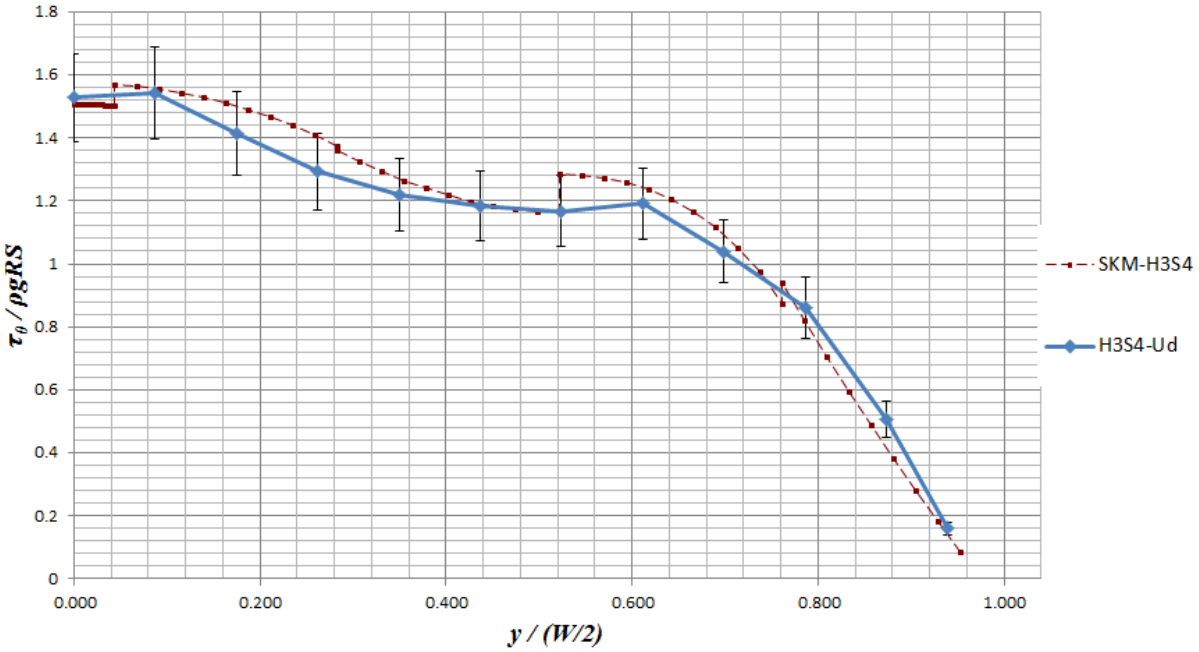

Figure C- 32. Dimensionless calibrated boundary shear stress distribution along the experimental data with their uncertainty bars, for H3S4 on rough surface, using h_c=7.02cm, S=0.004943, $f_{1,2}$= 0.0484, f_3=0.0506, f_4=0.0502, f_5=0.0553, f_6=0.0596, $p_{1,2}$=-1, p_3=-1, p_4=1.5, p_5=-2, p_6=0.5, C=0.155, and λ=0.07.

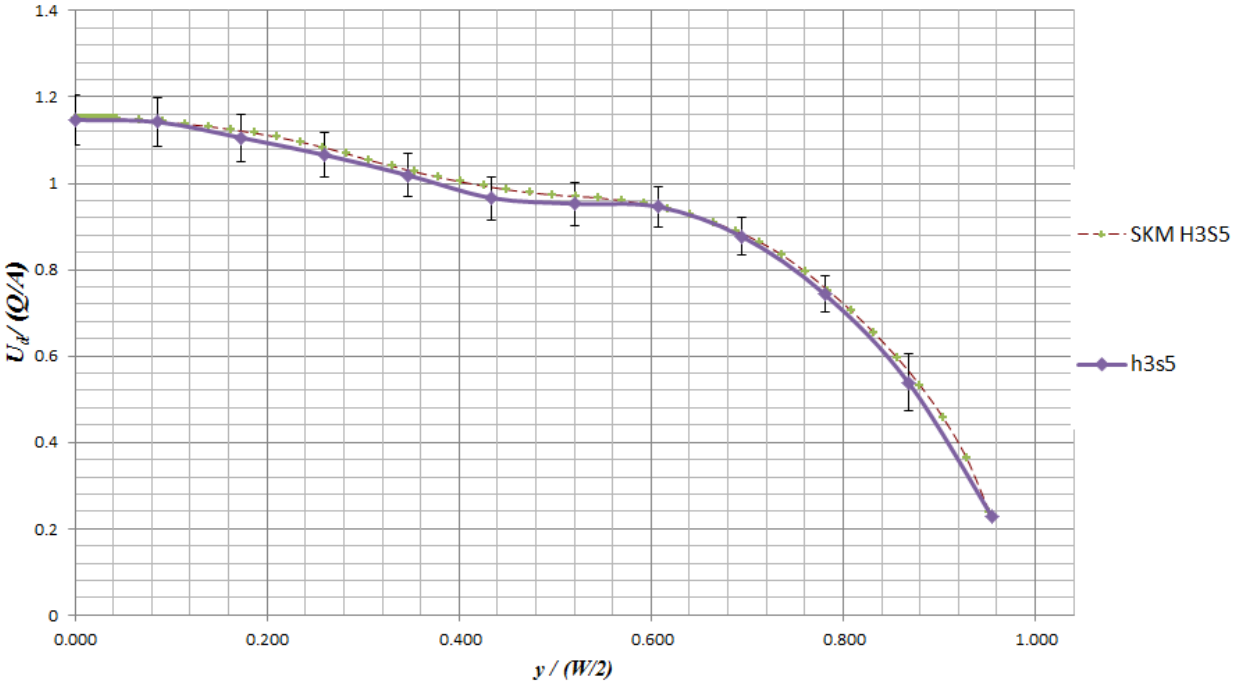

Figure C- 33. Dimensionless calibrated velocity distributions along the experimental data with their uncertainty bars, for H3S5 on rough surface, using h_c=7.12cm, S=0.001742, $f_{1,2}$= 0.0472, f_3=0.0494, f_4=0.0490, f_5=0.0539, f_6=0.0581, $p_{1,2}$=1, p_3=1, p_4=8, p_5=-1, p_6=2, C=0.045, and λ=0.07

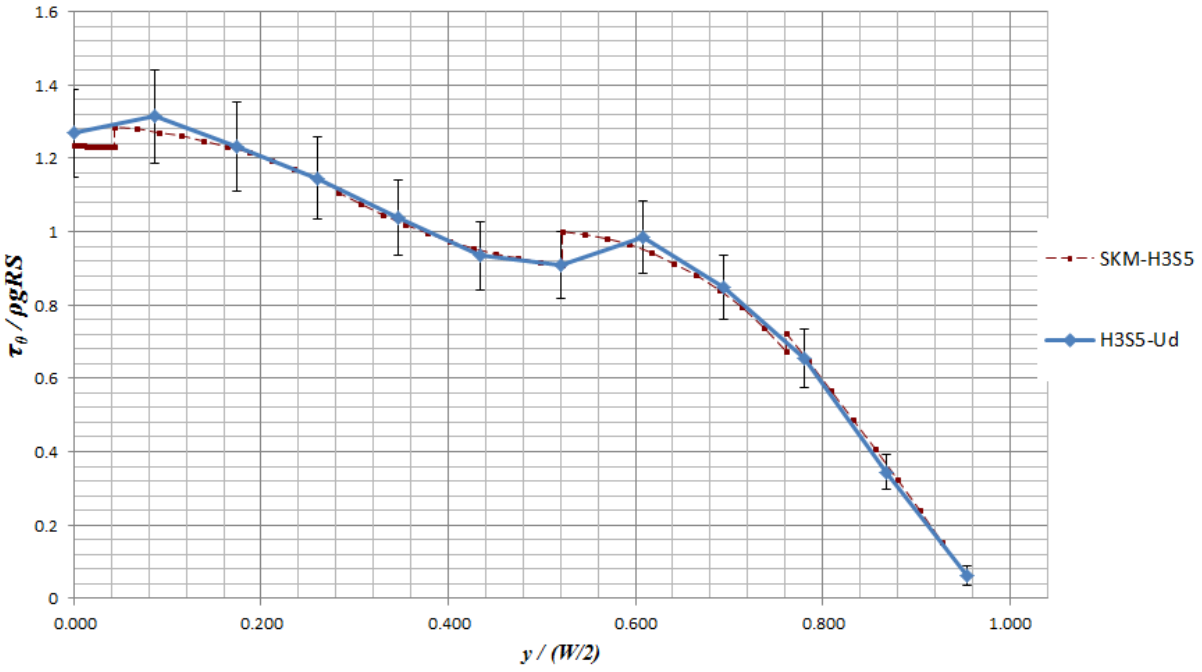

Figure C- 34. Dimensionless calibrated boundary shear stress distribution along the experimental data with their uncertainty bars, for H3S5 on rough surface, using h_c=7.12cm, S=0.001742, $f_{1,2}$= 0.0472, f_3=0.0494, f_4=0.0490, f_5=0.0539, f_6=0.0581, $p_{1,2}$=1, p_3=1, p_4=8, p_5=-1, p_6=2, C=0.045, and λ=0.07.

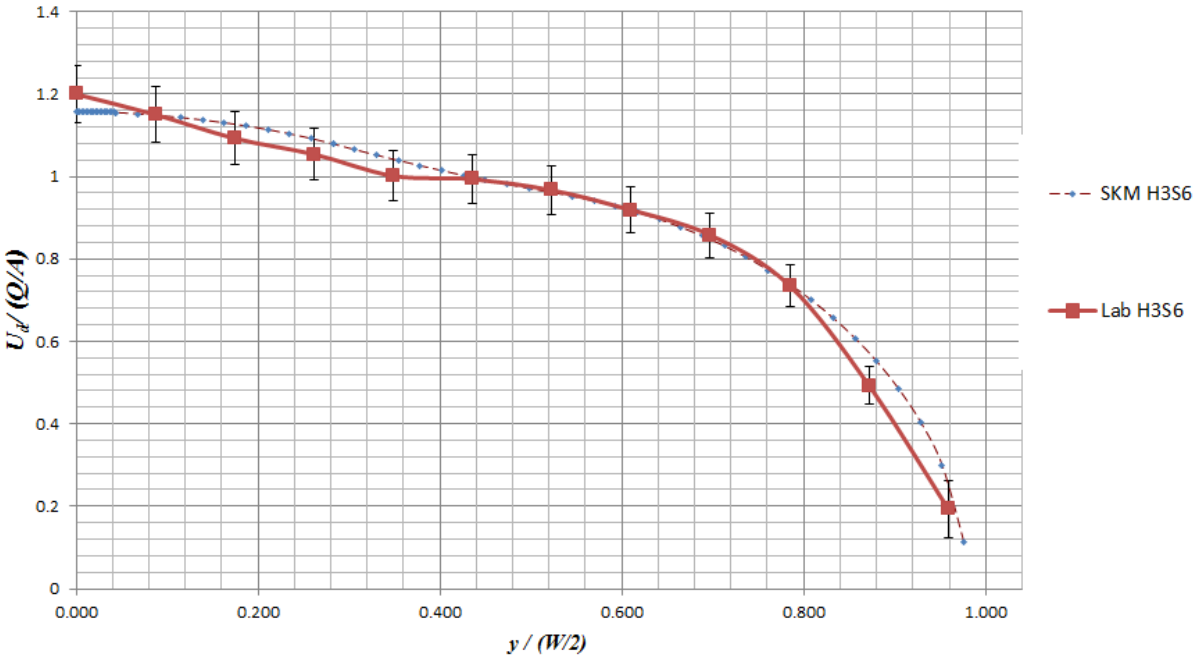

Figure C- 35. Dimensionless calibrated velocity distributions along the experimental data with their uncertainty bars, for H3S6 on rough surface, using h_c=7.09cm, S=0.001482, $f_{1,2}$= 0.0447, f_3=0.0467, f_4=0.0464, f_5=0.0510, f_6=0.0550, $p_{1,2}$=1, p_3=2, p_4=4, p_5=1, p_6=1, C=0.050, and λ=0.07.

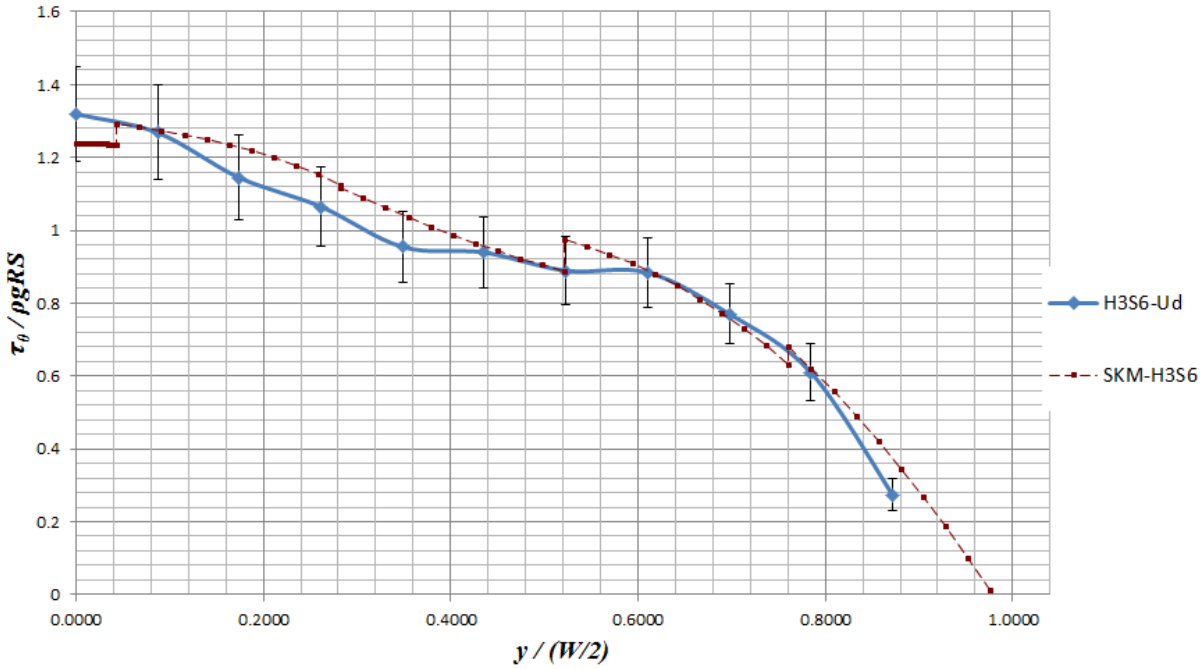

Figure C- 36. Dimensionless calibrated boundary shear stress distribution along the experimental data with their uncertainty bars, for H3S6 on rough surface, using h_c=7.09cm, S=0.001482, $f_{1,2}$= 0.0447, f_3=0.0467, f_4=0.0464, f_5=0.0510, f_6=0.0550, $p_{1,2}$=1, p_3=2, p_4=4, p_5=1, p_6=1, C=0.050, and λ=0.07.